Dielectric Properties and Cooperative Dynamics of Protic and Aprotic Room-Temperature Ionic Liquids

Dissertation
zur Erlangung des
Doktorgrades der Naturwissenschaften
(Dr. rer. nat.)
der Naturwissenschaftlichen Fakultät IV
Chemie und Pharmazie
der Universität Regensburg

vorgelegt von
Thomas Sonnleitner
aus Regensburg

Regensburg 2013

Promotionsgesuch eingereicht am:	10.12.2013
Tag des Kolloquiums:	31.01.2014
Die Arbeit wurde angeleitet von:	Apl. Prof. Dr. R. Buchner
Prüfungsausschuss:	Apl. Prof. Dr. R. Buchner Prof. Dr. W. Kunz Prof. Dr. A. Pfitzner Prof. Dr. J. Daub (Vorsitzender)

für
meine Eltern
meine Schwester
und Susi

Vorwort

Diese Doktorarbeit entstand in der Zeit von Oktober 2010 bis Dezember 2013 am Institut für Physikalische und Theoretische Chemie der naturwissenschaftlichen Fakultät IV – Chemie und Pharmazie – der Universität Regensburg.

An erster Stelle möchte ich mich bei Herrn Apl. Prof. Dr. Richard Buchner für die Erteilung des Themas bedanken. Sein Interesse am Fortschritt der Arbeit, die stete Bereitschaft zur fachlichen Diskussion sowie seine wertvollen Ratschläge haben wesentlich zum Gelingen dieser Arbeit beigetragen. Neben den zahlreichen Dienstbesprechungen danke ich ihm besonders für die Ermöglichung mehrerer Konferenzteilnahmen und Forschungsaufenthalte.

Des Weiteren gilt mein Dank dem Leiter des Lehrstuhls, Herrn Prof. Dr. W. Kunz für die Bereitstellung der Laboratorien und Verbrauchsmaterialien.

Der deutschen Forschungsgemeinschaft (DFG) sei für die Finanzierung sowie die Bereitstellung der Mittel zur Durchführung des Projektes im Rahmen des Schwerpunktprogramms 1191 gedankt.

Ferner möchte ich mich bei folgenden Kooperationspartnern bedanken, ohne deren Unterstützung wesentliche Teile dieser Arbeit nicht möglich gewesen wären:

- Herrn Prof. Dr. Glenn Hefter (Murdoch University, Western Australia) danke ich für seine stete Diskussionsbereitschaft und die große Unterstützung hinsichtlich des in Kapitel 3.1 präsentierten Materials. Ihm und seiner Frau Miriam sei ebenfalls für die ein oder andere Dienstbesprechung gedankt.

- Herrn Prof. Dr. Klaas Wynne und Dr. David Turton (Glasgow University, Glasgow, UK) danke ich ganz besonders für zwei Forschungsaufenthalte in Glasgow, welche für mich nicht nur fachlich, sondern auch persönlich von unschätzbarem Wert waren. Besonders danken möchte ich Dr. David Turton für die intensive Zusammenarbeit auf dem Gebiet der Ferninfrarot- und Optischen Kerr-Effekt Spektroskopie, wodurch wesentliche Teile dieser Arbeit entstanden sind.

- Herrn Dr. M. Walther (Albert-Ludwigs-Universität, Freiburg) sowie seinen Mitarbeitern, Dipl. Phys. Alex Ortner und Dipl. Phys. Stefan Waselikowski danke ich im Besonderen für die Durchführung der THz-TDS-Messungen zahlreicher Proben.

- Herrn Dr. Johannes Hunger (Max-Planck Institut, Mainz, Germany) danke ich außerordentlich für die fruchtbare Zusammenarbeit und die vielen wertvollen Diskussionen auf dem Gebiet der Dielektrischen Relaxationsspektroskopie.

- Herrn Prof. Dr. O. Steinhauser und Dr. C. Schröder (University of Vienna, Austria) möchte ich für die Zusammenarbeit und Diskussionen auf zahlreichen Konferenzen danken.

- Frau M. Sc. Viktoriya Nikitina danke ich für die gute Zusammenarbeit bezüglich des in Kapitel 5 präsentierten Materials.

- Herrn Prof. Dr. Y. Umebayashi und M. Sc. Hiroyuki Doi (Niigata University, Niigata, Japan) danke ich für die angenehme Zusammenarbeit und die zur Verfügungstellung einiger Messungen des in Kapitel 3.2 präsentierten Materials. Besonders möchte ich mich bei M. Sc. Hiroyuki Doi für die herausragende Betreuung bei der ICSC Konferenz in Kyoto bedanken. In diesem Zusammenhang gilt mein Dank auch Herrn Dr. M. Kanakubo (National Institute of Advanced Industrial Science and Technology, Sendai, Japan), welcher die Teilnahme ermöglicht hat.

Bei allen Mitarbeitern und Kollegen des Lehrstuhls möchte ich mich für die freundschaftliche Atmosphäre und stete Hilfsbereitschaft bedanken. Dabei richtet sich mein besonderer Dank an die ehemaligen Mitarbeiter des AK Buchner, Herrn Dr. Johannes Hunger, Herrn Dr. Alexander Stoppa, Herrn Dr. Hafiz Rahman und Frau Dr. Saadia Shaukat, für die freundschaftliche Aufnahme in die Arbeitsgruppe, die Einweisung in die Messinstrumente und ihre zahlreichen Tipps, welche entscheidend zum Gelingen dieser Arbeit beigetragen haben. Des Weiteren gilt mein besonderer Dank Herrn Dr. Andreas Eiberweiser für die langjährige Zusammenarbeit. Die freundschaftliche Arbeitsatmosphäre und seine stete Diskussionsbereitschaft über fachliche und nicht-fachliche Themen waren für mich eine Bereicherung. Ebenso bedanke ich mich ganz herzlich bei meinem aktuellen Kollegen M. Sc. Andreas Nazet, welcher mir besonders mit seinen fundierten Programmierkenntnissen jederzeit mit Rat und Tat zur Seite stand.

Ganz besonders möchte ich auch meiner Familie und meiner Freundin Susi danken, welche stets mit großem Interesse meinen Werdegang verfolgt haben und mich jederzeit unterstützt haben.

Für die mentale Unterstützung am Arbeitsplatz möchte ich mich herzlich bei meiner Mensa-Essensgruppe und allen Teilnehmern der Kaffeerunde bedanken, welche täglich für einen angenehmen Ausgleich gesorgt haben.

Nicht zuletzt möchte ich allen Mitarbeitern der Werkstätten für die schnelle und gewissenhafte Erledigung der Aufträge meinen Dank aussprechen.

Contents

Constants and symbols

Constants

Electric field constant	ε_o	$= 8.854187816 \cdot 10^{-12}\,\mathrm{C^2(Jm)^{-1}}$
Avogadro's constant	N_A	$= 6.0221367 \cdot 10^{23}\,\mathrm{mol^{-1}}$
Speed of light	c	$= 2.99792458 \cdot 10^{8}\,\mathrm{m\,s^{-1}}$
Boltzmann's constant	k_B	$= 1.380658 \cdot 10^{-23}\,\mathrm{J\,K^{-1}}$
Permittivity of vacuum	μ_0	$= 4\pi \cdot 10^{-7}\,\mathrm{(Js)^2(C^2m)^{-1}}$
Planck's constant	h	$= 6.6260755 \cdot 10^{-34}\,\mathrm{Js}$

Symbols

$\vec{E}$	electric field strength ($\mathrm{V\,m^{-1}}$)	$\vec{P}$	polarization ($\mathrm{C\,m^{-2}}$)
n	refractive index	$\hat{\varepsilon}$	complex dielectric permittivity
χ	electric susceptibility	ε'	real part of $\hat{\varepsilon}$
ω	angular frequency ($\mathrm{s^{-1}}$)	ε''	imaginary part of $\hat{\varepsilon}$
τ	relaxation time (s)	ε_∞	$\lim_{\nu\to\infty}(\varepsilon')$
η	viscosity (Pa s)	ε_s	$\lim_{\nu\to 0}(\varepsilon')$
T	temperature (K)	μ	dipole moment ($\mathrm{C\,m}$)
t	time (s)	ν	frequency (Hz)
c	molarity ($\mathrm{mol\ dm^{-3}}$)	λ	wavelength (m)
κ	conductivity ($\mathrm{S\ m^{-1}}$)	ρ	density ($\mathrm{kg\,m^{-3}}$)

Acronyms

AN	acetonitrile	AIL	aprotic ionic liquid
BN	benzonitrile	1-BuOH	1-butanol
CC	Cole-Col	CD	Cole-Davidson
CIP	contact ion-pair	D	Debye
DCA	dicyanamide	DHO	damped harmonic oscillator
DMA	*N*,*N*-dimethylacetamide	DMF	*N*,*N*-dimethylformamide
DR(S)	dielectric relaxation (spectroscopy)	EAN	ethylammonium nitrate
FIR	far-infrared	HN	Havriliak-Negami
G	antisymmetrized Gaussian	IFM	interferometer
IL	ionic liquid	IR	infrared
MD	molecular dynamics	C_1Im	1-methylimidazole
NMR	nuclear magnetic resonance	OKE	optical Kerr-effect
TPX	polymethylpentene	PAN	propylammonium nitrate
PIL	protic ionic liquid	PRT	platinum resistance thermometer
PTFE	polytetrafluoroethylene	RTIL	room temperature ionic liquid
SED	Stokes-Einstein-Debye	SIP	solvent separated ion-pair
TDR	time-domain reflectometry	TFSA	bis(trifluoromethanesulfonyl)-amide
THz-TDS	terahertz time-domain spectroscopy	vdW	van der Waals
VFT	Vogel-Fulcher-Tammann	VNA	vector network analyzer

Introduction

For more than two decades ionic liquids (ILs) have been attracting increasing attention due to their unique combination of properties.[1–4] Entirely consisting of ionic species, ILs represent a sub-class of compounds, which are traditionally known as molten salts. With the onset of intensive IL research in the late 1990's, the term "ionic liquid" has been established to denote those salts with melting points or glass-transition temperatures below 100 °C.[1,5] Possibly the first discovered salt that meets this condition was ethanolammonium nitrate and was reported as early as in 1888 by Gabriel[6] with a melting point of $\sim 52 - 55\,^{\circ}\mathrm{C}$.[7] A separate niche of ILs are those being liquid at ambient temperatures, therefore commonly referred to as room-temperature ionic liquids (RTILs). In 1914, Walden reported the physical properties of ethylammonium nitrate (EAN, melting point: 14 °C),[8] which today is widely acknowledged as the advent of the field of ILs but has not received much attention at that time. A "new class of room-temperature ionic liquids"[9] based on dialkylimidazolium chloroaluminates has been reported in 1982 followed, ten years later, by the discovery of apparently "air and water stable 1-ethyl-3-methylimidazolium-based ionic liquids"[10] formed with weakly coordinating anions such as hexafluorophosphate PF_6^- and tetrafluoroborate, BF_4^-, representing another benchmark in IL research. Because of the later observed hydrolysis of PF_6^-,[11] which is accompanied by the undesirable release of hydrofluoric acid, the development of ILs based on more hydrophobic anions such as bis(trifluoromethanesulfonyl)amide ($TFSA^-$) received increasing interest, which, apart from their lower hygroscopicity, have attracted particular attention for potential applications in electrochemical devices, due to their enhanced electrochemical windows.[12,13] Since that time, the interest in ILs has continuously grown, which has manifested itself not only in a nearly exponential increase of publications[13] but also in scientific programs such as the "DFG-SPP 1191 priority program: ionic liquids" started in 2006 specifically dedicated to improve "understanding of the special nature of ionic liquids through fundamental research".[14] Nowadays, ILs are known to offer important advantages in electrochemistry,[15] organic synthesis and catalysis[5,16,17] because of their negligible vapor pressure,[18] high thermal and electrochemical stability,[19,20] and solubilizing capabilities.[21–23] Furthermore, due to the almost unlimited possible combinations of cations and anions, the properties of ILs can be fine-tuned selectively for specific applications,[13,24,25] which brought them the name of "designer solvents". The issue of ILs' toxicity has been controversially discussed over many years. Recently, toxicity and biodegradability studies received increasing attention eventually leading to the consensus that the commonly accepted notion of the low toxicity of ILs is incorrect.[23,26,27]

Generally, the wide field of ILs can be subdivided into two major sub-groups: protic ILs

(PILs) and aprotic ILs (AILs). In contrast to AILs, PILs, whose most prominent representative is EAN,[7,28] are formed by the combination of a Brønsted acid and a Brønsted base through proton transfer reaction. This leads to their key characteristics, which is the ability to form hydrogen-bonded networks.

At the beginning of this thesis in 2010, the most intensively studied ILs among the group of AILs, were those based on 1-alkyl-3-methylimidazolium cations.[2,17,29,30] Of particular relevance for the present work is the progress in understanding *structural* and *dynamical* properties of ILs. Also in this regard, early investigations using spectroscopic techniques[29,31–39] and MD simulations[40–45] have mainly focused on neat 1-alkyl-3-methylimidazolium ILs and their binary mixtures with molecular solvents.[46–51] This also applies to investigations of the dielectric properties of RTILs, where Weingärtner *et al.*[30,52–55] and Buchner *et al.*[46,47,49,56–58] have certainly published the most important contributions. With the beginning of the present work, two comprehensive theses[59,60] have been finished in our group, primarily dealing with dynamics of binary mixtures of ILs with polar molecular solvents but also with those of a representative set of neat 1-alkyl-3-methylimidazolium ILs.
As a consequence, PILs and AILs constituted of other cations such as pyridinium, pyrrolidinium, phosphonium or sulfonium have been out of the major focus of IL research, except for some recent investigations that include studies using NMR-relaxation,[61–63] far-infrared (FIR) spectroscopy,[64–66] optical heterodyne-detected Kerr-effect (OKE) spectroscopy,[67–69] time-resolved fluorescence spectroscopy,[70] quasi-elastic neutron scattering (QENS)[71] and MD simulations.[72–74] In particular, dielectric studies are very scarce up to now. Apart from few works,[46,52,54,75] which, however, were limited in their investigated frequency and/or temperature range, dielectric properties and intermolecular dynamics of PILs and non-imidazolium AILs have been almost unexplored.
The static dielectric permittivity, ε_s, represents a fundamental quantity for characterizing the polarity of a solvent. The question of "how polar are ionic liquids?"[76] has been controversially discussed for a long time, mainly because inappropriate methods have been used for the determination of ε_s. Eventually, this dispute was settled by means of dielectric relaxation spectroscopy (DRS),[52,58,76] which represents the only technique available for directly determining ε_s of conducting samples. Apart from that, dielectric spectra provide valuable insight into dynamical properties of liquids within the MHz to THz frequency region.[57,77] In particular, comparative studies using other spectroscopic techniques such as OKE spectroscopy have shown to be powerful tools for investigating the dynamics of liquids as complex as RTILs.[36] Although considerable effort has been made, still no satisfactory picture of the molecular-level dynamics of RTILs in general and of PILs and non-imidazolium AILs in particular has emerged up to date.

Aims of this study

The overall aim of this thesis is the investigation of the dielectric properties and intermolecular dynamics of RTILs. DRS is used as the main technique and is complemented by OKE spectroscopy, for most of the studied neat ILs. Additionally, physicochemical properties such as density, viscosity and electrical conductivity are reported. In general the present

work can be subdivided into three parts:

First, dielectric properties and dynamics of representative neat PILs are investigated (Chapter 3). The archetypal PILs EAN and propylammonium nitrate (PAN) are studied over the exceptional wide frequency range $0.2 \leq \nu/\mathrm{GHz} \leq 10\,000$ by means of DRS and OKE spectroscopy (Section 3.1). Both EAN and PAN exhibit rather simple chemical structures and thus can be viewed as model PILs. EAN has been studied by DRS[52], THz spectroscopy[75] and FIR spectroscopy,[64,65] however, limitations in either frequency or temperature range prevented a detailed analysis of the intermolecular dynamics. Therefore, in the present work, measurements of DR and OKE spectra over a temperature range of 60 K supplemented by DR and OKE spectra of partially deuterated (d_3-)EAN at 25 °C enables extensive characterization of the dynamics of EAN and PAN ranging from MHz to THz frequencies. The results so obtained improve and partially correct hitherto accepted interpretations.
Furthermore, a set of 1-methylimidazolium PILs is studied in collaboration with a Japanese research group (Prof. Dr. Umebayashi, Niigata University, Niigata, Japan) by DRS in the limited frequency range $0.2 \leq \nu/\mathrm{GHz} \leq 89$ (Section 3.2). In particular, the influence of proton transfer and temperature on the dynamics of the equimolar mixture of 1-methylimidazole (C_1Im) with acetic acid (HOAc) will be investigated. This system has been studied by calorimetric titration[78] and Raman spectroscopy,[79] however, controversial results with respect to the degree of proton transfer have been obtained. In this regard, an attempt is made to provide new insights by quantitative analysis of the present DR spectra.

Second, broadband DR and OKE spectra ($0.2 \leq \nu/\mathrm{GHz} \leq 10\,000$) of a set of four representative neat non-imidazolium AILs are recorded in the temperature range of $5 \leq \vartheta/^\circ\mathrm{C} \leq 65$ (Chapter 4). These ILs were chosen, because of their commercial availability at a sufficient purity, thus serving as model non-imidazolium AILs. Based on the $TFSA^-$ and the dicyanamide (DCA^-) anion 1-alkyl-3-methylimidazolium cations are replaced by pyridinium, pyrrolidinium and sulfonium cations to scrutinize the effect of cation variation on DR and OKE spectra. Particular focus was on the diffusional dynamics taking place from MHz to GHz frequencies associated with fluctuations of mesoscale clusters and the cooperative relaxation of anions and cations. In this regard, temperature and viscosity dependence of DR and OKE relaxation times provide valuable insights into the molecular-level dynamics of RTILs and how these may determine macroscopic transport properties such as viscosity and electrical conductivity, which is of exceptional importance for scientific and industrial applications.

Third, the binary mixture of EAN and acetonitrile (AN) is investigated as a model system of a PIL+molecular solvent mixture (Chapter 5). Therefore, DR spectra are recorded in the frequency range $0.2 \leq \nu/\mathrm{GHz} \leq 89$ at 25 °C over the entire composition range. As mentioned above, most publications dealing with the dynamics of binary mixtures of ILs with molecular solvents have focused on salts with 1-alkyl-3-methylimidazolium cations but only little is known about PIL-containing systems, up to now.[80,81] In practical applications ILs are generally mixed with other compounds. Thus, it is essential to understand

their structure and dynamics. In this regard, the transition from IL-like dynamics to that of conventional electrolyte solutions is of particular interest, which will be addressed in the present work. Additionally, the formation of ion pairs, which is a common feature of conventional electrolyte solutions at low salt concentrations[77,82] will be quantitatively investigated in the present EAN+AN mixtures. Furthermore, information on solvent/solute dynamics will be extracted providing insight into intermolecular interactions and their dependence on composition.

To analyze DR and OKE spectra recorded over such a broad frequency range ($0.2 \leq \nu/\mathrm{GHz} \leq 10\,000$), a new fitting program was required (Appendix A.2). In close collaboration with Dr. D. A. Turton (Glasgow University, Glasgow, UK), who developed a rudimentary version, a fitting routine (DRSFit) based on the commercially available IGOR software (Wavemetrics, V.6.31) has been established in our group. The ability of fitting DR as well as OKE spectra and implementation of new empirical model functions rank among the key advantages of this program.

Chapter 1

Theoretical Background

1.1 Fundamentals of dielectric relaxation

1.1.1 Polarization

Electrodynamic theory is based on Maxwell's equations, which form a set of four linear partial differential equations that are capable to describe all classical phenomena of electromagnetic radiation.[83,84] Within this theory the response of a material to an applied low-intensity electric field, $\vec{E}$, is described by the phenomenon of polarization, $\vec{P}$, which is defined as the macroscopic dipole moment of the sample per unit volume. It results from an effective charge separation in the medium and is proportional to $\vec{E}$ by

$$\vec{P} = \chi \varepsilon_0 \vec{E} \tag{1.1}$$

in case of a linear and isotropic medium. The proportionality factor $\chi (= \varepsilon_\mathrm{s} - 1)$ is the electric susceptibility and ε_0 and ε_s are the permittivity of free-space and the relative permittivity of the medium, respectively.[85] Although $\vec{P}$ is defined as a macroscopic quantity, it can be also interpreted on a microscopic level by splitting it up into two contributions

$$\vec{P} = \vec{P}_\mu + \vec{P}_\alpha \tag{1.2}$$

where $\vec{P}_\mu$ and $\vec{P}_\alpha$ are the dipolar (orientational) and induced polarization, respectively. Within the continuum approach, $\vec{P}_\mu$ is explained by the alignment of permanent dipoles embedded in a continuum of permittivity, ε_s, along the applied electric field. Its establishment takes place on the picosecond to nanosecond time scale, which corresponds to frequencies in the microwave region. It is associated with rotations of the dipole vectors and is given as

$$\vec{P}_\mu = \sum_j \rho_j \langle \mu_j \rangle \tag{1.3}$$

where ρ_j is the dipole density and $\langle \mu_j \rangle$ the ensemble average of the permanent dipole vector.[86] The complete alignment, however, is counteracted by the thermal motion of the molecules, which makes $\vec{P}$ strongly dependent on the temperature.
The induced polarization, $\vec{P}_\alpha$, can be understood as an intramolecular translational effect,

that can be separated into two contributions: the atomic polarization that results from the displacement of the nuclei of a molecule relative to each other (vibrations) and the electronic polarization that is caused by the displacement of the electrons relative to the positive charges (nuclei).[86] It is expressed as

$$\vec{P}_\alpha = \sum_j \rho_j \alpha_j (\vec{E}_{\text{int}})_j \tag{1.4}$$

where α_j is the polarizability and $(\vec{E}_{\text{int}})_j$ the internal field (cavity field) of the jth particle, which is defined as the total electric field acting on a particle minus the field generated by the particle itself.[86]
The fact that $\vec{P}_\mu$ and $\vec{P}_\alpha$ take place on sufficiently different time scales permits both to be considered as linearly independent. By introduction of ε_∞, $\vec{P}_\mu$ and $\vec{P}_\alpha$ can be written as

$$\vec{P}_\mu = (\varepsilon_{\text{s}} - \varepsilon_\infty)\varepsilon_0 \vec{E} \tag{1.5}$$

$$\vec{P}_\alpha = (\varepsilon_\infty - 1)\varepsilon_0 \vec{E} \tag{1.6}$$

where ε_∞ is the permittivity at frequencies at which the orientational polarization is completely decayed, but the induced polarization still remained unchanged (typically at a few THz).[87]

1.1.2 Response function

In case of rapidly changing electric fields, the polarization is no longer directly proportional to the applied field strength as stated by Eq. 1.1, because $\vec{P}$ then depends on the values of $\vec{E}$ at all moments before the time t at which $\vec{P}$ is considered.[86] Thus, the generalized relation between the polarization and an arbitrary time-dependent electric field is given by

$$\vec{P}(t) = \varepsilon_0 \chi \int_{-\infty}^{0} f_{\text{P}}(t - t')\vec{E}(t')\mathrm{d}t' \tag{1.7}$$

where $f_{\text{P}}(t - t')$ is the pulse-response function of the polarization, which in turn is defined as the negative time-derivative of the step response function, $F_{\text{P}}(t - t')$,[86]

$$f_{\text{P}}(t - t') = -\frac{\partial F_{\text{P}}(t - t')}{\partial (t - t')} \text{ normalized by } \int_0^\infty f_{\text{P}}(t')\mathrm{d}t' = 1. \tag{1.8}$$

In a time-domain experiment, a polarization $\vec{P}$ in a dielectric medium, which is generated by application of an external field, $\vec{E}$, decreases from $\vec{P}(0)$ to $\vec{P}(\infty) = 0$ when the field is switched off at $t = 0$. It is then assumed that on the time scale of a dielectric experiment, $\vec{P}_\alpha$ breaks down "instantaneously", whereas $\vec{P}_\mu$ decays monotonically to its final value of

$\vec{P}_\mu(\infty) = 0$.[87] This can be mathematically expressed as

$$\vec{P}_\mu(t) = \vec{P}_\mu(0) \cdot F_\mathrm{P}(t) \;\text{ with }\; F_\mathrm{P}(0) = 1 \;\text{ and }\; F_\mathrm{P}(\infty) = 0 \tag{1.9}$$

where the step-response function, $F_\mathrm{P}(t)$, is defined as the time-correlation function of the orientational polarization and is given as[88]

$$F_\mathrm{P}(t) = \frac{\langle \vec{P}_\mu(0) \cdot \vec{P}_\mu(t) \rangle}{\langle \vec{P}_\mu(0) \cdot \vec{P}_\mu(0) \rangle} \tag{1.10}$$

In case of a harmonically oscillating field, $\vec{E}(t) = \vec{E}_0 \exp(\mathrm{i}\omega t)$, the frequency-dependent orientational polarization is then written as

$$\vec{P}_\mu(\omega, t) = \varepsilon_0(\varepsilon_\mathrm{s} - \varepsilon_\infty)\vec{E}(t) \int_0^\infty \exp(\mathrm{i}\omega t') f_\mathrm{P}(t')\mathrm{d}t' \tag{1.11}$$

with

$$\int_0^\infty \exp(\mathrm{i}\omega t') f_\mathrm{P}(t')\mathrm{d}t' = \mathcal{L}_{\mathrm{i}\omega}[f_\mathrm{P}(t')] \tag{1.12}$$

where $\mathcal{L}_{\mathrm{i}\omega}[f_\mathrm{P}(t')]$ is the Laplace transformation of the pulse-response function.
With this relation, the permittivity can be expressed as a complex quantity, which is defined as[89]

$$\hat{\varepsilon}(\omega) = \varepsilon'(\omega) - \mathrm{i}\varepsilon''(\omega) = \varepsilon_\infty + (\varepsilon_\mathrm{s} - \varepsilon_\infty) \cdot \mathcal{L}_{\mathrm{i}\omega}[f_\mathrm{P}(t')] = \varepsilon_\infty + (\varepsilon_\mathrm{s} - \varepsilon_\infty) \cdot \tilde{F}_\mathrm{P}(\omega) \tag{1.13}$$

where the relaxation function, $\tilde{F}_\mathrm{P}(\omega)$, is the frequency analogue to the step-response function, $F_\mathrm{P}(t)$.
In Eq. 1.13 the real part, $\varepsilon'(\omega)$ of $\hat{\varepsilon}(\omega)$ represents the relative permittivity and is a measure of the polarization of the medium at a certain angular frequency, $\omega = 2\pi\nu$, whereas the imaginary part, $\varepsilon''(\omega)$, known as the dielectric loss or absorption describes the energy dissipation in the system. The phase shift between the electric field and the polarization is expressed by the loss angle, $\tan\delta = \varepsilon''(\omega)/\varepsilon'(\omega)$, which can be interpreted as a measure of the deviation of the system from equilibrium.[90]
In Figure 1.1 a schematic broadband dielectric spectrum is shown. Apart from possible interfacial polarization effects, which may contribute to $\hat{\varepsilon}(\nu)$ for heterogeneous systems at MHz frequencies,[86,91] the main contribution in the microwave region arises from rotational motions of molecules with permanent dipole moment. As the frequency, $\nu(= \omega/2\pi)$, increases dispersion of $\varepsilon'(\nu)$, accompanied by a simultaneously emerging absorption band in $\varepsilon''(\nu)$, is observed. This is a consequence of the inability of the molecules to follow the applied electric field. In addition to molecular rotations, "cage rattling" motions, intermolecular vibrations (e.g. hydrogen-bonding), and librations, which are described as hindered rotations or tumbling motions of the dipoles confined in intermolecular potentials, contribute to $\hat{\varepsilon}(\nu)$ at frequencies up to several THz.[86] Due to the coupling of dipoles to their environment, the band-shape of all these processes, in particular of relaxations, is

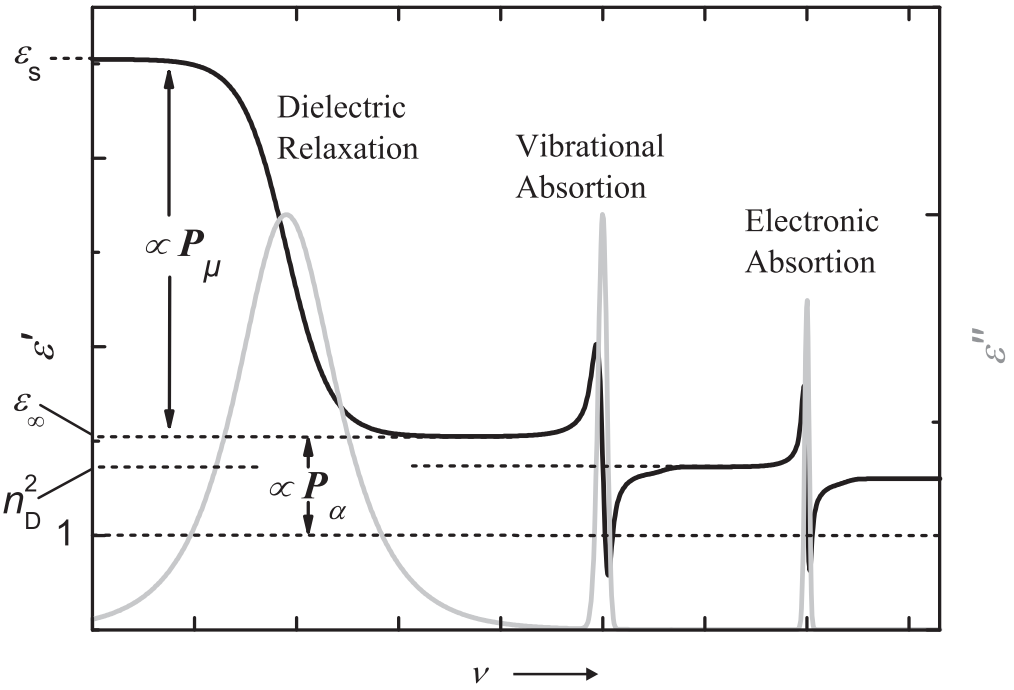

Figure 1.1: Schematic spectrum of the complex permittivity, $\hat{\varepsilon}(\nu)$, with real part, $\varepsilon'(\nu)$ (black solid line), and imaginary part, $\varepsilon''(\nu)$ (gray solid line). Exemplarily, a dielectric relaxation process (microwave region), an intramolecular vibration (infrared region) and an electronic resonance (ultra-violet region) is shown.

rather broad. Along with the entire decay of the orientational polarization, $\varepsilon'(\nu)$ reaches its high frequency limit, ε_∞, and thus marks the transition to intramolecular processes, which are associated with the induced polarization, $\vec{P}_\alpha$, including molecular vibrations (IR region) and electronic excitations (UV/Vis region). The intramolecular nature manifests itself in resonance-type dispersion steps and absorption peaks, which are narrower than those of intermolecular bands.[92]

1.1.3 Optical constants

As discussed in Section 1.1.1 the interaction of electromagnetic radiation with matter is described by Maxwell's equation and leads to a polarization, $\vec{P}$ (Eq. 1.1), of the dielectric medium, which can be expressed in terms of the complex permittivity, $\hat{\varepsilon}(\nu)$ (Eq. 1.13). For a plane wave travelling a distance, z, through an isotropic medium, the electric field, $\vec{E}(t,z)$, is defined by[86]

$$\vec{E}(t,z) = \vec{E}_0 \exp(i\omega t) \cdot \exp(-\hat{\gamma} z) \tag{1.14}$$

where $\hat{\gamma}$ is the complex propagation coefficient, which is given by[93]

$$\hat{\gamma} = \alpha_\mathrm{a} + \mathrm{i}\beta = [\hat{\mu}\mu_0(\mathrm{i}\omega\hat{\kappa} - \hat{\varepsilon}\varepsilon_0\omega^2)]^{\frac{1}{2}} \tag{1.15}$$

with attenuation coefficient, α_a, and phase constant, β. Furthermore in Eq. 1.15, $\hat{\mu}$ and $\hat{\kappa}$ are the complex permeability and the complex conductivity, respectively. Both quantities are defined in analogy to $\hat{\varepsilon}$ by

$$\hat{\mu}(\omega) = \mu'(\omega) - \mathrm{i}\mu''(\omega) \tag{1.16}$$

$$\hat{\kappa}(\omega) = \kappa'(\omega) - \mathrm{i}\kappa''(\omega) \tag{1.17}$$

In case of non-magnetic samples ($\hat{\mu} = 1$), as all of the studied liquids in this work, Eq. 1.15 reduces to

$$\hat{\gamma} = \frac{\mathrm{i}\omega}{c_0}\sqrt{\hat{\varepsilon}(\omega) + \frac{\hat{\kappa}(\omega)}{\mathrm{i}\omega\varepsilon_0}} = \mathrm{i}k_0\sqrt{\eta(\omega)} = \mathrm{i}\hat{k} \tag{1.18}$$

where $k_0 = \omega\sqrt{\varepsilon_0\mu_0} = \omega/c_0 = 2\pi/\lambda_0$ is the propagation constant of free space of a wave with wavelength λ_0 and $\eta(\omega)$ is the generalized complex permittivity of the medium.[94] For coaxial lines and free-space methods Eq. 1.18 is valid and $\hat{\gamma}$ in Eq. 1.14 can be replaced by $\mathrm{i}\hat{k}$ (Eq. 1.26). For waveguide instruments $\hat{\gamma}$ has to be modified according to the boundary conditions imposed by the geometry of the waveguide, as will be discussed in Section 2.2.1.[94] The generalized complex permittivity, $\hat{\eta}(\omega)$, which is the experimentally accessible quantity, is then related to $\hat{\varepsilon}(\omega)$ via

$$\varepsilon'(\omega) = \eta'(\omega) + \frac{\kappa''(\omega)}{\omega\varepsilon_0} \tag{1.19}$$

$$\varepsilon''(\omega) = \eta''(\omega) - \frac{\kappa'(\omega)}{\omega\varepsilon_0} \tag{1.20}$$

These two equations (Eqs. 1.19 and 1.20) reveal that $\hat{\varepsilon}$ and $\hat{\kappa}$ cannot be measured independently. As the theory of Debye and Falkenhagen[95] predicts a dispersion of the conductivity, this makes a separation of $\hat{\varepsilon}$ and $\hat{\kappa}$ impossible and thus particularly affects the discussion of dielectric parameters of conductive systems. However, the dispersion of $\hat{\kappa}$ is typically small[96] with its known limits $\lim_{\omega\to 0}\kappa' = \kappa$ and $\lim_{\omega\to 0}\kappa'' = 0$ with dc conductivity, κ. Application of these limits to Eqs. 1.19 & 1.20 lead to

$$\varepsilon'(\omega) = \eta'(\omega) \tag{1.21}$$

$$\varepsilon''(\omega) = \eta''(\omega) - \frac{\kappa}{\omega\varepsilon_0} \tag{1.22}$$

This implies that for conductive samples, $\hat{\varepsilon}(\omega)$ is obtained from $\hat{\eta}(\omega)$ by subtracting the Ohmic loss contribution associated with κ. As a consequence, a potential dispersion of the conductivity is incorporated in $\hat{\varepsilon}$, thus exacerbating the interpretation of dielectric parameters.

The generalized complex permittivity, $\hat{\eta}(\omega)$ is further related to the complex refractive

index, $\hat{n}(\omega)$ via

$$\hat{n}(\omega) = \sqrt{\hat{\eta}(\omega)} = n(\omega) - \mathrm{i}\xi(\omega) \tag{1.23}$$

where n is the refractive index that appears in Snell's law and ξ the absorption constant.[a] The relation of both quantities to $\eta'(\omega)$ and $\eta''(\omega)$ is given by[97]

$$n(\omega)^2 = \frac{1}{2}\sqrt{\eta'(\omega)^2 + \eta''(\omega)^2} + \eta'(\omega) \tag{1.24}$$

$$\xi(\omega)^2 = \frac{1}{2}\sqrt{\eta'(\omega)^2 + \eta''(\omega)^2} - \eta'(\omega) \tag{1.25}$$

Following Ref. 94, insertion of Eqs. 1.18 and 1.23 into Eq. 1.14 yields an expression for travelling waves without boundary conditions

$$\vec{E}(t,z) = \vec{E}_0 \exp[-\xi k_0 z] \exp[\mathrm{i}(\omega t - n k_0 z)] = \vec{E}_0 \exp[-\alpha_\mathrm{a} z] \exp[\mathrm{i}(\omega t - \beta z)] \tag{1.26}$$

that holds for free-space methods (Section 2.2.3) and coaxial lines (Section 2.2.2). Comparison of Eq. 1.26 with Eq. 1.15 then reveals that the attenuation coefficient $\alpha_\mathrm{a} = \xi k_0$ and the phase constant $\beta = n k_0 = 2\pi/\lambda_\mathrm{M}$, with λ_M as the medium wavelength. Using the definition of the intensity, $I(z)$,

$$I(z) \propto \vec{E} \cdot \vec{E}^* \tag{1.27}$$

where $\vec{E}^*$ is the complex conjugate of $\vec{E}$, leads directly to the absorption law of Lambert-Beer[98]

$$\frac{I(z)}{I(0)} = \mathrm{e}^{-2\alpha_\mathrm{a} z} := \mathrm{e}^{-\alpha z} \tag{1.28}$$

with $\alpha = 2\alpha_\mathrm{a}$ defined as the absorption coefficient. Accordingly, permittivity spectra $\hat{\eta}(\nu)$ can be converted into absorption spectra $\alpha(\nu)$, via the absorption constant ξ defined by Eq. 1.25 and with $\omega = 2\pi\nu$ by

$$\alpha(\nu) = \frac{4\pi\nu}{c_0}\xi \tag{1.29}$$

thus forming the basis of the concatenation of far-infrared and dielectric spectra, as described in Section 2.2.4.

[a] Note that the latter is commonly labelled as k or κ. However, to avoid confusion with propagation constant and conductivity, ξ is used here.

1.2 Empirical models[b]

To describe the spectra recorded in this work (dielectric and OKE spectra), various empirical and semi-empirical model functions are available in literature.[86,92] Especially broadband spectra ranging from hundreds of MHz to tens of THz are comprised of a superposition of several intermolecular modes. Ideally the spectra can be decomposed into their individual contributions and thus can be modelled by sums of n single relaxation and resonance processes with amplitude, $S_j = \varepsilon_j - \varepsilon_{j+1}$, and band shape, $F_j(\omega)$,

$$\hat{\varepsilon}(\omega) = \varepsilon_\infty + \sum_{j=1}^{n} S_j F_j(\omega) \tag{1.30}$$

At lower frequencies ($\lesssim 100\,\mathrm{GHz}$) the measured intensity is best described by relaxation functions (Section 1.2.1), whereas at higher frequencies ($\gtrsim 100\,\mathrm{GHz}$) resonance-type bandshapes (Section 1.2.2) are more appropriate. In this section the model functions used in this work are presented.

1.2.1 Relaxation processes

Debye equation

The simplest approach to describe the dielectric spectrum of a liquid is the Debye equation.[99] As shown by Pellat[100] it is based on the assumption that the decrease of the orientational polarization in the absence of an external electric field follows a time law of first order with a characteristic time constant τ,

$$\frac{\partial}{\partial t}\vec{P}_\mu(t) = -\frac{1}{\tau}\vec{P}_\mu(t). \tag{1.31}$$

Solution of this equation yields

$$\vec{P}_\mu(t) = \vec{P}_\mu(0)\exp\left(-\frac{t}{\tau}\right) \tag{1.32}$$

where the exponential term represents the step-response function according to Eq. 1.10. Using Eq. 1.8 the pulse response function can be determined, which in turn allows the calculation of the response function, $F_\mathrm{D}(\omega)$ (Eq. 1.13), yielding the Debye equation (D; curve 1 in Figure 1.2)

$$F_\mathrm{D}(\omega) = \frac{1}{1 + \mathrm{i}\omega\tau} \tag{1.33}$$

[b] Note that although the model functions presented in this section are primarily introduced for describing $\hat{\varepsilon}(\omega)$, the imaginary part of OKE spectra can be treated equivalently.

Extensions of the Debye equation

Most of the real spectra cannot be solely modelled by a mono-exponential relaxation using the Debye equation. In these cases band-shape functions that describe a distribution of relaxation times are more desirable. However, from such an approach no closed analytical form can be obtained in the frequency domain. Alternatively, the Debye model can be extended by using empirical parameters in order to symmetrically and/or asymmetrically broaden the dispersion and absorption curve of Eq. 1.33. The broadening is interpretable as a symmetric and/or asymmetric relaxation time distribution with its most probable relaxation time τ.

The general equation of this empirical approach is the **Havriliak-Negami equation** (HN) that exhibits both a symmetric, α, and an asymmetric, β, width parameter:[101]

$$F_{\mathrm{HN}}(\omega) = \frac{1}{[1 + (\mathrm{i}\omega\tau)^{1-\alpha}]^{\beta}} \tag{1.34}$$

The broadening parameters can adopt values of $0 \leq \alpha_j < 1$ and $0 < \beta_j \leq 1$ (curve 4 in Figure 1.2).
For $\alpha = 0$ Eq. 1.34 turns into the **Cole-Davidson equation**[102,103] (CD)

$$F_{\mathrm{CD}}(\omega) = \frac{1}{(1 + \mathrm{i}\omega\tau)^{\beta}}. \tag{1.35}$$

It describes a dispersion and a loss curve with its maximum at $\omega_{\max} = 1/\tau$, which are asymmetrically broadened to higher frequencies, whereas the low-frequency wing has a Debye-type shape (curve 3 in Figure 1.2).
A symmetrically broadened relaxation model is obtained by setting $\beta = 1$ in Eq. 1.34, which yields the **Cole-Cole equation**[104,105] (CC; curve 2 in Figure 1.2)

$$F_{\mathrm{CC}}(\omega) = \frac{1}{1 + (\mathrm{i}\omega\tau)^{1-\alpha}}. \tag{1.36}$$

For $\alpha = 0$ and $\beta = 1$ Eqs. 1.34, 1.35 and 1.36 turn into the Debye model (Eq. 1.33). These four basic relaxation models are illustrated in Figure 1.2.

Modification of the Debye approach

Although the Havriliak-Negami function (Eq. 1.34) and its limiting forms (Eqs. 1.33, 1.36 and 1.35) have proven to be suitable for describing dielectric spectra up to GHz frequencies, the models become physically unreasonable in the THz range, where librational motions and inertial effects contribute. The problem originates from the fact that in the time domain the step response function, $F_{\mathrm{P}}(t)$, in Eq. 1.32 does not start with zero slope at $t = 0$, but rises instantaneously. As a consequence in the frequency domain, the Debye equation, and even more the CC, CD and HN function (due to the broadening), suggest an intensity of relaxation processes at frequencies higher than the librational bands, because

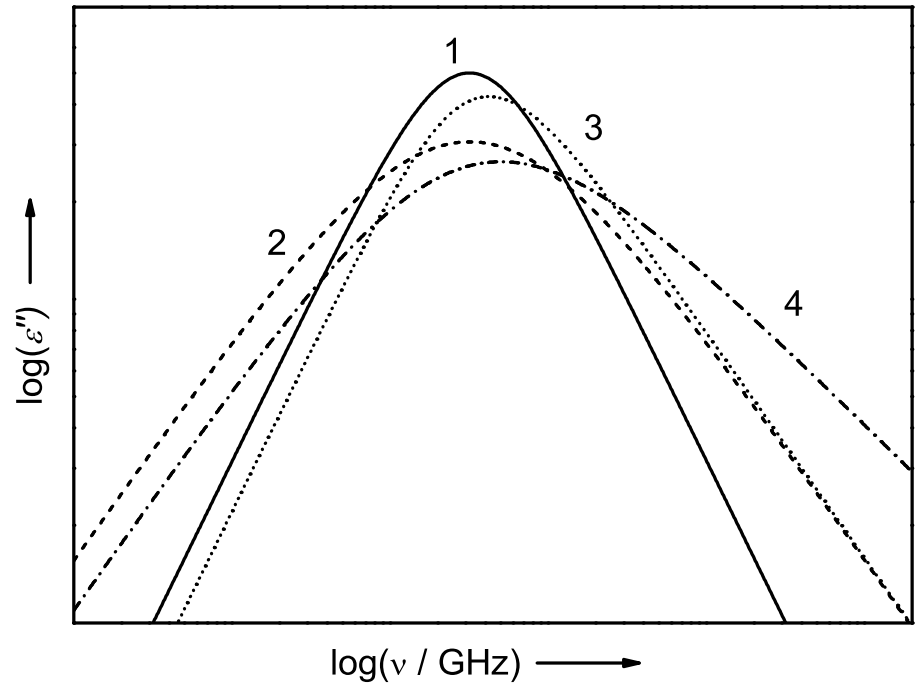

Figure 1.2: Band-shapes of Debye (1), Cole-Cole (2), Cole-Davidson (3) and Havriliak-Nagemi equation (4) on a double logarithmic scale with width parameter $\alpha = 0.3$ and $\beta = 0.7$.

Eqs. 1.33 to 1.36 decay too slowly at high ω. This however, is not physical as a relaxation process initially evolves from a librational fluctuation.[86] In other words, Eqs. 1.33 to 1.36 do not take inertial effects into account. Accordingly, Turton *et al.*[106] modified the HN function with respect to this issue by applying an inertial rise rate $\gamma_{\mathrm{lib}} \approx \langle\omega_{\mathrm{lib}}\rangle/2\pi$, with $\langle\omega_{\mathrm{lib}}\rangle$ as the average resonance angular frequency of the librational modes, which results in a faster decay of the relaxation contribution. This yields the inertia-corrected HN equation (HNi)

$$F_{\mathrm{HNi}}(\omega) = (S^0_{\mathrm{HNi}})^{-1}\left[\frac{1}{(1+(\mathrm{i}\omega\tau)^{1-\alpha})^{\beta}} - \frac{1}{(1+(\mathrm{i}\omega\tau+\gamma_{\mathrm{lib}}\tau)^{1-\alpha})^{\beta}}\right] \tag{1.37}$$

A similar problem occurs if the relaxation process depends on a lower frequency mode with τ_0. Again a modification is introduced,[106] which terminates the relaxation at lower frequencies. This is referred to as "α-termination" and is deduced from the relaxation behavior of glass forming liquids. By taking both correction into account, Eq. 1.34 is rewritten in its modified form (HNm) as

$$F_{\mathrm{HNm}}(\omega) = (S^0_{\mathrm{HNm}})^{-1}\left[\frac{1}{(1+(\mathrm{i}\omega\tau+\tau/\tau_0)^{1-\alpha})^{\beta}} - \frac{1}{(1+(\mathrm{i}\omega\tau+\gamma_{\mathrm{lib}}\tau+\tau/\tau_0)^{1-\alpha})^{\beta}}\right] \tag{1.38}$$

The limiting forms of the HNi (Di, CCi or CDi) and HNm (Dm, CCm or CDm) functions are obtained in analogy to those of the HN model (Eq. 1.34). As described in detail elsewhere,[107] Eq. 1.38 turns into a so-called constant loss (CL) term in the limit of $\alpha \to 1$ (or $\beta \to 0$) spanning from librations (γ_{lib}) to relaxations (τ_0). Although it is has proven to

be useful for describing featureless intensity of dielectric and OKE spectra (Section 3.1 and Chapter 4), it cannot be regarded as a relaxation process but instead should be interpreted as a composite.
As a consequence of these modifications not the true amplitude, S_j, is obtained from the fit but the output amplitude, $S'_j = S_j/S^0_j$. Therefore, Eqs. 1.38 and 1.37 have to be normalized by the factors

$$S^0_{\mathrm{HNi}} = 1 - \frac{1}{(1+(\gamma_{\mathrm{lib}}\tau)^{1-\alpha})^{\beta}} \tag{1.39}$$

and

$$S^0_{\mathrm{HNm}} = \frac{1}{(1+(\tau/\tau_0)^{1-\alpha})^{\beta}} - \frac{1}{(1+(\gamma_{\mathrm{lib}}\tau+\tau/\tau_0)^{1-\alpha})^{\beta}} \tag{1.40}$$

and thus S_j is calculated through $S_j = S'_j \cdot S^0_j$.

1.2.2 Resonance processes

Damped harmonic oscillator Intermolecular vibrations and librations, which typically take place at $\nu \gtrsim 100\,\mathrm{GHz}$ are best modelled by a resonance band-shape. A very common model is the damped harmonic oscillator (DHO), which is derived by assuming a oscillator that is exposed to a damping force and driven by a harmonically oscillating field. The solution of Newton's equation, which describes the time-dependent motion of an effective charge yields[92]

$$F_{\mathrm{DHO}}(\omega) = \frac{\omega_0^2}{(\omega_0^2-\omega^2)+\mathrm{i}\omega/\tau_{\mathrm{D}}} = \frac{\nu_0^2}{(\nu_0^2-\nu^2)+\mathrm{i}\nu\gamma} \tag{1.41}$$

where $\omega_0 = \sqrt{k/m} = 2\pi\nu_0$ (with k as the force constant) is the angular resonance frequency and $\gamma = 1/(2\pi\tau_{\mathrm{D}})$ the damping rate of the oscillator. In the limit of $\tau_{\mathrm{D}} \ll \omega_0$ Eq. 1.41 reduces to the Debye function.

Gaussian function Another function to describe resonances is the antisymmetrized Gaussian.[108] It is often used to model librational motions[109] and is particularly useful to describe the rather steep decay of $\varepsilon''(\omega)$ at high ω, where the intensity associated with orientational polarization ceases.[107]
In the time domain the Gaussian (G) is a real function and can be expressed as

$$f_{\mathrm{G}}(t) = \exp\left(-\frac{t^2\gamma^2}{2}\right)\sin(\omega_0 t) \quad \text{for} \quad t > 0 \tag{1.42}$$

where ω_0 is the angular resonance frequency and γ the damping rate. Fourier transformation yields the expression in the frequency domain, which is[110]

$$F_{\mathrm{G}}(\omega) = \exp\left(-\frac{\omega-\omega_0}{2\gamma^2}\right)\left[\mathrm{i} - \mathrm{erfi}\left(\frac{\omega-\omega_0}{\sqrt{2}\gamma}\right)\right] - \exp\left(-\frac{\omega+\omega_0}{2\gamma^2}\right)\left[\mathrm{i} - \mathrm{erfi}\left(\frac{\omega+\omega_0}{\sqrt{2}\gamma}\right)\right] \tag{1.43}$$

with erfi(z) as the imaginary error function. It can be solved using Dawson's integral, D(z), which is defined as[111]

$$\mathrm{D}(z) = \exp(-z^2) \int_0^z \exp(t^2)\mathrm{d}t = \frac{\sqrt{\pi}}{2} \exp(-z^2)\mathrm{erfi}(z) \tag{1.44}$$

Insertion of Eq. 1.44 into 1.43 yields

$$\begin{aligned} F_{\mathrm{G}}(\omega) = (S_{\mathrm{G}}^0)^{-1} \Bigg[& \frac{2}{\sqrt{\pi}} \mathrm{D}\left(\frac{\omega+\omega_0}{\sqrt{2}\gamma}\right) - \frac{2}{\sqrt{\pi}} \mathrm{D}\left(\frac{\omega-\omega_0}{\sqrt{2}\gamma}\right) \\ & + \mathrm{i}\left(\exp\left[-\frac{(\omega-\omega_0)^2}{2\gamma^2}\right] - \exp\left[-\frac{(\omega+\omega_0)^2}{2\gamma^2}\right]\right)\Bigg] \end{aligned} \tag{1.45}$$

where $S_{j,\mathrm{G}}^0$ is the normalization factor in the limit of $\omega \to 0$:

$$S_{\mathrm{G}}^0 = \frac{4}{\sqrt{\pi}} \mathrm{D}\left(\frac{\omega_0}{\sqrt{2}\gamma}\right) \tag{1.46}$$

1.3 Microscopic models of dielectric relaxation

The formal description of experimental data using the equations presented in Section 1.2 yields macroscopic relaxation parameters such as amplitude, S_j, and relaxation time, τ_j. In this section models based on the continuum approach are presented to link these parameters to molecular properties, thus permitting an inference to the structural and dynamical nature of a system.

1.3.1 Onsager equation

The common models that are used to describe the response of a reorienting dipole in condensed phases to an electric field are all based on a continuum approach.[86,99] Within this approach it is assumed that a single dipole is embedded in a dielectric continuum, which is characterized by its macroscopic properties. Based on these assumptions Onsager[112] deduced the following equation for spherical particles

$$\varepsilon_0(\varepsilon_{\mathrm{s}} - 1)\vec{E} = \vec{E}_c \cdot \sum_j \frac{\rho_j}{1 - \alpha_j f_j} \left(\alpha_j + \frac{1}{3k_{\mathrm{B}}T} \cdot \frac{\mu_j^2}{1 - \alpha_j f_j}\right) \tag{1.47}$$

disregarding specific interactions and the anisotropy of the surrounding field. In Eq. 1.47, ρ_j is the dipole density, α_j the polarizability, f_j the reaction field factor and μ_j the gas-phase dipole moment of the jth species. $\vec{E}_{\mathrm{c}}$ is denoted as the cavity field and is related to the external field $\vec{E}$ via

$$\vec{E}_{\mathrm{c}} = \frac{3\varepsilon_{\mathrm{s}}}{2\varepsilon_{\mathrm{s}} + 1}\vec{E} \tag{1.48}$$

for a spherical cavity formed by a dipole in the dielectric.[86] Insertion of Eq. 1.48 into Eq. 1.47 yields the general expression of the Onsager equation, which links the static per-

mittivity, ε_s, to the molecular dipole moment, μ_j:

$$\frac{(\varepsilon_s - 1)(2\varepsilon_s + 1)\varepsilon_0}{3\varepsilon_s} = \sum_j \frac{\rho_j}{1 - \alpha_j f_j} \left(\alpha_j + \frac{1}{3k_B T} \cdot \frac{\mu_j^2}{1 - \alpha_j f_j} \right) \tag{1.49}$$

For liquids that consist of solely one dipolar species exhibiting one dispersion step, i.e. $j = 1$, Eq. 1.49 simplifies to

$$\frac{(\varepsilon_s - \varepsilon_\infty)(2\varepsilon_s + \varepsilon_\infty)}{\varepsilon_s(\varepsilon_\infty + 2)^2} = \frac{\rho\mu^2}{9\varepsilon_0 k_B T}. \tag{1.50}$$

1.3.2 Kirkwood-Fröhlich equation

The model of Onsager can be extended by taking specific intermolecular interaction into account, which can be achieved with the help of statistical mechanics. It leads to the introduction of the Kirkwood factor, g_K, as shown by Kirkwood and Fröhlich:[113,114]

$$\frac{(\varepsilon_s - \varepsilon_\infty)(2\varepsilon_s + \varepsilon_\infty)}{\varepsilon_s(\varepsilon_\infty + 2)^2} = \frac{\rho\mu^2}{9\varepsilon_0 k_B T} \cdot g_K \tag{1.51}$$

The Kirkwood factor, g_K is a measure for the interaction between the particles. In case of a preferentially parallel arrangement of neighboring dipoles $g_K > 1$, whereas $g_K < 1$ is characteristic for an antiparallel alignment. For $g_K = 1$ Eq. 1.51 turns into Eq. 1.49 and implies randomly oriented (i.e. uncorrelated) dipoles. Similar conclusions can be drawn from the temperature dependence of g_K, which is interpreted as break-up of parallel ($\mathrm{d}g_K/\mathrm{d}T < 0$) and antiparallel ($\mathrm{d}g_K/\mathrm{d}T > 0$) correlations.

1.3.3 Cavell-equation

An even more general expression is the Cavell equation[115], which enables the description of spectra that consist of more than one dispersion step. For ellipsoidal particles Hetzenauer deduced the form[116]

$$\frac{\varepsilon_s + A_j(1 - \varepsilon_s)}{\varepsilon_s} \cdot S_j = \frac{N_A c_j}{3k_B T \varepsilon_0} \cdot \mu_{\mathrm{eff},j}^2 \tag{1.52}$$

It relates the dielectric amplitude, S_j, with the concentration, c_j, and the effective dipole moment, $\mu_{\mathrm{eff},j}$, of the dipolar species j responsible for this relaxation process. Dipole-dipole correlations are taken into account by the factor g_j. Although it is an empirical parameter and thus differs from the Kirkwood factor, g_K (Eq. 1.51), it provides a measure of parallel or antiparallel correlation similar to g_K.[86] The shape of the relaxing particle is regarded by the shape factor, A_j. If c_j is known, $\mu_{\mathrm{eff},j}$ can be calculated using Eq. 1.52 and is defined as

$$\mu_{\mathrm{eff},j} = \sqrt{g_j}\mu_{\mathrm{app},j} = \sqrt{g_j}\frac{\mu_j}{1 - f_j\alpha_j} \tag{1.53}$$

where $\mu_{\mathrm{app},j}$ is the apparent dipole moment. The latter represents the uncorrelated gas-phase dipole moment, μ_j, corrected for cavity- and reaction field effects, which are considered by the polarizability α_j and the reaction field factor f_j. For ellipsoidal particles with

half axes $a_j > b_j > c_j$ the latter can be calculated from the geometry of the particle and is given by[86,117]

$$f_j = \frac{3}{4\pi\varepsilon_0 a_j b_j c_j} \frac{A_j(1-A_j)(\varepsilon_\mathrm{s}-1)}{\varepsilon_\mathrm{s}+(1-\varepsilon_\mathrm{s})A_j}. \tag{1.54}$$

The general form of shape factor A_j is[86]

$$A_j = \frac{a_j b_j c_j}{2} \int_0^\infty \frac{\mathrm{d}s}{(s+a_j^2)^{3/2}(s+b_j^2)^{1/2}(s+c_j^2)^{1/2}}. \tag{1.55}$$

Although, the integral in Eq. 1.55 cannot be evaluated in closed form, limiting variants are given by Scholte[118] for prolate ellipsoids ($a_j > b_j = c_j$)

$$A_j = -\frac{1}{p_j^2-1} + \frac{p_j}{(p_j^2-1)^{3/2}} \ln\left(p_j + \sqrt{p_j^2-1}\right) \quad \text{with} \quad p_j = \frac{a_j}{b_j} \tag{1.56}$$

and oblate ellipsoids ($a_j < b_j = c_j$)

$$A_j = \frac{1}{1-p_j^2} - \frac{p_j}{(1-p_j)^{3/2}} \cos^{-1} p_j \quad \text{with} \quad p_j = \frac{a_j}{b_j}. \tag{1.57}$$

In addition, extensive tabulations of A_j as a function of a_j, b_j and c_j are available in literature.[119,120]

For spherical particles $A_j = 1/3$ and then f_j reduces to

$$f_j = \frac{1}{4\pi\varepsilon_0 a_j^3} \cdot \frac{2\varepsilon_\mathrm{s}-2}{2\varepsilon_\mathrm{s}+1} \tag{1.58}$$

1.3.4 Debye model of rotational diffusion

The Debye model of rotational diffusion represents the simplest approach that relates the molecular relaxation time of a particle, $\tau^{(n)}$, to its molecular dimensions by assuming that the reorientation of spherical rigid dipoles is induced by uncorrelated collisions between the particles. Thereby, inertial effects and specific interactions between the dipoles were neglected and the internal field is assumed according to Lorentz.[99] Within these approximations the dipole correlation function can be expressed as a single exponential according to[86]

$$C_n(t) = \frac{\langle \mu(0)\cdot\mu(t)\rangle}{\langle \mu(0)\cdot\mu(0)\rangle} = \exp\left(-\frac{t}{\tau^{(n)}}\right) \tag{1.59}$$

Within this model relaxation times, $\tau^{(n)}$, of rank n are interrelated by

$$\tau^{(n)} = \frac{2}{n(n+1)}\tau^{(1)} \tag{1.60}$$

where the rank of $\tau^{(n)}$ is determined by the type of experiment. For dielectric and infrared spectroscopy an intramolecular vector is probed and thus $n = 1$, whereas NMR,

femtosecond-timeresolved IR (fs-IR), Raman or OKE spectroscopy detect a tensorial quantity yielding single-particle relaxation times with $n = 2$. This implies that relaxations in dielectric experiments are 3 times slower than e.g. in OKE (i.e. $\tau^{(1)} = 3\tau^{(2)}$; only valid for rotational diffusion). In Debye's model $\tau^{(n)}$ is determined by the friction factor ζ via

$$\tau^{(n)} = \frac{\zeta}{n(n+1)k_{\mathrm{B}}T} \tag{1.61}$$

where it is assumed that ζ can be calculated according to Stokes for a macroscopic sphere of radius, a, in a viscous medium of viscosity, η, which is given by $\zeta = 8\pi\eta a^3$. Application of this macroscopic hydrodynamic model to microscopic level, then leads to the Stokes-Einstein-Debye equation[99]

$$\tau^{(n)} = \frac{6V_{\mathrm{m}}}{n(n+1)k_{\mathrm{B}}T}\eta \tag{1.62}$$

where $V_{\mathrm{m}} = 4/3\pi a^3$ is the molecular volume of the sphere. The viscosity, η, in Eq. 1.62 should be actually regarded as a microscopic viscosity that describes η in the vicinity of the relaxing particle. However, its value is usually unknown and is not necessarily equal to that of macroscopic viscosity. Moreover, the relation between both is unclear. Because of that the model is of limited use, which becomes evident as in many cases a plot of $\tau^{(n)}$ vs. η indeed obeys a linear relation, but exhibits an axis intercept and the volumes extracted from the slope are frequently incompatible with the actual molecular volumes. Therefore, Dote *et al.*[121] introduced the effective volume of rotation, V_{eff}, and added an empirical axis intercept, $\tau_0^{(n)}$, to Eq. 1.62 yielding

$$\tau^{(n)} = \frac{6V_{\mathrm{eff}}}{n(n+1)k_{\mathrm{B}}T}\eta + \tau_0^{(n)} \tag{1.63}$$

where the latter is occasionally interpreted as the correlation time of the freely rotating particle. The effective volume, $V_{\mathrm{eff}} = V_{\mathrm{m}}Cf_\perp$, is defined as the product of the molecular volume with the shape factor, $f_\perp$, and the hydrodynamic friction coefficient, C. The latter is an empirical parameter and accounts for the discrepancy between macroscopic and microscopic viscosity with its limiting values of *stick* ($C_{\mathrm{stick}} = 1$) and *slip* ($C_{\mathrm{slip}} = 1 - f_\perp^{-2/3}$) determining the boundary conditions of rotational friction. For prolate ellipsoids with major (a) and minor half-axis (b), $f_\perp$ can be calculated according to Dote *et al.*[122]

$$f_\perp = \frac{2}{3}\frac{1-\alpha_\perp^4}{(2-\alpha_\perp^2)\alpha_\perp^2(1-\alpha_\perp^2)^{-1/2}\ln\left[\frac{1+[1-\alpha_\perp^2]^{1/2}}{\alpha_\perp}\right]-\alpha_\perp^2} \tag{1.64}$$

with $\alpha_\perp = b/a$. For oblate spheroids Kalman *et al.*[123] gave the following equation to calculate $f_\perp$

$$f_\perp = \frac{2}{3}\frac{1-\beta_\perp^4}{(2-\beta_\perp^2)\beta_\perp^2(\beta_\perp^2-1)^{-1/2}\arctan(\beta_\perp^2-1)^{1/2}-\beta_\perp^2} \tag{1.65}$$

with $\beta_\perp = a/b$.

1.3.5 Model of jump relaxation

The model of rotational diffusion was shown to be applicable to systems of large solute molecules reorienting in a solvent consisting of small molecules. However, in many real systems this condition is not fulfilled and the above relations do not hold anymore.[86] The relaxation behavior in such liquids can be explained by assuming that the molecular reorientation is not continuous, as for rotational diffusion, but through instantaneous jumps over a finite angle. This means that the molecule remains in its orientation for a certain time interval, before it reorients over a finite angle in an infinitely small time.[86] This concept was derived on the basis of reorientation in molecular crystals, where it is assumed that the oriented molecule is placed in a potential well, whose energy barrier has to be overcome in the course of a reorientation to reach an adjacent potential well with a certain probability. Therefore, a function $K(\theta, t)$ is introduced describing a distribution of jump angles, which can be expressed as a series of Legendre polynomials $P_n(\cos\theta)$ according to[86]

$$K(\theta, t) = \sum_{n=0}^{\infty} (2n+1) A_n P_n(\cos\theta) \tag{1.66}$$

with

$$A_n = \frac{1}{2} \int_0^{\pi} K(\theta, t) \sin\theta P_n(\cos\theta) \mathrm{d}\theta. \tag{1.67}$$

The corresponding correlation function can then be expressed as an exponential function equivalent to Eq. 1.59 with relaxation times of rank n

$$\tau^{(n)} = \frac{1}{k(1 - A_n)} \tag{1.68}$$

where k is the probability factor of a jump. In the limit that orientations before and after the jump are uncorrelated, $A_n = 0$ for any $n > 0$ and thus, all correlation times become $\tau^{(n)} = 1/k$. If only jumps over a single angle, α, are possible, $A_n = P_n(\cos\alpha)$ and thus,

$$\tau^{(n)} = \frac{1}{k(1 - P_n(\cos\alpha))} \tag{1.69}$$

This implicates that a first-rank relaxation ($n = 1$) can be faster than a second-rank relaxation ($n = 2$) if $\cos\alpha < -1/3$ (i.e. $\alpha > 109.5\,^{\circ}$). For small angles of α Eq. 1.69 turns into the model of rotational diffusion (Eq. 1.60).[86]

1.3.6 Microscopic and macroscopic relaxation times

In dielectric as well as is OKE experiments the experimentally accessible relaxation time, τ, is a collective property[86] and has to be converted into a molecular correlation time, $\tau^{(n)}$ to relate it to microscopic properties.
For dielectric relaxation times, $\tau^{(1)}$, this can be achieved by the equations suggested by

Powles,[124] who deduced the following approach for a single Debye relaxation

$$\tau^{(1)} = \frac{2\varepsilon_\mathrm{s} + \varepsilon_\infty}{3\varepsilon_\mathrm{s}} \times \tau \tag{1.70}$$

and generalized it for several Debye relaxation times, $\tau_j^{(1)}$, according to

$$\tau_j^{(1)} = \frac{2\varepsilon_j + \varepsilon_{j+1}}{3\varepsilon_j} \times \tau_j \;\text{ with }\; j > 0 \tag{1.71}$$

where $\varepsilon_j = \varepsilon_\mathrm{s}$ for $j = 1$. Glarum extended the approach of Powles for a Cole-Cole relaxation[125] yielding

$$\tau^{(1)} = \left(\frac{2\varepsilon_\mathrm{s} + \varepsilon_\infty}{3\varepsilon_\mathrm{s}}\right)^{1/(1-\alpha)} \times \tau \tag{1.72}$$

where α is the width parameter of the Cole-Cole equation (Eq. 1.36).
Additionally, Madden and Kivelson[126] modified the equation of Powles and Glarum by taking dipole-dipole correlations into account

$$\tau^{(1)} = \frac{2\varepsilon_\mathrm{s} + \varepsilon_\infty}{3\varepsilon_\mathrm{s}} \times \frac{\dot{g}}{g_\mathrm{K}} \times \tau \tag{1.73}$$

with g_K as the Kirkwood correlation factor and $\dot{g}$ as the dynamical correlation factor.

1.4 Temperature dependence of relaxation times

1.4.1 Arrhenius equation

The Arrhenius equation represents one of the oldest approaches to describe the temperature dependence of reaction rates of chemical reactions and transport properties such as viscosity and conductivity.[127] It is an empirical equation, which in case of relaxation times can be written as

$$\ln \tau = \ln \tau_0 + \frac{E_\mathrm{A}}{RT} \tag{1.74}$$

From a plot of $\ln \tau$ vs. $1/T$ the pre-exponential or frequency factor, τ_0, is obtained from the axis intercept and the activation energy, E_A, is determined by the slope. Whilst τ_0 can be interpreted as the shortest possible relaxation time, E_A is assumed to be temperature-independent and describes the height of the potential barrier that has to be overcome to evolve from the initial to the final energy state on the potential energy surface.[128]

1.4.2 Eyring equation

The theory of Eyring[129] (transition state theory) is based on the model of energy hypersurface and enables the description of the temperature dependence of chemical reactions

and rate processes.[128] By introduction of the Gibbs energy of activation, $\Delta_{\neq}G = \Delta_{\neq}H - T\Delta_{\neq}S$, the following equation is obtained for relaxation times:

$$\ln \tau = \ln \frac{h}{k_{\mathrm{B}}T} + \frac{\Delta_{\neq}H}{RT} - \frac{\Delta_{\neq}S}{R} \tag{1.75}$$

where h is Planck's constant and $\Delta_{\neq}H$ and $\Delta_{\neq}S$ the corresponding enthalpy and entropy, respectively.[130] As for the Arrhenius equation, a linear relation is found for a plot of $\ln \tau = f(1/T)$ and the parameters of Eq. 1.74 and 1.75 can be interrelated through[128]

$$E_{\mathrm{A}} = \Delta_{\neq}H - RT \tag{1.76}$$

$$\ln \tau_0 = \ln \frac{h}{k_{\mathrm{B}}T} - \frac{\Delta_{\neq}S}{R} \tag{1.77}$$

$$\tag{1.78}$$

1.4.3 Vogel-Fulcher-Tammann equation

For many glass-forming liquids the temperature dependence of the viscosity, in particular in a temperature range close to the glass-transition, typically does not follow the Arrhenius equation (Eq. 1.74). In such cases the Vogel-Fulcher-Tammann (VFT) equation[131,132] is commonly used, which is derived on the basis of the free volume that is required to enable the reorientation of a molecule. As pointed out by Doolittle[133] the free volume is defined as the difference between the macroscopic volume and the volume arising from thermal expansion of the liquid. A general expression of the VFT equation for a transport property, Y, is given by

$$\ln Y = \ln Y_0 + \frac{B_{\mathrm{VFT}}}{T - T_0} \tag{1.79}$$

where $Y = \kappa^{-1}, \eta, \tau, ...$ of a glass-forming liquid above its glass-transition temperature, T_{g}. In Eq. 1.79 Y_0 and B_{VFT} are fit parameters and the fraction B_{VFT}/T_0 is interpreted as the fragility parameter, D, which is a measure of the structural strength of the system.[134] For large values of D, the liquids are indicated as *strong* and show nearly Arrhenius behavior. The parameter T_0 is the VFT-temperature, which is typically 30 K below T_{g} determined by differential scanning calometry.[135] Moreover, it is equal to the Kauzmann temperature, which is defined by the intersection of the entropy curve of the supercooled liquid and the solid.[136]

Chapter 2

Experimental

2.1 Materials and Sample Handling

Acetonitrile (AN) was purchased from VWR (Prolabo, anhydrous) with a nominal water content of < 30 ppm, which was additionally confirmed by coulometric Karl-Fischer titration. For preparation of the EAN+AN mixtures (Chapter 5) AN was used as delivered.

***N*-Butyl-*N*-methylpyrrolidinium dicyanamide ([P_{14}][DCA])** was purchased from Iolitec (Heilbronn, Germany) with a purity of > 98 %. The halide impurities were specified to be < 2 % and the water content after one week of drying in high vacuum ($< 10^{-8}$ bar) at 40 °C was determined to < 200 ppm by coulometric Karl-Fischer titration.

***N*-Butylpyridinium bis(trifluoromethanesulfonyl)amide ([C_4pyr][TFSA])** was purchased from Iolitec (Heilbronn, Germany) with a purity of > 99 %. The nominal halide impurities were < 100 ppm and the water content after one week of drying in high vacuum ($< 10^{-8}$ bar) at 40 °C was determined to < 10 ppm by coulometric Karl-Fischer titration.

Diethylmethylsulfonium bis(trifluoromethanesulfonyl)amide ([S_{221}][TFSA]) was purchased from Iolitec (Heilbronn, Germany) with a purity of > 99 %. The nominal halide impurities were < 100 ppm and the water content after one week of drying in high vacuum ($< 10^{-8}$ bar) at 40 °C was measured to be < 20 ppm by coulometric Karl-Fischer titration.

Ethylammonium nitrate (EAN) was kindly provided by Dr. O. Zech (University of Regensburg). It was prepared by the reaction of equimolar amounts of ethylamine with nitric acid as described by Evans *et al.*[137] Water was first removed through rotary evaporation, followed by lyophilization. The obtained crude EAN was recrystallized trice from acetonitrile. The purity of the product was checked by ^{1}H-NMR spectroscopy, which showed no detectable ^{1}H-containing impurities.
Additionally, batches of EAN were purchased from Iolitec (>97 % purity, Heilbronn, Germany). The halide impurities specified by the manufacturer were less than 100 ppm.

Partially deuterated d_3-EAN was prepared by adding fresh D_2O (99.9%, Deutero GmbH, Kastellaun, Germany) to commercial EAN then stirring for 24 h. The solution was then evaporated under vacuum and the whole process repeated. The product so obtained was found to be 91 % deuterated by ^{1}H-NMR spectroscopy, corresponding to an average composition $[EtND_{2.7}H_{0.3}]^+$.
All batches of EAN and d_3-EAN were dried under high vacuum ($p < 10^{-8}$ bar) for at least 12 days at 40 °C. Subsequent coulometric Karl-Fischer titration yielded water contents of < 100 ppm for EAN and < 200 ppm for d_3-EAN.

***N*-Methylimidazole (C_1Im)** (Alfa Aesar, 99 %) was kindly provided by Prof. A. Jacobi von Wangelin (University of Regensburg). The water content measured by coulometric Karl-Fischer titration was 1500 ppm.

***N*-Methylimidazole + acetic acid ([C_1Im][HOAc])** was kindly provided by Prof. Umebayashi (Niigata University, Niigata, Japan) and synthesized by his co-workers through mixing of equivalent amount of distilled C_1Im (Tokyo Chemical Industry, 99 %) and purified acetic acid (HOAc; Tokyo Chemical Industry, 99.5 %)) with a gradual droplet addition of the acid to the base avoiding vaporization by generation of the heat of mixing. The prepared compound was dried in vacuum for several weeks at room temperature. Purity and water content of the final equimolar mixture were checked by elemental analysis and Karl-Fischer titration, respectively.

***N*-Methylimidazolium bis(trifluoromethanesulfonyl)amide ([C_1ImH][TFSA])**
Analogous to the description of [C_1Im][HOAc]. Bis(trifluoromethanesulfonyl)amine (HTFSA; Morita Chemical Industries) was used without further purification.

***N*-Methylimidazolium difluoroacetate ([C_1ImH][DFA])** Analogous to the description of [C_1Im][HOAc]. Difluoroacetic acid (HDFA; Morita Chemical Industries) was used without further purification.

***N*-Methylimidazolium trifluoroacetate ([C_1ImH][TFA])** Analogous to the description of [C_1Im][HOAc]. Trifluoroacetic acid (HTFA; Tokyo Chemical Industry, 99 %) was purified by distillation under ambient pressure prior to use.

Propylammonium nitrate (PAN) was kindly provided by Prof. K. Seddon and Dr. N. Plechkova (Queens University Ionic Liquids Laboratories (QUILL), Belfast, UK). After drying for one week in high vacuum ($< 10^{-8}$ bar) at 40 °C the water content was measured to be < 500 ppm by coulometric Karl-Fischer titration.

Triethylsulfonium bis(trifluoromethanesulfonyl)amide ([S_{222}][TFSA]) was purchased from Iolitec (Heilbronn, Germany) with a purity of > 99 %. The nominal halide impurities were 90 ppm and the water content after one week of drying in high vacuum ($< 10^{-8}$ bar) at 40 °C was determined to < 20 ppm by coulometric Karl-Fischer titration.

Sample preparation and handling Because ionic liquids are known to be more or less hygroscopic, mainly depending on the anion,[138] all samples (including AN and C_1Im) were stored in a nitrogen-filled glove-box with a dew point of approximately $-50\,°C$ that corresponds to water content of $\sim 40\,\text{ppm}$ to avoid uptake of water. All subsequent steps of sample preparation and measurements of neat compounds were performed under dry N_2. Mixtures of ILs with volatile solvents (EAN+AN) were measured (if possible) under saturated solvent atmosphere to prevent vaporization. Solutions were prepared under dry nitrogen using an analytical balance without buoyancy corrections and thus concentrations were accurate to about $\pm 0.2\,\%$.

2.2 Measurement of Dielectric Properties

2.2.1 Interferometry

The use of coaxial lines connected to a vector network analyzer as described in Section 2.2.2 is restricted to frequencies up to $\sim 50\,\text{GHz}$ as the efficiency of the propagation of electromagnetical waves and the dimensions required for coaxial cells become critically low. On the other hand free-space methods as described in Section 2.2.3 are also not applicable at frequencies $\lesssim 80\,\text{GHz}$ due to diffraction effects and the mechanical instability of the optical components.[94] Consequently, wave propagation of E-band frequencies ($60 \leq \nu/\text{GHz} \leq 90$) is best accomplished by waveguides. The measurement principle of the setup available in Regensburg is based on a transmission experiment, where a high precision receiver (Micro-Tel 1259) is able to detect the signal amplitude (absorption coefficient, α_a) as a function of path length but not the phase information. To obtain the latter, the setup has to be operated as an interferometer of the Mach-Zehnder type.[94,139] This allows the determination of the medium wavelength, λ_M, which is related to the phase coefficient $\beta = 2\pi/\lambda_\text{M}$. Then, the complex wave propagation coefficient, $\hat{\gamma}$, in a rectangular waveguide can be expressed as

$$\hat{\gamma}^2 = \left(\alpha_\text{a} + \text{i}\frac{2\pi}{\lambda_\text{M}}\right)^2 = k_\text{c}^2 - \hat{k}^2 \tag{2.1}$$

where k_c is denoted as the cut-off wavenumber. For the TE_{10} mode $k_\text{c} = \pi/a$, which results from the confinement of the propagating wave imposed by the dimensions a and b (with $a > b$) of the waveguide.[93] Using the relation $\hat{k}^2 = k_0^2\hat{\eta}(\omega)$, real and imaginary part of the generalized complex permittivity can be obtained through

$$\eta'(\nu) = \left(\frac{c_0}{\nu}\right)^2 \left[\left(\frac{1}{\lambda_\text{M}}\right)^2 - \left(\frac{\alpha_\text{a}}{2\pi}\right)^2 + \left(\frac{k_\text{c}}{2\pi}\right)^2\right] \tag{2.2}$$

$$\eta''(\nu) = \left(\frac{c_0}{\nu}\right)^2 \left(\frac{\alpha_\text{a}}{\pi\lambda_\text{M}}\right) \tag{2.3}$$

Instrumentation and measurement principle[139] A scheme of the interferometer setup used in this work is displayed in Figure 2.1. Individual frequencies (60.00, 66.00, 72.00, 79.00, 89.00 GHz) are generated by five phase-locked Gunn diodes (**PLO**) referenced to a 100 MHz reference oscillator. The selection of the desired **PLO** is achieved by the PLO-control unit (**PLO-D**) and its output is fed into the interferometer line. The signal is then equally split into a reference and a measuring beam by the directional coupler (**2a**). Whilst the reference beam passes through a set of two coarse (**1b,c**) and one precision (**9**) attenuators for amplitude tuning, the measuring line contains a precision phase shifter (**4**), two E/H tuners (**5a,b**), the cell (**C**) and the probe (**P**). The cell consists of a piece of gold-plated waveguide with its bottom sealed by a mica window and is surrounded by a thermostat jacket. The gold-plated ceramic probe is coaxially mounted on a vertically movable table and is connected to the continuing line by a flexible waveguide (**6b**), which enables its up and down movement. Mounting of a polyethylene tube around **C** and **P** enables performance under nitrogen and saturated solvent atmosphere. Both beams are recombined by a directional coupler (**2b**), down-converted (**8** and **MMC**) and detected by a high precision computer-controlled receiver (**RE**). The temperature is controlled by a thermostat (Lauda RKS 20-D) with an accuracy of $\pm 0.02\,^{\circ}\mathrm{C}$ and measured by a Pt-100 temperature sensor.
For an interferometer measurement, the probe is immersed into the sample-filled cell and moved downwards to its zero position, z_0'. At this position the detected signal, A (in dB), which is the relative attenuation of the signal, is maximized with the help of the E/H tuners to yield $A_{\max}$. To obtain the phase information, destructive interference between reference and sample beam is adjusted by attenuator (**9**) and phase shifter (**4**) at a probe position, z_0, where $A \approx (A_{\max} + 10\,\mathrm{dB})/2$. After setting the probe back to its starting position ($z_0' = 0$), the signal A is measured as a function of path length through computer-controlled upward movement of the probe.

Theoretical aspects[139,140] The starting point of the derivation of the working equation is a time-dependent electric field in the harmonic approximation that propagates through the reference line and is given as

$$\hat{E}_1(t) = E_0 \exp(\mathrm{i}\omega t) \tag{2.4}$$

Definition of $x = z_0 - z_0'$ as the relative distance of the probe from the interference minimum permits the electromagnetic wave of the sample beam to be expressed as

$$\hat{E}_2(t, x) = E_0 \exp(-\alpha_\mathrm{a} x) \exp[\mathrm{i}(\omega t + \pi - \beta x)] \tag{2.5}$$

where π in the second exponential stems from the condition of fully destructive interference as a result of a phase shift, $\Delta\phi$, of the interfering waves

$$\Delta\phi = (2n + 1)\pi \quad \text{with} \quad n \in \mathbb{Z} \tag{2.6}$$

The detected signal at the receiver is then the superposition of the electric fields $\hat{E}_1(t)$ and $\hat{E}_2(t, x)$ and is written as

$$\hat{E}(t, x) = E_0 \exp(\mathrm{i}\omega t)\,[1 + \exp(-\alpha_\mathrm{a} x) \exp(\mathrm{i}(\pi - \beta x))] \tag{2.7}$$

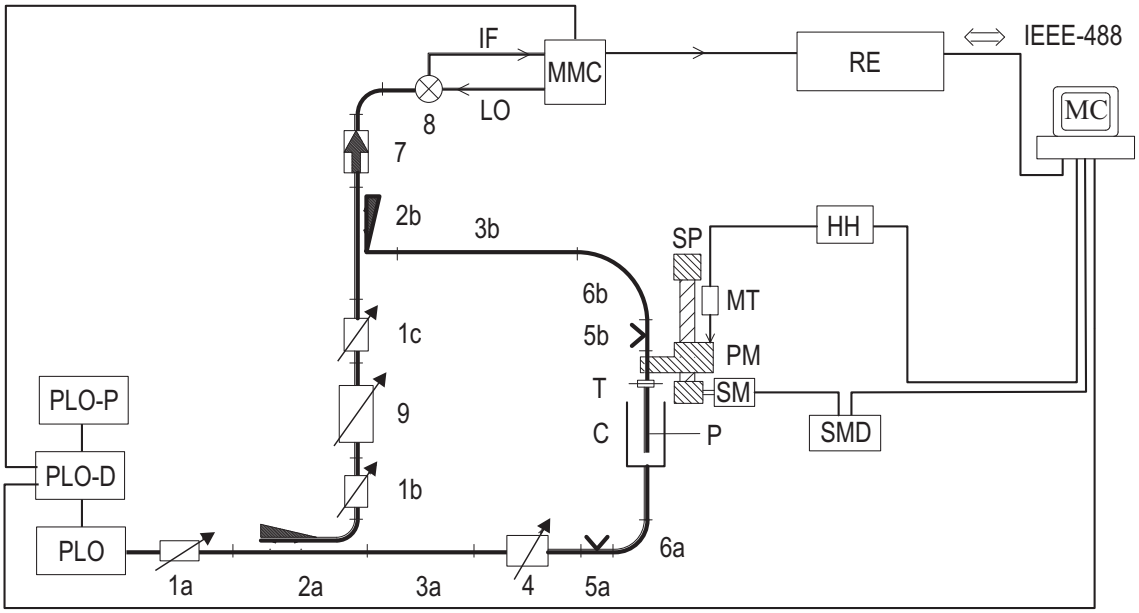

Figure 2.1: Block diagram of the E-band equipment:[139] **1a,b,c**: represent variable attenuators; **2a,b**: directional couplers; **3a,b**: waveguide sections; **4**: precision phase shifter; **5a,b**: E/H tuners; **6a,b**: flexible waveguides; **7**: isolator; **8**: harmonic mixer; **9**: variable precision attenuator; **C**: cell; **HH**: bidirectional counter; **MC**: microcomputer; **MMC**: millimeterwave to micrometerwave converter; **MT**: digital length gauge; **P**: probe; **PLO**: phase locked oscillators; **PLO-D**: PLO-control unit; **PLO-P**: PLO-power supply; **PM**: probe mount; **RE**: precision receiver; **SM**: stepping motor; **SMD**: stepping motor control; **SP**: spindle and spindle mount; **T**: tapered transmission. thick lines represent waveguides and normal lines symbolize data transfer connections.

The power, P, of the signal that reaches the detector is obtained from the square of the amplitude of the electric field

$$P = \hat{E} \cdot \hat{E}^* = E_0^2 \cdot I(x) \tag{2.8}$$

with $I(x)$ being the interference function

$$\begin{aligned} I(x) &= [1 + \exp(-\alpha_\mathrm{a} x)\exp(\mathrm{i}(\pi - \beta x))] \cdot [1 + \exp(-\alpha_\mathrm{a} x)\exp(\mathrm{i}(\pi - \beta x))] \\ &= 1 + \exp(-2\alpha_\mathrm{a} x) + \exp(-\alpha_\mathrm{a} x) \cdot 2\cos(-\pi + \beta x) \end{aligned} \tag{2.9}$$

The experimentally accessible quantity is the relative attenuation of the signal as a function of the path length, $A(x)$, which is related to P by

$$A(x) = 10 \lg \frac{P(x)}{P_\mathrm{ref}} \tag{2.10}$$

As P_{ref} is usually unknown, the measured attenuation is normalized by A_0 that corresponds to $P_0 = E_0^2$:

$$\begin{aligned} A_{\mathrm{rel}}(x) &= A(x) - A_0 \\ &= 10\lg\frac{P(x)}{P_{\mathrm{ref}}} - 10\lg\frac{P_0}{P_{\mathrm{ref}}} \\ &= 10\lg\frac{P(x)}{P_0} \\ &= 10\lg\frac{E_0^2 \cdot I(x)}{E_0^2} \end{aligned} \tag{2.11}$$

Then, insertion of Eq. 2.9 into 2.11 yields the working equation,[139] which can be fitted to the recorded data

$$\begin{aligned} A(z_0 - z_0') = A_0 + 10\lg\,[(1 + \exp(-2p\alpha_{\mathrm{dB}}(z_0 - z_0'))] \\ - 2\cos\left[\frac{2\pi}{\lambda_M}(z_0 - z_0')\right] \cdot \exp(-p\alpha_{\mathrm{dB}}(z_0 - z_0')) \end{aligned} \tag{2.12}$$

with the factor $p = (20\lg e \cdot \mathrm{dB/Np})$ for conversion of α_{dB} (in dB) into α_{a} (in Np). Insertion of α_{a} and λ_{M} into Eqs. 2.2 and 2.3 yields the complex permittivity.

2.2.2 Vector Network Analysis

As a result of ongoing technological developments vector network analyzers (VNA) received increasing attention for measuring dielectric properties of electrical networks, as they enable the simultaneous detection of amplitude and phase information over a large frequency range in a rather time-saving way. The signal transmission of electromagnetic waves at MHz to GHz frequencies is best accomplished by coaxial lines. In two-port setups, an arbitrary electrical network is characterized by the determination of reflected and transmitted electrical signals, expressed in terms of a scattering matrix, **S**, which is defined as

$$\begin{pmatrix} \hat{b}_1 \\ \hat{b}_2 \end{pmatrix} = \begin{pmatrix} \hat{S}_{11} & \hat{S}_{12} \\ \hat{S}_{21} & \hat{S}_{22} \end{pmatrix} \begin{pmatrix} \hat{a}_1 \\ \hat{a}_2 \end{pmatrix} \tag{2.13}$$

with $\hat{a}_j$ and $\hat{b}_j$ as incident and reflected waves at port j, respectively.[98,141]
In case of reflection measurements (one-port setup with $j = 1$) of an electrical network, characterized by an impedance step from $\hat{Z}_1$ to $\hat{Z}_2$, the complex scattering coefficient, $\hat{S}_{11}$, is related to the normalized aperture admittance, $\hat{Y} = \hat{Z}_2/\hat{Z}_1$ via

$$\hat{S}_{11} = \frac{1 - \hat{Y}}{1 + \hat{Y}} \tag{2.14}$$

For one-port measurements calibration of the setup is required to account for systematic errors in directivity, $\hat{e}_{\mathrm{d}}$ (caused by imperfections of directional couplers), frequency response, $\hat{e}_{\mathrm{r}}$ (caused by response differences between reference and measurement paths), and source

match, $\hat{e}_\mathrm{s}$ (caused by re-reflected signals from the sample to the port).[142–144] Thus, the determination of the actual scattering coefficient, $\hat{S}_{11}^\mathrm{a}$, from the measured one, $\hat{S}_{11}^\mathrm{m}$, which are related through

$$\hat{S}_{11}^\mathrm{a} = \frac{\hat{S}_{11}^\mathrm{m} - \hat{e}_\mathrm{d}}{\hat{e}_\mathrm{s}(\hat{S}_{11}^\mathrm{m} - \hat{e}_\mathrm{d}) + \hat{e}_\mathrm{r}} \tag{2.15}$$

is enabled by measuring three calibration standards. In this work an open(air)-short(purified mercury)-load(standard liquid) calibration was applied. After calibration rearrangement of the experimental setup must be avoided as mechanical stress on the coaxial lines may cause significant systematic errors.[94]

Open-ended coaxial probes

Dielectric spectra in the frequency range $0.2 \leq \nu/\mathrm{GHz} \leq 50$ were recorded using a dielectric probe kit (85070E) connected via an electronic calibration module (Agilent ECal N4693) to an Agilent E8364B VNA. As the ECal module measures well known reflection standards during the experiment, systematic drifts due to thermal expansion are compensated thus stabilizing the calibration.[145]
The dielectric probe kit contains two distinct dielectric probes suitable for the frequency ranges $0.2 \leq \nu/\mathrm{GHz} \leq 20$ (85070E-020, high temperature) and $1.0 \leq \nu/\mathrm{GHz} \leq 50$ (85070E-050, performance), which are both mounted in a thermostated cell as described by Schrödle.[140]
The temperature was controlled with an accuracy of ± 0.02°C by a Huber CC505 thermostat and measured with a platinum resistance thermometer (PRT, Pt-100) linked to an Agilent 34970A datalogger.
As implemented in the Agilent 85070C Software package, a simplified coaxial aperture opening model[142,146,147] was used to calculate the dielectric properties of the sample, $\hat{\eta}_\mathrm{m}$, from the normalized aperture admittance of the probe head, by numerical solution of

$$\hat{Y} = \frac{\mathrm{i}\hat{k}_\mathrm{m}^2}{\pi\hat{k}_\mathrm{c}^2 \ln(D/d)} \left[\mathrm{i}\left(I_1 - \frac{\hat{k}_\mathrm{m}^2 I_3}{2} + \frac{\hat{k}_\mathrm{m}^4 I_5}{24} - \frac{\hat{k}_\mathrm{m}^6 I_7}{720} + \ldots \right) + \left(I_2 \hat{k}_\mathrm{m} - \frac{\hat{k}_\mathrm{m}^3 I_4}{6} + \frac{\hat{k}_\mathrm{m}^5 I_6}{24} - \ldots \right) \right] \tag{2.16}$$

with the propagation constants within the dielectric material in the probe head, $\hat{k}_\mathrm{c} = \omega\sqrt{\hat{\eta}_\mathrm{c}\varepsilon_0\mu_0}$ and within the sample, $\hat{k}_\mathrm{m} = \omega\sqrt{\hat{\eta}_\mathrm{m}\varepsilon_0\mu_0}$. From an implemented theoretical approach the first 28 probe constants, I_i, are calculated where d and D are the radii of inner and outer conductor of the coaxial line, respectively.
Prior to measurement the VNA has to be calibrated according to Eq. 2.15 by an open-short-load calibration using air, purified mercury and a suitable reference liquid, respectively, whereas the latter should have similar dielectric properties (i.e. dielectric constant and relaxation times) as the sample. For all neat ionic liquids studied in this work DMA (Sigma Aldrich > 99.9%) was used as a primary standard at all investigated temperatures with the dielectric parameters given in Ref. 148.
In case of considerable deviations of the dielectric properties of the sample from that of the reference, a secondary calibration of the conductivity-corrected (Eq. 1.22) raw permittivity

spectrum, $\hat{\varepsilon}_{\mathrm{raw}}(\nu)$, is required to account for imperfections in the aperture impedance model (Eq. 2.16). This is achieved by application of a complex Padé approximation[149]

$$\hat{\varepsilon}_{\mathrm{corr}}(\omega) = P_{n/m}[\hat{\varepsilon}_{\mathrm{raw}}(\omega)] = \frac{\hat{A}_0(\omega) + \hat{A}_1(\omega) \cdot \hat{\varepsilon}_{\mathrm{raw}}(\omega) + \ldots + \hat{A}_n(\omega) \cdot [\hat{\varepsilon}_{\mathrm{raw}}(\omega)]^n}{1 + \hat{B}_1(\omega) \cdot \hat{\varepsilon}_{\mathrm{raw}}(\omega) + \ldots + \hat{B}_m(\omega) \cdot [\hat{\varepsilon}_{\mathrm{raw}}(\omega)]^m} \tag{2.17}$$

where $\hat{A}_n(\omega)$ and $\hat{B}_m(\omega)$ are the complex approximation constants. The corrected permittivity spectrum, $\hat{\varepsilon}_{\mathrm{corr}}$, is then obtained either analytically or by a complex fit algorithm[89] from a set of at least three secondary calibration standards of known dielectric properties. For ionic liquids a combination of DMA, benzonitrile (BN; Sigma Aldrich, > 99.9%) and 1-butanol (1-BuOH; Merck, for spectroscopy) was found to be most convenient, as these standards cover a large range of dielectric properties, allowing the application of a $P_{1/1}$ calibration. For automation the whole data processing procedure, starting from formatting raw permittivity spectra over conductivity correction (Section 1.1.3) to Padé calibration (Eq. 2.17), was implemented in a combined MATLAB/MAPLE script.
The effect of Padé correction is illustrated in Figure 2.2 by comparison of one-port reflection measurements before (■ and ▲) and after (□ and △) Padé correction with data obtained from absolute transmission measurements (○ and ◊).

Cut-Off type coaxial cells

Coaxial cells of the cut-off type, previously developed for a Time-Domain-Reflection (TDR) setup,[89,140] were connected to the VNA allowing the determination of the frequency-dependent complex permittivity from $0.05 \lesssim \nu/\mathrm{GHz} \lesssim 1.0$.[59] The different geometry of the cells compared to that of the open-ended type (see above) requires a different mathematical expression for the aperture impedance, which is given in its normalized form as[59,150]

$$\hat{Y} = \left[-2\pi Z_{\mathrm{L}} \ln\left(\frac{d}{D}\right) \sqrt{\frac{\varepsilon_0}{\mu_0} \cdot \hat{\eta}(\omega)} \tanh\left(\frac{\mathrm{i}\omega l}{c}\sqrt{\hat{\eta}(\omega)}\right) + \mathrm{i}\omega\hat{\eta}(\omega) Z_{\mathrm{L}} C_{\mathrm{s}} \right]^{-1} \tag{2.18}$$

where Z_{L} is the wave resistance of the feeding line (typically 50 Ω) and C_{s} the discontinuity capacity of the coaxial to circular waveguide transition. The electrical model turns into that previously used in TDR experiments for $C_{\mathrm{s}} = 0$.[89,140,151] Subsequently, the permittivity spectra, $\hat{\eta}(\omega)$, are obtained by numerical solution of Eq. 2.18.
Prior to measurement the VNA is calibrated in the frequency range of interest by a one-port calibration as implemented in the Agilent software using the ECal module. After that, the coaxial line is connected to the measurement cell and a three-point calibration, which was found to be essential,[59] using open, short and load is applied to calibrate the VNA with respect to the sample-coaxial line interface. With this, errors in directivity, frequency response and source match can be determined according to Eq. 2.15, which permits the calculation of the actual complex scattering parameter $\hat{S}_{11}$. For open calibration $\hat{S}_{11}$ of the empty cell (air) was measured, whereas NaCl(aq, 5 mol kg^{-1}) and NaCl(aq, 0.2 mol kg^{-1}) were used for short-circuit calibration. Due to the fact that for the two latter the conductivity contribution dominates the dielectric response in the measured frequency range, the usage of dielectric parameters of minor quality is of no consequence.[152] Concerning

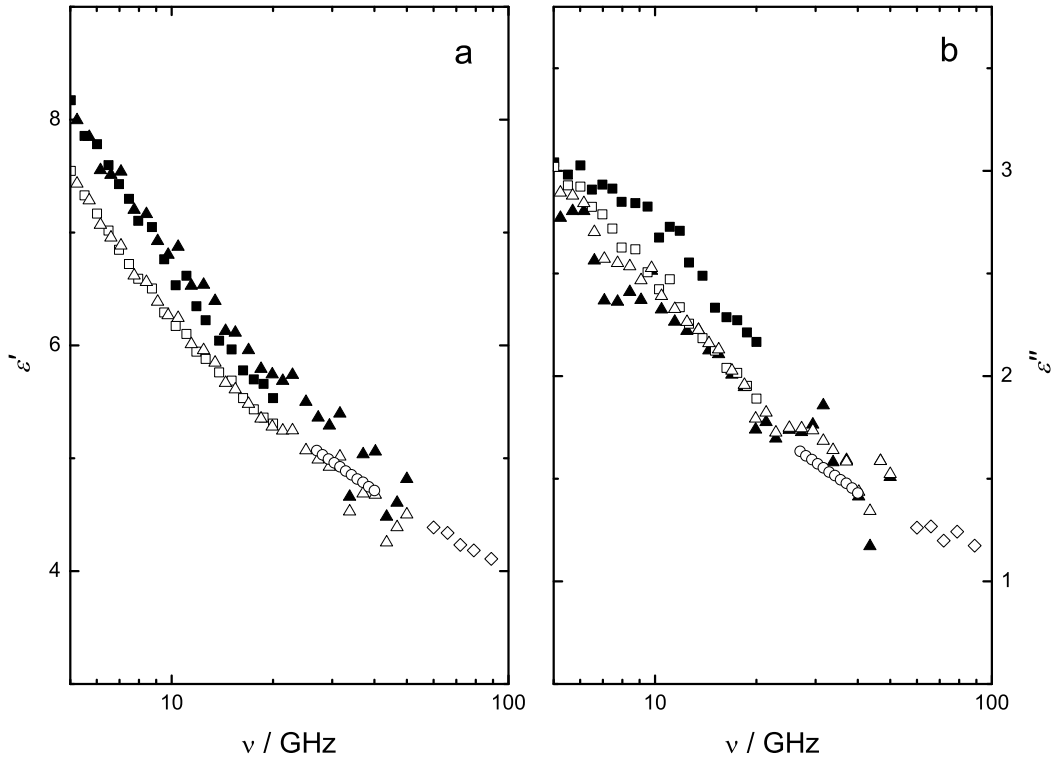

Figure 2.2: Dielectric permittivity (**a**) and loss (**b**) spectrum of $[S_{222}][TFSA]$ at 25 °C ($\kappa = 0.73\,S\,m^{-1}$). Full symbols are raw spectra measured with 20 GHz (■) and 50 GHz (▲) probe heads, respectively. Open symbols (□ and △) are the corresponding Padé-corrected dielectric spectra (DMA-BN-1-BuOH) together with data obtained from absolute transmission experiments in the A-band (○) and E-band (◊) frequency range.

the load standard Hunger introduced the so-called "calibration triangle", which allows to assess the suitability of the third reference.[59] It intends that in the complex plane, the $\hat{S}_{11}$ values of the sample should be enclosed by those of the three calibration standards at the measured frequencies. Although this approach provides a good indication for the selection of an appropriate reference liquid, it was found that this requirement must not be necessarily fulfilled as it is shown in Figures 2.3 and 2.4 for PAN at 15 °C. This means that although the triangle spanned by the set air-NaCl-1-propanol does not comprise the data point of PAN at 1 GHz, it yields a dielectric spectrum of similar ($\varepsilon''(\nu)$) or even better quality ($\varepsilon'(\nu)$) than that of air-NaCl-DMA that meets the proposed condition. This in turn suggests, that the choice of the reference liquid is of minor importance but the geometry of the cell represents the determining prerequisite for a successful measurement.
The cells were temperature-controlled by a Julabo FP-45 thermostat that was stable to ±0.1 °C. The temperature was measured by Pt-100 resistance connected to a high precision thermometer (ASL F250).

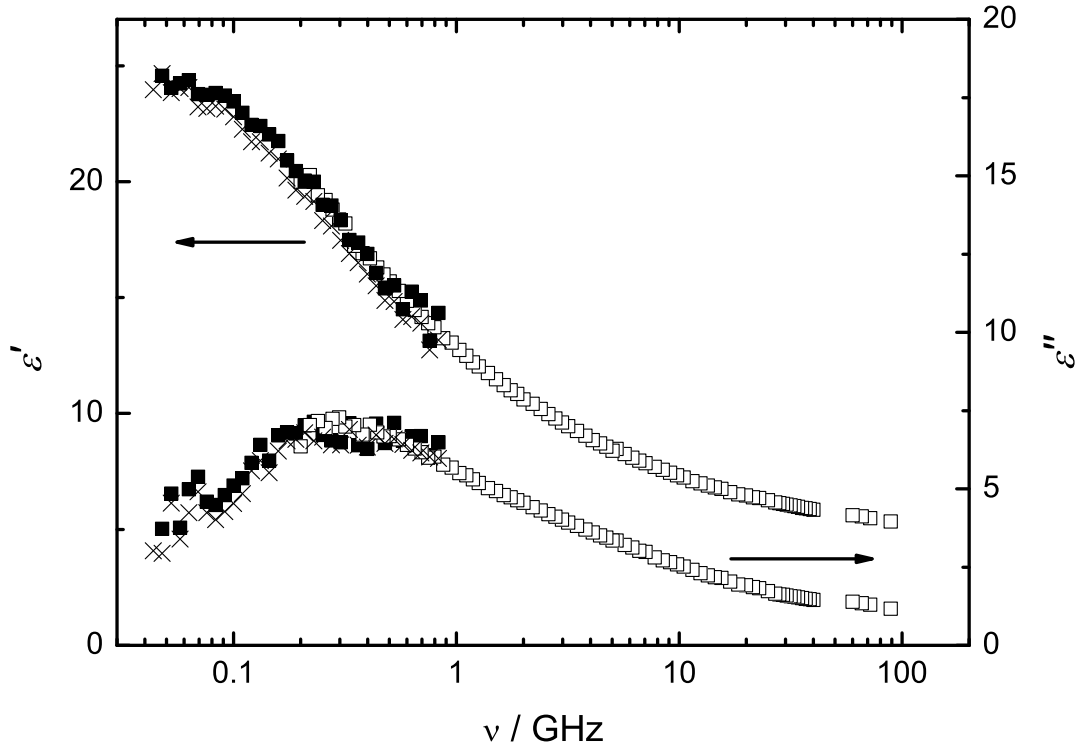

Figure 2.3: Dielectric permittivity, $\varepsilon'(\nu)$, and loss, $\varepsilon''(\nu)$, of PAN at 15 °C. Open squares (□) represent permittivity spectra measured with open-ended dielectric probes and the E-band interferometer. Low-frequency data points were measured using the TS3 Cut-Off type cell and calibrated with air-NaCl-1-propanol (■) and air-NaCl-DMA (×).

Waveguide transmission cells

As the VNA used in this work is able to generate frequencies up to 50 GHz, waveguide transmission cells available for X-, Ku- and A-band, which were previously operated equivalently to the E-band interferometer setup (Section 2.2.1), were connected to the Agilent E8364B VNA as described by Hunger.[59] Furthermore, the ability of detecting amplitude and phase simultaneously allows the determination of the complex permittivity by a simple transmission experiment, where the complex $\hat{S}_{12}$ parameter is recorded as a function of the optical path length, z, at each measured frequency. From the slopes of the linear regression of phase and magnitude of $\hat{S}_{12}(z)$ the medium wavelength, λ_{M}, and the absorption coefficient, α_{dB}, is obtained, respectively. This in turn allows the calculation of the complex permittivity according to the Eqs. 2.2 and 2.3.
The stepper motor of the dielectric probe, the VNA and a precision gauge for the determination of the optical path length were controlled by a personal computer, thus automating the measurement. A Huber CC505 thermostat was used to control the temperature of the A-band transmission cells with an accuracy of ±0.02 °C, whereas X- and Ku-band cells were hooked to a Julabo FP 50 thermostat enabling a temperature stability of ±0.05 °C. Via an Agilent 34970A datalogger the temperature was sampled and measured by a pla-

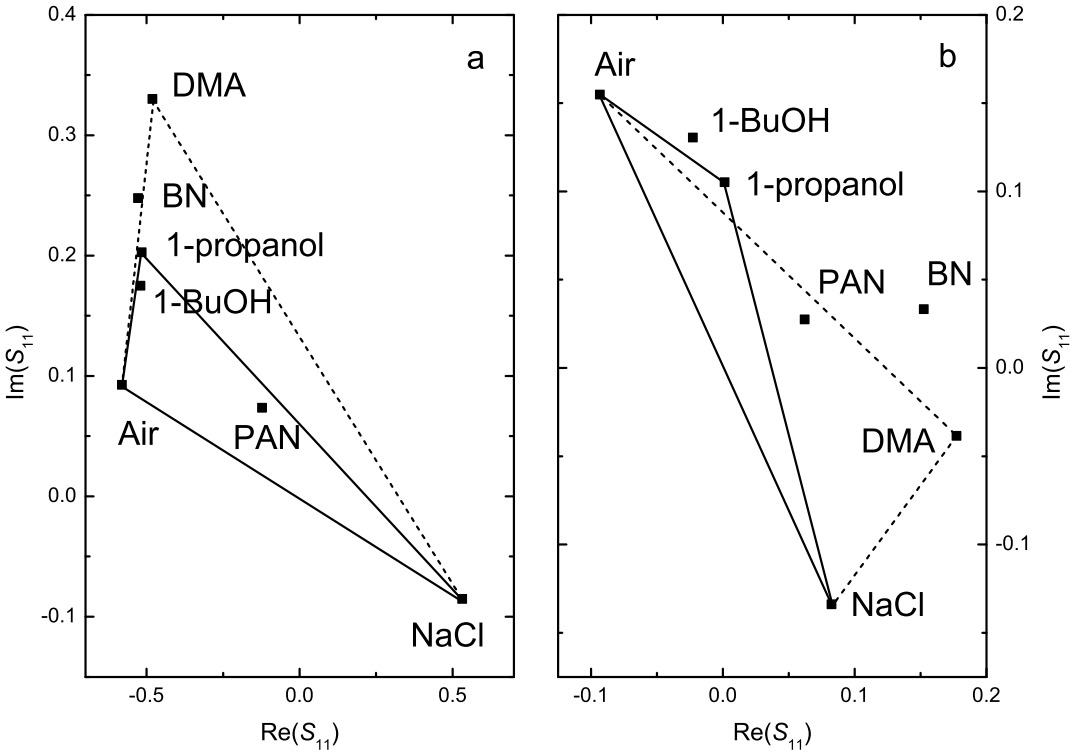

Figure 2.4: Complex scattering parameter $\hat{S}_{11}$ of various reference liquids and PAN at 100 MHz (**a**) and 1 GHz (**b**) measured with the TS3 cell[89] at 15 °C. Full lines indicate the triangle spanned by the set of standards air-NaCl-1-propanol and dashed lines that of air-NaCl-DMA.

tinum resistance thermometer (PRT, Pt-100) in a 4-wire configuration.
The outstanding advantage of these waveguide transmission setups is that they provide accurate and absolute permittivity data superseding any calibration. Therefore in this work, A-band measurements were mainly used to crosscheck the suitability of the secondary calibration standards used for Padé-calibration of permittivity spectra obtained with the open-ended coaxial cells. In case of strong deviations data measured with the 50 GHz probe head were replaced by the A-band data. Due to the expense of the studied ILs it was refrained from using X-, and Ku-band cells, because of their exceeding requirements of sample volume.

2.2.3 Time-domain THz-pulse Spectroscopy

In collaboration with the group of Dr. M. Walther (Albert-Ludwigs-Universität Freiburg, Germany), dielectric spectra measured by means of time-domain THz-pulse spectrometry (THz-TDS)[153–155] operating in transmission and reflection geometry (Figure 2.5) were used. Pulses with a duration of $\sim$ 20 fs and a repetition rate of 80 MHz are generated by a mode-locked Ti:sapphire laser (Femtosource, Femtolasers Inc.; $\sim$ 790 nm center wavelength) pumped by a 532 nm Nd:YVO_4 solid state laser (Verdi, Coherent Inc.) and split into

an excitation and detection beam. The first drives a THz emitter antenna (**E**) that consists of metal stripes (separated by $\sim 50\,\mu$m) on a semiconducting gallium-arsenide (GaAs) substrate and is biased by a DC voltage ($+40\,$V).[156,157] The laser pulse is focused in between these stripes leading to the creation of charge carriers, which are accelerated in the applied field. In that way, a current between the semiconducting structure is induced causing the emission of electromagnetic radiation in the frequency range of $0.1 < \nu/\mathrm{THz} < 5$. The second beam passes a delay line (**D**) permitting the measurement of the temporal profile of the THz electric field before gating the THz detector (**R**). This consists of a H-shaped metal structure on a low temperature-grown GaAs substrate, where a photocurrent proportional to the incident electric field is induced. This current is measured with the help of a lock-in amplifier and a chopper wheel (**Ch**) operating at 330 Hz. Both transmission and reflection setup are purged with dry nitrogen to avoid absorption of THz radiation by water vapor.[156] All spectra used in this work were measured by co-workers of Dr. M. Walther.

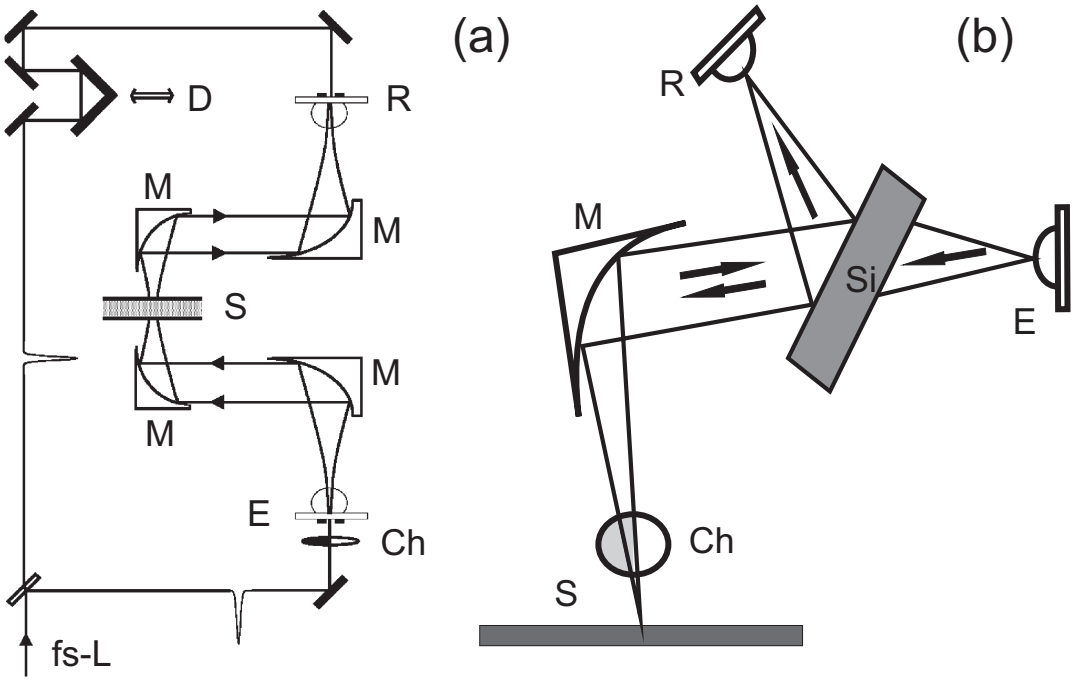

Figure 2.5: Scheme of time-domain THz-pulse setup in (**a**) transmission[59,140] and (**b**) reflection geometry consisting of femtosecond laser (**fs-L**), chopper wheel (**Ch**), parabolic mirrors (**M**), silicon wafer (**Si**), sample (**S**), emitter antenna (**E**), receiver antenna (**R**) and delay line (**D**).

Transmission setup[156,158] With the transmission setup (Figure 2.5a) a frequency range of $0.08 \lesssim \nu/\mathrm{THz} \lesssim 1.5$ can be covered. As described in Ref. 140 the sample is placed in the cell consisting of two parallel PTFE windows with an effective path length of $\sim 1.5\,$mm. The temperature is controlled by a Julabo FP-50 thermostat and measured with a calibrated Pt-100 resistance sensor with an overall accuracy of $\pm 1\,^{\circ}$C.[156]

In the transmission experiment the temporal profile of the electric field strength, $E(t)$, of the THz transient is recorded and subsequently transformed to the frequency-domain by Fourier transformation, yielding $\hat{E}(\omega)$. Normalization of the sample signal by a reference pulse through the empty cell yields the ratio

$$\frac{\hat{E}_{\text{sample}}}{\hat{E}_{\text{ref}}} \equiv Ae^{\text{i}\phi} = \frac{n_{\text{s}}(\omega)(n_{\text{w}}+n_{\text{air}})^2}{(n_{\text{s}}(\omega)+n_{\text{w}})^2} \exp\left[-\xi(\omega)\omega\frac{z}{c_0}\right] \exp\left[\text{i}(n_{\text{s}}(\omega)-1)\omega\frac{z}{c_0}\right]. \tag{2.19}$$

where the first factor results from the attenuation of the signal due to transmission through air-cell and cell-sample (index 's') interfaces. The refractive index of the cell window, $n_{\text{w}} = 1.433$,[159] was assumed to be frequency-independent. The refractive index of the sample, n_{s}, is then directly obtained from the phase, ϕ, through

$$n_{\text{s}}(\omega) = n_{\text{air}} + \frac{\phi c_0}{\omega z} \tag{2.20}$$

with $n_{\text{air}} = 1.00027$ and z as the optical path length. The absorption coefficient can be extracted from the complex amplitude, A, with the help of Eq. 1.29 by

$$\alpha_{\text{s}}(\omega) = -\frac{2}{z}\ln\left[\frac{(n_{\text{s}}(\omega)+n_{\text{w}})^2}{n_{\text{s}}(\omega)(n_{\text{w}}+n_{\text{air}})^2}A\right]. \tag{2.21}$$

Conversion of n_{s} and α_{s} into real and imaginary part of $\hat{\eta}(\omega)$ is then achieved by using Eq. 1.29 and insertion into

$$\eta' = n_{\text{s}}^2 - \xi^2 \tag{2.22}$$

$$\eta'' = -2n_{\text{s}}\xi \tag{2.23}$$

Reflection setup[156,158] To overcome the limitations in frequency range of the transmission setup for highly absorbing samples, a setup working in reflection geometry (Figure 2.5b) is used, thus allowing measurements up to ~ 3 THz. Whilst generation and detection of the THz pulses is in analogy to that in the transmission setup, the emitted pulse passes through a beam splitter (**Si**) before it is focused on the sample (**S**), which is placed on a silicon window. The pulse is reflected from the Si-sample interface and detected at the receiver (**R**). According to Fresnel's equation the reflected electric field strength, E_{r}, in case of normal incidence and planar reflection surfaces is given as

$$E_{\text{r}} = E_{\text{inc}}\frac{\hat{n}_{\text{Si}}-\hat{n}_j}{\hat{n}_{\text{Si}}-\hat{n}_j} \tag{2.24}$$

where $\hat{n}_{\text{Si}} = n_{\text{Si}} = 3.42$ is the refractive index of the silicon window and $\hat{n}_j$ (with j =air,s) that of the sample or of air. The latter was used as a reference. From the ratio

$$\frac{E_{\text{s}}}{E_{\text{air}}} = \frac{n_{\text{Si}}-\hat{n}_{\text{s}}}{n_{\text{Si}}+\hat{n}_{\text{s}}} \cdot \frac{n_{\text{air}}+n_{\text{Si}}}{n_{\text{Si}}-n_{\text{air}}} \tag{2.25}$$

the complex refractive index of the sample can be obtained, which is then used to calculate the generalized complex permittivity according to Eq. 1.23.

2.2.4 Far-infrared Spectroscopy

For substances, where the dispersion, $\varepsilon'(\nu)$, has not decayed to n_D^2 at $\sim 3\,\mathrm{THz}$, the frequency range has to be extended in order to obtain a complete dielectric spectrum, which captures all processes that contribute to the orientational polarization (Figure 1.1). Therefore, far-infrared spectroscopic measurements were performed in collaboration with the group of Prof. Dr. Klaas Wynne (Glasgow University, Glasgow, UK) using a Bruker Vertex 70 FTIR spectrometer based on a Michelson-interferometer. The sample was placed between two polymethylpentene (TPX) windows separated by PTFE spacers of $20\,\mu\mathrm{m}$ or $56\,\mu\mathrm{m}$ thickness (depending on the absorption strength of the sample) to adjust the path length. The windows were then fixed in a temperature-controlled cell holder, mounted in the nitrogen-purged measurement chamber of the spectrometer. The major difference

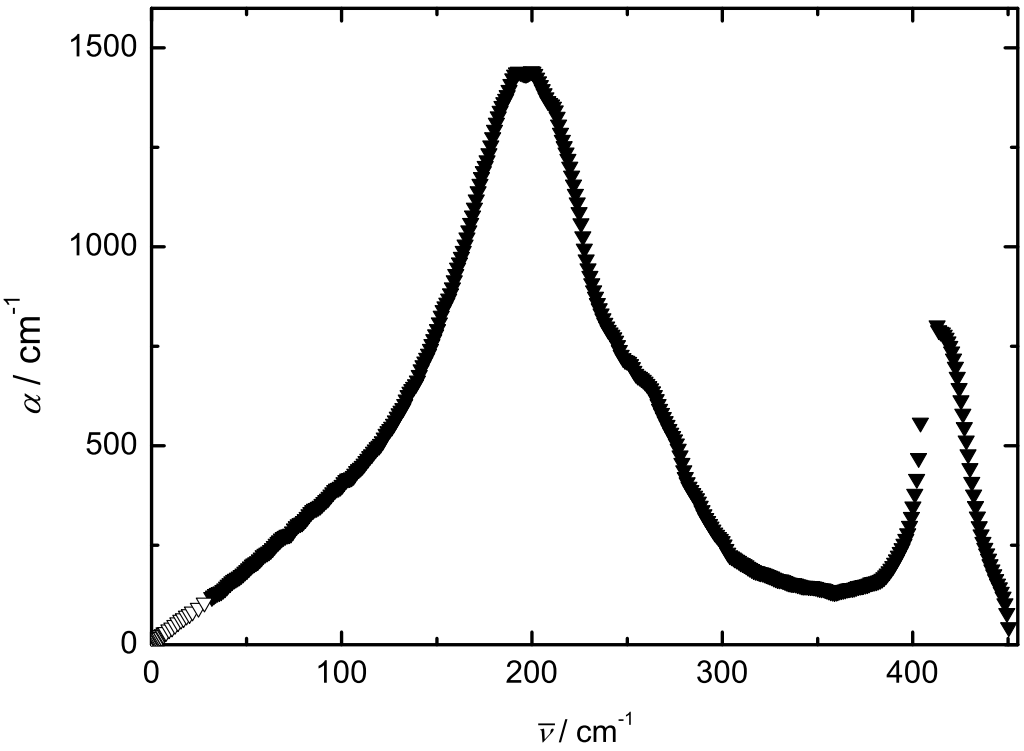

Figure 2.6: Absorption spectrum, $\alpha(\bar{\nu})$, of EAN at 25 °C. Open triangles (▽) represent data obtained from VNA, interferometry and THz-TDS experiments and full triangles (▼) are data measured by FTIR spectroscopy.

to the techniques described in Section 2.2.1-2.2.3 is that commercial FTIR instruments as used in this work are not able to determine the complex refractive index, $\hat{n}$, but only the absorption coefficient, α (Section 1.1.3).[97] Thus, to obtain the complex permittivity spectrum, $\hat{\varepsilon}(\nu)$, the refractive index has to be calculated according to the Kramers-Kronig

relation,[160] which relates real and imaginary part of $\hat{n}$ via

$$n(\bar{\nu}') - n_\infty = \frac{1}{2\pi^2} \int_0^\infty \frac{\alpha(\bar{\nu})}{\bar{\nu}^2 - \bar{\nu}'^2} \mathrm{d}\bar{\nu} \tag{2.26}$$

with n_∞ as the refractive index at infinite frequencies. The integration from 0 to ∞ requires that α is zero at the upper and lower integration limit. For $\bar{\nu} \to 0$, this is achieved by combining the FIR spectrum with the data obtained from VNA, IFM and THz-TDS measurements. In this work the concatenation of individual spectra was automated by implementing the procedure described by Hunger[59] into a MATLAB script. First, the combined dielectric spectrum, $\hat{\varepsilon}(\nu)$, measured with VNA, interferometry and THZ-TDS was formally fitted using empirical model functions (Section 1.2) and then converted into the complex refractive index representation, $\hat{n}$, according to Eqs. 1.24 and 1.25. Second, α values obtained from FTIR spectroscopy were adjusted by a scaling factor and an offset correction to match low-frequency data in the overlapping frequency range at $\sim 30\,\mathrm{cm}^{-1}$. In this procedure the adjustment of the FIR α-spectrum accounts for the rather uncertain optical path length of the FTIR cell (due to varying tightness of the screws to fix the windows in the cell) and for fluctuations of the intensity of the radiation source (offset correction). Third, from the so obtained complete absorption spectrum, the refractive index is then calculated via numerical integration according to Eq. 2.26 using the trapezoidal method. To avoid the occurrence of discontinuities at $\bar{\nu} = \bar{\nu}'$ integration was performed at $\bar{\nu}' = (\nu_i + \nu_{i+1})/2$.[161] Subsequently, $n(\bar{\nu})$ was obtained via linear interpolation of $n(\bar{\nu}')$ and combined with data of n obtained from VNA, IFM and THz-TDS measurements by using n_∞ as an adjustable parameter.

2.3 Optical Kerr-Effect Spectroscopy

Optical heterodyne-detected Kerr-effect spectroscopy (OKE) is a third-order nonlinear spectroscopy, which measures the time-derivative of the two-point time-correlation function of the anisotropic part of the many-body polarizability tensor, Π, given by[107]

$$S(t) \propto \frac{1}{k_\mathrm{B}T} \frac{\mathrm{d}}{\mathrm{d}t} \langle \Pi_{xy}(t) \Pi_{xy}(0) \rangle \tag{2.27}$$

Thus, the technique can be considered as time-domain Raman spectroscopy as its spectrum is equivalent to the low-frequency depolarized Rayleigh spectrum multiplied by a Bose-Einstein factor.[33] Moreover, as OKE spectroscopy is sensitive to changes of polarizability, it represents a complementary technique to dielectric relaxation spectroscopy that probes the changes of the macroscopic dipole moment (Section 1.1.1).[162]

Instrumentation[33,106,163] Within this work OKE measurements were performed at Glasgow University (Glasgow, UK) in the group of Prof. Dr. Klaas Wynne and supervised and assisted by Dr. D. Turton. Because of the slow dynamics of the studied ionic liquids, a wide time span ranging from tens of femtoseconds to nanoseconds is required to

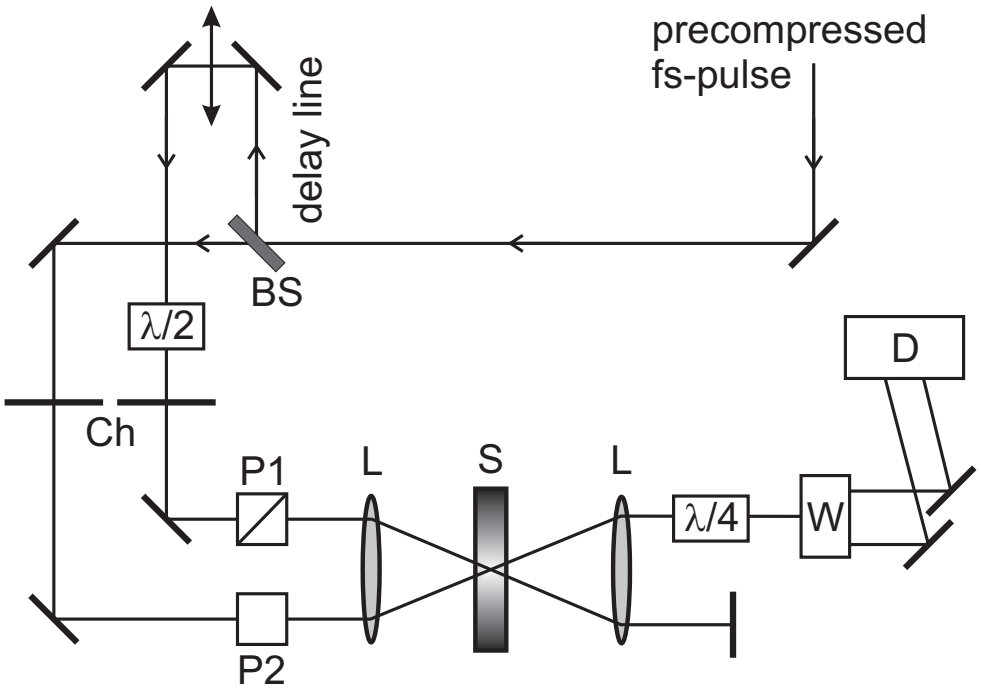

Figure 2.7: Scheme of OKE setup consisting of beamsplitter, (**BS**), chopper wheel (**Ch**), lenses (**L**), polarizers (**P1 & P2**), $\lambda/2$ and $\lambda/4$ plates, cuvette with sample (**S**), Wollaston prism (**W**), and detector (**D**).

capture the entire intermolecular motions. This was achieved by combining the data obtained from two setups: One with a large dynamical range for probing long-time dynamics up to nanoseconds and one with high time resolution, suitable for femto- to picosecond dynamics. The assembly of the latter is schematically shown in Figure 2.7.
A linearly polarized laser pulse with a center wavelength of 800 nm, an energy of 8 nJ and $\sim$ 20 fs duration at a repetition rate of 76 MHz is generated by a mode-locked Ti:sapphire laser, which is pumped by a Nd:YAG laser (Coherent Verdi). After precompensation for group-velocity dispersion in the setup, the beam is split (**BS**) into pump (90 %) and probe (10 %) beam, whereupon the pump beam is guided through a delay line of 500 nm resolution (3.3 fs) and a maximum delay of 4 ns. With the help of two polarizers (**P1 & P2**) an angle of 45 ° between pump and probe-beam polarization is adjusted. After that, the two beams are focused into the sample (**S**) contained in a 2 mm path length quartz cuvette placed in a temperature-controlled cell holder. The heterodyne component to the signal is introduced by slight rotation of the input polarizer ($\approx 1\,°$) leading to the generation of a so-called local oscillator. The output signal, now consisting of background, homodyne and heterodyne components, passes a quarter-wave plate, which provokes a fully circular polarization of the beam. The signal is then separated into its horizontal and vertical components by a Wollaston prism (**W**), before it is measured by a pair of photodiodes wired up for balanced detection (**D**). The balanced-detection technique enables the electronic subtraction of horizontal and vertical component, thereby cancelling the background and homodyne signal and thus allows the direct measurement of the pure heterodyne signal.

To improve the signal-to-noise ratio pump and probe beam are mechanically chopped (**Ch**) with lock-in amplification. Although chopping considerably attenuates the signal, it minimizes spurious signals due to scattering and reflection of the pump light from the sample and cell windows.
The measurement principle is the same for the second setup, which is specially suited for probing slow dynamics up to nanoseconds. A laser pulse (~ 25 ps duration) with a center wavelength of 800 nm and an energy of 2.5 mJ at a repetition rate of 1 kHz is generated by a regenerative amplifier (Coherent Legend USX). To obtain signals with greater dynamical range, the pulse is stretched to ~ 1 ps duration and attenuated to 2.5 μJ. Furthermore, the delay stage is passed twice by the pump beam to allow measurements to longer decay times. In both configurations at least 16 scans per trace were performed each with approximately 250 points. The data of the two setups overlap between ~ 1 and ~ 10 ps, allowing the concatenation to a single data set.
In both setups, the sample cuvette was mounted in a temperature-controlled cryostat (Oxford Instruments, *Optistat DN*) for measurements from 5 to 25 °C, whereas between 35 to 65 °C a home-built copper block controlled by low-voltage electrical heaters was used.

Theoretical aspects and analysis of the OKE signal The technique is based on the optical Kerr-effect, which can be understood as the induction of a transient birefringence in the sample by an intensive polarized light beam. As the birefringence is a result of electronic and nuclear orientation along the electric field, the sample is no longer isotropic and the refractive index parallel to the field differs from that perpendicular to it. Accordingly, the induced polarization, P, has to be expressed in its general form including higher-order contributions[164]

$$\vec{P} = \varepsilon_0[\chi^{(1)} \cdot \vec{E} + \chi^{(2)} \cdot \vec{E} \cdot \vec{E} + \chi^{(3)} \cdot \vec{E} \cdot \vec{E} \cdot \vec{E} + ...], \tag{2.28}$$

where $\chi^{(1)}(= 1 - \varepsilon)$ is the linear optical susceptibility and $\chi^{(2)}$ the second-order susceptibility. The latter, however, can be neglected as it is zero for all centrosymmetric and isotropic materials. The third-order susceptibility, $\chi^{(3)}$, is responsible for a change in the refractive index and is related to n via[165]

$$n = n_0 + \frac{\chi^{(3)}}{2n_0}|E_0|^2 \tag{2.29}$$

where, n_0 is the linear and $n_2 = \chi^{(3)}/2n_0$ the second-order refractive index. Note that n, n_0 and n_2 are actually complex quantities. However, as OKE spectroscopy is an off-resonant experiment, the imaginary part (absorption) of the refractive index can be neglected.[165]

The light intensity, $I(\tau)$, finally reaching the detector can be expressed as a convolution of the measured zero-background intensity autocorrelation of the laser pulse, $G^{(2)}(t)$, with the sample response function $R_{\mathrm{OKE}}(t)$[165]

$$I(\tau) \propto \int R_{\mathrm{OKE}}(t - \tau)G^{(2)}(t)\mathrm{d}t. \tag{2.30}$$

As $G^{(2)}(t)$ is accurately determined by a two-photon diode placed at the sample position with identical geometry, the sample response, $R_{\mathrm{OKE}}(t)$, can be obtained via deconvolution

of Eq. 2.30 through forward complex Fourier transformation,

$$F[R_{\mathrm{OKE}}(t)] = \frac{F[I(\tau)]}{F[G^{(2)}(t)]} = \hat{D}(\omega) \tag{2.31}$$

yielding the spectrum, $\hat{D}(\omega)$, which is proportional to the third-order susceptibility, $\chi^{(3)}$.[166] Within the validity of the Born-Oppenheimer approximation the sample response function can be separated into its electronic response, $\sigma(t)$, arising from the electronic part of the nonlinear susceptibility and its contribution associated with nuclear dynamics, $S(t)$, according to[167,168]

$$R_{\mathrm{OKE}}(t) = \sigma(t) + S(t) \tag{2.32}$$

Because $\sigma(t)$ is real it does not contribute to the imaginary part of $\hat{D}(\omega)$, and thus $\Im\hat{D}(\omega)$ exclusively attributed to the nuclear response of the sample can be obtained via inverse Fourier transformation

$$S(t) = 2F^{-1}[\Im\hat{D}(\omega)] \quad \text{for} \quad t \geqslant 0 \tag{2.33}$$

In this way, the macroscopic response of the OKE experiment is related to microscopic properties via Eq. 2.27, as the many-body polarizability tensor represents the sum of all single-molecule polarizabilities and the interaction-induced components.[169]

2.4 Data processing

As both dielectric and OKE spectroscopy measure macroscopic quantities, it needs an appropriate mathematical description to interpret the experimental spectra on a molecular level. Therefore, in this work a new fitting routine (DRSFit) based on the commercially available IGOR software (Wavemetrics, V.6.31) was developed (Appendix A.2) in collaboration with Dr. D. Turton (Glasgow University, UK). The key advantages of DRSFit over the hitherto used MWFIT program is the ability of fitting OKE spectra (in addition to DR spectra) and the implementation of the antisymmetrized Gaussian as a very useful model to describe resonant THz contributions of dielectric and OKE spectra. Additionally, two modifications of the Havriliak-Negami functions (Eqs. 1.37 and 1.38) are implemented to preserve its physical meaning at THz frequencies.[106] Normalized amplitudes of relaxation and resonance functions are directly exported by DRSFit and a correction procedure for electrode polarization effects can be optionally applied.

Prior to fitting, dielectric spectra of conducting samples have to be corrected for the conductivity contribution. Thus, as a first approximation the experimentally measured dc conductivity, κ, is subtracted from the imaginary part of the generalized dielectric permittivity, $\eta''(\nu)$, to obtain $\varepsilon''(\nu)$ according to Eq. 1.22. However, due to fringing field effects caused by geometrical imperfections of the VNA probe head,[170] the corrected conductivity, κ_{fit}, may differ from κ by up to $\sim 10\,\%$. Therefore, κ_{fit} is treated as an additional fit parameter and is adjusted to yield the best fit, provided that no systematic deviations in $\varepsilon'(\nu)$ are observed.

In general, the empirical models presented in Section 1.2 are appropriate to describe relaxation and resonance processes in liquids. However, it should be recognized that fitting

DR and OKE spectra over such a broad frequency range is a formidable task because relaxation processes in condensed phase are rather broad and a successful formal description is not necessary physically reasonable. In particular, cross-terms that arise from coupling between translational and reorientational dynamics cannot be described by a line-shape analysis. Nevertheless, the following criteria are helpful to select an appropriate fit model:

- The reduced error function, χ^2_r, which is a measure of the quality of the fit should be minimized,
$$\chi^2_\mathrm{r} = \frac{1}{2N - m - 1}\left[\sum_{k=1}^{N} \delta\varepsilon'(\nu_k)^2 + \sum_{k=1}^{N} \delta\varepsilon''(\nu_k)^2\right] \tag{2.34}$$
where $\delta\varepsilon'$ and $\delta\varepsilon''$ are the residuals, N is the number of data triple (ν, ε', ε'') and m the number of adjustable parameters.
- The number of relaxation and resonance modes should be reasonably small.
- The fitting parameters should be physically reasonable, i.e. no negative relaxation times and/or amplitudes
- No change of the fitting model within a concentration or temperature series, except for physical reasons.

Furthermore, special care should be taken to ensure a uniform point density of the spectra over the entire frequency range. Especially for broadband spectra ranging from $\sim 200\,\mathrm{MHz}$ to $\sim 10\,\mathrm{THz}$ irregularities are commonly observed, which are mainly caused by the lack of data points between 89 GHz and $\sim 300\,\mathrm{GHz}$. Therefore, the point density can be optionally unified by linear interpolation implemented in the DRSFit fitting routine to stabilize the fit. The simultaneous fit of $\varepsilon'(\nu)$ and $\varepsilon''(\nu)$ is conducted by DRSFit using the Levenberg-Marquardt algorithm.[171]

2.5 Auxiliary Measurements

2.5.1 Density

Density measurements were performed using a vibrating tube densimeter (DMA 5000 M, Anton Paar, Graz, Austria) with an uncertainty of $\pm 5 \cdot 10^{-6}\,\mathrm{g\,mL^{-1}}$. It measures the period of vibration, τ, of a U-shaped borosilicate glass tube filled with the sample, where τ is related to the density, ρ, by

$$\rho = A \times \left(\frac{\tau}{\tau_0}\right)^2 \times f_1 - B \times f_2. \tag{2.35}$$

A and B are calibration constants, τ_0 is the period of a reference oscillator and f_1 and f_2 are factors to correct for temperature, viscosity and nonlinear effects. Compensation of temperature effects plays an important role for measurements far from room-temperature,

as the instrument is calibrated with water at 20 °C only. The temperature of the sample is controlled by Peltier-elements and measured by integrated Pt-100 resistance thermometer allowing density measurements nominally between 0 and 90 °C.

2.5.2 Viscosity

Dynamic viscosities, η, were determined using an automated rolling ball viscometer (AMVn, Anton Paar, Graz, Austria). Therefore, a glass capillary equipped with a steel ball is filled with the sample and mounted in the heating block of the instrument. At a given angle, the rolling time, t, of the steel ball through the capillary is measured and is related to the η according to

$$\eta = K \times (\rho_\mathrm{b} - \rho)t \tag{2.36}$$

where K is the calibration constant and ρ_b and ρ are the densities of the steel ball and the sample, respectively. Selection of a capillary of appropriate diameter (1.6 mm, 1.8 mm, 3.0 mm and 4.0 mm) permits viscosities to be measured in a range between 0.3-2500 mPa s. The repeatability and reproducibility stated by the manufacturer are $< 0.1\,\%$ and $< 0.5\,\%$, respectively. Inclination angles of 30 ° and 70 ° were found to yield most accurate results. The temperature of the sample is controlled by Pt-100 resistance sensors and viscosities can be nominally measured from 5 to 135 °C. In practice, however, only measurements up to ~ 100 °C were feasible, due to technical shortcomings of the heating block.

2.5.3 Electrical Conductivity

Conductivity measurements were performed using a computer-controlled setup, which is described elsewhere.[172] In the temperature range $-35 \leq \vartheta/°\mathrm{C} \leq 65$ a set of five two-electrode capillary cells (with cell constants $C = 25 - 360\,\mathrm{cm}^{-1}$) were used and the temperature was controlled by a Huber (Unistat 705) thermostat. Conductivities between 75 to 190 °C were determined with a set of four two-electrode capillary cells (with cell constants $C = 12 - 46\,\mathrm{cm}^{-1}$) using a homemade precision thermostat as described elsewhere.[60] All used capillary cells were calibrated with KCl(aq)[173] and the temperature was measured with a NIST-traceable Pt sensor and bridge (ASL). The cell resistance, $R(\nu)$, was measured with a relative uncertainty of ≤ 0.0005 in the frequency range of $0.1 \leq \nu/\mathrm{kHz} \leq 10$ and extrapolated to infinite frequency, R_∞, to eliminate electrode polarization effects using the empirical equation

$$R(\nu) = R_\infty + a \cdot \nu^b \tag{2.37}$$

where a and b are fitting parameters specific for the cell. From the extrapolated resistances, R_∞, the specific conductivities were then determined according to $\kappa = C/R_\infty$ having an estimated uncertainty of $\leq 0.5\,\%$.

2.5.4 Refractive indices

Refractive indices, n_D, were measured at 589 nm using an Abbemat automated digital refractometer WR (Anton Paar GmbH, Graz, Austria). At ambient conditions, resolution

and accuracy stated by the manufacturer were 10^{-6} and 10^{-4}, respectively. The temperature was controlled by built-in Peltier elements with a stability of $\pm 0.002\,^{\circ}\mathrm{C}$ and an accuracy of $\pm 0.05\,^{\circ}\mathrm{C}$. To avoid uptake of water during the measurement, the cell was covered by a lid equipped with an inert-gas line allowing measurements under nitrogen atmosphere. The refractive indices so obtained are summarized in Table A.9.

2.5.5 Quantum Mechanical Calculations

For evaluation of the experimental results, molecular properties of molecules, ions and ion-pairs were performed using MOPAC2009[174] with the PM3 or PM6 Hamiltonian.[175] For geometry optimization the eigenvector-following (EF) routine was used. Condensed phase dipole moments (apparent dipole moments, μ_{app}) were obtained using the COSMO technique.[176] Solvent effects were accounted for by assuming appropriate static permittivities. Molecular diameters were determined from the longest atomic distances and addition of van der Waals radii.[177] For molecular volumes, V_{m}, van der Waals volumes were used, calculated from the optimized geometry using WINMOSTAR.[178] Calculations of polarizability tensors were performed using the ORCA program package.[179] After geometry optimization using the 6-311G basis set, single point energy DFT calculations were performed using the 6-31G(2d,2p) basis set.

Chapter 3

Neat Protic Ionic Liquids

Protic ionic liquids (PILs) represent a sub-group of RTILs and are produced by the combination of a Brønsted acid and a Brønsted base through proton transfer reaction.[7] The presence of proton-donor and proton-acceptor sites is responsible for their key characteristics, which is the ability of forming a hydrogen-bonded network thus distinguishing them from other aprotic ILs.[137,180] Depending on the degree of proton transfer from acid to base PILs usually have a non-negligible vapor pressure and some of them can be even distilled[18] with their boiling point occurring below the decomposition temperature.[181] Furthermore, PILs have attracted particular interest as possible replacements for aqueous solutions in batteries and fuel cells, where their relatively high electrical conductivity via ion or proton conduction is of exceptional importance.[24,182–184] However, to tap their full potential in industrial and scientific applications, the knowledge of their liquid structure as well as their microscopic dynamics is essential.

3.1 Ethyl- and Propylammonium Nitrates

Parts of the material presented in this chapter have been published in the paper:

David A. Turton, Thomas Sonnleitner, Glenn Hefter, Andreas Thoman, Markus Walther, Richard Buchner and Klaas Wynne *"Structure and dynamics in protic ionic liquids: A combined ultrafast optical Kerr-effect (OKE) & dielectric study"*, *Faraday Discuss.* **2012** *154*, 145-153.

3.1.1 Introduction

Undoubtedly the best known PIL is ethylammonium nitrate (EAN, $[EtNH_3^+][NO_3^-]$), first investigated almost 100 years ago by Walden.[8] Because of its intrinsic scientific interest as a possible analogue for water,[7,28,185,186] EAN has received considerable attention over the last few years. Given the ongoing interest in ILs in general and PILs in particular with respect to industrial applications,[3,20,25] EAN can serve as a model PIL due to its simple chemical

structure. Recent studies have included small angle neutron scattering (SANS),[187,188] X-ray diffraction (XRD),[189,190] and molecular dynamics (MD) simulations.[191,192] Of more direct relevance to the present investigation, Fumino *et al.*[64,66] have reported the far-infrared (FIR) spectra of EAN and related compounds while Weingärtner and co-workers[52] have measured the dielectric spectrum of EAN up to 40 GHz over the temperature range: $15 \leq \vartheta/°C \leq 80$, subsequently extending their 25 °C spectrum up to 2 THz using time-domain THz spectroscopy (THz-TDS).[75]

These studies have established some important properties of EAN including its static permittivity or dielectric constant, ε_s. The presence of low energy modes in the FIR spectrum has attracted special interest[64] because of their apparent similarity to water. However, unambiguous interpretation of these weak, strongly overlapping and possibly coupled modes is not easy, particularly when using information from only one technique. For this reason Fumino *et al.*[64] employed density field theory (DFT) calculations to assist with their assignments. Nevertheless, a complete understanding of the structure and dynamics of EAN is still lacking.

The combination of ultra-fast optical Kerr-effect (OKE) and broadband dielectric relaxation (DR) spectroscopies, augmented by THz-TDS and FIR measurements has been shown to be a powerful means of investigating the structure and dynamics of imidazolium-based ILs.[36,107] Accordingly, this chapter presents a detailed DR/OKE study of EAN, supplemented by DR spectra of propylammonium nitrate (PAN), with both covering the unusually broad frequency range from approximately 200 MHz to 10 THz, at temperatures: $5 \leq \vartheta/°C \leq 65$. A preliminary discussion of some of these data has appeared[107] but is extended here by further quantitative analysis and a more detailed examination of the important high-frequency processes, including measurements on partially deuterated (d_3-) EAN at 25 °C.

3.1.2 Data acquisition and processing

Syntheses or purchase of the materials used in this study are described in Section 2.1. Dielectric measurements were performed as described in Section 2.2 using an Agilent E8364B VNA combined with two probes operating in the frequency ranges $0.2 \leq \nu/\text{GHz} \leq 20$ (85070E-020 probe) and $1 \leq \nu/\text{GHz} \leq 50$ (85070E-050 probe) and two waveguide interferometers (IFMs) covering the frequencies from $27 \leq \nu/\text{GHz} \leq 40$ and from $60 \leq \nu/\text{GHz} \leq 89$.[139] Air, purified mercury and DMA were used respectively as open, short and load standards for the calibration of the VNA setup. Raw VNA data were corrected for calibration errors with a Padé approximation (Eq. 2.17) using purified BN and 1-BuOH as secondary calibration standards.[149] All DRS experiments were carried out from 5 °C to 65 °C in 10 °C steps, with a temperature stability and accuracy of ± 0.05 °C. For PAN, low frequency dielectric measurements were performed at 5, 15 and 25 °C using the cut-off type reflection cell, TS3 (Section 2.2.2).[193]

Data in the THz region were collected using a transmission/reflection time-domain THz spectrometer (THz-TDS)[153] (at Freiburg; Section 2.2.3), a Bruker Vertex 70 FTIR spectrometer[36] for EAN and a Bruker IFS 66v FTIR for PAN (at Glasgow; Section 2.2.4).

These instruments covered the frequency ranges $0.3 \leq \nu/\mathrm{THz} \leq 3$ and $0.9 \leq \nu/\mathrm{THz} \leq 12$, respectively. Far-infrared (FIR) absorbance data were converted to complex permittivities using the Kramers-Kronig relation (Eq. 2.26) as described in Section 2.2.4.[194] Both THz and FIR spectra were measured from 5 °C to 65 °C in 20 °C steps with a temperature stability of ±0.5 °C. Combination of all these data provided dielectric spectra (Figures 3.3 and 3.4) covering $0.2 \leq \nu/\mathrm{GHz} \leq 10\,000$. Additionally, THz-TDS and FTIR measurements of d_3-EAN were performed at 25 °C between 25 cm^{-1} and 450 cm^{-1} ($0.7 \lesssim \nu/\mathrm{THz} \lesssim 13$).
As described in Section 1.1.3, dielectric spectra of conducting samples have to be corrected for conductivity contributions to obtain the pure dielectric response, $\hat{\varepsilon}(\nu)$. Accordingly, κ was treated as an additional adjustable parameter to yield the best description of the experimental data. For reasons mentioned in Section 2.2.2, fitted conductivities derived in this manner usually differ from experimental values: for the present systems by ∼ 2-16 %.

As described in Section 2.3, two OKE setups were employed to capture the entire time span of the orientational and intermolecular dynamics of EAN. For the faster dynamics a Coherent Mira-SEED oscillator was used that generated 800 nm pulses with an energy of 8 nJ and a pulse duration of 20 fs at a repetition rate of 76 MHz. The parent beam was split into 80 %-pump and 20 %-probe beams which were cofocused into a quartz cuvette containing the sample. For lower temperatures the sample was controlled to ±0.1 °C by a cryostat (Oxford Instruments, DN). Above room temperature a home-built copper heating block was employed. A 600 mm delay line, with a resolution of 50 nm (0.33 fs) gave a time scale of 4 ns, resulting in a bandwidth of *ca.* 250 MHz.[36] For slower dynamics a similar setup using a regeneratively-amplified laser (Coherent Legend USX) with a stretched pulse duration of *ca.* 1 ps was used to increase the signal-to-noise ratio of the weak relaxation signal at longer times. The two time-domain signals were concatenated, Fourier-transformed to the frequency domain, and deconvoluted from the instantaneous response,[107] to yield the spectra as shown in Figure 3.2. OKE spectra of PAN were not measured within this work and have been published elsewhere.[107]

3.1.3 Results

3.1.3.1 Densities, Viscosities and Conductivities

For density measurements a vibrating-tube densimeter (Anton Paar, Graz, Austria, DMA 5000 M) with a temperature stability of ±0.01 °C was used. Densities, ρ, of EAN and PAN were measured with a precision of $\pm 5 \cdot 10^{-6}\,\mathrm{g\,cm^{-3}}$ from 15 °C to 65 °C and 5 °C to 65 °C in 10 °C steps, respectively, using the calibration supplied by the manufacturer (Section 2.5.1). For EAN no density measurements were made at $\vartheta < 15$ °C to avoid possible damage to the vibrating glass-tube in the event of solidification. Viscosities, η, were determined using an automated rolling ball microviscometer (Anton Paar, Graz, Austria, AMVn) with a reproducibility of ∼0.5% in the range of 5 °C to 125 °C in 10 °C steps (Section 2.5.2). The accuracy of the temperature was ±0.05 °C. Electrical conductivities, κ, of EAN were measured between -5 °C and 125 °C (±0.01 °C) in 10 °C steps with a programmable precision LCR meter (Hameg, Mainhausen, Germany, HM8118) with an

accuracy of 0.05% (Section 2.5.3). Capillary cells were used as described elsewhere;[195] the overall relative uncertainty in κ was estimated to be $\pm 0.5\%$. None of the physicochemical properties of d_3-EAN, nor κ(PAN) could be measured, due to material constraints.
Table 3.1 lists the data obtained for ρ and η for EAN and PAN and κ(EAN) as functions of temperature. The densities followed the linear relations

$$\text{EAN}: \quad \rho(T/K) = 1.39072 - 6.05056 \cdot 10^{-4} \cdot T/K \tag{3.1}$$

$$\text{PAN}: \quad \rho(T/K) = 1.32833 - 5.95470 \cdot 10^{-4} \cdot T/K \tag{3.2}$$

The EAN values are in good agreement ($\sim 0.1\,\%$) with the data of Weingärtner *et al.*[52] but differ by $\sim$0.5 % and $\sim$0.7 %, respectively, from those of Greaves *et al.*[196] and Poole *et al.*[197,198] At 25 °C ρ(PAN) is in only modest agreement with the values of Greaves *et al.*[7] ($\sim 0.5\,\%$) and Atkin *et al.* ($\sim 0.8\,\%$).

Table 3.1: Temperature dependence of density, ρ and viscosity, η, of EAN and PAN and electrical conductivity, κ, of EAN.

	EAN			PAN	
T / K	ρ / g cm^{-3}	η / mPa s	κ / S m^{-1}	ρ / g cm^{-3}	η / mPa s
268.15	—	—	0.693	—	—
278.15	—	86.5	1.09	1.16319	152
288.15	1.21657	56.0	1.61	1.15685	92.1
298.15	1.21027	38.6	2.24	1.15063	60.2
308.15	1.20411	27.9	2.98	1.14454	41.3
318.15	1.19807	21.0	3.38	1.13855	29.8
328.15	1.19213	16.4	4.78	1.13266	22.4
338.15	1.18631	13.1	5.82	1.12686	17.5
348.15	—	10.5	6.93	—	13.9
358.15	—	8.70	8.12	—	11.4
368.15	—	7.39	9.37	—	9.48
378.15	—	6.33	10.7	—	7.65
388.15	—	5.50	12.0	—	6.53
398.15	—	4.82	13.4	—	—

The effects of temperature on η and, for EAN, κ (expressed as the resistivity, κ^{-1}) are displayed in logarithmic form in Figure 3.1. The present viscosities of EAN are systematically higher than those reported in the literature. At 25 °C where the most extensive comparison is possible, the literature values are 34.9 mPa s[52], 26.9 mPa s[197], 32.1 mPa s[198] and 36 mPa s,[199] compared with the present value of 38.6 mPa s (Table 3.1). The temperature dependence of the present viscosities, however, is almost identical (Figure 3.1a) to that of Weingärtner *et al.*[52], which suggests the differences in η may arise from impurities. The

latter also probably accounts for the difference of the present η(PAN)= 60.2 mPa s (Table 3.1) and that of Greaves *et al.*[7] (η = 66.6 mPa s). The present electrical conductivities of EAN are in reasonable agreement ($\sim$ 3 %) with the values reported (albeit over a much smaller temperature range) by Oleinikova *et al.*[200] (Figure 3.1b).

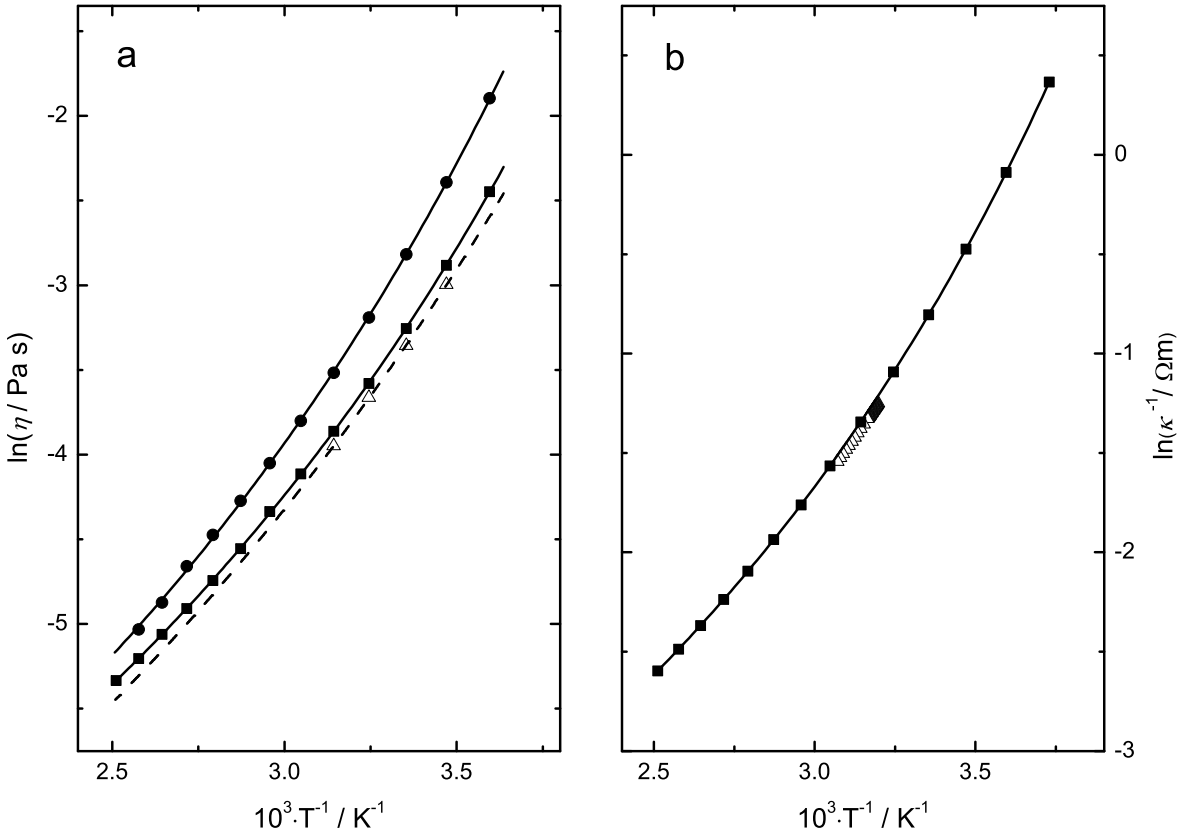

Figure 3.1: Physical properties of EAN (■) and PAN (●) as functions of temperature: (**a**) viscosity, η and (**b**) electrical resistivity, κ^{-1}; (△) literature data;[52,200] solid and dashed lines are VFT-fits (Eq. 1.79).

Both the viscosities of EAN and PAN and the electrical conductivities of EAN follow the Vogel-Fulcher-Tammann (VFT) model (Eq. 1.79), which is commonly used to describe the temperature dependence of transport properties, $Y(= \eta,\ \kappa^{-1}, \tau)$, of glass-forming liquids above their glass-transition temperature. In Eq. 1.79, Y_0, B_{VFT} and T_0 (the so-called Vogel temperature) are fitting parameters.[201] The fit results are listed in Table 3.2 along with corresponding literature data.[52,200] The present values of the so-called fragility parameter, B_{VFT}, of EAN are in only modest agreement with those of Weingärtner *et al.*[52] and Oleinikova *et al.*[200] especially for the viscosities, but the T_0 values agree well. As T_0 is usually about 30 K below the glass-transition temperature, T_{g},[202] the present value of T_0 =147.65 K for EAN is also consistent with the result of T_{g} =181.65 K reported by Belieres *et al.*[199] The present VFT parameters of PAN are broadly compatible with those of Smith *et al.*[203] but less with those of Bouzón Capelo *et al.*[204]

Table 3.2: VFT parameters for viscosity, η, and resistivity, κ^{-1}, of EAN and PAN of the present work (p.w.) and from the literature.

	EAN				PAN		
	$\eta(T)$		$\kappa^{-1}(T)$		$\eta(T)$		$\kappa^{-1}(T)$
VFT parameters	p.w.	lit.[52]	p.w.	lit.[200]	p.w.	lit.[203]	lit.[204]
$\ln Y_0$	-8.47	-8.84	-5.10	-5.10	-8.62	-7.85	-4.16
B_{VFT} / K	786.4	903.5	601.4	599.6	855.6	676	485.7
T_0 / K	147.5	133.6	158.2	157.2	150.7	169	181.9

3.1.3.2 Spectroscopic Model Selection

Representative OKE and DR spectra of EAN and DR spectra of PAN over the frequency range: $200\,\mathrm{MHz} \leq \nu \leq 10\,\mathrm{THz}$ at temperatures from (5 to 65) °C are presented in Figures 3.2, 3.3 and 3.4, respectively. It should be stressed that the dielectric spectra were resampled (Appendix A.2) prior to fitting. This was necessary to achieve an equal point density over the entire frequency range and to stabilize the fit of the small intensities at high frequencies.

To understand the spectra on a molecular level an appropriate mathematical description of the experimental data is necessary. Molecular reorientations in solution are usually best regarded as relaxation processes, while librations and intermolecular vibrations are better modelled as resonances. These two types of processes normally (as here) occur on quite different time scales, which aids in the separation of their contributions to the spectra. The present spectra were formally described using combinations of the equations presented in Section 1.2. However, before describing the procedural details it is important to recognize that fitting DR and OKE spectra over such a broad frequency range is a formidable task that cannot be performed *ab initio*; it therefore follows that the description adopted invariably involves some degree of choice.

The major difficulties in fitting the present spectra can be summarized as follows. First, resonance and (particularly) relaxation modes are often broad and generally strongly overlapping. Second, there are certain theoretical and computational problems associated with some of the standard mathematical models used to describe the modes (see below). Third, the present (in particular the DR) spectra exhibit a featureless and low, but finite, intensity over the intermediate frequency range $0.1 \lesssim \nu/\mathrm{THz} \lesssim 2$, which is particularly hard to model. Fourth, the accuracy of the spectra is limited by the unwanted conductivity contribution (Eq. 1.22), which swamps the DR (but not the OKE) signal at low frequencies (say, $\nu \lesssim 0.5\,\mathrm{GHz}$) and by current technological limitations of the apparatus at higher frequencies (say, $\nu \gtrsim 100\,\mathrm{GHz}$). Lastly, there are no *a priori* guidelines that limit the number or nature of the modes present, which is especially critical because the modes are expected to be strongly coupled.[205]

Bearing in mind these difficulties, after extensive investigations of the possibilities, the following description (presented in five dot points) was adopted for the OKE and DR spectra

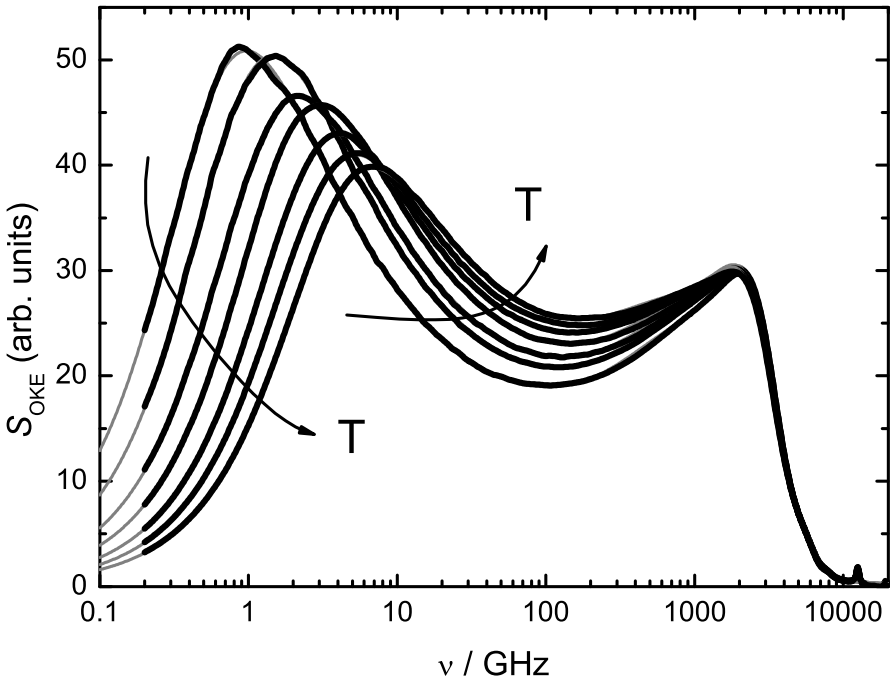

Figure 3.2: Optical Kerr-Effect spectra of EAN from 5 °C to 65 °C in 10 °C steps. Black dots are experimental data; thin gray lines represent the total fit.

of EAN. As will be shown subsequently this description was also found to be applicable without modification to PAN (Section 3.1.5.3) and d_3-EAN (Section 3.1.5.2).

- The broad-band OKE and DR spectra of EAN at all temperatures (Figures 3.2 and 3.3) show two clear features: a dominant temperature-dependent relaxation process in the low GHz region and a much narrower temperature-independent resonance process in the THz region. The dominant low GHz process is the so-called α-relaxation, which was found to be best described by an inertia-corrected Cole-Davidson (CDi) function (Eq. 1.37 with $\alpha_{\mathrm{CDi}} = 0$). For stabilization of the fits of the DR spectra the width parameter was fixed at $\beta = 0.5$ at all temperatures, as it varied only slightly with T when allowed to float. An asymmetrical (i.e. a CD) band shape, broadened to higher frequencies, was preferred over the symmetrically-broadened (CC) function used for other ILs,[58] because the low frequency wing of the α-mode of EAN exhibited a Debye, rather than a broadened, band shape (Figure 3.5). The high frequency (inertial) termination of the α relaxation was achieved by fixing γ_{lib} at 3 THz and 5 THz for the fits of the OKE and DR spectra, respectively.

- As discussed elsewhere,[107] the featureless intensity of the OKE spectrum in the intermediate frequency range $50 \lesssim \nu/\mathrm{GHz} \lesssim 1000$ (i.e., from the α-relaxation to the librational modes) was approximated by a modified Cole-Cole function (CCm; Eq. 1.38). In the limit of $\alpha_{\mathrm{CCm}} \rightarrow 1$ this contribution appears as a constant loss (CL),[107] which corresponds to a logarithmic decay in the time domain, which is typical for glass-forming liquids.[34,206] The CL contribution is made compatible with the

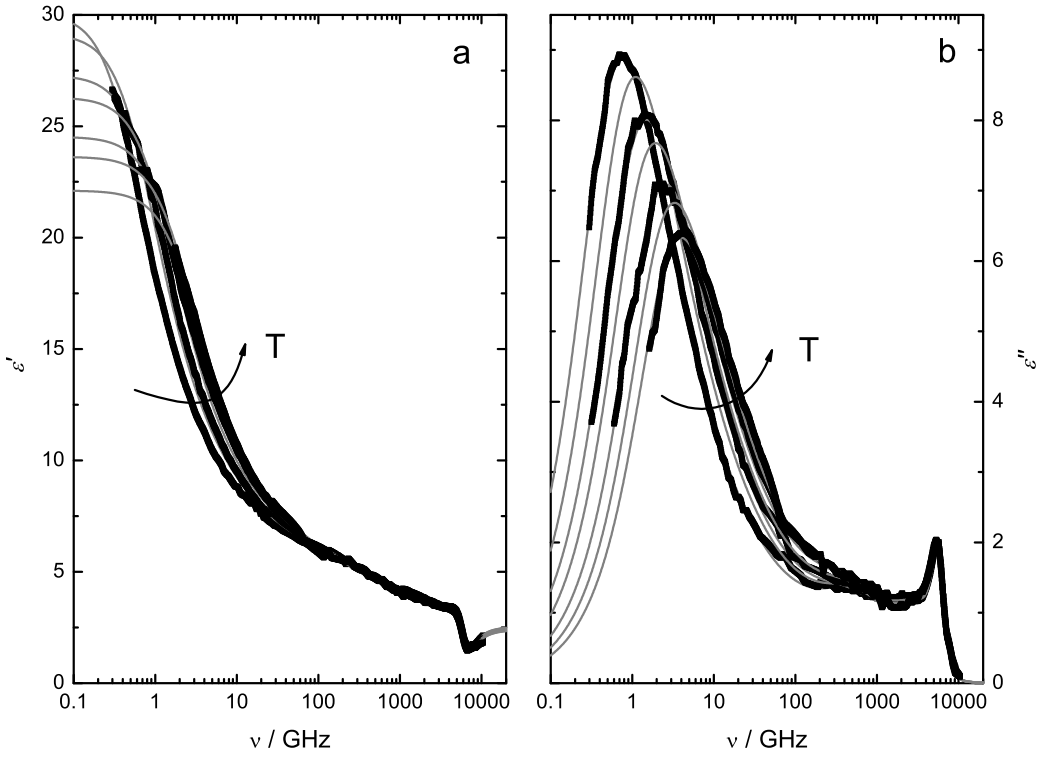

Figure 3.3: (**a**) Permittivity, $\varepsilon'(\nu)$, and (**b**) dielectric loss, $\varepsilon''(\nu)$, of EAN from 5 °C to 65 °C in 20 °C steps. For visual clarity data at 15, 35, and 55 °C are not displayed. Black squares are resampled experimental data; thin gray lines represent the overall fit.

spectroscopic dynamics in the intermediate region by the application of an inertial correction at high frequencies and the α-termination at low frequencies (Eq. 1.38). This CL "mode" is undoubtedly a composite but little can be said at this stage about the nature of the processes involved or their relative contributions.
In the course of re-analyzing the high frequency part of the OKE and DR spectra it was found necessary to modify slightly the previous[107] fit model. In doing so, it turned out that the CL contribution, which is indispensable for describing the OKE spectra, can be neglected in the DR spectra. This is because the amplitude of this contribution is much smaller in the latter and the inclusion of a CL contribution did not improve the fit in the rather poorly defined region near 100 GHz and overall in terms of χ^2_r. Furthermore, application of the CL term to the DR spectra of PAN produced negative value of the CL amplitude, S_{CL}. These findings do not prove the absence of a CL contribution; more likely it is subsumed in the neighboring CDi and DHO_1 modes. Removal of the CL contribution in all the DR spectra reduced the number of fitting parameters, consistent with the criteria for model selection (Section 2.4).

- While there was no specific indication of a mode at ~ 1 THz in the present spectra of EAN (Figures 3.2 and 3.3), OKE measurements at low T clearly indicated the

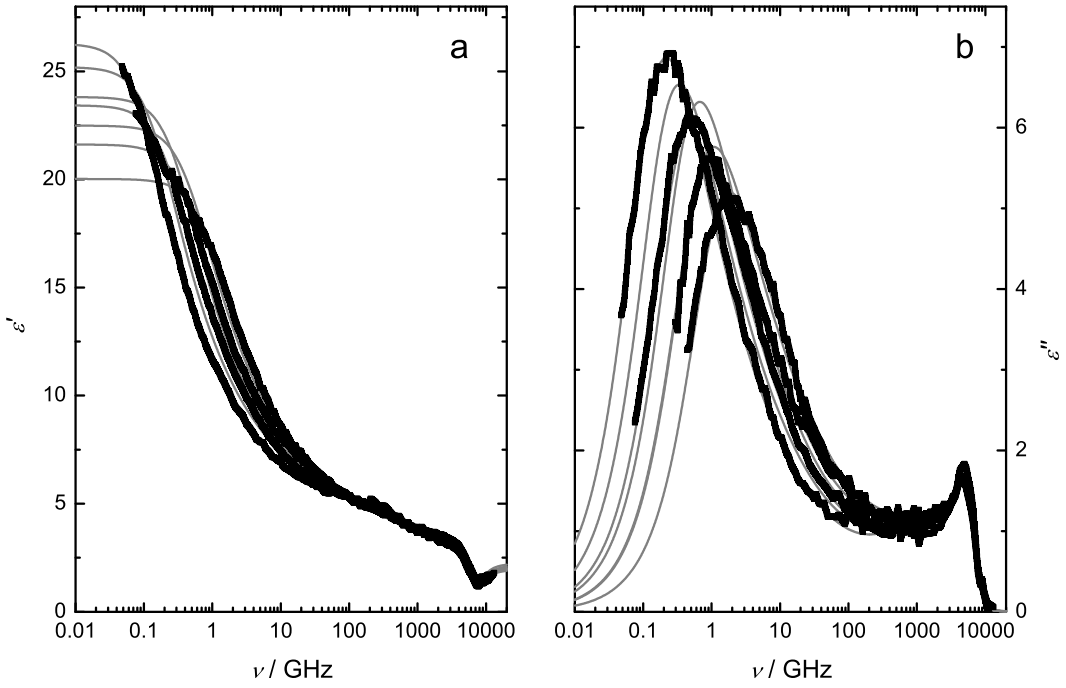

Figure 3.4: (**a**) Permittivity, $\varepsilon'(\nu)$, and (**b**) dielectric loss, $\varepsilon''(\nu)$, of PAN from 5 °C to 65 °C in 20 °C steps. For visual clarity data at 15, 35, and 55 °C are not displayed. Black squares are resampled experimental data; thin gray lines represent the overall fit.

existence of such a mode for PAN.[107] Accordingly, an analogous mode, DHO_1, was assumed for EAN.

- At $\nu > 1\,\mathrm{THz}$, both OKE and DR spectra of EAN were dominated by apparent modes at $\sim 2\,\mathrm{THz}$ (Figure 3.2) and $\sim 5.5\,\mathrm{THz}$ (Figure 3.3), respectively. To account for the observed intensities in this frequency range Gaussians were preferred over DHOs as they better describe the steep decay of the OKE and $\varepsilon''(\nu)$ intensities at $5.5 \lesssim \nu/\mathrm{THz} \lesssim 7.2$. It was established for the OKE spectra that the intensity in this region was best described by a large-amplitude Gaussian, G_1, centered at $\sim 2\,\mathrm{THz}$ and a second weaker Gaussian, G_2', that accounted for the poorly defined shoulder at $\sim 5\,\mathrm{THz}$ (Figures 3.2 and 3.5a). For the DR spectra (Figure 3.5b), the G_1 mode was again required; however, while a G_2' mode at $\sim 5.5\,\mathrm{THz}$ provided reasonable fits,[107] considerable improvement was achieved by splitting it into two Gaussians, G_2 and G_3. Support for the existence of this additional process comes from the DR spectra of PAN, which show a small but distinct shoulder at 7.7 THz (Figure 3.6 inset). These findings in turn suggest that the G_2' mode in the OKE spectra (Figure 3.5a) is almost certainly a composite, consistent with its resonance frequency lying between those of G_2 and G_3.

- To account for the remaining intensity at high frequencies in both DR and OKE spectra: a poorly defined shoulder in EAN (Figure 3.5 inset) and a small peak in PAN (Figure 3.6 inset), a mode, DHO_2, corresponding to the intramolecular mode

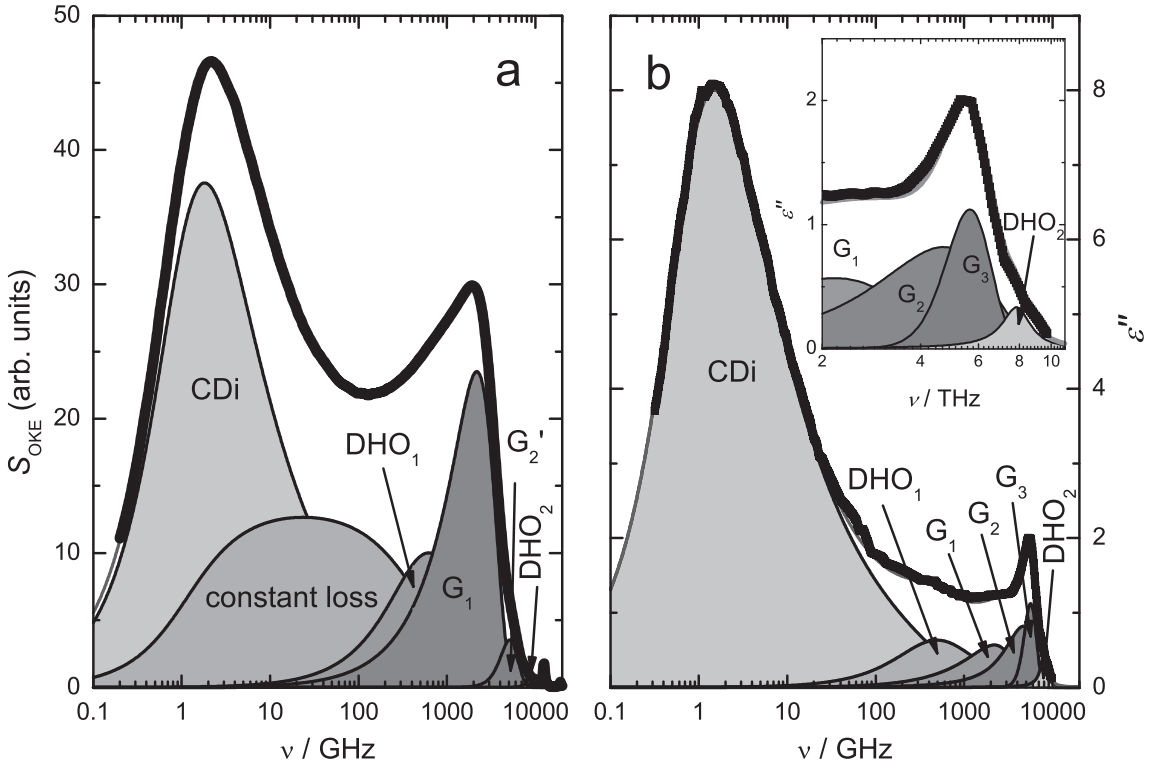

Figure 3.5: The imaginary part of (**a**) OKE and (**b**) dielectric spectra of EAN at 25 °C. Black squares are resampled experimental data and gray lines represent the overall fit. Shaded areas indicate the contributions of the individual processes assuming a (CDi + CL + DHO_1 + G_1 + G_2' + DHO_2) model for the OKE spectrum and a (CDi + DHO_1 + G_1 + G_2 + G_3 + DHO_2) model for the DR spectrum.

reported by Fumino *et al.*[64] at 7.9 THz (263.3 cm^{-1}) in the FIR spectrum of EAN, was included at very high frequencies. The resonance frequency of this mode was fixed at 7.9 THz and its amplitude, S_{DHO2}, and damping constant, γ_{DHO2}, were arbitrarily set to the values listed in Tables 3.3 and 3.4 to achieve convergence.

The overall fits obtained for the OKE and DR spectra at 25 °C using these (CDi + CL + DHO_1 + G_1 + G_2' + DHO_2) and (CDi + DHO_1 + G_1 + G_2 + G_3 + DHO_2) models, respectively, are shown in Figure 3.5. Similar fits were obtained at 5, 45 and 65 °C (not shown) and the parameters so derived are summarized in Tables 3.3 & 3.4. Note however that, due to the absence of THz-TDS and FIR data at 15, 35 and 55 °C, parameters for the resonance modes (DHO_1, G_1, G_2 & G_3) at these temperatures were obtained by linear interpolation. The DR and OKE spectra of d_3-EAN at 25 °C were also fitted with the same models as used for EAN with fixed $\gamma_{lib} = 5$ THz and $\nu_{0,DHO2} = 7.7$ THz.

Measurements on PAN. For the DR spectra of PAN the same mathematical model (CDi + DHO_1 + G_1 + G_2 + G_3 + DHO_2) provided a fully satisfactory fit over the studied temperature range (Figure 3.6) and the parameters so derived are listed in Table 3.5. As

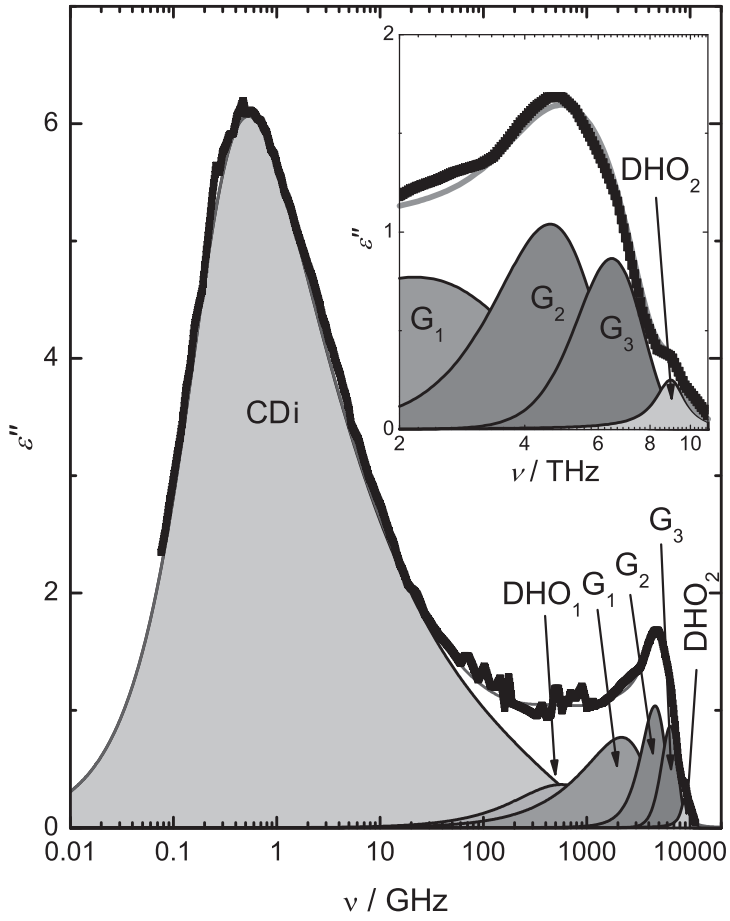

Figure 3.6: Dielectric loss spectrum of PAN at 25 °C. Black squares are resampled experimental data and the gray line represents the overall fit of the (CDi + DHO_1 + G_1 + G_2 + G_3 + DHO_2) model. Shaded areas indicate the contributions of the individual processes.

for EAN the parameters of the resonance modes (DHO_1, G_1, G_2 & G_3) of PAN at 15, 35 and 55 °C were obtained by linear interpolation. The resonance frequency of the DHO_2 mode, $\nu_{0,DHO2}$, in PAN was fixed at 9.0 THz consistent with that reported by Fumino *et al.*[64] and its amplitude, S_{DHO2}, and damping constant, γ_{DHO2}, were set arbitrarily to the values listed in Table 3.5 to achieve convergence. The inertial rise rate, γ_{lib}, was fixed at 5 THz.

Comparison of the DR spectra of EAN and PAN (Figures 3.3 and 3.4) revealed that the latter were significantly more scattered over the entire frequency range. In particular, the increased noise of the THz-TDS data exacerbated an unambiguous concatenation of the FIR and lower frequency spectra. This introduces additional uncertainties into the fit of the intermediate and high frequency regions of the PAN spectra; nevertheless, the fit parameters so obtained complement the EAN data (Section 3.1.5.3).

Table 3.3: OKE fit parameters of EAN as a function of temperature and of d_3-EAN at 25 °C: relaxation and resonance amplitudes S_j, relaxation times, τ_α, Cole-Davidson parameter β, resonance frequencies, $\nu_{0,j}$, damping constants, γ_j, and reduced error function, χ^2_r.[a]

IL	T / K	S_α	β	τ_α	S_{CL}	S_{DHO1}	γ_{DHO1}	$\nu_{0,DHO1}$
EAN	278.15	111	0.569	291	51.8	17.5	4.83	1.67
	288.15	108	0.562	197	51.9	18.0	4.54	1.62
	298.15	95.7	0.569	136	51.7	17.4	4.09	1.51
	308.15	89.5	0.597	96.1	53.3	17.4	4.24	1.53
	318.15	81.0	0.593	73.0	52.6	17.3	4.10	1.47
	328.15	74.6	0.593	58.6	52.6	17.3	4.20	1.49
	338.15	70.6	0.594	46.4	50.7	17.6	4.18	1.48
d_3-EAN	298.15	106	0.569[c]	148	70.0	22.2	4.09[c]	1.50

IL	T / K	S_{G1}	γ_{G1}	$\nu_{0,G1}$	$S_{G2'}$	$\gamma_{G2'}$	$\nu_{0,G2'}$	S^b_{DHO2}	γ^b_{DHO2}	χ^2_r
EAN	278.15	26.0	1.23	2.22	1.24	1.12	5.17	0.05	1.5	0.0493
	288.15	26.4	1.24	2.19	1.31	1.16	5.19	0.05	1.5	0.0396
	298.15	26.7	1.25	2.17	1.36	1.17	5.15	0.05	1.5	0.0291
	308.15	26.7	1.25	2.13	1.52	1.24	5.11	0.05	1.5	0.0225
	318.15	27.4	1.27	2.10	1.51	1.25	5.12	0.05	1.5	0.0258
	328.15	26.8	1.26	2.08	1.62	1.28	5.04	0.05	1.5	0.0279
	338.15	26.6	1.26	2.05	1.72	1.31	4.98	0.05	1.5	0.0276
d_3-EAN	298.15	36.3	1.25[c]	2.15	2.06	1.17[c]	5.12	0.05	1.5	0.056

[a] Units: τ_α in ps, $\nu_{0,j}$ in THz, γ_j in THz; [b] Parameter fixed; [c] Parameter fixed to that of EAN;

Table 3.4: DR fit parameters of EAN as a function of temperature and of d_3-EAN at 25 °C: static permittivity, ε_s, relaxation and resonance amplitudes S_j, relaxation time, τ_α, Cole-Davidson parameter β, resonance frequencies, $\nu_{0,j}$, damping constants, γ_j, high frequency limit of ε', ε_∞ and reduced error function, χ^2_r.[a]

IL	T / K	ε_s	S_α	β[b]	τ_α	S_{DHO1}	γ^b_{DHO1}	$\nu^c_{0,DHO1}$	S_{G1}	γ_{G1}	$\nu_{0,G1}$
EAN	278.15	30.0	24.5	0.5	354	1.72	5.0	1.67	0.238	0.765	2.22
	288.15	29.1	23.7	0.5	250	*1.44*	5.0	1.62	*0.462*	*1.05*	2.19[c]
	298.15	27.3	21.9	0.5	185	1.15	5.0	1.51	0.670	1.34	2.17[c]
	308.15	26.3	20.9	0.5	143	*1.19*	5.0	1.53	*0.733*	*1.65*	2.13[c]
	318.15	24.5	19.2	0.5	107	1.23	5.0	1.47	0.756	1.93	2.10[c]
	328.15	23.6	18.3	0.5	83.3	*1.12*	5.0	1.49	*0.802*	*1.96*	2.08[c]
	338.15	22.1	16.9	0.5	69.8	0.999	5.0	1.48	0.841	1.98	2.05[c]
d_3-EAN	298.15	27.2	21.8	0.5	192	1.34	5.0	1.51	0.641	1.34[d]	2.17[c]

IL	T / K	S_{G2}	γ_{G2}	$\nu_{0,G2}$	S_{G3}	γ_{G3}	$\nu_{0,G3}$	S^b_{DHO2}	γ^b_{DHO2}	ε_∞	$\chi^2_r \cdot 10^4$
EAN	278.15	0.714	1.58	4.85	0.167	0.722	5.81	0.08	1.9	2.58	51
	288.15	*0.695*	*1.72*	*4.78*	*0.220*	*0.799*	*5.74*	0.08	1.9	2.57	165
	298.15	0.638	1.83	4.69	0.290	0.892	5.65	0.08	1.9	2.55	76
	308.15	*0.600*	*1.96*	*4.65*	*0.312*	*0.915*	*5.65*	0.08	1.9	2.49	78
	318.15	0.543	2.07	4.59	0.328	0.914	5.61	0.08	1.9	2.42	161
	328.15	*0.458*	*2.09*	*4.54*	*0.381*	*0.974*	*5.58*	0.08	1.9	2.44	291
	338.15	0.379	2.12	4.47	0.428	1.01	5.54	0.08	1.9	2.45	102
d_3-EAN	298.15	0.701	1.83[d]	4.63	0.265	0.892[d]	5.21	0.035	1.9	2.40	84

[a] Units: τ_α in ps, $\nu_{0,j}$ in THz, γ_j in THz; [b] Parameter fixed; [c] Parameter fixed to that of OKE fit; [d] Parameter fixed to that of EAN; Italic values were interpolated (see text).

Table 3.5: DR fit parameters of PAN as a function of temperature: static permittivity, ε_s, relaxation and resonance amplitudes S_j, relaxation time, τ_α, Cole-Davidson parameter β, resonance frequencies, $\nu_{0,j}$, damping constants, γ_j, high frequency limit of ε', ε_∞ and reduced error function, χ^2_r.[a]

T / K	ε_s	S_α	β	τ_α	S_{DHO1}	γ^b_{DHO1}	$\nu^b_{0,DHO1}$	S_{G1}	γ_{G1}	$\nu_{0,G1}$
278.15	26.3	21.6	0.394	1536	0.674	5.0	1.61	1.06	1.61[b]	1.80[b]
288.15	25.2	20.6	0.391	988	*0.670*	5.0	1.61	*1.03*	*1.71*	*1.81*
298.15	23.4	18.8	0.398	628	0.662	5.0	1.61	1.00	1.81	1.81
308.15	23.8	19.2	0.409	483	*0.684*	5.0	1.61	*1.08*	*1.91*	*1.75*
318.15	21.6	17.0	0.391	342	0.710	5.0	1.61	1.16	2.00[b]	1.70[b]
328.15	22.5	18.2	0.370	325	*0.588*	5.0	1.61	*1.05*	*2.06*	*1.69*
338.15	20.0	15.6	0.400[b]	179	0.468	5.0	1.61	0.936	2.12	1.67

T / K	S_{G2}	γ_{G2}	$\nu_{0,G2}$	S_{G3}	γ_{G3}	$\nu_{0,G3}$	S^b_{DHO2}	γ^b_{DHO2}	ε_∞	$\chi^2_r \cdot 10^4$
278.15	0.540	1.17	4.72	0.264	1.14	6.58	0.05	1.8	2.05	104
288.15	*0.517*	*1.21*	*4.67*	*0.264*	*1.16*	*6.53*	0.05	1.8	2.11	210
298.15	0.493	1.24	4.60	0.262	1.18	6.47	0.05	1.8	2.17	156
308.15	*0.413*	*1.14*	*4.52*	*0.275*	*1.17*	*6.41*	0.05	1.8	2.07	57
318.15	0.334	1.03	4.50[b]	0.285	1.15	6.36	0.05	1.8	2.05	72
328.15	*0.348*	*1.07*	*4.39*	*0.308*	*1.18*	*6.30*	0.05	1.8	1.98	54
338.15	0.359	1.10	4.30	0.335	1.21	6.22	0.05	1.8	2.26	99

[a] Units: τ_α in ps, $\nu_{0,j}$ in THz, γ_j in THz; [b] Parameter fixed; Italic values were interpolated;

3.1.4 Discussion of "slow" dynamics[a]

3.1.4.1 Static Permittivity

Before going on to discuss the details of the modes identified in the OKE and dielectric spectra it is useful to consider the behavior of the latter in the low frequency limit. Dielectric spectroscopy is the only experimental method currently available for measuring the static permittivity (dielectric constant) of a conducting liquid.[57] The values of the static permittivity ($\varepsilon_s = \lim_{\nu\to 0} \varepsilon'(\nu) = \sum_j S_j + \varepsilon_\infty$) obtained for EAN and PAN from the fits of the present DR spectra are shown as a function of temperature in Figure 3.7. As for other ILs,[58] ε_s exhibits a monotonic (in fact approximately linear) decrease with increasing temperature, with $d\varepsilon_s/dT$=–0.13 K^{-1} (EAN) or –0.09 K^{-1} (PAN). These large negative values of $d\varepsilon_s/dT$ are about three times greater than for typical aprotic ILs[58] but are common for H-bonded molecular liquids such as alcohols, where they are ascribed to a partial break-up of the H-bond networks with increasing T. As would be expected from their protic natures the values of $\varepsilon_s \approx 27.3$ (EAN) and 23.4 (PAN) at 25 °C are considerably higher than those observed for aprotic ILs, which are typically <20.[53,55,58] It should be noted in passing that there is some uncertainty in the determination of ε_s for both EAN and PAN. This is because the dominant α-relaxation process (Section 3.1.4.2) slows down considerably (shifts to lower frequencies) at lower T, which means that $\varepsilon'(\nu)$ does not reach its plateau within the accessible frequency range (Figures 3.3a and 3.4a). Measurements at lower ν do not help because the dielectric signal is swamped by the conductivity contribution (Eq. 1.22). These difficulties, and the limited accuracy of existing dielectric instrumentation, readily account for the small differences (ca. 3-5 %) between the present values of ε_s and of $d\varepsilon_s/dT$ of EAN and those of Weingärtner *et al.*[52] (Figure 3.7).

3.1.4.2 The α-Relaxation Process

General aspects. The dominant process in both the DR and OKE spectra of EAN and PAN in the low GHz region (Figures 3.2 - 3.6) is the so-called α-relaxation, which corresponds to the structural relaxation of (the rotational motions of molecular-level species) each liquid. Because of its three-fold symmetry axis, the nitrate anion has a zero dipole moment but due to its π-electrons it is highly polarizable and, because of its planar geometry, it has a high anisotropy ($\alpha_\parallel \approx 5.6$ Å^3, $\alpha_\perp \approx 3.1$ Å^3).[207] It follows that the OKE spectra of EAN mainly reflect the motions of NO_3^-. Conversely, the ethyl- and propylammonium cations ($EtNH_3^+$ & $PrNH_3^+$) are only weakly polarizable and anisotropic but have considerable permanent dipole moments (μ_g = 3.9 D and 6.8 D, from MOPAC calculations[174]), which make them primary contributors to the dielectric signal. Indeed, EAN and PAN can be viewed as almost perfect compounds for complementary investigation by OKE and DR spectroscopies.[107]

The amplitude of the α-relaxation decreased considerably with increasing T in both the OKE and DR spectra (Figures 3.2 and 3.3). Furthemore, the peak maximum shifted from 0.8(0.7) to 6(4) GHz in the OKE(DR) spectra for EAN (Figures 3.2 and 3.3) and from 0.2 to 2 GHz in the DR spectra of PAN (Figure 3.4). These features of the α-relaxation are

[a] Arbitrarily defined here as corresponding to $\nu \lesssim 100$ GHz.

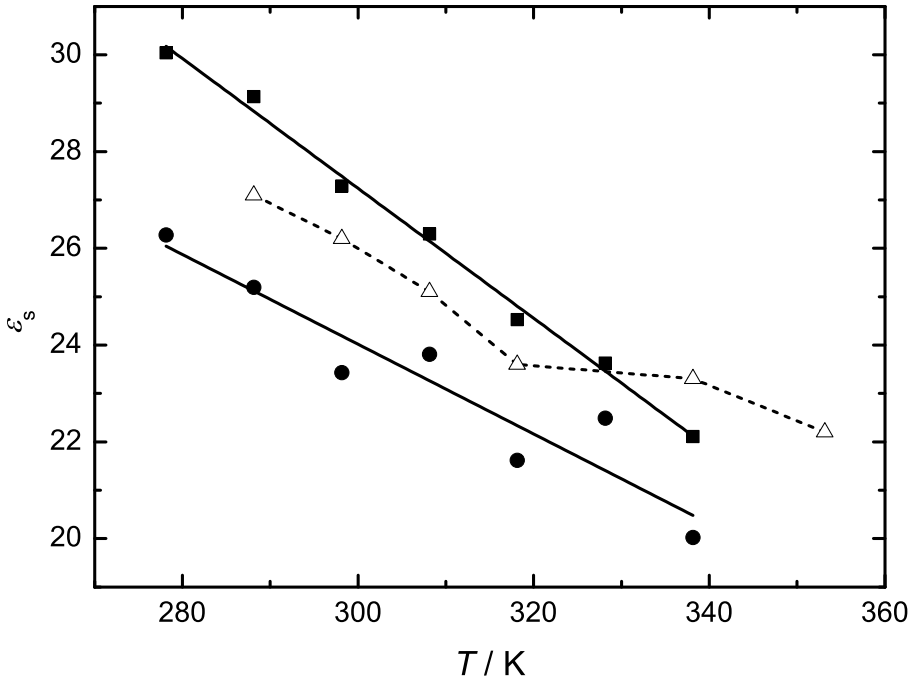

Figure 3.7: Static permittivity, ε_s, of EAN (■) and PAN (●), present work, as a function of temperature; (△) EAN values of Weingärtner *et al.*[52] Solid lines (—) are linear regressions of the present data.

broadly similar to those observed for imidazolium-based ILs,[36] (although in contrast to the latter, but as would be expected, there is no evidence of the sub-α mode, thought to be a breathing mode of π-stacked cation aggregates).[36]

Relaxation times. The relaxation times of the α process, τ_α, in the DR and OKE spectra of EAN and PAN decay exponentially with increasing T thus permitting application of the Arrhenius equation. The viscosity, as discussed above (Section 3.1.3.1), follows the VFT relation over the same range. As a consequence, Stokes-Einstein-Debye (SED) plots (Eq. 1.63) of $\tau_\alpha^{\mathrm{DR}}$(EAN), $\tau_\alpha^{\mathrm{OKE}}$(EAN) and $\tau_\alpha^{\mathrm{DR}}$(PAN) against $\eta/k_{\mathrm{B}}T$ depart from linearity at low T,[107] which implies a decoupling of the molecular-level rotational motions from the bulk viscosity. It was found that the effective volumes of rotation, V_{eff}, extracted from the slopes of the SED plots were rather small and not compatible with the rotational motions of the anions (out-of-plane rotation for NO_3^-) or the cations (end-over-end rotation for RNH_3^+).[107] The non-linearity of the SED plots is instead consistent with a high degree of rotational cooperativity between the anions and cations, rather than the simple independent rotational diffusion assumed in the SED theory.
For EAN, further evidence for such cooperative motions comes from a comparison of DRS with time-resolved femtosecond-IR spectroscopy (fs-IRS).[208] As fs-IRS probes the rotation of the N–H bonds of $EtNH_3^+$, it is also sensitive to the rotations of the cation, which manifests itself in virtually identical activation energies ($E_{\mathrm{A}}^{\mathrm{IR}} = 21.4 \pm 0.6\,\mathrm{kJ\,mol^{-1}}$, $E_{\mathrm{A}}^{\mathrm{DR}} = 21.6 \pm 0.3\,\mathrm{kJ\,mol^{-1}}$).

The fs-IR relaxation times, τ^{IR}, are of rank $n = 2$ (Section 1.3.4) in contrast to the first-rank relaxation time measured via DRS, $\tau_\alpha^{\mathrm{DR}}$. Within the rotational diffusion model, where specific interactions of the rotating entity with its surroundings are ignored, a ratio of $\tau_{\alpha,\max}^{\mathrm{DR}}/\tau^{\mathrm{IR}} = 3$ is expected.[86] For EAN, however, $\tau_{\alpha,\max}^{\mathrm{DR}}/\tau^{\mathrm{IR}} = 1.4$ on average.[b] This is consistent with the α-relaxation process for EAN occurring via a jump mechanism, as previously proposed for aprotic ILs,[36,44] rather than through rotational diffusion. In water, where molecular reorientation is also thought to take place via large-angle jumps,[210,211] the ratio of first- to second-rank rotational correlation times is ~ 2 from which it was concluded that the relaxation rate in water is determined by the rate of H-bond breaking.[210,212] It seems likely that this is also the case in EAN, with the even lower value of $\tau_{\alpha,\max}^{\mathrm{DR}}/\tau^{\mathrm{IR}}$ reflecting the very strong cation-anion (H-bond) interactions. Knowledge of the ratio $\tau_{\alpha,\max}^{\mathrm{DR}}/\tau^{\mathrm{IR}}$ permits calculation of the jump angle via Eq. 1.69, yielding $\alpha \approx 106\,^\circ$.[208] This value is almost identical with the tetrahedral angle of the ammonium group, which is again consistent with strong, directed H-bond interactions between $\mathrm{EtNH_3^+}$ and $\mathrm{NO_3^-}$.
This conclusion is also supported by the similarity of the activation energies for both EAN and PAN obtained from $\tau_\alpha^{\mathrm{DR}}$ ($E_{\mathrm{A}}^{\mathrm{DR}}(\mathrm{EAN}) = 21.6 \pm 0.3\,\mathrm{kJ\,mol^{-1}}$; $E_{\mathrm{A}}^{\mathrm{DR}}(\mathrm{PAN}) = 26.0 \pm 1.7\,\mathrm{kJ\,mol^{-1}}$) and $\tau_\alpha^{\mathrm{OKE}}$ ($E_{\mathrm{A}}^{\mathrm{OKE}}(\mathrm{EAN}) = 24.0\,\mathrm{kJ\,mol^{-1}}$; $E_{\mathrm{A}}^{\mathrm{OKE}}(\mathrm{PAN}) = 25.5\,\mathrm{kJ\,mol^{-1}}$).[107,213] These relatively high E_{A} values, and particularly their similarity, indicate a high degree of cooperativity between the rotating species and their neighbors. Finally, such cooperativity is also implied by the similarity of $\tau_\alpha^{\mathrm{DR}}$ and $\tau_\alpha^{\mathrm{OKE}}$ at all T, which suggests that anion dynamics are slowed down to the time scale of cation reorientation as a result of strong inter-ionic interactions.

Amplitudes. The amplitudes (intensities) of the α-relaxation process in the DR spectra, S_α^{DR}, of both EAN and PAN arise from the relaxation of the dipolar species present. In a PIL this includes cooperative fluctuations of the H-bond network, including H-bond making and breaking. For EAN and PAN, S_α^{DR} also includes contributions from the rotational and translational motions of $\mathrm{EtNH_3^+}$ and $\mathrm{PrNH_3^+}$, which have gas phase dipole moments, $\mu_{\mathrm{g}} = 3.86\,\mathrm{D}$[214] and $6.84\,\mathrm{D}$(MOPAC[174]), respectively, and any ion pairs (IPs) or larger clusters that have $\mu \neq 0$ and an appropriate lifetime. The $\mathrm{NO_3^-}$ ion has no dipole moment and thus makes no *direct* contribution to the DR spectrum. The corresponding OKE amplitude, S_α^{OKE}, arises from changes in polarizability anisotropy, which as argued above (Section 3.1.4.2) mainly reflects the motions of the $\mathrm{NO_3^-}$ ion, along with any IPs or larger clusters containing $\mathrm{NO_3^-}$ that have the relevant characteristics. Note that, as with all neat ILs investigated to date,[58] there is no evidence in the DR spectra for the existence of discreet IPs in the present ILs; furthermore, any larger clusters detected by DR and OKE will not necessarily be identical. Nor is it known *a priori* what the relative contributions to S_α might be due to the ions, IPs and clusters (if present).
In this work, quantitative evaluation of S_α^{DR} was made via the Cavell equation (Eq. 1.52),[115] which relates the amplitude of a relaxation process to the effective dipole moment of the relaxing species, $\mu_{\mathrm{eff},j}$. To apply Eq. 1.52 the shape of $\mathrm{EtNH_3^+}$ and $\mathrm{PrNH_3^+}$ was approx-

[b] Note that for comparison with the fs-IR relaxation times, the Cole-Davidson relaxation times, $\tau_\alpha^{\mathrm{DR}}$, obtained from the dielectric fit were converted into relaxation times of the α peak maximum, $\tau_{\alpha,\max}^{\mathrm{DR}}$, using the equation given in Ref. 209.

imated as a prolate ellipsoid (Eq. 1.56). The values of μ_{eff} so obtained decrease linearly with increasing T (Figure 3.8). Within the likely experimental errors, the μ_{eff} values up to 45 °C agree with those of Weingärtner *et al.*[52], but their values at 65 and 80 °C appear to be outliers. For EAN, μ_{eff} coincides with the apparent dipole moment, $\mu_{\text{app}} = 4.9\,\text{D}$, of $EtNH_3^+$ (Eq. 1.53) predicted by MOPAC,[174] consistent with the assumption that S_α^{DR} mostly arises from cation reorientation. The value of μ_{eff} for PAN is significantly higher than that for EAN (Figure 3.8) as would be expected from its higher MOPAC-calculated value ($\mu_{\text{app}} = 7.9\,\text{D}$).[c] The decrease of μ_{eff} with increasing T contrasts with all imidazolium-based ILs studied to date, for which μ_{eff} was found to be independent of T[58] (which has been interpreted as indicating an absence of structural change). The negative values of $\text{d}\mu_{\text{eff}}/\text{d}T$ of EAN and possibly PAN (Figure 3.8) therefore imply increasing dipole-dipole interactions in these PILs at lower T. This is consistent with the formation of higher order clusters in these ILs and perhaps also with an increasing micro-heterogeneity as proposed by Hayes *et al.*[188] Whatever the exact nature of the species formed, it is likely that they are also responsible for the decoupling of viscosity and rotational motions (Section 3.1.4.2). The fact that $\varepsilon_{\text{s}}(\text{PAN}) < \varepsilon_{\text{s}}(\text{EAN})$ despite having a larger value of μ_{eff} can be reasonably ascribed to the lower dipole density in PAN.

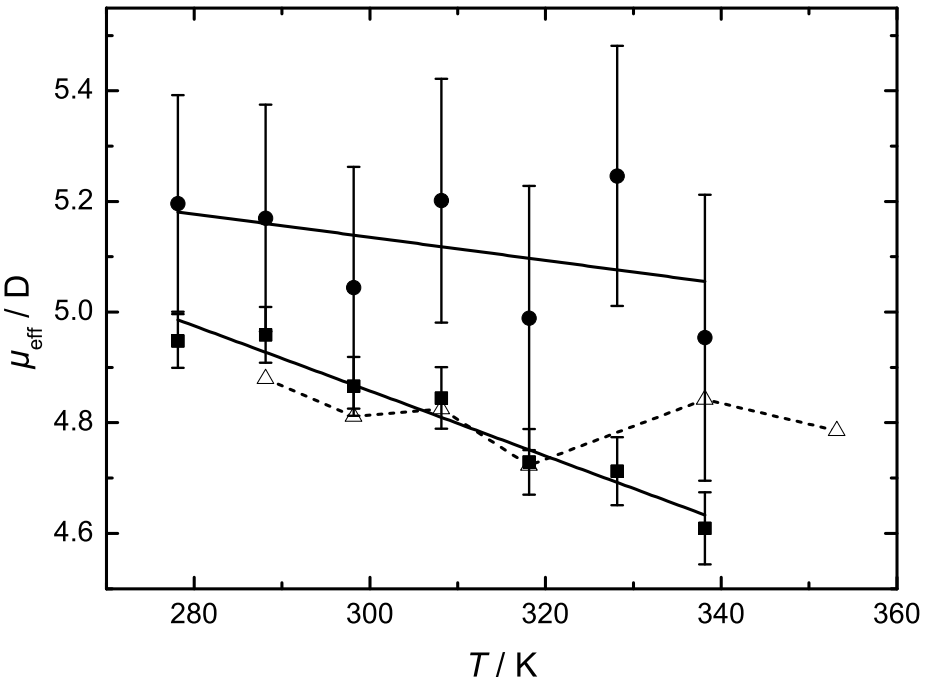

Figure 3.8: Effective dipole moment, μ_{eff}, of the α process as a function of temperature: this work, EAN (■) and PAN (●) and literature values for EAN (△).[52] Solid lines (—) represent linear fits of the present data.

[c]The difference between μ_{eff} and μ_{app} of PAN can be explained by the fact that in liquid phase the pivot does not necessarily coincide with the center of gravity but more likely with the center of hydrodynamic stress;[117] the higher flexibility of $PrNH_3^+$ may also play a role.

3.1.5 Discussion of "fast" dynamics[d]

3.1.5.1 EAN

The observed intensity of the broadband DR and OKE spectra of ILs in the frequency range $0.1 < \nu/\mathrm{THz} < 13$ (ca. 3 to 400 cm^{-1}) mostly arises from librations and intermolecular vibrations.[36,215–217] For protic ILs, low energy intramolecular vibrations and proton transfers may also contribute. Because of the strong inter-ionic interactions in PILs and the extensive coupling and overlapping of rotational, vibrational and translational modes,[205] unambiguous deconvolution and assignment of modes is difficult as discussed above (Section 3.1.3.2). Nevertheless, the different "selection rules" for OKE, sensitive to fluctuations of the polarizability anisotropy, and DRS, probing dipole fluctuations, means that a combination of OKE and DR spectroscopy can provide some valuable insights into the dynamics of PILs.

Based on their FIR absorption measurements, Fumino *et al.*[64] assigned contributions in the 50 to 400 cm^{-1} range to intermolecular H-bond bending and stretching (Table 3.6), drawing particular attention to their similarity to those observed for water.[217,218] However, in addition to such vibrations, intensity in this region must also reflect the librational motions of NO_3^- and $EtNH_3^+$. The contributions of these motions to the OKE and DR spectra can be estimated using the free-rotator approximation of Bartoli.[219] This model predicts that because of their moments of inertia ($EtNH_3^+$: $I_B = 100.6 \cdot 10^{-47}\,\mathrm{kg\,m^2}$, $I_C = 114.4 \cdot 10^{-47}\,\mathrm{kg\,m^2}$; NO_3^-: $I_A = I_B = 61.9 \cdot 10^{-47}\,\mathrm{kg\,m^2}$)[174] the libration frequencies of NO_3^- and $EtNH_3^+$ should be reduced by factors of ∼7 and ∼9, respectively, compared to water. Using the value of ∼680 cm^{-1} for the libration mode of water[220] and assuming for simplicity that the same mean-square torque is acting, values of ∼2.9 THz (97 cm^{-1}) for NO_3^- and ∼2.3 THz (76 cm^{-1}) for $EtNH_3^+$ are obtained. It is therefore essential to consider possible librational contributions to the FIR band assignments.

Table 3.6: Comparison for EAN of the resonance frequencies, $\bar{\nu}_0$ / cm^{-1}, of the present OKE and DR modes, DHO_1, G_1, G_2, G_2', G_3 (intermolecular) and DHO_2 (intramolecular) at 65 °C with the FIR absorption modes reported at 80 °C by Fumino *et al.*[64]

Mode	$\bar{\nu}_0^{\mathrm{OKE}}$	$\bar{\nu}_0^{\mathrm{DR}}$	$\bar{\nu}_0^{\mathrm{FIR,\,64}}$	Assignment of Fumino *et al.*[64]
DHO_1	49.4	49.4*	–‡	–‡
G_1	68.4	68.4*	60	δ(HBs): H-bond bending
G_2	–	149.1	132	ν_s(HBs): symmetric H-bond stretching
G_2'	166.1	–	–	
G_3	–	184.8	199	ν_{as}(HBs): asymmetric H-bond stretching
DHO_2	263.3	263.3	265.2	ethyl group torsion

* Fixed to that of the OKE fit; ‡ Not detected

[d] Arbitrarily defined here as corresponding to $\nu \gtrsim 100$ GHz, which includes the "intermediate" frequency region.

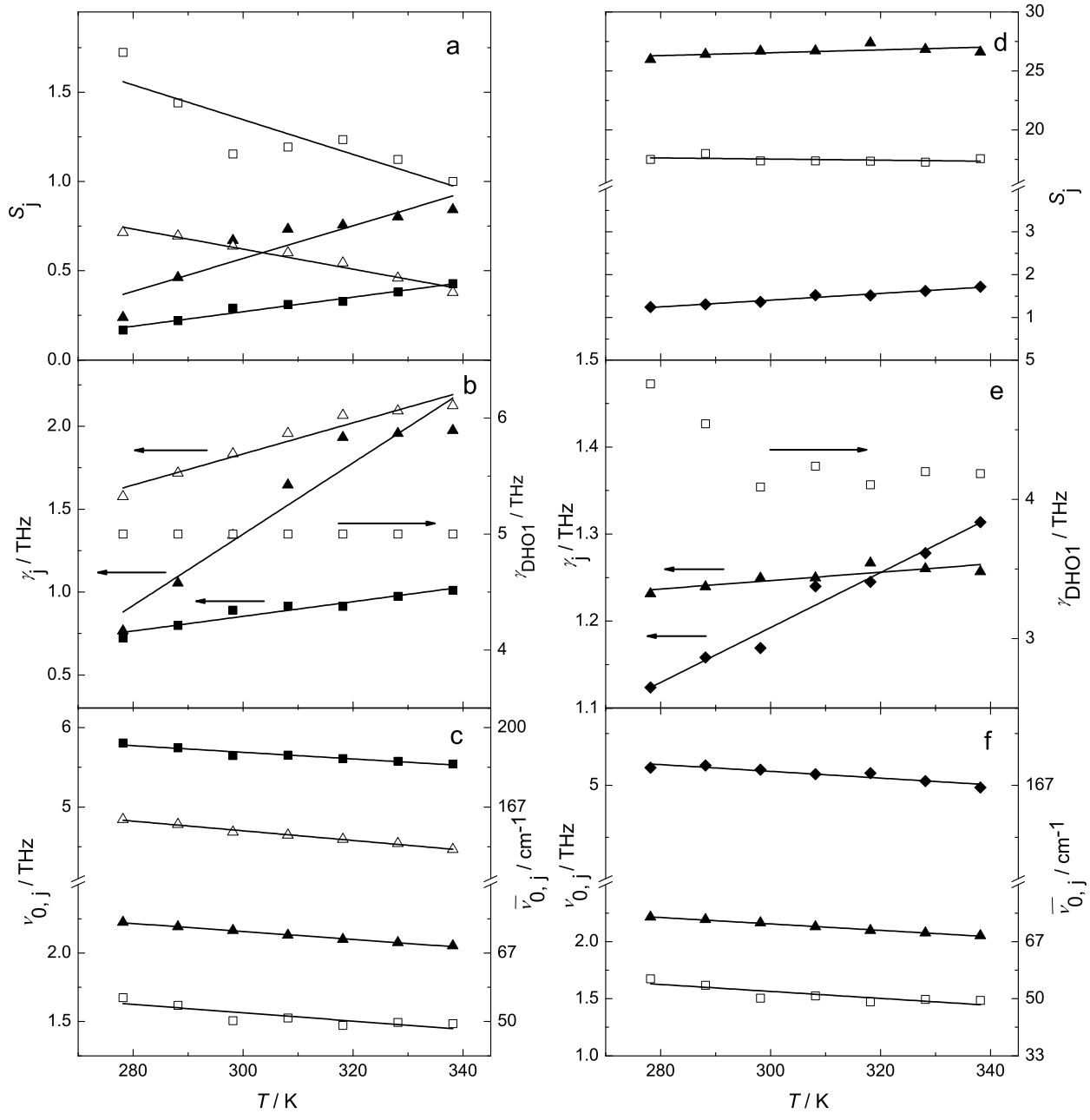

Figure 3.9: Fit parameters for the high-frequency resonance processes of EAN as a function of temperature: (**a**) amplitudes, S_j, (**b**) damping constants, γ_j, and (**c**) resonance frequencies, $\nu_{0,j}$, of DHO_1 (□), G_1 (▲), G_2 (△) and G_3 (■) modes for the DR spectra; (**d**) S_j, (**e**) γ_j, and (**f**) $\nu_{0,j}$, of DHO_1 (□), G_1 (▲), G_2' (♦) modes for the OKE spectra. Solid lines represent linear regressions.

OKE fits. As discussed above, the high-frequency parts of the OKE spectra for EAN were best fitted by a model consisting of a damped harmonic oscillator, DHO_1 ($\sim 1.5\,THz$), two Gaussians, G_1 ($\sim 2\,THz$) and G_2' ($\sim 5\,THz$), plus an additional mode (DHO_2; 7.9 THz) that accounted for the small peak in the OKE spectra, which also shows up in the DR spectra as a shoulder and is associated with the ethyl-group torsion (Table 3.6).[64]
Figures 3.9 d,e,f display the temperature-dependent amplitudes, bandwidths and resonance frequencies of the proposed high frequency processes. The amplitudes are only weakly affected by T: $S_{G2'}$ and S_{G1} increase slightly, while S_{DHO1} is more or less constant over the investigated range. On the other hand, the damping constants differ in their temperature dependence: γ_{G1} and $\gamma_{G2'}$ increase with increasing T (with a larger slope for the latter), whereas γ_{DHO1} is approximately constant. The resonance frequencies of all processes decrease with increasing T. For librations this decrease is generally explained by the general increase in molecular motions, and the weakening of the surrounding cage as the density decreases. However, these same factors also lower the force constants of intermolecular vibrations, such as H-bond bending or stretching, which in turn lowers ν_0 as T increases. It is therefore not possible to use these observations to determine whether these modes are librations or vibrations.
The resonance frequency (Table 3.6) of the G_1 mode in OKE ($68.4\,cm^{-1}$ at 338 K) is compatible with the FIR mode at $\sim 60\,cm^{-1}$ at 353 K, assigned by Fumino *et al.*[64] to H-bond bending. However, the present OKE measurements indicate that this mode mainly arises from librational motions of the nitrate anion. The justifications for this statement are as follows. First, OKE is primarily sensitive to rotational motions and thus would not be expected to detect H-bond bending.[162,221] Second, the OKE spectra of *all* liquids show a pronounced librational peak in this frequency range, independent of the presence or absence of H-bonds.[215,216,222,223] Finally, the small increase in S_{G1} with increasing T is expected for librational motions, due to increasing thermal motions, whereas for vibrations, amplitudes usually decrease.
It can be speculated that G_2' in the OKE spectra is related to cation motions as $S_{G2'} < S_{G1}$ (Figure 3.5a), consistent with the polarizability anisotropies of NO_3^- and $EtNH_3^+$. The frequency of G_2' in the OKE spectra lies between those of the G_2 and G_3 modes in the DR spectra, which suggests that G_2' is a composite mode that can be resolved in the DR but not in the OKE spectra. Furthermore, the slight increase in $S_{G2'}$ with increasing T implies that the librational portion (as discussed later) predominates in G_2', consistent with the fact that OKE is mainly sensitive to rotational motions.

DRS fits. As described in Section 3.1.3.2 the high-frequency part of the DR spectra of EAN was fitted by a model consisting of a damped harmonic oscillator, DHO_1 ($\sim 1.5\,THz$), three Gaussians, G_1 ($\sim 2.0\,THz$), G_2 ($\sim 4.5\,THz$), and G_3 ($\sim 5.6\,THz$) plus an additional mode (DHO_2; 7.9 THz) that is associated with the intramolecular torsion of the ethyl group of $EtNH_3^+$ (Table 3.6).[64]
It is reiterated here (see also Section 3.1.3.2) that this is not the only possible model that can describe the observed DR spectra. This uncertainty is due in part to strongly overlapping contributions from coupled multiple-particle interactions and also because of significant experimental limitations particularly in the low-THz range. Thus although the

present model provided the best description of the DR spectra at low ($\lesssim 50\,\mathrm{GHz}$) and very high frequencies ($\gtrsim 500\,\mathrm{GHz}$), it underestimates the experimental intensities at the intermediate frequencies (Figure 3.5). Nevertheless, as argued above inclusion of further processes, e.g. a constant loss term[107] or an additional Debye function at $\sim 2\,\mathrm{ps}$, yielded no improvement in the fits. It seems likely that systematic experimental errors are mostly responsible for these deviations. Fortunately, the imperfectly-fitted intermediate frequency range is well separated from the high frequency ($\nu > 1\,\mathrm{THz}$) region, which is of special interest because of what it may reveal about the similarities (or otherwise) of EAN and water.[64,217,220]

All the fit parameters for the modes in this region of the dielectric spectra of EAN and PAN show reasonably smooth trends with temperature (Figures 3.9 a,b,c). As for the OKE fits (Figures 3.9 d,e,f), the resonance frequencies decrease slightly with increasing T for all modes. But again this trend does not distinguish between librational and vibrational contributions because, as observed for water,[224,225] ν_0 of H-bond stretching also decreases with increasing T. On the other hand, the corresponding amplitudes differ in their temperature dependence: S_{G1} and S_{G3} increase with increasing T, whereas S_{DHO1} and S_{G2} decrease. This must mean that all of the Gaussian modes cannot be due to intermolecular H-bond vibrations, as proposed by Fumino *et al.*,[64] since all Gaussian modes would be expected to decrease with increasing T as H-bonds are weakened or broken.

Whilst $\mathrm{G_1}$ in OKE can be confidently assigned to nitrate libration, its relatively weak equivalent in DRS could be related to the collision-induced part of this mode: first because $\nu_{\mathrm{G1}}^{\mathrm{DR}} \approx \nu_{\mathrm{G1}}^{\mathrm{OKE}}$ and secondly because S_{G1} increases with T, as one would expect for an interaction-induced contribution (and a libration) because of the increasing collision rate due to increasing thermal motions. For H-bond vibrations the opposite trend is expected because of the decreasing density and H-bond disruption. A similar situation is found for $\mathrm{G_3}$: as its amplitude increases with increasing T, it is reasonable to associate it with cation librations.[226]

Contrary to S_{G1} and S_{G3}, the magnitude of S_{G2} decreases with increasing T. Such a trend is compatible with H-bond vibrations, as observed for water.[64,226] If so, $\mathrm{G_2}$ can be attributed to H-bond stretching, which is more energetic than H-bond bending. This would mean that H-bond bending (if such a contribution exists) might be a possible origin of the $\mathrm{DHO_1}$ mode. Such an assignment is compatible with that of Fumino *et al.*[64] and is supported by the decreasing amplitude of $\mathrm{DHO_1}$ with increasing T. It should be noted, however, that $\mathrm{DHO_1}$ may also include a contribution from the CL term.

3.1.5.2 Deuterated EAN

The H atoms bound to the ammonium group of EAN were $\sim 91\,\%$ replaced by deuterium atoms, which corresponds to an average composition of $[\mathrm{EtND_{2.7}H_{0.3}}]^+$ which, for convenience, will referred to as $\mathrm{d_3}$-EAN. Due to time and material constraints, DR and OKE spectra of $\mathrm{d_3}$-EAN were recorded only at $25\,^{\circ}\mathrm{C}$. Both spectra were found to be fitted satisfactorily with the same models used for EAN (Section 3.1.3.2).

The OKE spectrum of $\mathrm{d_3}$-EAN and its overall fit are compared to that of EAN in Figure 3.10 a. The two spectra match almost perfectly, showing no isotopic shift (IS) and provid-

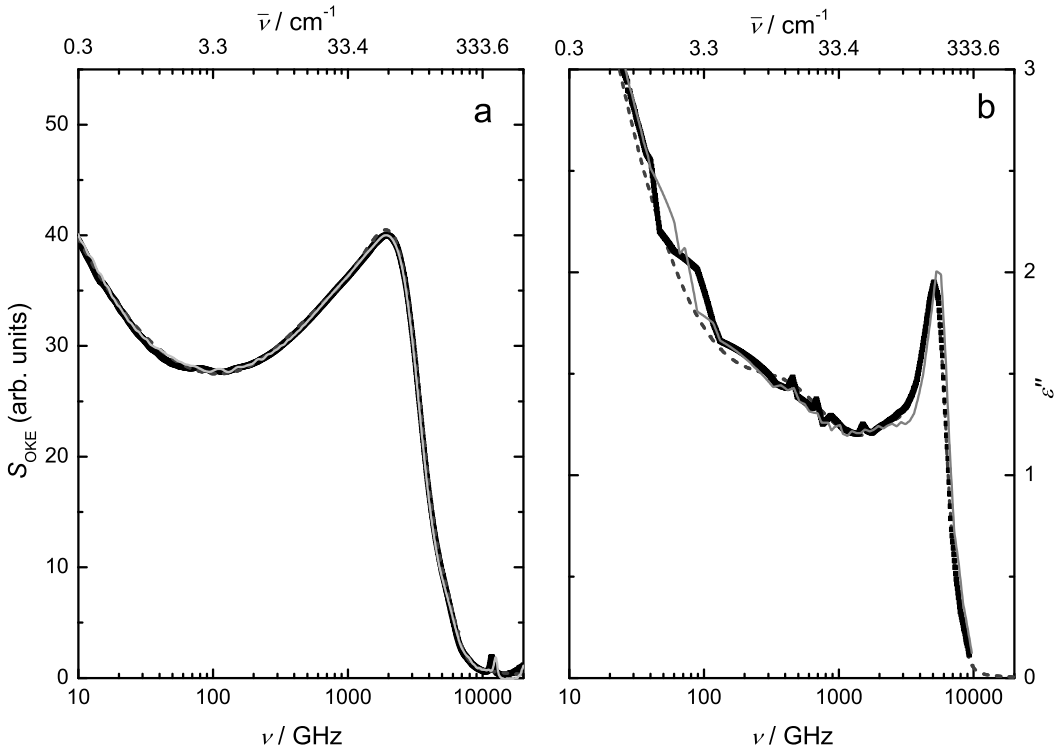

Figure 3.10: (**a**) OKE and (**b**) DR spectra of EAN (gray solid lines) and d_3-EAN (■) with its total fit (dashed lines) at 25 °C.

ing nearly identical fit parameters (Table 3.3). Although the calculated IS for a H-bond vibration ($\sim 2\,\%$, see below) is at the present detection limit, the close similarity of the OKE spectra of EAN and d_3-EAN is compatible with the assignment of G_1 to nitrate libration. However, it must be noted that almost no ISs were observed for H-bond vibrations in water[220] so the absence of a detectable IS for G_1(EAN) is not definitive. The situation is different for the dielectric spectrum. Figure 3.11 compares the relative absorption spectrum, $\alpha_{\mathrm{rel}}(\bar{\nu})$,[e] of d_3-EAN at 25 °C with that of EAN at 25 °C (present work) and 80 °C.[64] Comparison of the present FIR spectrum of EAN with that of Fumino *et al.*[64] reveals qualitative agreement, but also shows that accurate low-frequency data ($\bar{\nu} < 100\,\mathrm{cm}^{-1}$) are critical, as $\alpha_{\mathrm{rel}}(\bar{\nu})$ of the latter[64] appears to be considerably overestimated in this frequency range.

A strong IS is observed for the pronounced resonance at $\sim 420\,\mathrm{cm}^{-1}$, associated with the intramolecular bending motion of the cation,[64] which is shifted to $\sim 380\,\mathrm{cm}^{-1}$ by deuteration. A smaller but still significant IS is also observed for the peak at $\sim 200\,\mathrm{cm}^{-1}$, which corresponds to the peak in $\varepsilon''(\nu)$ at ~ 5.5 THz (Figure 3.10b). If G_2 is due to H-bond stretching and G_3 to cation librations (as proposed in Section 3.1.5.1) the effects of deuteration should be different. For H-bond stretching an IS of $(\mu_{\mathrm{EAN}}/\mu_{\mathrm{d3EAN}})^{1/2} = 0.982$, where μ is the reduced mass, would be expected in the gas-phase. For librations, IS $= (I_{\mathrm{EA+}}/I_{\mathrm{d3EA+}})^{1/2}$

[e]The relative absorption spectra, $\alpha_{\mathrm{rel}}(\bar{\nu})$ for d_3-EAN and EAN were obtained from the broadband DR spectra ($0.2 \lesssim \nu/\mathrm{GHz} \lesssim 10000$) using Eqs. 1.29 and 1.25, after subtraction of S_α from the total intensity.

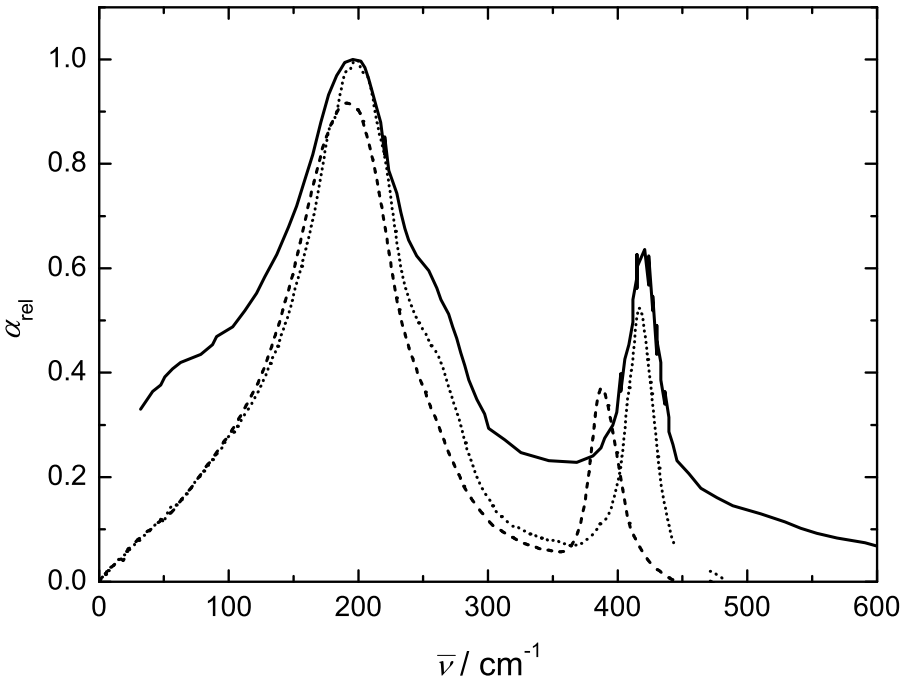

Figure 3.11: FIR absorption spectra as $\alpha_{\mathrm{rel}}(\bar{\nu})$, of EAN (dotted line) and d_3-EAN (dashed line) at 25 °C (this work) and of EAN at 80 °C (full line).[64]

should be 0.938 or 0.944 (depending on the axis of $EtNH_3^+$), where I is the moment of inertia. The relevant moments of inertia determined by MOPAC2009[174] for EAN and d_3-EAN (assuming rigid molecules) are $I_B = 100.6035 \times 10^{-47}\,\mathrm{kg\,m^2}$ & $I_C = 114.4250 \times 10^{-47}\,\mathrm{kg\,m^2}$ and $I_B = 114.3995 \times 10^{-47}\,\mathrm{kg\,m^2}$ & $I_C = 128.4374 \times 10^{-47}\,\mathrm{kg\,m^2}$, respectively.[f] The experimental ratios of the resonance frequencies are $\nu_{0,G2}^{d3EAN}/\nu_{0,G2}^{EAN} = 0.989$ and $\nu_{0,G3}^{d3EAN}/\nu_{0,G3}^{EAN} = 0.923$. These values differ significantly from each other and, more importantly, are gratifyingly close to the values of 0.982 predicted for H-bond stretching (G_2) and 0.938/0.944 for cation libration (G_3). These assignments are also consistent with the the temperature dependences of S_{G2} and S_{G3}.

3.1.5.3 PAN

The high-frequency region of the DR spectra of PAN was fitted with the same model as that derived for EAN (Section 3.1.3.2): a damped harmonic oscillator, DHO_1 (at ~ 1.6 THz), three Gaussians, G_1 (~ 2.0 THz), G_2 (~ 4.8 THz), and G_3 (~ 6.5 THz) plus an additional mode (DHO_2 at 9.0 THz) associated with the intramolecular torsion of the propyl chain of $PrNH_3^+$ with respect to the NH_3^+ group and includes the intramolecular bending vibration of the propyl chain.[64,65]

It is not surprising (given their similar chemical structures) that the model used to describe the DR spectra of EAN should also be applicable to PAN. Conversely, this provides circumstantial evidence for the reasonableness of the EAN model. For example, the some-

[f] Indices 'B' and 'C' denote the principle axes of inertia perpendicular to the dipole vector.

what ad hoc introduction (Section 3.1.5.1) of an additional Gaussian (G_3) centered at $\sim 6\,\mathrm{GHz}$ to best describe the DR spectrum of EAN at high frequencies, is supported by the clear-cut presence of a shoulder at $\sim 7\,\mathrm{THz}$ in the DR spectrum of PAN in addition to the pronounced peak at $\sim 5\,\mathrm{THz}$ described by G_2 (Figures 3.4 and 3.6). This provides strong support for more than one mode being responsible for the observed intensity in this region, consistent with the published FIR spectra.[64,65]

The amplitudes of the DHO_1, G_1, G_2 and G_3 modes for PAN are plotted in Figure 3.12a. For all S_j, the effect of T was the same as for EAN,[g] thus supporting the present mode assignment. The resonance frequencies $\nu_{0,G1}$, $\nu_{0,G2}$ and $\nu_{0,G3}$ of PAN decrease with increasing T (Figure 3.12b) as observed for EAN (Figure 3.9c) with the partial exception of $\nu_{0,G1}$. It is observed that $\nu_{0,G3}$ differs significantly (by $\sim 0.8\,\mathrm{THz}$) between PAN and EAN, whereas $\nu_{0,G2}$ is almost the same (compare Figures 3.9c and 3.12b). Again such a difference is consistent with the assignment of G_2 and G_3 to different molecular-level processes.[h]

The present model provides a consistent description of the fast dynamics of EAN and PAN. In particular, it shows that the observed DR and OKE intensities at high frequencies ($\bar{\nu} \gtrsim 50\,\mathrm{cm}^{-1}$) cannot be due to H-bond vibrations *alone* as has been proposed on the basis of FIR measurements.[64,65] Rather, there are also significant additional contributions from anion and cation librations (the G_1 and G_3 modes). In this context, further experimental studies using improved instrumentation and more sophisticated computer simulations will be required to more fully comprehend the complex dynamical behavior of PILs.

3.1.5.4 Intermediate frequency range

MD simulations and further experimental studies are especially required to increase our understanding of the dynamics of PILs in the intermediate frequency range. Both the DR and OKE spectra of EAN and PAN, like those observed for other ILs,[36,56] show a finite but featureless intensity over the approximate frequency range $0.05 \lesssim \nu/\mathrm{THz} \lesssim 1$. This intensity reflects the strong coupling and/or overlap of the potentially numerous rotational and translational modes expected to occur in this region. For PILs such as EAN and PAN, fast proton transfers may also occur on this timescale. The combination of these factors makes a definitive separation and identification of the contributing processes impracticable at present. Accordingly, in the OKE spectrum of EAN the intensity at intermediate frequencies was described by a large-amplitude constant-loss term with amplitude, S_{CL}, which substitutes for all the possible contributions. In contrast, in the DR spectrum of EAN and PAN, where this intensity is considerably smaller, it was more appropriate to subsume it in the CDi and DHO_1 amplitudes.

For supercooled liquids, contributions on this time scale have been referred to as β-relaxations by Johari and Goldstein.[227,228] Although specific contributions to the β-relaxation

[g] Except perhaps S_{G1}, which increases with increasing T for EAN (Figure 3.9a, ▲) but is almost constant for PAN (Figure 3.12a, ▲). However, this difference may result from the considerable scatter in the THz-TDS data (Figure 3.4) and the absence of OKE data to fix $\nu_{0,G1}$.

[h] Note, however, that the harmonic oscillator model would predict $\nu_{0,G3}(\mathrm{EAN}) > \nu_{0,G3}(\mathrm{PAN})$, opposite to the present results. This possibly reflects the effects of the greater length (size) and flexibility of the propyl chain on the librational cage. In contrast G_2, assigned here to H-bond stretching, would be expected to be less affected when Et is replaced by Pr, because of its translational character.

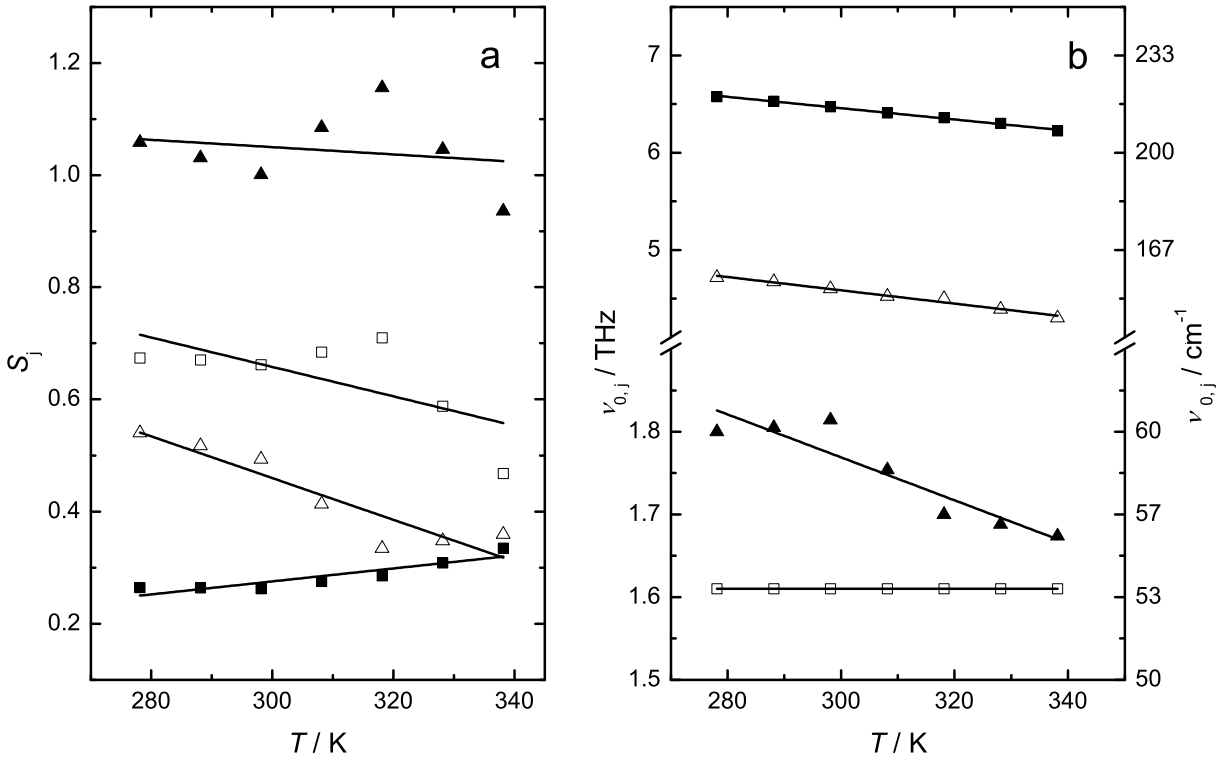

Figure 3.12: (**a**) Amplitudes, S_j, and (**b**) resonance frequencies, $\nu_{0,j}$, of the high-frequency resonance processes DHO_1 (□), G_1 (▲), G_2 (△) and G_3 (■) obtained from the fit of the DR spectra of PAN as a function of temperature. Solid lines are linear regressions.

are unknown, it seems likely that they originate, at least in part, from the motions of mobile clusters in an almost frozen environment, as proposed for glass-forming systems.[229–231] Such motions are at least notionally comparable with the "cage rattling" translational motions suggested for imidazolium-based ILs in the same spectral region.[163]
An additional contribution might be analogous to the "frame tumbling" proposed for water.[211] In contrast to librations this motion involves H-bond exchange and can be seen as a preliminary (faster) stage of the H-bond making and breaking associated with the α relaxation. Support for the presence of such a process in EAN comes from a MD simulation of the closely related methylammonium nitrate (MAN).[232] This simulation predicts that H-bond making and breaking takes place within $\sim 0.5\,\mathrm{ps}$ while proton hopping happens within $\sim 3\,\mathrm{ps}$. Both processes are potential candidates for the observed intensity in the intermediate frequency range.

3.1.6 Conclusions

The combination of broadband DR and OKE spectroscopy covering the exceptionally wide frequency range of $0.1 \lesssim \nu/\mathrm{GHz} \lesssim 10\,000$ and (for most measurements) a temperature range of $5 \leq \vartheta/^\circ\,\mathrm{C} \leq 65$ has provided detailed insights into the dynamics of the archetypal

protic ionic liquid EAN and its congener PAN.
At lower frequencies ($\nu \lesssim 100\,\mathrm{GHz}$) the α-relaxation in the DR and OKE spectra for EAN and PAN could reasonably be assigned to the reorientation of the cations and the anions, respectively. A high degree of cooperativity in these motions was evident from the observed departures of the relaxation times from SED behavior and the similarities of the activation energies, $E_\mathrm{A}^\mathrm{OKE}$ and E_A^DR. This is consistent with the presence of strong and directed inter-ionic interactions undoubtedly associated with strong H-bonding between the anions and cations. Moreover, comparison of τ_α^DR for EAN with those of fs-IR spectroscopy[208] indicated that the relaxation mechanism of the ions is not diffusive, but instead occurs through large-angle jump reorientations, with the jump angle being consistent with the pseudo-tetrahedral geometry of the alkylammonium ion. This suggests that in addition to the expected coulombic interactions, H-bonding between $EtNH_3^+$ and NO_3^- plays an important role in determining the molecular dynamics of EAN. The negative temperature-dependence of μ_eff for EAN and PAN, also supports the picture of PIL relaxations as being highly cooperative.
Whilst the origins of the featureless intensity in the intermediate frequency region ($0.05 \lesssim \nu/\mathrm{THz} \lesssim 1$) remain unclear, detailed insights into the high-frequency dynamics could be obtained. Analysis of the DR and OKE spectra of EAN supplemented by the DR spectra of PAN as a function of temperature and OKE and DR spectra of d_3-EAN at 25 °C indicated that in the frequency range $1 \lesssim \nu/\mathrm{THz} \lesssim 10$, intermolecular (i.e., inter-ionic) H-bond vibrations (bending and stretching) overlap with anion and cation librations (Table 3.7). These results in part confirm the assignments of various features in the FIR spectrum by Fumino *et al.*[64] (Table 3.6) but also show that ion librations contribute significantly to that spectrum. The present assignments are broadly supported by the isotopic shifts observed in the FIR spectrum of d_3-EAN.

Table 3.7: Present assignment of the resonance modes, DHO_1, G_1, G_2, G_3 and DHO_2 for the DR spectra of EAN and PAN and the OKE spectra of EAN.

Mode	Assignment
DHO_1	Intermolecular H-bond bending
G_1	NO_3^- librations
G_2	Intermolecular H-bond stretching
G_3	RNH_3^+ librations
DHO_2[64]	Alkyl torsion (+ propyl bending for PAN)

While much has been learnt from the present investigation, further experimental studies using improved equipment and more sophisticated MD simulations that can quantitatively reproduce the DR and OKE spectra will be required for a fuller understanding of the dynamics of typical PILs such as EAN.

3.2 1-Methylimidazolium-based Protic ILs

Parts of the dielectric measurements presented in this section were performed by M. Sc. Hiroyuki Doi (Niigata University, Niigata, Japan) during his research visit in our laboratories in Regensburg.

3.2.1 Introduction

In the previous Section 3.1 the dynamics of the paradigmatic protic ILs, EAN and PAN, were studied in detail. Both EAN and PAN are formed by an essentially complete proton transfer between their parent acids and bases, both of which exhibit conductive behavior similar to aprotic ILs. Thus (based on the large ΔpK_a value of their "parents") they can be considered as "good ionic liquids" according to the classification proposed by Angell *et al.*[4,233] In contrast, ILs formed from weak acids and bases (small ΔpK_a) belong to the class of "poor ionic liquids" and typically show a lower electrical conductivity. Apart from the electrical conductivity, other physicochemical properties such as viscosity and vapor pressure are also determined by the degree of proton transfer (ΔpK_a),[182,234,235] which therefore represents an important parameter for designing PILs with specific properties.[24,181,183] Thus, knowledge of the conditions that influence the degree of proton transfer is essential, particularly with regard to technical applications in fuel cells.[233,236–238]
Recently, an equimolar mixture of the dipolar liquid *N*-methylimidazole (C_1Im) and acetic acid (HOAc) was studied as a model system by our collaborators (Prof. Dr. Y. Umebayashi *et al.* from Niigata University, Niigata, Japan) using Raman spectroscopy and quantum mechanical calculations.[79] With respect to ΔpK_a, [C_1Im][HOAc] can be assigned to the group of "poor" ILs and in fact, it was demonstrated that neutral species (i.e. the parent acid and base) are predominant in this mixture.[79] This implies that the equilibrium lies to the left side:[a]

$$C_1Im + HOAc \overset{K_a}{\rightleftharpoons} C_1ImH^+ + OAc^- \tag{3.3}$$

However, it was observed that despite the vanishing amount of ionic species, [C_1Im][HOAc] exhibits a considerable electrical conductivity,[181] which even exceeds the "ideal line" in the Walden plot.[79] Proton conduction was held responsible for that and it was suggested that such liquids be referred to as *pseudo*-protic ILs.[79]
In this work, dielectric relaxation spectroscopy (DRS) is used to extend the work of Doi *et al.*,[79] on 1-methylimidazolium PILs by investigating their dynamics and as the only technique available to directly determine their dielectric constants.[57] The overall aims of this study were to understand the influence of proton transfer and temperature on the dynamics of PILs. In addition to [C_1Im][HOAc], dielectric spectra were also measured for neat C_1Im and PILs consisting of C_1Im and stronger acids such as difluoroacetic acid (HDFA, CF_2HCOOH), trifluoroacetic acid (HTFA, CF_3COOH) and bis(trifluoromethanesulfonyl)amine (HTFSA, $HN(SO_2CF_3)_2$), which are known to be completely dissociated when mixed 1:1 with C_1Im.[78] It is shown that the dynamics of

[a]For convenience this equilibrium will be characterized by the equilibrium constant K_a.

[C_1Im][HOAc] resemble those of conventional mixtures of organic solvents, whereas those of [C_1Im][DFA], [C_1Im][TFA] and [C_1Im][TFSA] show typical characteristics of aprotic and protic ILs. Analysis of the dielectric amplitudes of [C_1Im][HOAc] enabled protonation ratio to be determined as a function of temperature, which in turn allowed calculation of the pK_a of [C_1Im][HOAc]. Moreover, it was possible to estimate the amount of acetic acid monomers present in [C_1Im][HOAc] from the dielectric amplitude.

3.2.2 Data acquisition and processing

3.2.2.1 Materials and physical properties

Materials were prepared and provided by the group of Prof. Dr. Y. Umebayashi (Niigata University, Niigata, Japan) as described in Section 2.1.
Densities, viscosities and electrical conductivities, which are required to analyze the dielectric data were taken from Ref. 79 and were interpolated if necessary.[b]

3.2.2.2 Dielectric Spectroscopy

The dielectric spectra of [C_1ImH][DFA], [C_1ImH][TFA] and [C_1ImH][TFSA] were recorded at 65 °C in the frequency range $0.2 \leq \nu/\,\mathrm{GHz} \leq 50$ only, due to their high melting points. Those of [C_1Im][HOAc] were measured between 5 to 65 °C in 10 °C steps in the range of $0.2 \leq \nu/\,\mathrm{GHz} \leq 89$. For comparison the spectrum of neat C_1Im was measured at 25 °C over the same frequency range. Open-ended coaxial probes and transmission A-Band cell connected to the VNA (Section 2.2.2) and the E-band interferometer (Section 2.2.1) were used. For Padé-calibration (Eq. 2.17) of the VNA data DMA, BN and 1-BuOH were used. As described in Section 2.4 raw dielectric spectra were corrected for conductivity contribution (Eq. 1.22) by subtraction of the experimental dc conductivity, κ. During fitting κ was treated as an additional parameter and differed from the experimental value by $\sim 13\,\%$ on average.
Molecular-level information from DR spectra is obtained by describing the experimental data with appropriate relaxation models based on Eq. 1.34 (Section 1.2). The spectra were fitted as described in Section 2.4 testing all reasonable combinations of HN, CD, CC and D equations up to $n = 4$. Possible models were assessed by their χ^2_r values and the smooth temperature dependence of the optimized parameters. For all studied samples the parameters so derived are summarized in Table 3.8.

3.2.3 Results

Neat C_1Im. The dielectric spectrum of neat C_1Im at 25 °C (Figure 3.13) was best described by a sum of a Cole-Cole (CC) and a Debye equation (D) (Table 3.8). The CC

[b] Note that densities of [C_1ImH][TFA] and [C_1ImH][TFSA] and viscosities of [C_1ImH][DFA], [C_1ImH][TFA] and [C_1ImH][TFSA] were only available at 70 °C.[239] Nevertheless, these values can be promptly used to analyze the dielectric spectra at 65 °C, as the uncertainties of the dielectric measurements exceed those of the so introduced error.

Table 3.8: Dielectric fit parameters of [C_1Im][HOAc] as a function of T, of neat C_1Im at 25 °C and of [C_1ImH][DFA], [C_1ImH][TFA] and [C_1ImH][TFSA] at 65 °C: static permittivity, ε_s, amplitudes, S_j, relaxation times, τ_j, width parameter α_1 and β_1, high frequency limit of ε', ε_∞, and reduced error function, χ^2_r.[a]

	T	ε_s	S_1	$(\alpha_1)^b$	τ_1	S_2	τ_2	S_3	τ_3	ε_∞	$\chi^2_r \cdot 10^4$
C_1Im	298.15	36.2	30.9	0.007	28.3	1.80	3.32	—	—	3.51	245
[C_1Im][HOAc]	278.15	31.8	24.9	0.631	882	1.84	42.7	0.94	2.40	4.18	99
	288.15	32.9	24.4	0.713	594	2.97	34.5	1.28	2.32	4.23	223
	298.15	31.7	23.8	0.734	416	2.50	28.0	1.48	2.55	3.95	78
	308.15	30.0	20.6	0.827	273	3.65	25.6	1.59	2.34	4.16	284
	318.15	27.9	18.9	0.831	230	3.21	24.0	1.87	2.40	3.91	182
	328.15	28.9	18.7	0.879	171	4.44	18.2	1.57	2.40	4.20	103
	338.15	27.1	17.1	0.899	130	4.21	14.9	1.68	2.72	4.11	257
[C_1ImH][DFA]	338.15	16.2	3.97	0.022	83.0	4.31	24.16	3.03	3.87	4.90	53
[C_1ImH][TFA]	338.15	12.5	3.36	0.045	82.4	2.70	25.01	2.54	3.28	3.88	66
[C_1ImH][TFSA]	338.15	15.0	6.39	0.094	121	3.09	22.46	1.82	2.82	3.74	50

[a] Units: T in K, τ_j in ps; [b] Corresponds to Cole-Davidson parameter, β_1, for [C_1Im][HOAc] at all temperatures;

process, centered at ∼ 5 GHz, can be reasonably ascribed to the rotational diffusion of individual C_1Im molecules, as it has been observed for neat DMA and *N*,*N*-dimethylformamide (DMF).[148,240] In contrast, an unambiguous assignment of the D mode is not straightforward. Due to the oblate shape of the C_1Im molecule its moment of inertia, I, is anisotropic (with $I_x < I_y \approx I_z$) and thus reorientations around different principle axes could be a possible scenario similar to what has been suggested for DMF by NMR measurements.[148,241] As the major component of the dipole vector, $\vec{\mu}$, is directed along I_x large-amplitude contributions should arise from rotations of $\vec{\mu}$ around *y*- and *z*-axes. As I_y and I_z are larger than I_x by factors of ∼ 2.5 and ∼ 3.5 (MOPAC[174]), respectively, rotations of $\vec{\mu}$ around *y*- and *z*-axes should have larger relaxation times than around the *x*-axis. This would be consistent with the observed amplitude and relaxation times of the present CC and D modes, as $S_1 > S_2$ and $\tau_1 > \tau_2$ (Table 3.8). However apart from that, the D mode could also incorporate motions arising from inertial effects, as eventually concluded for DMF and DMA[148] and/or with internal reorientations that lead to changes of the permanent dipole moment, as observed for propylene carbonate and butylene carbonate.[240]

[C_1Im][HOAc]. The dielectric spectrum of [C_1Im][HOAc] measured in the temperature range of $5 \leq \vartheta/°C \leq 65$ (Figure 3.14) is dominated by a pronounced relaxation peak at ∼ 1 GHz. This process, which in case of ILs is often referred to as α-relaxation, shifts to higher frequencies with increasing T, indicating an acceleration of the underlying dynamics consistent with decreasing viscosity.[79] Extrapolation of ε' to $\nu \to 0$ permits estimation of the static permittivity, ε_s, although the accuracy of this determination is limited by

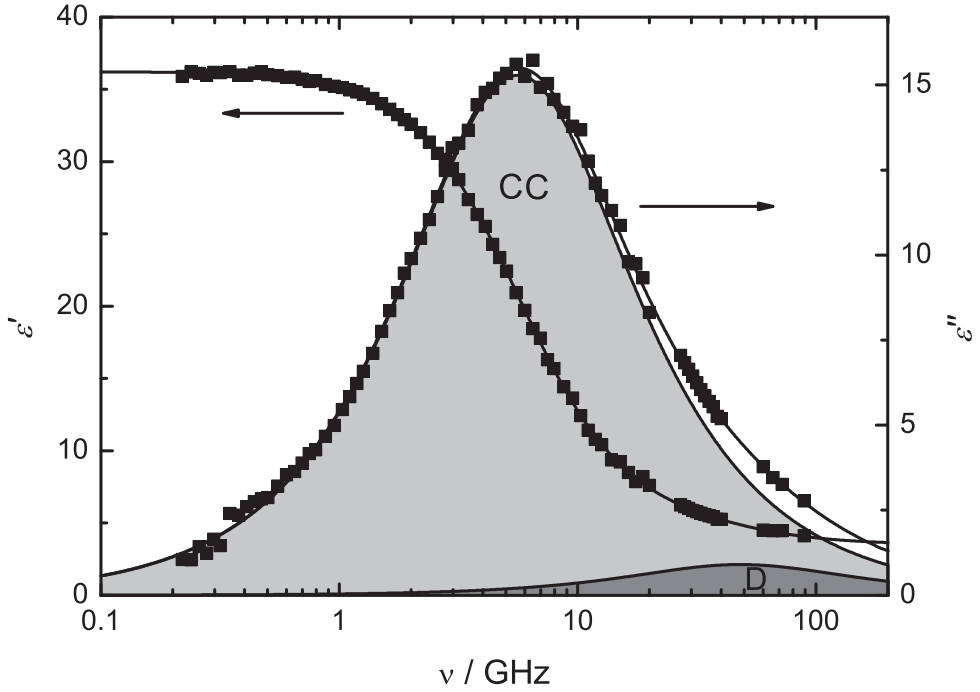

Figure 3.13: Dielectric permittivity, ε', and loss, ε'', spectrum (■) of neat C_1Im at 25 °C with total fit (—) and individual functions of the CC+D model (shaded areas).

the poorly defined low-frequency plateau of ε' (Figure 3.14a). It is observed that ε_s of $[C_1Im][HOAc]$ is considerably larger than that of many aprotic ILs,[55,58] for which $\varepsilon_s < 20$ typically but comparable with those of protic ILs like EAN and PAN (Section 3.1). Likewise the temperature coefficient $d\varepsilon_s/dT$=–0.09 K^{-1} is of similar magnitude as that of PILs ($d\varepsilon_s/dT$=–0.13 K^{-1} (EAN) and –0.09 K^{-1} (PAN)) and H-bonded molecular liquids such as alcohols, where they are ascribed to a partial break-up of their H-bond networks with increasing T.[242]

At all T, the spectrum of $[C_1Im][HOAc]$ is best modelled by a sum of a Cole-Davidson mode (CD; at ∼ 0.7 GHz) and two Debye functions (D_1 and D_2; at ∼ 6 GHz and ∼ 50 GHz, respectively) (Figure 3.15 and Table 3.8). Given that the proton transfer from HOAc to C_1Im is rather incomplete, as suggested by Raman measurements,[79] the CD process can be mainly assigned to the reorientation of neutral C_1Im molecules and (to a much smaller extent) C_1ImH^+ ions.[c] The D_1 mode of $[C_1Im][HOAc]$ can be associated with reorientations of HOAc and OAc^- monomers, although it is well-known from experimental and theoretical studies that the liquid structure of pure acetic acid mainly consists of chain-like clusters,[243,244] and that in binary mixtures with organic solvents oligomeric and dimeric species are present in addition to HOAc monomers.[234,244,245] However, as shown in Section 3.2.4.2, the amplitude of the D_1 process, S_2, can only be reasonably evaluated when assuming an equilibrium of HOAc monomers and cyclic dimers.

[c]Note that the D mode present in neat C_1Im is most likely subsumed in the high frequency wing of the CD mode of $[C_1Im][HOAc]$.

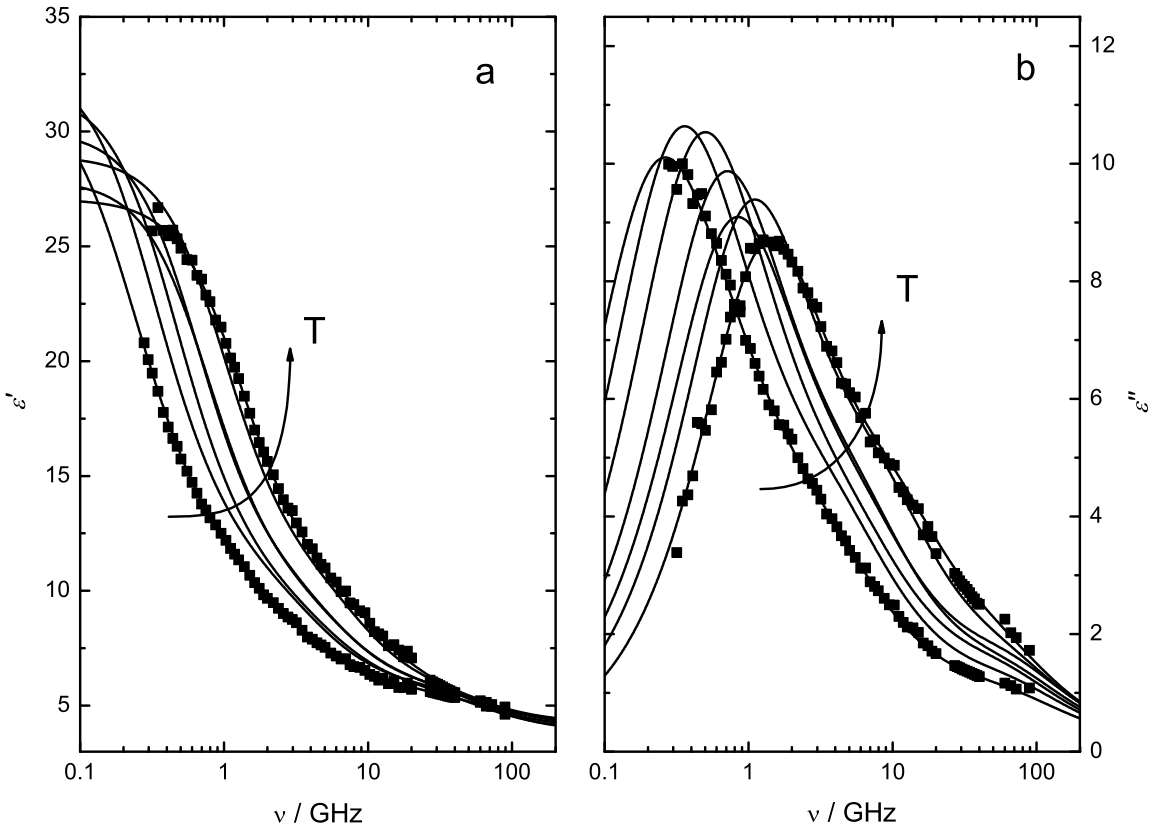

Figure 3.14: **(a)** Dielectric permittivity, ε', and **(b)** loss, ε'', spectra (■) of [C_1Im][HOAc] from 5 to 65 °C in 10 °C steps with total fit (—). Only spectra at 5 and 65 °C are displayed for visual clarity.

[C_1ImH][DFA], [C_1ImH][TFA] and [C_1ImH][TFSA]. The overall shape of the dielectric spectra of [C_1ImH][DFA], [C_1ImH][TFA] and [C_1ImH][TFSA] is similar to that of [C_1Im][HOAc]. The striking difference, however, is their significantly lower ε_s compared to [C_1Im][HOAc] (Figure 3.15). Furthermore, the peak maximum of $\varepsilon''(\nu)$ of [C_1ImH][DFA], [C_1ImH][TFA] and [C_1ImH][TFSA] is centered at considerably higher frequencies than that of [C_1Im][HOAc], despite their significantly higher viscosities (Table 3.9).
The spectra of [C_1ImH][DFA], [C_1ImH][TFA] and [C_1ImH][TFSA] were best described by a sum of a CC function centered at ~ 2 GHz and two Debye equations (D_1 & D_2) at ~ 7 GHz and ~ 50 GHz, respectively (Table 3.8).
For 1-alkyl-3-methylimidazolium ILs, the low frequency process is associated with the reorientation of imidazolium-based cations, which was found to occur in a jump-like fashion, rather than through rotational diffusion.[36,58,213] It seems likely that this is also the case for the CC process of [C_1ImH][DFA], [C_1ImH][TFA] and [C_1ImH][TFSA], as these mixtures can be readily considered as typical RTILs, with respect to their high protonation ratio reported by Kanzaki *et al.*[78]
It was found that dielectric spectra of ILs composed of dipolar anions show an additional mode specific for anion relaxation, which is typically centered at higher frequen-

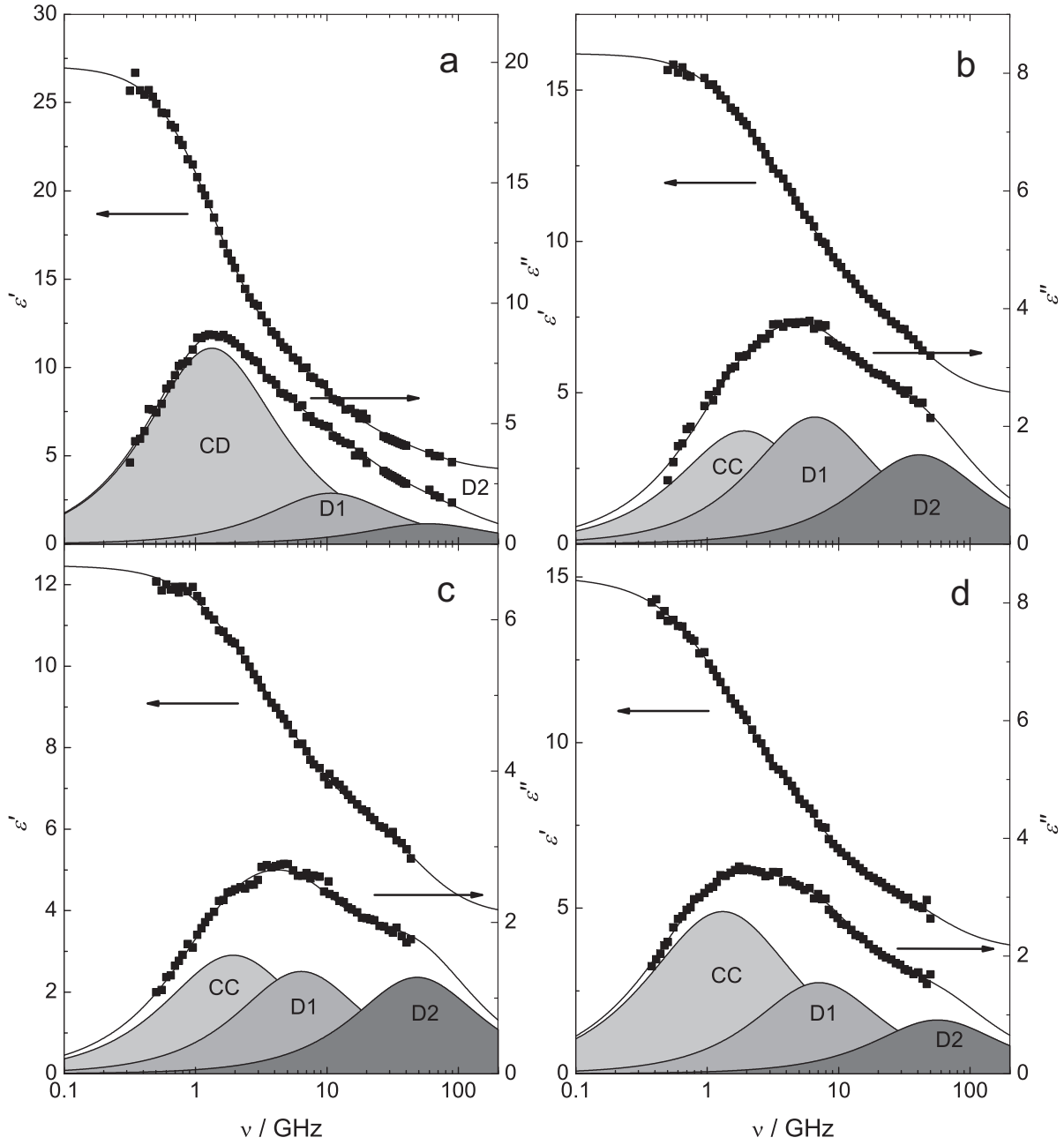

Figure 3.15: Dielectric spectra (■) of **(a)** [C_1Im][HOAc], **(b)** [C_1ImH][DFA], **(c)** [C_1ImH][TFA] and **(d)** [C_1ImH][TFSA] at 65 °C total fit (—) and contributing modes (shaded areas).

cies than the cation relaxation process.[47] Thus, the D_1 mode of the present spectra of [C_1ImH][DFA], [C_1ImH][TFA] and [C_1ImH][TFSA] can be reasonably assigned to contributions from DFA^-, TFA^- and $TFSA^-$ as all of these anions possess permanent dipole moments (Section 3.2.4.2). However, it should be noted that particularly for ILs rotations of anions and cations are strongly coupled and their contributions overlap and that trans-

lational motions may contribute on a similar time scale as rotations.[45] Thus, although such empirical decompositions have provided reasonable descriptions of dielectric spectra of ILs, they cannot be considered as "proven".

The D_2 mode present in all studied mixtures is centered at the upper frequency limit of the present spectra ($\sim 50\,\mathrm{GHz}$) and thus, can be reasonably interpreted as a composite that subsumes all processes taking place in the THz-range such as "cage-rattling", intermolecular vibrations and librations.[36,58,107] As such processes cannot directly be captured by the instrumentation used here, a detailed interpretation of D_2 is impossible.

3.2.4 Discussion

3.2.4.1 Relaxation times

Stokes-Einstein-Debye approach. The Stokes-Einstein-Debye (SED) model[121] (Eq. 1.63) relates the rotational correlation time, τ'_j, of process j with the solution viscosity, η. In the present analysis macroscopic relaxation times, τ_j, obtained from the dielectric fit (Table 3.8) were converted into microscopic rotational correlation times, τ'_j, via the Powles-Glarum equation (Eqs. 1.71 and 1.72).[125] Although this theory is strictly speaking only valid on a macroscopic level, it has provided valuable insights into molecular-level dynamics,[57,85] including those of complex liquids like ILs.[58,107] The effective volume of rotation, $V_{\mathrm{eff}} (= V_{\mathrm{m}} f_{\perp} C)$, defined by the product of the molecular volume, V_{m},[246] shape factor, $f_{\perp}$, and friction coefficient, C, can be obtained from the slope of a SED plot ($\tau_j = f(\eta)$). The frictional conditions of the relaxing particle generally adopts values between *slip* ($C_{\mathrm{slip}} = 1 - f^{-2/3}$) and *stick* ($C_{\mathrm{stick}} = 1$) boundary conditions. Figure 3.16 shows the SED plots of τ'_1 and τ'_2 of [C_1Im][HOAc]. The corresponding $V_{\mathrm{eff},1}$ and $V_{\mathrm{eff},2}$ of [C_1Im][HOAc] were obtained from the slopes. For [C_1ImH][DFA], [C_1ImH][TFA] and [C_1ImH][TFSA] $V_{\mathrm{eff},j}$ was calculated at 65 °C and for neat C_1Im at 25 °C using Eq. 1.63. The shape factors, $f_{\perp}$, of the dipolar species were calculated on the basis of the axial ratios obtained from their MOPAC-calculated optimized geometries using Eqs. 1.65 and 1.64.[122,123] Approximating C_1Im, C_1ImH^+, HOAc, DFA^- and TFA^- as oblate, and $TFSA^-$ as prolate, ellipsoids, $C_{\mathrm{exp},j} = V_{\mathrm{eff}}/V_{\mathrm{m}} f_{\perp}$, were obtained (Table 3.9).
For the first process ($j = 1$), $C_{\mathrm{exp},1}$ of [C_1Im][HOAc] is found to be ~ 3.5 times higher than that of neat C_1Im and even ~ 6 times higher than those of the other ILs (Table 3.9). This indicates that the rotational friction acting on C_1Im in [C_1Im][HOAc] is strongly enhanced with respect to neat C_1Im, which can be reasonably explained by the existence of H-bonds between C_1Im and HOAc. Because the linear relation of Eq. 1.63 is obeyed and such large values of C_{exp} are very uncommon for ILs,[58,107] this suggests that relaxation of C_1Im molecules in [C_1Im][HOAc] is through rotational diffusion typical for conventional mixtures of organic solvents, rather than for ILs. This is consistent with the results from Raman spectroscopy that neutral species predominate in [C_1Im][HOAc].[79]
In this picture, the small $C_{\mathrm{exp},1}$ values of [C_1ImH][DFA], [C_1ImH][TFA] and [C_1ImH][TFSA] suggest a less hindered rotation of the cation dipole than in neat C_1Im. This seems unrealistic given that the essentially complete proton transfer in all these mixtures[247]

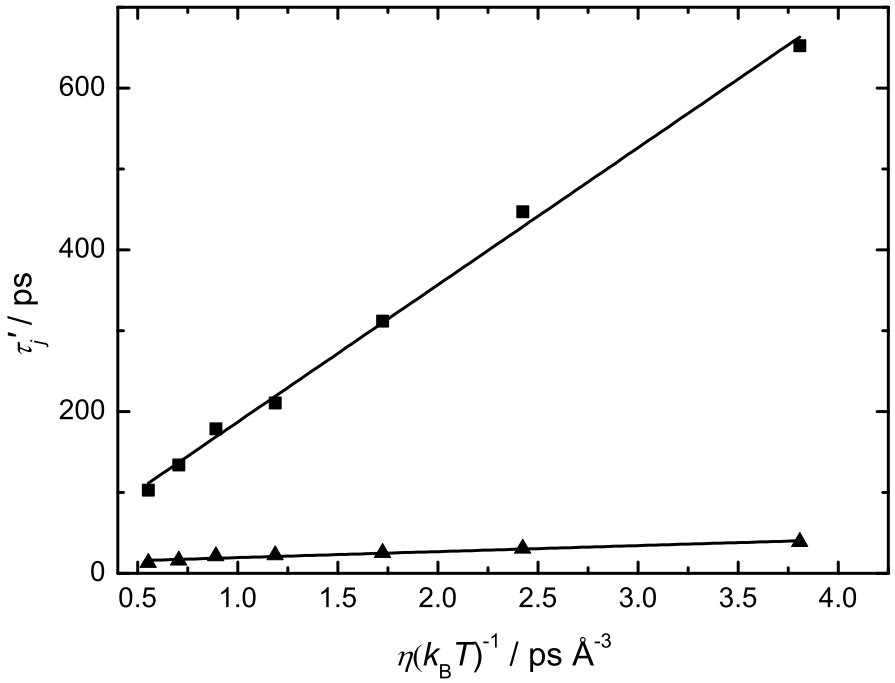

Figure 3.16: SED plot of rotational correlation times τ_1' (■) and τ_2' (▲) of [C_1Im][HOAc]. Solid lines represent linear regressions (Eq. 1.63).

induces coulombic interactions, which strongly enhance the friction between the relaxing particles and their environment.[248,249] As a result of such strong interionic interactions, ion relaxation in aprotic and protic ILs has been shown to occur through a jump mechanism.[36,44,208,213,249] Among other things, this manifests itself as an extraordinarily small friction coefficient; even *sub*-slip behavior is occasionally observed.[58] Although the latter is not the case here ($C_{\mathrm{slip}} = 0.056$) the small value of $C_{\mathrm{exp},1}$ of [C_1ImH][DFA], [C_1ImH][TFA] and [C_1ImH][TFSA] compared to that of neat C_1Im indicates dynamical behavior along the lines of ILs. Whether the mechanism is indeed through large-angle jumps as observed for other ILs[36,208] cannot be unambiguously determined at this stage. This would require spectroscopic methods such as optical Kerr-effect or fs-IR spectroscopy that can detect second-rank relaxation times (Section 3.1 and Chapter 4). Nevertheless, the decrease of $C_{\mathrm{exp},1}$ with increasing acidity (in aqueous solution) of the acid in the order of HOAc<HDFA<HTFA<HTFSA (Table 3.9) probably reflects the extent of induced coulomb interactions arising from the increasing degree of proton transfer.

For $C_{\mathrm{exp},2}$ no significant differences were observed among [C_1Im][HOAc], [C_1ImH][DFA] and [C_1ImH][TFA] (Table 3.9), whereas $C_{\mathrm{exp},2}$ of [C_1ImH][TFSA] was considerably smaller. This is partially a result of the prolate shape of $TFSA^-$ leading to a larger value for $f_\perp$ but is also explained by the viscosity of [C_1ImH][TFSA], which is the highest among the present mixtures, at an virtually identical correlation time, τ_2' (Table 3.9).

Table 3.9: Friction coefficients, $C_{\mathrm{exp},j}$ and rotational correlation times, τ_j', of the first ($j = 1$) and second ($j = 2$) relaxation process and viscosity, η, of neat C_1Im, [C_1Im][HOAc], [C_1ImH][DFA], [C_1ImH][TFA] and [C_1ImH][TFSA] at 65 °C if not specified otherwise.[a]

	τ_1'	$C_{\mathrm{exp},1}$	τ_2'	$C_{\mathrm{exp},2}$	η
neat C_1Im[b]	20.2	0.179	—	—	1.73
[C_1Im][HOAc]	103	0.631	12.8	0.043	2.58
[C_1ImH][DFA]	76.1	0.112	21.3	0.044	11.5[c]
[C_1ImH][TFA]	74.7	0.095	22.5	0.038	13.3[c]
[C_1ImH][TFSA]	103	0.089	19.8	0.009	19.4[c]

[a] Units: τ_j' in ps, η in mPa s; [b] at 25 °C; [c] at 70 °C;

Activation energies. As ILs are glass-forming liquids, the temperature dependence of their transport properties is known to follow Vogel-Fulcher-Tammann (VFT) behavior.[154,250,251] However, with the limited temperature range investigated here, and the rather small number of data points, application of the simpler two-parameter Arrhenius equation is reasonable.[58,107] To compare the activation energies so obtained with other transport properties such as viscosity, η, and electrical conductivity, κ, the temperature dependence of the two latter was also approximated by Arrhenius equations at comparable temperatures (283.15 K to 343.15 K), although they are actually better described by the VFT function over the entire measured temperature range.[79]

As already mentioned in the last section, both relaxation times, τ_1 and τ_2 of [C_1Im][HOAc] are decreasing with increasing temperature indicating that the underlying molecular process is thermally activated. Activation energies of $E_\mathrm{A}(\tau_1) = (24.8 \pm 0.8)\,\mathrm{kJ\,mol^{-1}}$ and $E_\mathrm{A}(\tau_2) = (12.8 \pm 1.0)\,\mathrm{kJ\,mol^{-1}}$ were obtained from $\tau_1(T)$ and $\tau_2(T)$, whereas $\eta(T)$ and $\kappa(T)$ yielded $E_\mathrm{A}(\eta) = (22.2 \pm 0.5)\,\mathrm{kJ\,mol^{-1}}$ and $E_\mathrm{A}(\kappa) = (17.2 \pm 1.3)\,\mathrm{kJ\,mol^{-1}}$, respectively.

The fact that $E_\mathrm{A}(\tau_1) \approx E_\mathrm{A}(\eta)$ suggests that rotational motions of C_1Im molecules in [C_1Im][HOAc] are coupled to viscosity, consistent with the observation that τ_1' linearly scales with η (see above). On the contrary, $E_\mathrm{A}(\kappa)$ is significantly smaller than $E_\mathrm{A}(\tau_1)$ and $E_\mathrm{A}(\eta)$ indicating that the charge transport is at least partially decoupled from viscosity and rotational motions of C_1Im. This is not surprising, because the charge transport is expected to take place via proton hopping, rather than through ion migration[79] and also indicates that the reorientational dynamics of C_1Im do not determine the transport of protons in the liquid.

The activation energy of the D_1 mode, $E_\mathrm{A}(\tau_2) = (12.8 \pm 1.0)\,\mathrm{kJ\,mol^{-1}}$, is considerably smaller than, $E_\mathrm{A}(\tau_1)$ and $E_\mathrm{A}(\eta)$ and thus suggests that the reorientation of HOAc/OAc^- is decoupled from viscosity. Binding energies of *two* H-bonds involved in a HOAc side-on dimer were calculated to $22.1\,\mathrm{kJ\,mol^{-1}}$ [252] and $26.7\,\mathrm{kJ\,mol^{-1}}$ [243] using *ab initio* methods. Consequently, the binding energy of *one* H-bond is $\sim 12\,\mathrm{kJ\,mol^{-1}}$, which is compatible with $E_\mathrm{A}(\tau_2)$ and also with the H-bond energy in water ($\sim 11\,\mathrm{kJ\,mol^{-1}}$).[253] This suggests that the relaxation of HOAc/OAc^- is determined by the cleavage of a H-bond or inversely, HOAc

relaxation could be the rate-determining step for proton transport in [C_1Im][HOAc]. If so, this would be in contrast to what has been observed for [C_1ImH][TFSA] by quasi-elastic neutron scattering (QENS) and NMR spectroscopy,[254,255] where C_1Im acts as the proton carrier. However in the present case, most of the protons are bound to HOAc consistent with the low degree of proton transfer in [C_1Im][HOAc] (Section 3.2.4.2). The low activation energy, $E_A(\tau_2)$, could then reasonably explain why the conductivity of [C_1Im][HOAc] is higher than expected from viscosity (Figure 3 in Ref. 79) despite the small fraction of ionic species.

3.2.4.2 Amplitudes.

According to the Cavell equation[115] (Eq. 1.52) the amplitude of a relaxation process is related to the dipole density and the effective dipole moment, $\mu_{\mathrm{eff},j}$, of the relaxing species j. Via the empirical correlation factor, g_j, $\mu_{\mathrm{eff},j}$ is connected to the apparent dipole moment, $\mu_{\mathrm{app},j}(=\mu_{\mathrm{eff,j}}/\sqrt{g_j})$, which in turn is related to the gas phase dipole moment, μ, by a cavity-field factor that takes into account polarizability effects of the cage surrounding particle j (Section 1.3.3).[d]

[C_1ImH][DFA], [C_1ImH][TFA] & [C_1ImH][TFSA] From the amplitudes, S_1 and S_2, of the CC and D_1 mode, $\mu_{\mathrm{eff},1}$ and $\mu_{\mathrm{eff},2}$, of [C_1ImH][DFA], [C_1ImH][TFA] and [C_1ImH][TFSA] were calculated at 65 °C, respectively (Table 3.10).
It is observed that the values of $\mu_{\mathrm{eff},1}$ of [C_1ImH][DFA] and [C_1ImH][TFA] coincide with the apparent dipole moments predicted by MOPAC for C_1ImH^+ of $\mu_{\mathrm{app,C1ImH+}} = 2.30$ D and 2.28 D, respectively (Table 3.10). This supports the assignment of the CC mode to cation relaxation consistent with findings of aprotic imidazolium-based ILs.[36,58] Although it is known from Raman spectroscopic measurements,[247] that at 25 °C only half of HDFA is dissociated in [C_1ImH][DFA], the present result indicates that, at least at 65 °C, C_1Im in [C_1ImH][DFA] is nearly completely protonated, in agreement with the IL-like dynamics (Section 3.2.4.1). For [C_1ImH][TFA], Raman spectra at 25 °C show no peaks specific for neutral species.[247] This implies that at 65 °C HTFA should be also completely dissociated, consistent with $\mu_{\mathrm{eff},1}$([C_1ImH][TFA])≈ $\mu_{\mathrm{app,C1ImH+}}$([$C_1$ImH][TFA]).
The values of $\mu_{\mathrm{eff},2}$ of [C_1ImH][DFA] and [C_1ImH][TFA] are considerably smaller than $\mu_{\mathrm{app,DFA-}} = 6.67$ D and $\mu_{\mathrm{app,TFA-}} = 6.00$ D obtained from MOPAC,[174] although the trend $\mu_{\mathrm{eff},2}$([C_1ImH][DFA])> $\mu_{\mathrm{eff},2}$([C_1ImH][TFA]) is the same. In fact, such differences between μ_{app} and μ_{eff} for dielectric modes associated with anion reorientation have been observed previously[47] and have been interpreted, at least in part, as an indication of strong antiparallel dipole-dipole correlations. This is also in line with unpublished results of 1-ethyl-3-methylimidazolium acetate at 25 °C indicating strong correlations of OAc^-, with $g_{\mathrm{OAc-}} = 0.07$.[256]
For [C_1ImH][TFSA] significant differences between $\mu_{\mathrm{eff},1}$ (Table 3.10) and $\mu_{\mathrm{app,C1ImH+}}$ =

[d]The shape of the cavity field is taken into account by the factor A (Eq. 1.55) and is determined by the geometry of the rotating particle. In the present case all dipolar species were approximated as oblate ellipsoids (Eq. 1.57), except $TFSA^-$ (prolate; Eq. 1.56), with their optimized geometries being obtained from MOPAC.[174]

2.30 D (MOPAC) are observed. Consistent with the high acidity of HTFSA, the proton transfer to C_1Im is expected to be complete in [C_1ImH][TFSA], consistent with the observed IL-like dynamics (Section 3.2.4.1). It seems likely that $\mu_{\text{eff},1} > \mu_{\text{app,C1ImH+}}$ is a result of strongly coupled and overlapping rotational and translational motions of cations and anions as proposed by MD simulations[45] and DRS results.[47]
For the evaluation of S_2 of [C_1ImH][TFSA] the conformational equilibrium of $TFSA^-$ [257] has to be taken into account as the conformers of $TFSA^-$ (C_1 and C_2) exhibit considerably different apparent dipole moments ($\mu_{\text{app,C1}} = 5.3$ D; $\mu_{\text{app,C2}} = 0.5$ D, obtained from MOPAC). In 1-ethyl-3-methylimidazolium TFSA and *N*-propyl- and *N*-butyl-*N*-methylpyrrolidinium TFSA the mole fraction of C_1-$TFSA^-$, $x_{C1} = 0.48$, has been determined at room temperature[258] and a nearly identical value ($x_{C1} = 0.49$) has been observed by DRS for [C_6mim][TFSA].[259] Assuming in a first approximation, that the same value of $x_{C1} = 0.49$ can be used in the present case, an average apparent dipole moment of $TFSA^-$, $\bar{\mu}_{\text{app,TFSA}-}$, can be estimated via

$$\bar{\mu}^2_{\text{app,TFSA}-} = x_{\text{C1}}\mu^2_{\text{app,C1}} + (1 - x_{\text{C1}})\mu^2_{\text{app,C2}}. \tag{3.4}$$

This yields $\bar{\mu}_{\text{app,TFSA}-} = 3.76$ D, which is compatible with $\mu_{\text{eff},2}$ (Table 3.10) and thus suggests assignment of the D_1 mode of [C_1ImH][TFSA] to the reorientation of $TFSA^-$.

Table 3.10: Effective dipole moments, $\mu_{\text{eff},1}$ and $\mu_{\text{eff},2}$, calculated S_1 and S_2 of [C_1ImH][DFA], [C_1ImH][TFA] and [C_1ImH][TFSA] via Eq. 1.52.[a]

	$\mu_{\text{eff},1}$	$\mu_{\text{eff},2}$
[C_1ImH][DFA]	2.30	2.61
[C_1ImH][TFA]	2.21	2.14
[C_1ImH][TFSA]	3.79	3.54

[a] Units: $\mu_{\text{eff},j}$ in D;

[C_1Im][HOAc]. For [C_1Im][HOAc], $\mu_{\text{eff},1}$ and $\mu_{\text{eff},2}$ were calculated from S_1 and S_2, respectively, and are plotted in Figure 3.17. It is observed that $\mu_{\text{eff},1}$ slightly decreases, whereas $\mu_{\text{eff},2}$ increases with increasing T.
Kanzaki *et al.*[78] have proposed from calorimetric titrations, that the proton transfer in [C_1Im][HOAc] is less than approximately 40 % complete at 25 °C. On the contrary, the same group reported that the amount of ions (C_1ImH^+/OAc^-) is less than 1 % at 25 °C based on Raman spectroscopy.[79] This considerable difference demonstrates the large uncertainties associated with the determination of the protonation ratio for such mixtures.
As the ions (C_1ImH^+/OAc^-) and the neutral species (C_1Im/HOAc) possess considerably different dipole moments (see below), the effect of proton transfer should be reflected in the present dielectric amplitudes. In fact, a shift of the equilibrium (Eq. 3.3) to the right would reasonably explain the observed trends of the effective dipole moments $\mu_{\text{eff},1}$ and $\mu_{\text{eff},2}$ with increasing T (Figure 3.17). According to that, an attempt is made to extract the degree of proton transfer from the present dielectric data, keeping in mind all required approximations associated with such an approach.

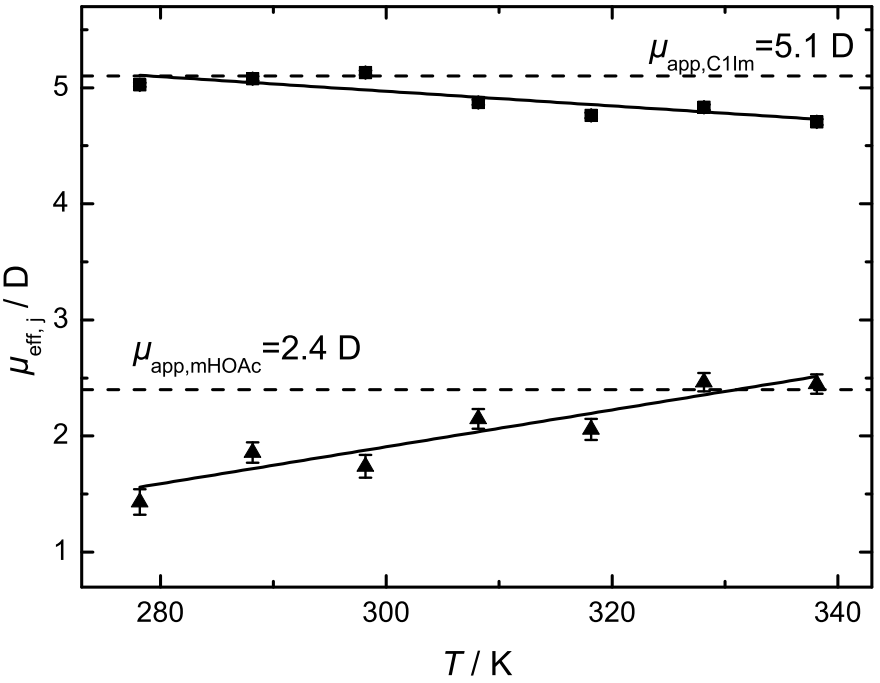

Figure 3.17: Effective dipole moments, $\mu_{\mathrm{eff},1}$ (■) and $\mu_{\mathrm{eff},1}$ (▲) obtained via Eq. 1.52 from S_1 and S_2, of [C_1Im][HOAc] as a function of T. Solid lines are linear regressions.

For the C_1Im molecule MOPAC yielded a gas phase dipole moment of $\mu_{\mathrm{C1Im}} = 4.16\,\mathrm{D}$, which quantitatively agrees with literature values calculated using a higher level of theory ($\mu_{\mathrm{C1Im}} = 4.17\,\mathrm{D}$ (HF/6-31G*), 4.19 D (HF/6-311G*) and 4.13 D (MP2/6-31G*)).[260] Experimental dipole moments of C_1Im are somewhat lower (3.6 D in benzene; 3.8 D in dioxan)[261] suggesting that μ_{C1Im} obtained from MOPAC is slightly overestimated. To correct for this difference, $\mu_{\mathrm{app,C1Im}}$ was calculated by scaling the experimental dipole moments with the cavity-field factor used by MOPAC,[174] yielding $\mu_{\mathrm{app,C1Im}}$=5.1 D. The apparent dipole moment of the C_1ImH^+ ($\mu_{\mathrm{app,C1ImH+}} = 2.23\,\mathrm{D}$) obtained by MOPAC is considerably smaller than $\mu_{\mathrm{app,C1Im}}$.[e]

It is observed that $\mu_{\mathrm{eff},1}$ of [C_1Im][HOAc] is constantly smaller (except at 25 °C) than $\mu_{\mathrm{app,C1Im}}$=5.1 D (Figure 3.17). Although antiparallel dipole-dipole correlations are possibly present in neat C_1Im,[f] correlations between C_1Im dipoles seem to be unlikely in an equimolar mixture, where C_1Im molecules are diluted by HOAc. Even if $\mu_{\mathrm{eff},1} < \mu_{\mathrm{app,C1Im}}$ was assumed to stem from correlations between C_1Im and HOAc, these could not explain $\mathrm{d}\mu_{\mathrm{eff},1}/\mathrm{d}T < 0$, as this would imply a preference of antiparallel alignment with increasing T.

Accordingly, the decrease of $\mu_{\mathrm{eff},1}$ can reasonably explained by a shift of the acid-base equi-

[e]Note that also this value might be slightly overestimated. However, due to the lack of experimental data in the literature, the value obtained from MOPAC was used.

[f]Evaluation of the low frequency amplitude of *neat* C_1Im, S_1, yielded an effective dipole moment of 4.65 D. It is smaller than $\mu_{\mathrm{app,C1Im}} = 5.1\,\mathrm{D}$ suggesting an antiparallel alignment of C_1Im dipoles with $g_{\mathrm{C1Im}} = 0.79$.

librium (Eq. 3.3) to the right, i.e. to an increasing fraction of C_1ImH^+ with increasing T. Thus, to a first approximation, the degree of proton transfer, α_{C1ImH+}, can be calculated from $\mu_{eff,1}$ via

$$\mu^2_{eff,1} = \alpha_{C1ImH+} g_{C1ImH+} \mu^2_{app,C1ImH+} + (1 - \alpha_{C1ImH+}) g_{C1Im} \mu^2_{app,C1Im} \tag{3.5}$$

assuming that the dipoles of C_1Im and C_1ImH^+ are uncorrelated, i.e. $g_{C1Im} = g_{C1ImH+} = 1$. The so derived values for $\alpha_{C1ImH+}(T)(= \alpha_{OAc-}(T))$ are plotted in Figure 3.18. It is observed that in the temperature range $5 \leq \vartheta/^\circ\,C \leq 35$ $\alpha_{C1ImH+} \lesssim 0.10$. This is significantly smaller than the value of $\alpha_{C1ImH+} = 0.43$ at 25 °C reported by Kanzaki *et al.*[78] but on the other hand also considerably exceeds that derived from Raman spectroscopy ($< 1\,\%$ at 25 °C).[79] Qualitatively speaking, the present results and those from literature imply that neutral species predominate in $[C_1Im][HOAc]$. This is consistent with the findings that the dynamics of $[C_1Im][HOAc]$ resemble those of conventional mixtures of organic solvents rather than those of ILs (Section 3.2.4.1). A quantification of the proton transfer in $[C_1Im][HOAc]$, however, provided no agreement with any of the literature values and thus implies that further experimental approaches are required elucidate this issue. Nevertheless, the increase of α_{C1ImH+} with increasing T suggests that the proton transfer between HOAc and C_1Im is stimulated with increasing T and suggests a successive increase of the IL-like character of $[C_1Im][HOAc]$.

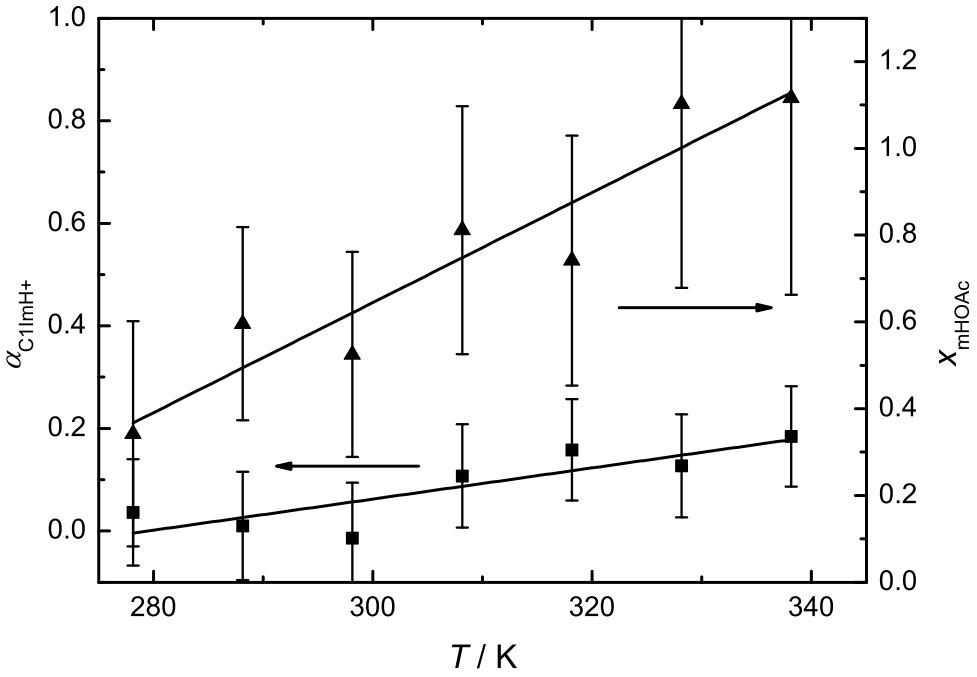

Figure 3.18: Degree of proton transfer, α_{C1ImH+} (■), in $[C_1Im][HOAc]$ calculated via Eq. 3.5. Fraction of acetic acid monomers, x_{mHOAc} (▲), estimated from Eq. 3.9. Solid lines are linear regressions.

Using the values of $\alpha_{\mathrm{C1ImH+}}(T)$ so obtained and Eq. 3.3 the corresponding equilibrium constant, $K_{\mathrm{a}}(T)$, of the proton transfer reaction can be calculated via

$$K_{\mathrm{a}}(T) = [(1 - \alpha_{\mathrm{C1ImH+}})c_0]^2 \tag{3.6}$$

with c_0 as the analytical concentration. This, in turn, allows the calculation of the $\mathrm{pK_a}(= -\log K_{\mathrm{a}}) = -1.77$ at 25 °C. Carrying on the analysis, enthalpy, ΔH, and entropy, ΔS, of the proton transfer reaction can be determined from the temperature dependence of $K_{\mathrm{a}}(T)$ using van't Hoff's relation (Figure 3.19). Thus, slope and intercept of the van't Hoff plot yields $\Delta H = (-6.3 \pm 1.4)\,\mathrm{kJ\,mol^{-1}}$ and $\Delta S = (11 \pm 5)\,\mathrm{J\,mol^{-1}\,K^{-1}}$, respectively, and the Gibbs energy change, ΔG, is obtained from $\Delta G = \Delta H - T\Delta S = -9.7\,\mathrm{kJ\,mol^{-1}}$ at 25 °C. This implies that the proton transfer reaction is an exothermic process and the present value ($\Delta H = (-6.3 \pm 1.4)\,\mathrm{kJ\,mol^{-1}}$) is virtually identical to the excess enthalpy of mixing of approximately $-6.5\,\mathrm{kJ\,mol^{-1}}$ reported for $[\mathrm{C_1Im}][\mathrm{HOAc}]$ at 25 °C by Kanzaki *et al.*[78] Moreover, this value is also comparable to the excess enthalpy of equimolar mixtures of triethylamine with propionic acid ($-13\,\mathrm{kJ\,mol^{-1}}$)[262] and chloroform ($-4.07\,\mathrm{kJ\,mol^{-1}}$),[263] which are also known to form 1:1 adducts.

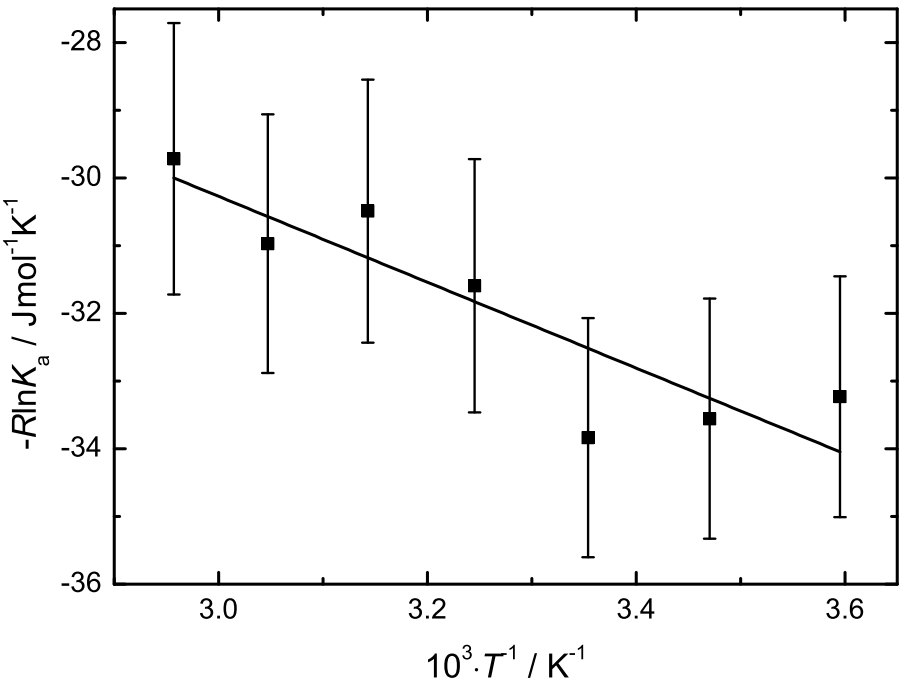

Figure 3.19: Van't Hoff plot ($-R \ln K_{\mathrm{a}}(T)$ vs. $1/T$) of $[\mathrm{C_1Im}][\mathrm{HOAc}]$. Solid lines represent linear regression.

For the $\mathrm{D_1}$ mode of $[\mathrm{C_1Im}][\mathrm{HOAc}]$ $\mu_{\mathrm{eff},2}$, obtained from S_2, increases with increasing T. The apparent dipole moment obtained by MOPAC[174] of a HOAc monomer, $\mu_{\mathrm{app,mHOAc}} = 2.40\,\mathrm{D}$

is considerably smaller than that of OAc^- $\mu_{app,mHOAc} = 5.30\,D$.[g] According to $d\mu_{eff,1}/dT < 0$ (see above), the increase of $\mu_{eff,2}$ with increasing T can be reasonably explained by a shift of the equilibrium (Eq. 3.3) from HOAc to OAc^-.
Thus, quantitative evaluation of $\mu_{eff,2}$ along the lines of Eq. 3.5 should yield the same values of $\alpha_{C1ImH+}(T)(= \alpha_{OAc-}(T))$ as obtained from $\mu_{eff,1}$ (Figure 3.18), provided that only monomers of HOAc and OAc^- are present in $[C_1Im][HOAc]$. However, this assumption seems unlikely to hold true, as the tendency of HOAc to form cyclic dimers (which are not detected by DRS, due to their zero dipole moment) is well known.[245] This becomes evident from Raman spectra of $[C_1Im][HOAc]$, where peaks specific for cyclic dimers have been observed.[79] Furthermore, evaluation of $\mu_{eff,2}$ of $[C_1ImH][DFA]$ and $[C_1ImH][TFA]$ suggested that also DFA^- and TFA^- seem to be strongly correlated ($g_{DFA-} = 0.15$ and $g_{TFA-} = 0.13$ at 65 °C). Assuming that g of acetate-based anions is independent of fluorination, g_{OAc-} of $[C_1Im][HOAc]$ can be approximated as their average, i.e. $g_{OAc-} \approx 1/2(g_{DFA-} + g_{TFA-}) = 0.14$ and $\mu_{eff,2}$ can be expressed as

$$\mu^2_{eff,2} = \alpha_{OAc-} g_{OAc-} \mu^2_{app,OAc-} + (1 - \alpha_{OAc-})\mu^2_{app,HOAc} \tag{3.7}$$

Assuming that HOAc is present as either monomers (mHOAc) or cyclic dimers (cdHOAc), $\mu_{app,HOAc}$ in Eq. 3.7 can be written as

$$\mu^2_{app,HOAc} = x_{mHOAc}\mu^2_{app,mHOAc} + (1 - x_{mHOAc})\mu^2_{app,cdHOAc} \tag{3.8}$$

with x_{mHOAc} as the molar fraction of HOAc monomers. As cdHOAc is centrosymmetric, $\mu_{app,cdHOAc} = 0$ and thus, insertion of Eq. 3.8 into 3.7 gives

$$\mu^2_{eff,2} = \alpha_{OAc-} g_{OAc-} \mu^2_{app,OAc-} + (1 - \alpha_{OAc-})x_{mHOAc}\mu^2_{app,mHOAc} \tag{3.9}$$

permitting the estimation of x_{mHOAc} in $[C_1Im][HOAc]$ (Figure 3.18).[h] It is observed that x_{mHOAc} increases with increasing T with $x_{mHOAc} \to 1$ at 65 °C, within the likely error; i.e. mHOAc is predominate at high T. This suggests that the increase of S_2 with increasing T is not only caused by the increase of α_{OAc-}, but also by the dissociation of non-polar cdHOAc into dipolar mHOAc. The latter has been also observed for HOAc in toluene, where the concentration of mHOAc increased at the expense of dimers with increasing T.[245]
This observation is further compatible with the increase of the Cole-Davidson parameter, β_1, with increasing T (Table 3.8). Because β_1 can be interpreted as a measure of homogeneity of the environment of the relaxing particle (here C_1Im/C_1ImH^+), the increase of β_1 indicates a randomization of $HOAc/OAc^-$.[58]

[g] As the gas phase dipole moment $\mu_{mHOAc} = 1.84\,D$ obtained from MOPAC[174] is in agreement with experimental values for HOAc in toluene (1.76 D at 298.15 K)[245], in benzene (1.50 D at 298.15 K and 1.68 D at 338.15 K)[264], in dioxane (1.76 D at 298.15 K)[264] and with values obtained from *ab initio* calculations (1.61 D[265], 1.79 D[266] and 1.89 D[267]), MOPAC-calculated values $\mu_{app,mHOAc}$ and $\mu_{app,OAc-}$ were used for the quantitative evaluation of $\mu_{eff,2}$.

[h] Note that g_{OAc-} represents the correlation factor of OAc^- at 65 °C. As it was also used for all lower T (where g_{OAc-} is supposed to be even smaller), the x_{mHOAc} so obtained should be considered as a lower limit.

As mentioned in Section 3.2.3 a detailed discussion of the second Debye mode (D_2), which was required to formally describe the dielectric spectra of all of the present mixtures, is not possible at present as D_2 is centered at the upper limit of our accessible frequency range. As already noted, this mode is almost certainly a composite. As observed for many other ILs, modes in this frequency region tend to incorporate intensities of the various processes taking place at THz frequencies such as "cage rattling" motions, intermolecular vibrations and librations.[36,213,268] Nevertheless, it is interesting to note that the amplitude S_3 of [C_1Im][HOAc] considerably increases with increasing T. The fact that - at 65 °C - S_3 of [C_1Im][HOAc] is still significantly smaller than S_3 of [C_1ImH][DFA], [C_1ImH][TFA] and [C_1ImH][TFSA] suggests that the increase of S_3 of [C_1Im][HOAc] possibly reflects the transition of [C_1Im][HOAc] from a conventional mixture of organic solvents to an IL. A more detailed investigation would require broadband dielectric spectra ranging up to tens of THz that capture the entire intensity associated with orientational polarization, as presented in Section 3.1, Chapter 4 and previous publications.[36,107]

3.2.5 Conclusions

In the present study, the equimolar mixture of C_1Im and HOAc was investigated by means of broadband dielectric spectroscopy in the frequency range of $0.2 \lesssim \nu/\mathrm{GHz} \lesssim 89$ and at temperatures between 5 and 65 °C. Spectra of [C_1Im][HOAc] were supplemented by those of neat C_1Im at 25 °C and [C_1ImH][DFA], [C_1ImH][TFA] and [C_1ImH][TFSA] at 65 °C. These measurements complement Raman spectroscopic studies on 1-methylimidazolium PILs of the Niigata group.[79,247]

The present results have shown that molecular-level reorientations of the above mixtures strongly depend on the degree of proton transfer. In [C_1ImH][DFA], [C_1ImH][TFA] and [C_1ImH][TFSA], where the proton transfer is essentially complete, the DR spectra were found to exhibit characteristic features of typical protic and aprotic ILs. Thus cation reorientation appears to occur via a jump mechanism[36,58,208] rather than by conventional rotational diffusion. The decrease of the rotational friction coefficient with increasing acidity of the parent acid can be interpreted as a measure of the extent of coulombic interactions arising from proton transfer to the parent imidazole.

In contrast, the relaxation mechanism of C_1Im in [C_1Im][HOAc] appears to be of diffusive nature, consistent with the rather incomplete proton transfer. This is suggested by the close correlation of viscosity and rotational motions (SED plots), and by the similarity of the activation energies of η and τ_1. As pointed out by Doi *et al.*[79], the decoupling of κ from η suggests that conductivity occurs through proton hopping rather than through ion migration. The results of the present study reveal a decoupling of κ from τ_1, which indicates that proton hopping in [C_1Im][HOAc] is not determined by the rotational motions of C_1Im/C_1ImH$^+$. Rather than that, the small activation energy associated with the reorientation of HOAc/OAc$^-$, $E_\mathrm{A}(\tau_2)$, could readily be the rate-determining step of proton conduction.

Quantitative analysis of the dielectric amplitudes of [C_1Im][HOAc] revealed that an increase of T promotes the proton transfer reaction implying a successive transition from a conventional mixture of organic solvents to a PIL. Moreover, it was inferred from the

increase of S_2 with increasing T that the amount of monomers of HOAc increases at the expense of cyclic dimers.
Many fundamental aspects of the dynamics and the dielectric properties of 1-methylimidazolium PILs have been learnt from the present study but further experiments are undoubtedly required to fully understand the dynamical behavior of these mixtures. Extension of the present dielectric spectra to THz frequencies and comparison with optical Kerr-effect or fs-IR spectroscopy would shed light on the underlying relaxation mechanisms in the present ILs.[36,107,208] Furthermore, molar ratios of [C_1Im][HOAc] different from the present equimolar mixture would be interesting to investigate by means of dielectric spectroscopy to elucidate the concentration dependence on ion relaxation and proton transfer reaction. In particular, further experimental effort is required for a reliable quantification of the protonation ratio in [C_1Im][HOAc]. In addition, high quality MD simulations are needed to obtain a more detailed picture of the molecular dynamics of 1-methylimidazolium PILs.

Chapter 4

Neat Aprotic Ionic Liquids

4.1 Introduction

The most intensively studied compounds among aprotic ILs (AILs) are those based on 1-alkyl-3-methylimidazolium cations. Whilst considerable experimental[30,38,51,57,269,270] and theoretical[43–45,271] efforts have been made to understand their structural and dynamical properties, neat AILs consisting of other cations such as pyridinium ($C_n pyr^+$), pyrrolidinium (P^+_{nm}) or trialkylsulfonium (TAS, S^+_{nmk}) were tended to be marginalized by hitherto IL research. On the other hand, non-imidazolium ILs based on amide anions such as dicyanamide (DCA^-), tricyanmethanide ($C(CN)^-_3$), bis(trifluoromethanesulfonyl)amide ($TFSA^-$) and its lower (bis(trifluorosulfonyl)amide; FSA^-) and higher (bis(pentafluoroethanesulfonyl)amide; $BETI^-$) analogs have attracted attention as potential electrolytes in lithium ion batteries,[272,273] fuel cells,[237,274] capacitors,[275] solar cells[276] and other electrochemical devices,[15,277,278] because of their relatively low viscosities, which, apart from their intrinsic conductivity, represents a key quantity of ILs for such applications.
Previous investigations include studies using NMR-relaxation,[61–63] optical heterodyne-detected Kerr-effect spectroscopy (OKE),[67–69] time-resolved fluorescence spectropscopy[70] Quasi-elastic neutron scattering (QENS)[71] and MD simulations.[72–74] Results of non-imidazolium ILs obtained from dielectric relaxation spectroscopy (DRS) were first reported by Weingärtner *et al.*,[54,55] although limitations in frequency range ($\nu \leq 20\,\mathrm{GHz}$) and measurements only at ambient conditions prevented detailed interpretations of the dynamical properties of the studied ILs.
Combination of broadband DRS and OKE spectroscopy has proven to be a powerful tool for gaining access to a fundamental understanding of molecular-level dynamics of ILs.[36,107] Particularly, the complementarity of the two techniques and the broad accessible frequency range ($0.2 \lesssim \nu/\mathrm{GHz} \lesssim 10\,000$) improves the accuracy of empirical decompositions of the experimental spectra and thus enables orientational dynamics of ILs to be scrutinized. Furthermore, investigation of the effect of temperature on dielectric and OKE response provides valuable information on activation energies of relaxation processes and their underlying species. Therefore, in the following chapter first temperature-dependent dielectric results supplemented by OKE spectroscopy of a set of four non-imidazolium model ILs are presented providing detailed insights into their complex dynamics.

4.2 Data acquisition and processing

The ILs investigated in this study were diethylmethylsulfonium- and triethylsulfonium bis(trifluoromethanesulfonyl)amide ([S_{221}][TFSA] and [S_{222}][TFSA], respectively), *N*-butyl-*N*-methylpyrrolidinium dicyanamide ([P_{14}][DCA]) and *N*-butylpyridinium bis(trifluoromethanesulfonyl)amide ([C_4pyr][TFSA]). Purification and sample handling are described in Section 2.1.

Dielectric relaxation spectroscopy (Section 2.2) was performed using an Agilent E8364B vector network analyzer (VNA) combined with two open-ended coaxial probes and a waveguide transmission cell operating in the frequency range $0.2 - 50\,\mathrm{GHz}$ (Section 2.2.2).[59] Additionally, the frequency range $60 \leq \nu/\mathrm{GHz} \leq 89$ was covered by an interferometer setup[139] (IFM; Section 2.2.1), except for [C_4pyr][TFSA] at 5, 15 and 25 °C due to its melting point of $\sim 26\,^{\circ}\mathrm{C}$.[279] Raw VNA data were corrected for calibration errors with a Padé approximation using DMA, BN and 1-BuOH as calibration standards (Eq. 2.17).[149] As open and short circuit standards air and purified mercury were used.
Data in the THz region (provided by the collaborators in Freiburg; Section 2.2.3) and FIR absorbance spectra (Section 2.2.4) were concatenated with the low-frequency data extending the dielectric spectra up to $\sim 10\,\mathrm{THz}$ as described in Section 2.2.4.
All dielectric experiments were carried out from 5 °C to 65 °C in 10 °C steps with a temperature stability of ±0.05 °C (VNA and IFM) and ±0.5 °C (THz-TDS and FIR).
To obtain the pure dielectric response, $\hat{\varepsilon}(\nu)$, dielectric spectra of conducting samples had to be corrected for conductivity contributions as described in Section 1.1.3. Therefore, κ, was treated as an additional adjustable parameter to yield the best description of the experimental data. Due to geometrical imperfections of the dielectric probe-heads, fitted conductivities may differ from the experimental values and were found to deviate for the present liquids by $\sim 2 - 12\,\%$.

Two OKE setups were used to cover the entire time range of the orientational and intermolecular dynamics of the present ILs as described in (Section 2.3). The two time-domain signals were concatenated, Fourier-transformed to the frequency domain, and deconvoluted from the instantaneous response.[107] For lower temperatures the sample was controlled to ±0.1 °C by a cryostat (Oxford Instruments, DN), whereas above room temperature a home-built copper heating block was used. All samples were measured in the temperature range $5 \leq \vartheta/^{\circ}\,\mathrm{C} \leq 65$.

Density measurements were performed using a tube vibrating densimeter (Anton Paar, Graz, Austria, DMA 5000 M). The accuracy of measured densities, ρ, was within $\pm 5 \cdot 10^{-6}\,\mathrm{g\,cm^{-3}}$ and temperature was controlled within ±0.01 °C (Section 2.5.1). Viscosities, η, were determined using an automated rolling ball microviscometer (Anton Paar, Graz, Austria, AMVn) with a reproducibility of $< 0.5\%$ in the range of 5 °C to 125 °C. The accuracy of the temperature was better than ±0.05 °C (Section 2.5.2). Electrical conductivities, κ, were measured using capillary cells with a relative uncertainty of ±0.5%. These

were connected to a LCR meter (Hameg, programmable LCR-Bridge HM8118) with an accuracy of 0.05% (Section 2.5.3). The temperature stability was typical ±0.01 °C.

4.3 Results

4.3.1 Densities, Viscosities and Conductivities

The values of ρ, η and κ of the present AILs are summarized in Tables A.3, A.5 and A.7.

[TAS][TFSA] ILs. At 25 °C the present density of $[S_{222}][TFSA]$ ($1.46014\,g\,cm^{-3}$) agrees with that of Matsumoto *et al.*[280] ($\rho = 1.46\,g\,cm^{-3}$) and is in modest agreement with the values reported by Weingärtner *et al.*[54] ($\rho = 1.465\,g\,cm^{-3}$) and Janus *et al.*[281] ($\rho = 1.468\,g\,cm^{-3}$). For $[S_{221}][TFSA]$ a value of $1.43\,g\,cm^{-3}$ was reported at 25 °C by Fang *et al.*[277] However, their value seems to be considerably underestimated, as ρ is known to decrease with increasing alkylation of the sulfonium cation.[277] Yang *et al.*[282] have reported a value of $1.59\,g\,cm^{-3}$ for $[S_{211}][TFSA]$, which is in line with the present values of $[S_{221}][TFSA]$ ($1.50071\,g\,cm^{-3}$) and $[S_{222}][TFSA]$ ($1.46014\,g\,cm^{-3}$) thus, supporting the reliability of the present measurements.
The viscosity of $[S_{222}][TFSA]$ ($\eta = 33.4\,mPa\,s$) at 25 °C is in agreement with the data reported in literature, which are 30 mPa s,[275,280,281] 33 mPa s[283] and 40 mPa s.[54] The same applies to $[S_{221}][TFSA]$, where the present values of $\eta = 40.7\,mPa\,s$ at 25 °C is compatible with that of Fang *et al.*[277] ($\eta = 36\,mPa\,s$).
Electrical conductivities of $[S_{222}][TFSA]$ at 25 °C reported in literature[275,280] ($\kappa = 0.71\,S\,m^{-1}$) are in acceptable agreement with that of the present work ($\kappa = 0.728\,S\,m^{-1}$). The value given by Weingärtner *et al.*[54], however, is significantly smaller ($\kappa = 0.512\,S\,m^{-1}$) but consistent with their high value of η, suggesting that impurities are responsible for these deviations. For $[S_{221}][TFSA]$ only Fang *et al.*[277] have reported a value of $\kappa = 0.58\,S\,m^{-1}$, which, however, is significantly smaller than the present $\kappa = 0.688\,S\,m^{-1}$ at 25 °C. This, however, is inconsistent with their smaller η, suggesting that shortcomings of their instruments account for this difference. The temperature dependence of η and κ of $[S_{221}][TFSA]$ and $[S_{222}][TFSA]$ are shown in logarithmic scale in Figures A.10 and A.11, respectively. Typical for transport properties of glass-forming liquids above their glass-transition temperature, η and κ of both salts follow the Vogel-Fulcher-Tammann (VFT) equation (Eq. 1.79). In accordance with the structural similarity of $[S_{221}][TFSA]$ and $[S_{222}][TFSA]$ all VFT parameters obtained from $\eta(T)$, respectively, $\kappa^{-1}(T)$ agree well between the two ILs (Table A.4). Moreover, the present B_{VFT} and T_0 of $[S_{222}][TFSA]$ obtained from $\kappa^{-1}(T)$ coincide with those reported by Okoturo *et al.*[283] ($B_{VFT} = 656\,K$; $T_0 = 159\,K$). In general, absolute values and/or temperature dependence of η and κ reported for $[S_{221}][TFSA]$[277] and $[S_{222}][TFSA]$[280,283] ILs differ from the present results (Figures A.10 and A.11), which can be almost certainly attributed to different levels of impurities of the samples but also demonstrates that for an accurate determination of VFT parameters coverage of a large temperature range is essential.

[C_4pyr][TFSA]. The present densities of [C_4pyr][TFSA] are in excellent agreement with those reported by Oliviera *et al.*[284] ($\sim 0.007\,\%$) and Tokuda *et al.*[279] ($\sim 0.03\,\%$). Likewise, the present values of η (61.4 mPa s at 25 °C) and κ (0.326 S m^{-1} at 25 °C) coincide with literature data (61.249 mPa s[284], 60 mPa s[279], 0.307 S m^{-1}[285], 0.33 S m^{-1}[279] at 25 °C). As becomes apparent from Figure A.12 the temperature dependence of η and κ (plotted as resistivity κ^{-1}) is best described by the VFT equation (Eq. 1.79) and the so derived parameters of the present transport properties agree well with those obtained from literature data (Table A.6). Moreover, the extrapolated value of $T_0 \approx 175$ K agrees with the finding that T_0 is typically ~ 30 K below the glass-transition temperature $T_g = 197.15$ K.[279]

[P_{14}][DCA]. The density of [P_{14}][DCA] at 25 °C of this work (1.01756 g cm^{-3}) is in moderate agreement ($\sim 0.4\,\%$) with those reported in the literature of 1.013 g cm^{-3}[286,287] and 1.01345 g cm^{-3}[288] but much less with that of MacFarlane *et al.*[289] of 0.95 g cm^{-3}. The present viscosity at 25 °C ($\eta = 41.8$ mPa s) lies within the literature values of 50 mPa s,[289] 36.5 mPa s[286] and 34 mPa s[287]. Differences of the present values of ρ and η to literature data may be attributed to different levels of impurities in the sample. To the authors knowledge no conductivity data of [P_{14}][DCA] have been published up to date. The temperature dependence of η and κ was best described by the VFT equation (Eq. 1.79), characteristic for glass-forming liquids (Figure A.13). It is observed that the so obtained VFT parameter of the present $\eta(T)$ agree well with those of $\kappa(T)$ and are broadly compatible with those derived from $\eta(T)$ of González *et al.*[287] (Table A.8). As observed for [C_4pyr][TFSA] T_0 is smaller than the glass-transition temperature, $T_g = 167 \pm 2$ K, determined by differential scanning calorimetry.[289]

4.3.2 Dielectric and Optical Kerr-Effect Spectroscopy

Dielectric and OKE spectra of the present AILs, measured over the frequency range $0.2 \leq \nu/\mathrm{GHz} \leq 10000$ from 5 to 65 °C, are shown in Figures 4.1, 4.2, 4.3, 4.4, 4.5 and 4.6. As observed for all PILs (Section 3.1)[107] and AILs[36,58] studied to date DR and OKE spectra of the present ILs are dominated by a large low-frequency peak at ~ 1 GHz, which is followed by a much weaker intensity at intermediate frequencies ($0.1 \lesssim \nu/\mathrm{THz} \lesssim 1$) that eventually ceases at ~ 5 THz marking the transition from inter- to intramolecular dynamics. In both DR and OKE spectra the peak maximum of the low-frequency peak, $\nu_{\max}$, shifts to higher frequencies with increasing temperature typical for relaxation processes,[86] whereas the high-frequency intensity ($\nu \gtrsim 100$ GHz) is essentially independent of temperature. Similar to imidazolium ILs but contrary to EAN and PAN, $\nu_{\max}^{\mathrm{OKE}} < \nu_{\max}^{\mathrm{DR}}$ at all temperatures for the studied AILs suggesting that relaxations in DRS are faster than in OKE spectroscopy which is in contrast to the predictions of the model of rotational diffusion (Section 1.3.4).

To obtain information of molecular dynamics from the present DR and OKE spectra a formal description of the experimental data is required using empirical model functions presented in Section 1.2. Relaxation processes, typically taking place at $\nu \lesssim 100$ GHz, are best regarded by Eq. 1.38 and its variants, whereas resonance processes contributing at $\nu \gtrsim 100$ GHz are commonly modelled by Eqs. 1.41 and 1.45.

Because of the same reasons mentioned in Sections 2.4 and 3.1.3.2 fitting DR and OKE spectra over such a wide frequency range is not trivial and is associated with several difficulties. In particular, the scatter of the present low-frequency DR spectra ($\nu \lesssim 100\,\mathrm{GHz}$) is considerably higher than that observed for the protic ionic liquids EAN and PAN (Section 3.1) but similar to that of imidazolium ILs.[36,58] This is a result of the lower dielectric loss at a comparable dc conductivity, which swamps $\varepsilon''(\nu)$ especially at low frequencies. The lower overall intensity also accounts for the considerable scatter in the THz-TDS spectra ($0.1 \lesssim \nu/\mathrm{THz} \lesssim 1$). The increased scatter in the OKE spectra particulary at $\nu \lesssim 100\,\mathrm{GHz}$ of [TAS][TFSA] compared to [C_4pyr][TFSA] and [P_{14}][DCA] can be attributed to the absence of highly anisotropic polarizable entities in the [TAS][TFSA] salts leading to a reduced overall OKE signal.

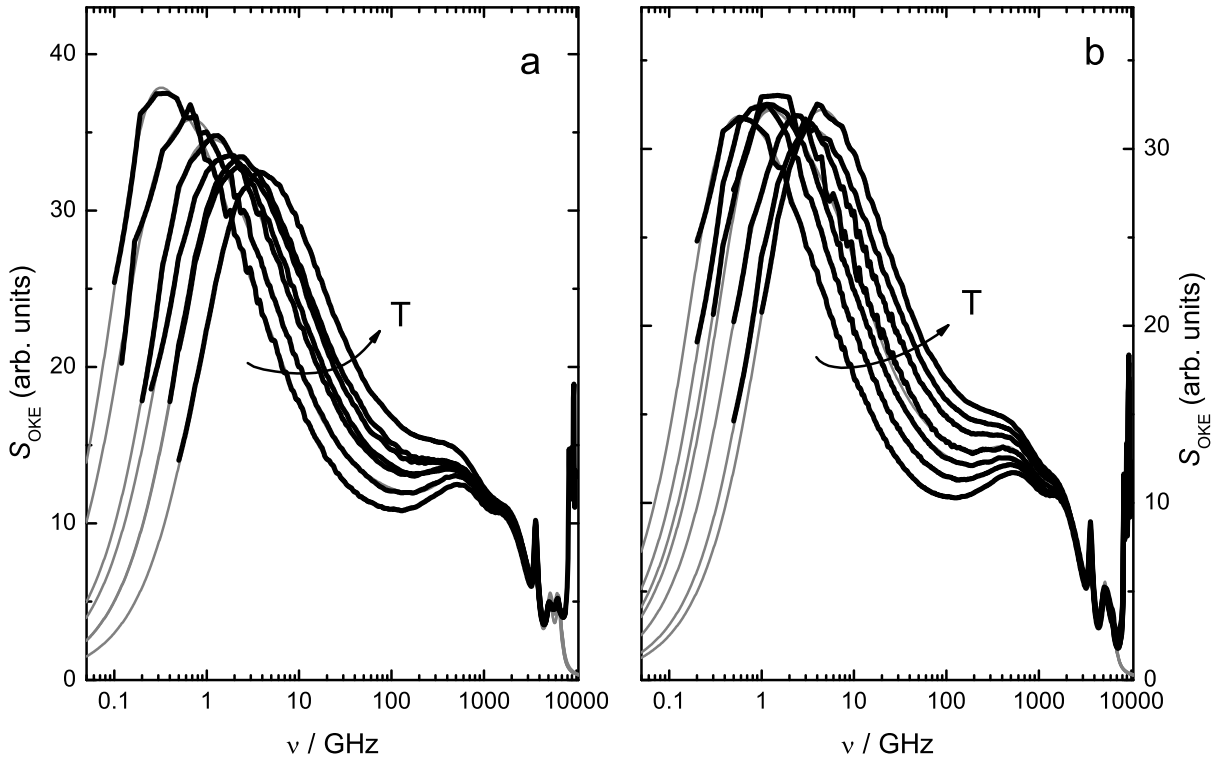

Figure 4.1: Optical Kerr-Effect spectra of (**a**) [S_{221}][TFSA] and (**b**) [S_{222}][TFSA] from 5 °C to 65 °C in 10 °C steps. Black dots are experimental data; gray lines represent the total fit.

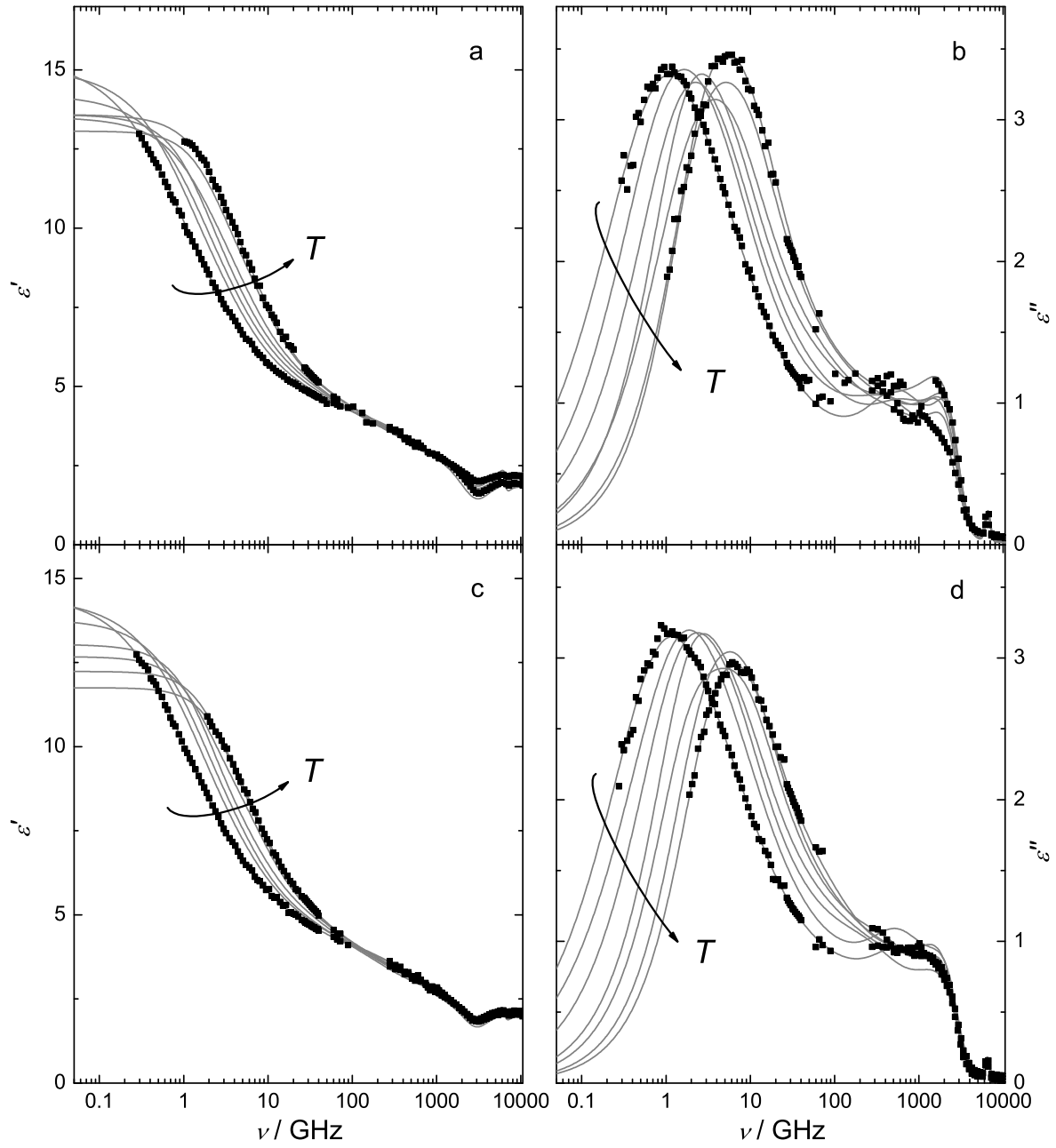

Figure 4.2: Permittivity, $\varepsilon'(\nu)$, and dielectric loss, $\varepsilon''(\nu)$, of (**a**) & (**b**) [S_{221}][TFSA] and (**c**) & (**d**) [S_{222}][TFSA], respectively, from 5 °C to 65 °C in 10 °C steps. For visual clarity only data at 5 and 65 °C are displayed. Black squares are experimental data; gray lines represent the overall fit.

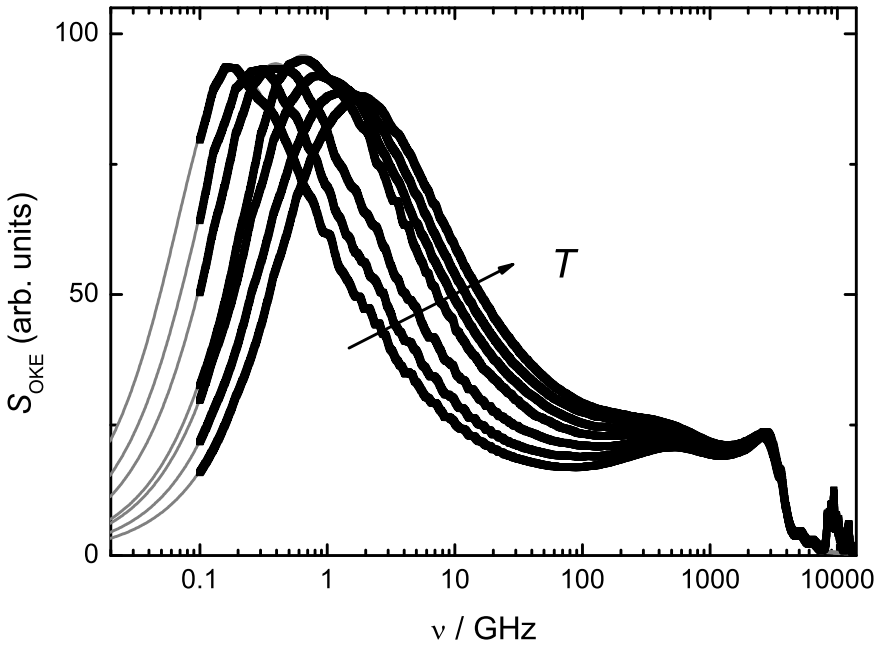

Figure 4.3: Optical Kerr-Effect spectra of [C_4pyr][TFSA] from 5 °C to 65 °C in 10 °C steps. Black dots are experimental data; gray lines represent the total fit.

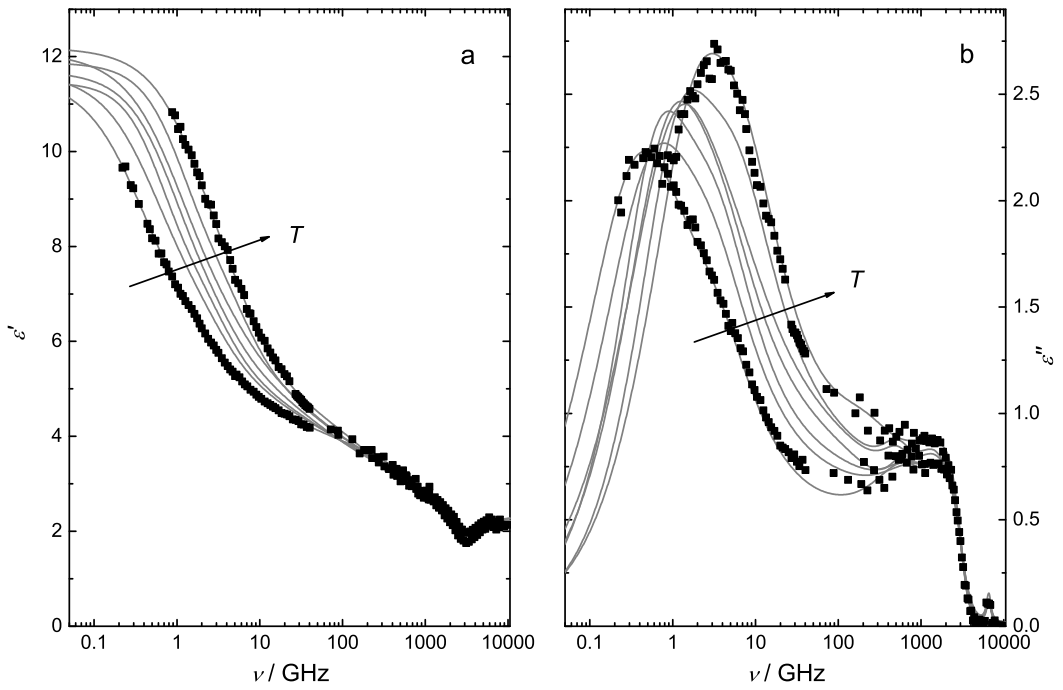

Figure 4.4: (**a**) Permittivity, $\varepsilon'(\nu)$, and (**b**) dielectric loss, $\varepsilon''(\nu)$, of [C_4pyr][TFSA] from 5 °C to 65 °C in 10 °C steps. For visual clarity only data at 5 and 65 °C are displayed. Black squares are experimental data; gray lines represent the overall fit.

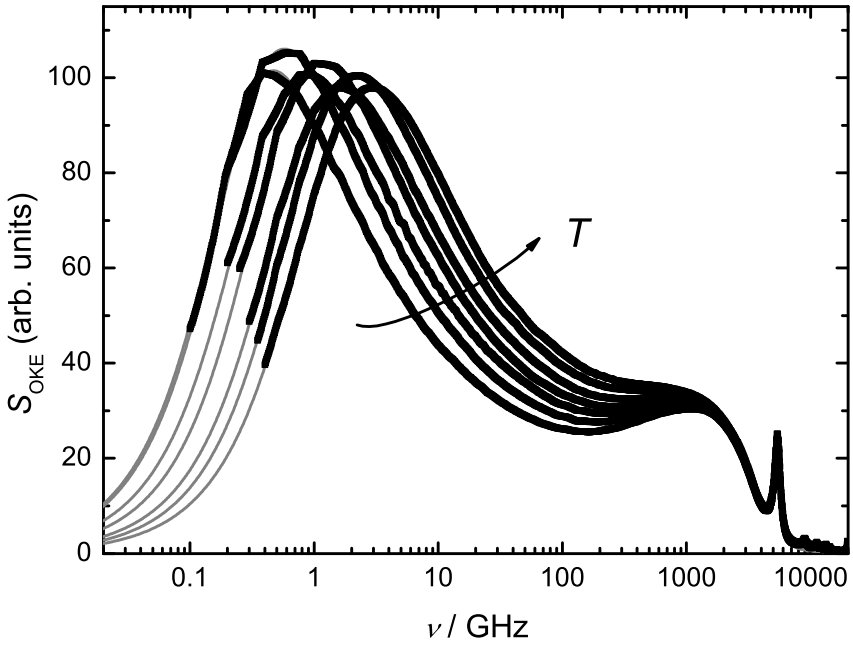

Figure 4.5: Optical Kerr-Effect spectra of $[P_{14}][DCA]$ from 5 °C to 65 °C in 10 °C steps. Black dots are experimental data; gray lines represent the total fit.

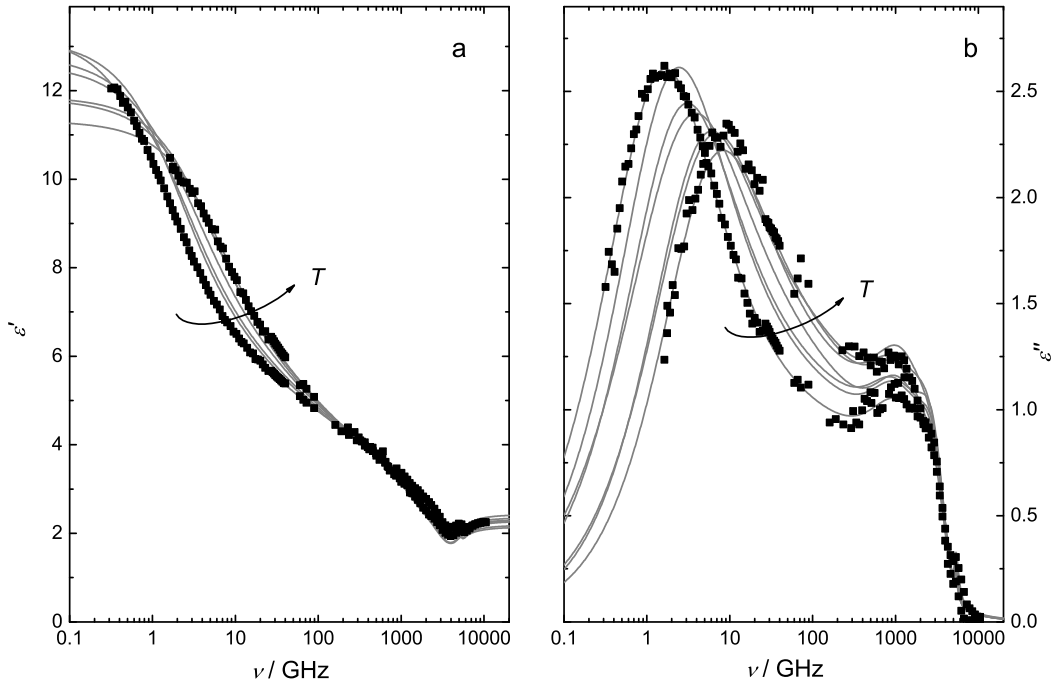

Figure 4.6: (**a**) Permittivity, $\varepsilon'(\nu)$, and (**b**) dielectric loss, $\varepsilon''(\nu)$, of $[P_{14}][DCA]$ from 5 °C to 65 °C in 10 °C steps. For visual clarity only data at 5 and 65 °C are displayed. Black squares are experimental data; gray lines represent the overall fit.

[TAS][TFSA] ILs. The fact that cations and anions of the present [TAS][TFSA] salts exhibit permanent dipole moments as well as polarizability anisotropies implies that all ionic species have to contribute to the DR *and* OKE signal and thus exacerbates the decomposition of the spectra. Due to the structural similarity of $[S_{221}][TFSA]$ and $[S_{222}][TFSA]$, the same relaxation model is expected to describe DR, respectively, OKE spectra of the present [TAS][TFSA] ILs. Along with the criteria of minimal χ^2_r, this provided a convenient strategy to eliminate numerous inappropriate models, due to insufficient fit quality and/or non-physical parameters (Section 2.4). Accordingly, the following fit model was established:
The pronounced temperature-dependent low-frequency relaxation process in the OKE spectra of both $[S_{221}][TFSA]$ and $[S_{222}][TFSA]$ was best described by a sum of three inertia-corrected Debye functions (Di_0, Di_1 and Di_2) centered at $\sim 0.5\,GHz$, $\sim 2\,GHz$ and $\sim 7\,GHz$, respectively, whereas in the DR spectra an inertia-corrected Cole-Cole equation (CCi; Eq. 1.37 with $\beta_{CCi} = 1$) at $\sim 1\,GHz$ and an inertia-corrected Debye function (Di_2; Eq. 1.37 with $\alpha_{Di} = 0$ and $\beta_{Di} = 1$) at $\sim 7\,GHz$ could be resolved. Inertial effects occurring at THz frequencies were regarded by fixing γ_{lib} at 1.5 THz for all relaxation modes (Di_0, Di_1, Di_2 and CCi) in DR and OKE spectra (Section 1.2.1). The presence of the Di_2 mode is typical for ILs consisting of dipolar anions (Section 3.2)[47] and thus can be reasonably associated with $TFSA^-$ reorientation. The CCi mode in the DR spectra is commonly referred to as α relaxation and known to be mainly related to cation relaxation.[36,48,58] In the OKE spectra the Di_1 mode essentially corresponds to the α mode. As observed for 1-alkyl-imidazolium ILs[36] an additional mode, Di_0, centered at lower frequencies than the α relaxation (sub-α mode) is resolved in the OKE spectra but not in the DR spectra of the present [TAS][TFSA] salts. This does not imply that such a mode is not present in the DR spectra but it seems likely that it is incorporated in the CCi mode, consistent with its symmetrically broadened shape.
The featureless intensity at intermediate frequencies in DR and OKE spectra was best modelled by a constant loss (CL) term. As discussed in Ref. 107 and Sections 1.2.1 and 3.1 such a contribution is generated by a CCm function (Eq. 1.38) in the limit of $\alpha_{CCm} \to 1$. At high frequencies its intensity is truncated at $\gamma_{lib} = 1.5\,THz$, whereas at low frequencies it is terminated by the relaxation time of the Di_2 mode, τ_2. Thus, it describes the featureless intensity of the present DR and OKE spectra between librational bands and relaxations. Note however, that such a CL contribution should not be considered as a relaxation process but rather as an auxiliary model function, which is almost certainly a composite.
At $\sim 500\,GHz$ ($\bar{\nu} \approx 17\,cm^{-1}$) a significant peak is clearly observed in the OKE spectra of both [TAS][TFSA] ILs. It was found to be best described by a damped harmonic oscillator, DHO_1, and can be assigned to $TFSA^-$-specific motions, which typically show up at $\sim 20\,cm^{-1}$.[68,290] The DHO_1 mode was also required to fit the DR spectra, although the scatter of the experimental data in this frequency range prevents the detection of a distinct peak.
At $\sim 2\,GHz$ the presence of a resonance process is evident in both DR and OKE spectra of the [TAS][TFSA] ILs and was best described by a Gaussian, G. As pointed out for EAN and PAN (Section 3.1) such a band-shape is particulary suited to describe the steep decay of the DR and OKE intensity at $\sim 3\,GHz$.[36,107]

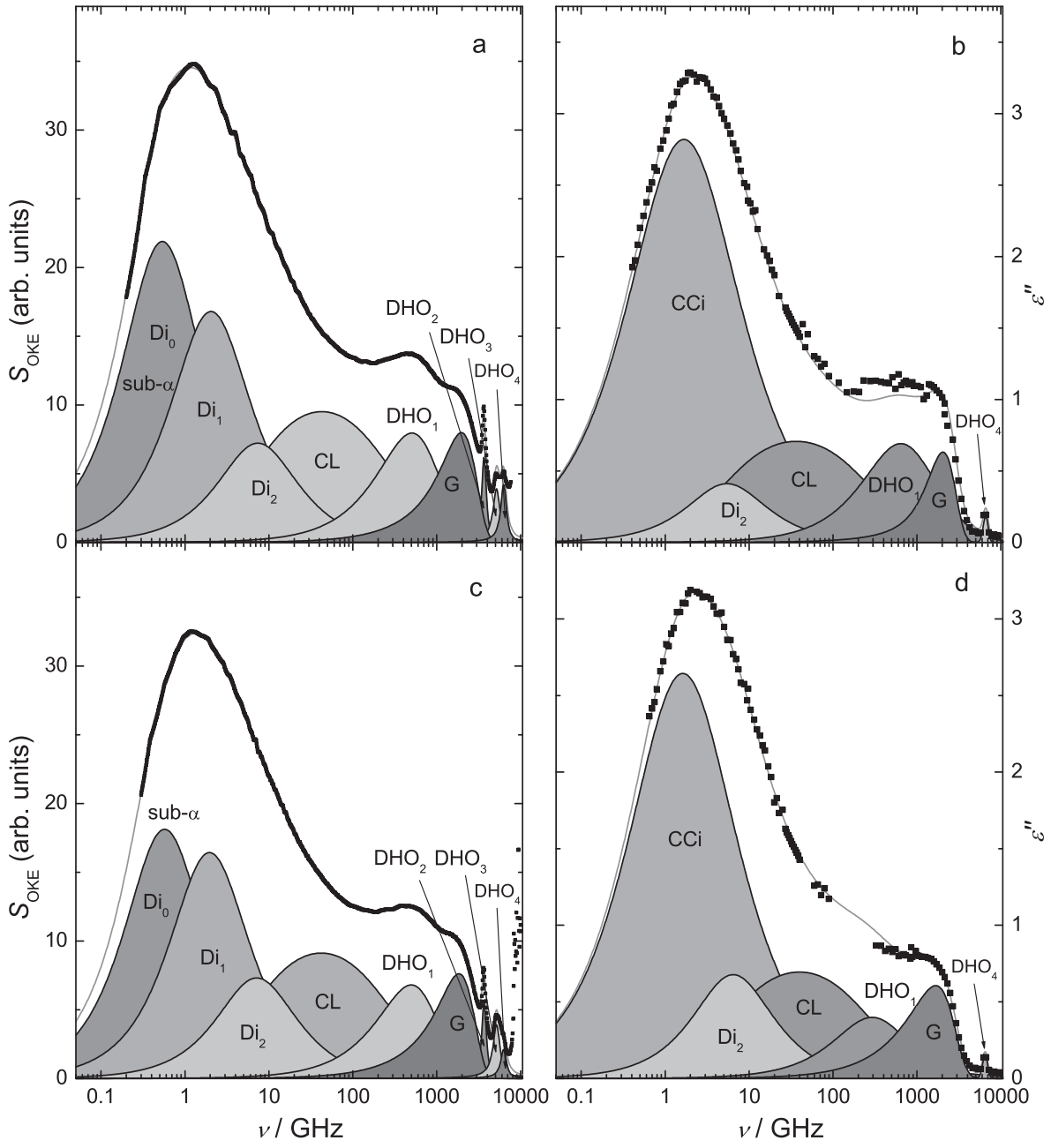

Figure 4.7: Imaginary parts of OKE and DR spectra of (**a**) & (**b**) $[S_{221}][TFSA]$ and of (**c**) & (**d**) $[S_{222}][TFSA]$ at 25 °C, respectively. Black squares are experimental data and gray lines represent the overall fit. Shaded areas indicate individual processes assuming a (Di_0 + Di_1 + Di_2 + CL + DHO_1 + G + DHO_2 + DHO_3 + DHO_4) model for the OKE spectra and a (CCi + Di_2 + CL + DHO_1 + G + DHO_4) model for the DR spectra (see text).

Table 4.1: OKE fit parameters of $[S_{221}][TFSA]$ and $[S_{222}][TFSA]$ as a function of temperature: relative amplitudes, $S_j^r = (S_j / \sum_j S_j) \cdot 10^2$, relaxation times, τ_j, resonance frequencies, $\nu_{0,j}$, damping constants, γ_j and reduced error function, χ_r^2.[a]

IL	T / K	S_0^r	τ_0	S_1^r	τ_1	S_2^r	τ_2	S_{CL}^r
$[S_{221}][TFSA]$	278.15	37.6	707	22.1	148	9.41	35.8	16.5
	288.15	26.8	637	25.8	168	12.6	39.9	20.4
	298.15	31.0	296	23.6	77.9	9.94	21.5	19.2
	308.15	24.2	282	26.3	82.8	12.1	23.0	21.2
	318.15	27.8	167	22.6	52.9	10.7	18.0	22.0
	328.15	28.5	164	23.0	50.0	9.93	16.5	22.3
	338.15	15.6	130	26.4	51.2	14.1	16.7	25.8
$[S_{222}][TFSA]$	278.15	35.5	440	23.1	102	8.85	25.2	16.4
	288.15	33.0	318	23.4	84.9	9.55	22.8	18.0
	298.15	27.9	278	25.2	81.1	11.0	22.2	20.2
	308.15	32.4	220[b]	16.4	70.0[b]	13.4	23.6	21.5
	318.15	21.8	201	27.3	58.7	11.6	16.9	22.9
	328.15	29.4	106	23.2	31.0	9.46	9.99	19.8
	338.15	24.6	91.0	23.6	32.1	11.1	11.3	22.6

IL	T / K	S_{DHO1}^r	γ_{DHO1}	$\nu_{0,DHO1}$	S_G^r	γ_G	$\nu_{0,G}$	$(S_{DHO2}^r)^b$	χ_r^2
$[S_{221}][TFSA]$	278.15	6.90	1.50	0.815	5.67	1.02	1.96	0.622	0.05449
	288.15	6.45	1.31	0.761	6.25	1.04	1.89	0.634	0.08482
	298.15	8.66	1.74	0.873	5.70	0.969	1.97	0.673	0.02397
	308.15	8.55	1.69	0.857	5.75	0.964	1.95	0.700	0.01451
	318.15	9.42	1.85	0.891	5.74	0.958	1.95	0.694	0.00583
	328.15	9.05	1.81	0.885	5.38	0.937	1.94	0.683	0.00769
	338.15	9.89	1.79	0.868	6.12	0.958	1.90	0.714	0.00809
$[S_{222}][TFSA]$	278.15	8.78	1.87	0.920	5.48	0.892	1.94	0.740	0.0289
	288.15	8.76	1.86	0.913	5.49	0.899	1.92	0.696	0.0149
	298.15	7.92	1.59	0.827	6.10	0.934	1.84	0.657	0.0144
	308.15	7.89	1.59	0.804	6.67	1.00	1.79	0.663	0.3141
	318.15	8.40	1.62	0.832	6.36	0.933	1.81	0.703	0.0227
	328.15	9.82	1.89	0.878	6.51	0.961	1.81	0.653	0.0113
	338.15	9.26	1.70	0.819	7.12	0.996	1.75	0.650	0.0107

[a] Units: τ_j in ps, $\nu_{0,j}$ in THz, γ_j in THz; [b] Parameter was fixed;

Table 4.2: DR fit parameters of [S_{221}][TFSA] and [S_{222}][TFSA] as a function of temperature: static permittivity, ε_s, resonance and relaxation amplitudes S_j, relaxation times, τ_j, Cole-Cole parameter α_1, resonance frequencies, $\nu_{0,j}$, damping constants, γ_j, high-frequency limit of ε', ε_∞ and reduced error function, χ^2_r.[a]

IL	T / K	ε_s	S_1	α_1	τ_1	S_2	τ_2	S_{CL}
[S_{221}][TFSA]	278.15	15.4	9.94	0.286	165	0.303	35.6	1.17
	288.15	15.0	9.19	0.254	117	0.596	27.9	1.38
	298.15	14.2	7.55	0.194	95.1	0.804	29.2	2.11
	308.15	13.6	5.80	0.076	85.0	1.50	25.0[b]	2.70
	318.15	13.5	5.76	0.157	73.2	1.49	24.4	2.65
	328.15	13.1	4.04	0.010	61.4	2.74	18.0[b]	2.56
	338.15	13.6	5.42	0.077	49.3	2.13	15.6	2.19
[S_{222}][TFSA]	278.15	14.6	8.77	0.252	158	0.516	30.1	1.53
	288.15	14.4	8.87	0.256	98.8	0.421	22.7	1.31
	298.15	13.8	6.80	0.168	98.0	1.32	24.6	2.02
	308.15	13.0	5.52	0.062	78.1	1.55	20.0[b]	2.43
	318.15	12.7	4.03	0.037	80.7	2.62	18.7	2.42
	328.15	12.2	3.44	0.000[b]	58.9	2.68	18.1	2.52
	338.15	11.7	3.09	0.000[b]	48.2	2.31	17.9	2.95

IL	T / K	S_{DHO1}	γ_{DHO1}	$\nu_{0,DHO1}$	S_G	γ_G	$\nu_{0,G}$	ε_∞	χ^2_r
[S_{221}][TFSA]	278.15	1.62	4.60	1.56	0.366	0.715	2.18	1.99	0.00244
	288.15	1.00	2.17	0.825	0.951	1.01	1.85	2.00	0.00183
	298.15	1.22	4.81	1.67	0.486	0.793	2.04	2.04	0.00364
	308.15	0.627	2.22	0.983	1.06	1.00	1.77	1.88	0.00221
	318.15	0.780	3.10	1.17	0.633	0.887	1.90	2.19	0.00364
	328.15	0.569	1.99	0.811	0.984	1.06	1.71	2.14	0.00639
	338.15	0.737	1.76	0.753	0.785	1.15	1.60	2.31	0.00356
[S_{222}][TFSA]	278.15	0.878	2.20	1.000	0.681	0.992	1.82	2.17	0.00144
	288.15	1.16	2.16	0.976	0.640	0.906	1.90	2.03	0.00134
	298.15	0.712	2.46	0.809	0.726	1.06	1.65	2.20	0.00129
	308.15	0.451	2.00[b]	0.750[b]	1.00	1.15	1.51	2.07	0.00245
	318.15	0.685	1.55	0.716	0.764	0.926	1.74	2.15	0.00377
	328.15	0.506	1.65	0.734	0.855	1.05	1.59	2.21	0.00183
	338.15	0.300	0.959	0.614	0.865	1.06	1.52	2.20	0.00124

[a] Units: τ_j in ps, $\nu_{0,j}$ in THz, γ_j in THz; [b] Parameter was fixed;

At frequencies $\nu \gtrsim 3\,\mathrm{THz}$ intramolecular vibrational motions specific for the $TFSA^-$ ion are observed.[67,291] In the OKE spectra three peaks are detected, which were described by three damped harmonic oscillators (DHO_2, DHO_3 & DHO_4). A comparison of OKE and DR spectra revealed that DHO_4 is both IR- and Raman-active, whereas DHO_2 and DHO_3 are only Raman-active as the two latter are not present in the DR spectra. Relative amplitudes, $S_j^{\mathrm{r}} = (S_j/\sum_j S_j) \cdot 10^2$, band widths and resonance frequencies, of the DHO_2 DHO_3 and DHO_4 mode were set arbitrarily to $\gamma_{\mathrm{DHO2}} = 0.56\,\mathrm{THz}$, $\nu_{0,\mathrm{DHO2}} = 3.76\,\mathrm{THz}$, $S^{\mathrm{r}}_{\mathrm{DHO3}} = 0.6$, $\gamma_{\mathrm{DHO3}} = 1.2\,\mathrm{THz}$, $\nu_{0,\mathrm{DHO3}} = 5.14\,\mathrm{THz}$ and $S^{\mathrm{r}}_{\mathrm{DHO4}} = 0.4$, $\gamma_{\mathrm{DHO4}} = 1.0\,\mathrm{THz}$, $\nu_{0,\mathrm{DHO4}} = 6.5\,\mathrm{THz}$ in the OKE fit and $S_{\mathrm{DHO4}} = 0.025$, $\gamma_{\mathrm{DHO4}} = 1.0\,\mathrm{THz}$, $\nu_{0,\mathrm{DHO4}} = 6.5\,\mathrm{THz}$ in the DR fit.
Representative fits are shown in Figure 4.7 with individual processes of the DR and OKE spectra of $[S_{221}][TFSA]$ and $[S_{222}][TFSA]$ at 25 °C. Similar fits were obtained at all other temperatures and the parameters so derived are summarized in Tables 4.1 and 4.2.

$[C_4pyr][TFSA]$. The α-relaxation peak of DR and OKE spectra of $[C_4pyr][TFSA]$ was best described by the same relaxation models, used for the present [TAS][TFSA] ILs (see above): For the OKE spectra of $[C_4pyr][TFSA]$ three inertia-corrected Debye functions (Di_0, Di_1 and Di_2) centered at $\sim 0.2\,\mathrm{GHz}$, $\sim 1\,\mathrm{GHz}$ and $\sim 4\,\mathrm{GHz}$, respectively, were used (Figure 4.8a), whereas an inertia-corrected Cole-Cole equation (CCi; Eq. 1.37 with $\beta_{\mathrm{CCi}} = 1$) at $\sim 1\,\mathrm{GHz}$ and an inertia-corrected Debye function (Di_2; Eq. 1.37 with $\alpha_{\mathrm{Di}} = 0$ and $\beta_{\mathrm{Di}} = 1$) at $\sim 4\,\mathrm{GHz}$ could be resolved in the DR spectra (Figure 4.8b). Each process (Di_0, Di_1, Di_2 and CCi) was corrected for inertial effects (Eq. 1.37) occurring at THz frequencies by $\gamma_{\mathrm{lib}} = 2.0\,\mathrm{THz}$ (Section 1.2). The band assignment is similar to that of the [TAS][TFSA] indicating that the Di_1/CCi and Di_2 modes are mainly associated with cation and anion reorientation, respectively, whereas the Di_0 mode represents the sub-α process.
As for the [TAS][TFSA] ILs the featureless intermediate frequency range ($0.1 \lesssim \nu/\mathrm{THz} \lesssim 1$) was best regarded by a constant loss (CL) contribution, which is terminated by $\gamma_{\mathrm{lib}} = 2.0\,\mathrm{THz}$ and τ_2.
The peak at $\sim 500\,\mathrm{GHz}$, which is evident in the OKE spectra and specific for $TFSA^-$, was modelled by a DHO_1 mode in DR and OKE spectra.
In contrast to the present [TAS][TFSA] ILs, *two* Gaussian modes, G_1 and G_2, were required to describe OKE and DR spectra of $[C_4pyr][TFSA]$ in the frequency range $1.0 \lesssim \nu/\mathrm{THz} \lesssim 4$. Whilst G_1 and G_2 are of similar magnitude in the OKE spectra, the G_1 mode is dominating over the rather weak G_2 mode in the DR spectra. In the OKE spectra (Figure 4.8a) an intramolecular mode of $TFSA^-$ (DHO_2; at 3.67 THz), which is only Raman- but not IR-active overlaps with G_1 and G_2 and is responsible for the small shoulder at $\sim 4\,\mathrm{THz}$ in the OKE spectra. At $\nu \gtrsim 4\,\mathrm{THz}$ further intramolecular processes, DHO_3 and DHO_4, specific for $TFSA^-$ are present consistent with the spectra of the [TAS][TFSA] ILs (Figure 4.7), where DHO_3 is only Raman-active and DHO_4 is detected in both OKE and DR spectra. Relative amplitudes, $S_j^{\mathrm{r}} = (S_j/\sum_j S_j) \cdot 10^2$, band widths and resonance frequencies, of the DHO_2, DHO_3 and DHO_4 modes were set arbitrarily to $\gamma_{\mathrm{DHO2}} = 0.26\,\mathrm{THz}$, $\nu_{0,\mathrm{DHO2}} = 3.76\,\mathrm{THz}$, $S^{\mathrm{r}}_{\mathrm{DHO3}} = 0.2$, $\gamma_{\mathrm{DHO3}} = 1.0\,\mathrm{THz}$, $\nu_{0,\mathrm{DHO3}} = 5.14\,\mathrm{THz}$ and $S^{\mathrm{r}}_{\mathrm{DHO4}} = 0.1$, $\gamma_{\mathrm{DHO4}} = 1.0\,\mathrm{THz}$, $\nu_{0,\mathrm{DHO4}} = 6.6\,\mathrm{THz}$ in the OKE fit and $S_{\mathrm{DHO4}} = 0.015$, $\gamma_{\mathrm{DHO4}} = 1.0\,\mathrm{THz}$,

$\nu_{0,\mathrm{DHO4}} = 6.6\,\mathrm{THz}$ in the DR fit.
Figure 4.8 shows a representative fit at 25 °C using the (Di_0 + Di_1 + Di_2 + CL + DHO_1 + G_1 + G_2 + DHO_2 + DHO_3 + DHO_4) model for OKE and the (CCi + Di_2 + CL + DHO_1 + G_1 + G_2 + DHO_4) model for DR spectra of [C_4pyr][TFSA]. Similar fits were obtained at all other temperatures and the parameters so derived are summarized in Tables 4.3 and 4.4.

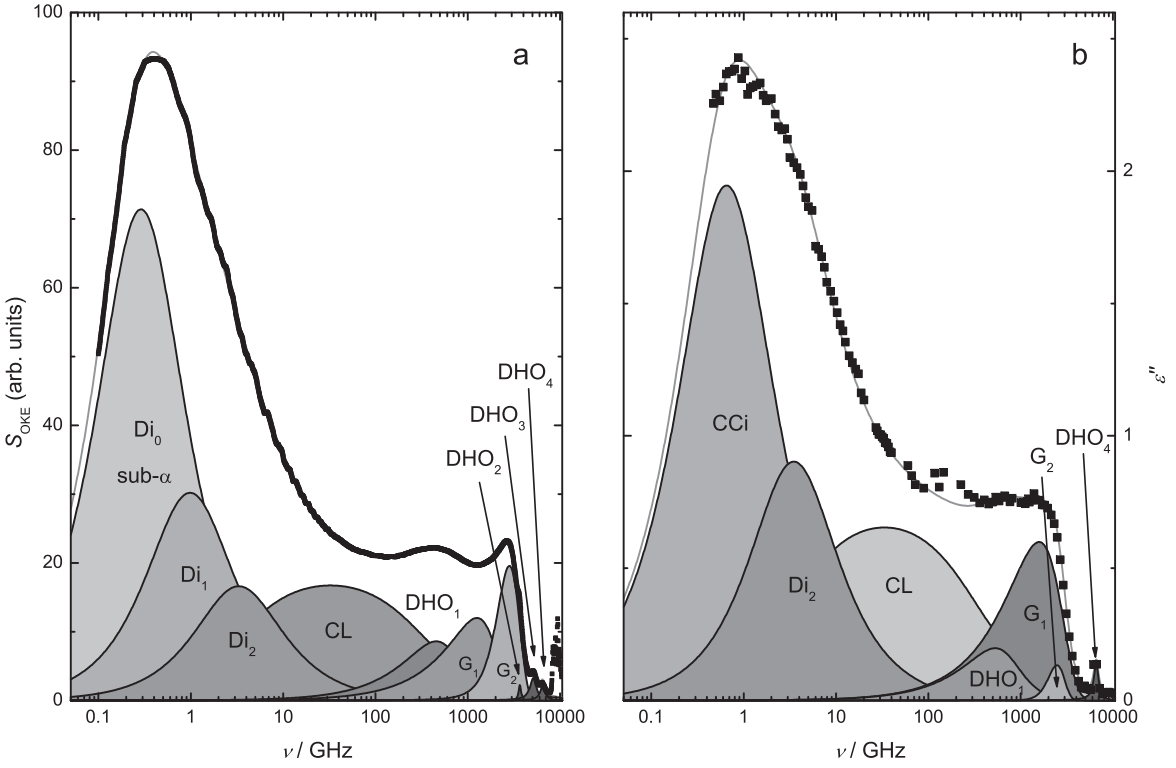

Figure 4.8: Imaginary parts of (**a**) OKE and (**b**) dielectric spectra of [C_4pyr][TFSA] at 25 °C. Black squares are experimental data and gray lines represent the overall fit. Shaded areas indicate the contributions of the individual processes of the (Di_0 + Di_1 + Di_2 + CL + DHO_1 + G_1 + G_2 + DHO_2 + DHO_3 + DHO_4) model for the OKE spectra and the (CCi + Di_2 + CL + DHO_1 + G_1 + G_2 + DHO_4) model for the DR spectra.

Table 4.3: OKE fit parameters of [C_4pyr][TFSA] as a function of temperature: relative relaxation and resonance amplitudes, $S_j^{\mathrm{r}} = (S_j / \sum_j S_j) \cdot 10^2$, relaxation times, τ_j, resonance frequencies, $\nu_{0,j}$, damping constants, γ_j, and reduced error function, χ_{r}^2.[a]

T / K	S_0^{r}	τ_0	S_1^{r}	τ_1	S_2^{r}	τ_2	$S_{\mathrm{CL}}^{\mathrm{r}}$	$S_{\mathrm{DHO1}}^{\mathrm{r}}$	γ_{DHO1}	$\nu_{0,\mathrm{DHO1}}$
278.15	47.2	1063	18.9	258	8.27	58.4	13.9	4.27	1.24	0.715
288.15	44.6	760	18.5	226	9.65	57.9	15.9	4.13	1.23	0.707
298.15	43.5	551	18.3	162	10.0	48.1	17.0	3.60	1.08	0.661
308.15	45.9	325	23.8	69.3	5.44	16.8	13.2	4.98	1.69	0.826
318.15	35.3	339	27.8	91.0	9.05	23.6	16.6	5.51	1.57	0.827
328.15	30.3	275	29.4	81.2	10.1	22.7	18.6	4.25	1.24	0.702
338.15	29.5	208	29.7	63.1	10.3	17.9	18.5	4.60	1.33	0.719

T / K	$S_{\mathrm{G1}}^{\mathrm{r}}$	γ_{G1}	$\nu_{0,\mathrm{G1}}$	$S_{\mathrm{G2}}^{\mathrm{r}}$	γ_{G2}	$\nu_{0,\mathrm{G2}}$	$S_{\mathrm{DHO2}}^{\mathrm{r}}$	χ_{r}^2
278.15	4.40	0.799	1.39	2.69	0.742	2.90	0.0543	0.258
288.15	4.20	0.778	1.34	2.76	0.758	2.87	0.0498	0.125
298.15	4.26	0.756	1.25	2.91	0.778	2.82	0.0506	0.191
308.15	4.30	0.913	1.56	2.06	0.732	2.94	0.0515	0.234
318.15	2.31	0.605	1.34	3.20	0.814	2.74	0.0433	0.058
328.15	3.68	0.690	1.20	3.33	0.822	2.73	0.0457	0.036
338.15	3.61	0.697	1.19	3.44	0.837	2.71	0.0429	0.048

[a] Units: τ_j in ps, $\nu_{0,j}$ in THz, γ_j in THz;

Table 4.4: DR fit parameters of [C_4pyr][TFSA] as a function of temperature: static permittivity, ε_s, relaxation and resonance amplitudes S_j, relaxation times, τ_j, Cole-Cole parameter α_1, resonance frequencies, $\nu_{0,j}$, damping constants, γ_j, high frequency limit of ε', ε_∞, and reduced error function, χ^2_r.[a]

T / K	ε_s	S_1	α_1	τ_1	S_2	τ_2	S_{CL}	S_{DHO1}	γ_{DHO1}	$\nu_{0,DHO1}$
278.15	11.6	5.74	0.207	409	0.961	47.7	1.36	0.426	1.28	0.725
288.15	11.7	5.24	0.183	284	1.14	49.0	1.89	0.330	1.67	0.859
298.15	11.5	4.17	0.0457	244	1.79	45.6	2.17	0.266	1.20	0.752
308.15	11.7	5.03	0.129	174	1.02	40.3	2.42	0.149	0.573	0.624
318.15	12.1	5.97	0.195	142	0.568	28.7	2.23	0.188	0.630	0.559
328.15	11.9	4.46	0.0752	136	1.89	25.1	2.18	0.214	0.640	0.563
338.15	12.2	5.43	0.153	83.3	1.42	20.2	1.69	0.493	1.53	0.577

T / K	S_{G1}	γ_{G1}	$\nu_{0,G1}$	S_{G2}	γ_{G2}	$\nu_{0,G2}$	ε_∞	χ^2_r
278.15	0.768	1.10	1.56	0.054	0.551	2.57	2.31	0.00194
288.15	0.699	1.17	1.25	0.092	0.585	2.49	2.29	0.00126
298.15	0.762	1.20	1.46	0.045	0.500	2.47	2.25	0.00104
308.15	0.750	1.00	1.47	0.066	0.556	2.60	2.26	0.00154
318.15	0.851	1.15	1.35	0.039	0.488	2.59	2.25	0.00277
328.15	0.898	1.27	1.27	0.008	0.290	2.63	2.21	0.00098
338.15	0.716	0.946	0.751	0.282	0.720	2.31	2.15	0.00416

[a] Units: τ_j in ps, $\nu_{0,j}$ in THz, γ_j in THz;

[P_{14}][DCA]. For [P_{14}][DCA] the low-frequency peak of the OKE spectra was best described by two inertia-corrected relaxation functions (Eq. 1.37; CDi mode and Di mode; Figure 4.9a), whereas only one process (CCi mode) could be resolved in the DR spectra consistent with the DR spectra of [P_{12}][DCA], which can be mainly associated with the reorientation of cations.[46,58] Inertial effects of the present relaxation processes were taken into account by $\gamma_{\mathrm{lib}} = 2.5\,\mathrm{THz}$.
As for all other present AILs the featureless intensity at intermediate frequencies ($0.1 \lesssim \nu/\mathrm{THz} \lesssim 1$) was best described by a constant loss (CL) contribution (Eq. 1.38 with $\alpha_{\mathrm{CCm}} \to 1$) terminated by $\gamma_{\mathrm{lib}} = 2.5\,\mathrm{THz}$ at high frequencies and by τ_1 at low frequencies.

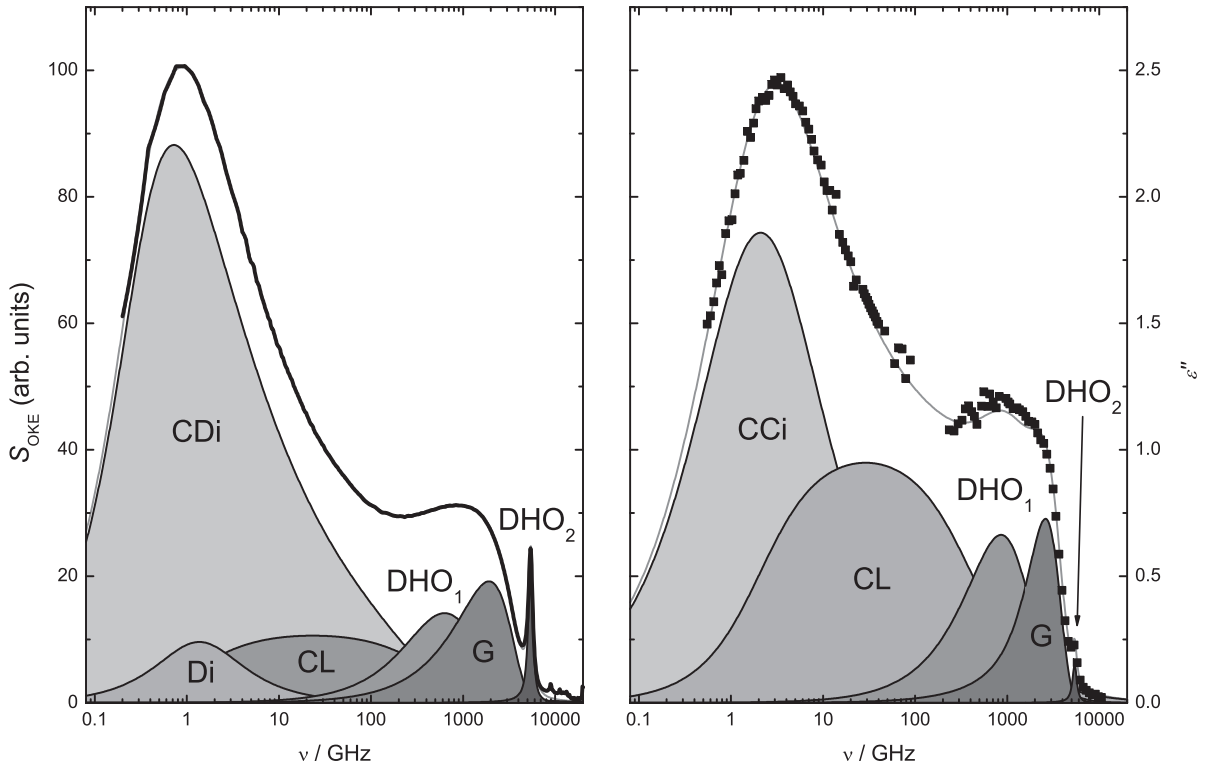

Figure 4.9: Imaginary parts of (**a**) OKE and (**b**) dielectric spectra of [P_{14}][DCA] at 25 °C. Black squares are experimental data and gray lines represent the overall fit. Shaded areas indicate the contributions of the individual processes assuming a (CDi + Di + CL + DHO_1 + G + DHO_2) model for the OKE spectra and a (CCi + CL + DHO_1 + G + DHO_2) model for the DR spectra.

At $\nu \gtrsim 1\,\mathrm{THz}$ the intensity of DR and OKE spectra of [P_{14}][DCA] could be modelled by the same number and type of resonance functions consisting of a sum of a damped harmonic oscillator, DHO_1, at $\sim 0.8\,\mathrm{THz}$, a Gaussian, G, at $\sim 2.0\,\mathrm{THz}$ and a DHO_2 at 5.4 THz. Whilst the DHO_1 and G mode are of intermolecular nature characterized by their broad shape, the narrow DHO_2 mode is assigned to intramolecular bending of DCA^-.[68,248,292] Figure 4.9 shows a representative fit of the OKE and DR spectra of [P_{14}][DCA] at 25 °C using the (CDi + Di + CL + DHO_1 + G + DHO_2) model for the OKE spectra and a (CCi

+ CL + DHO_1 + G + DHO_2) model for the DR spectra. Similar fits were obtained at all other temperatures and the parameters so derived are summarized in Tables 4.5 and 4.6.

Table 4.5: OKE fit parameters of $[P_{14}][DCA]$ as a function of temperature: relative relaxation and resonance amplitudes, $S_j^r = (S_j / \sum_j S_j) \cdot 10^2$, relaxation times, τ_j, Cole-Davidson parameter β_1, resonance frequencies, $\nu_{0,j}$, damping constants, γ_j, and reduced error function, χ_r^2.[a]

T / K	S_0^r	β_0	τ_0	S_1^r	τ_1	S_{CL}^r	S_{DHO1}^r	γ_{DHO1}	$\nu_{0,DHO1}$
278.15	67.0	0.591	549	3.83	58.3	16.2	7.00	3.78	1.62
288.15	71.8	0.469	562	2.43	112	12.8	6.02	3.65	1.45
298.15	70.5	0.399	457	5.06	116	10.9	6.31	3.45	1.38
308.15	69.9	0.416	333	5.39	83.1	11.0	6.08	2.97	1.25
318.15	67.7	0.406	244	5.97	64.4	11.9	6.36	2.89	1.24
328.15	61.9	0.464	181	7.89	45.2	16.2	6.23	2.98	1.27
338.15	59.3	0.443	147	9.65	37.6	16.6	6.54	2.96	1.26

T / K	S_G^r	γ_G	$\nu_{0,G}$	$(S_{DHO2}^r)^b$	$(\gamma_{DHO2})^b$	$(\nu_{0,DHO2})^b$	χ_r^2
278.15	5.17	1.25	2.09	0.791	0.70	5.4	0.306
288.15	6.12	1.43	1.82	0.743	0.70	5.4	0.215
298.15	6.47	1.47	1.75	0.769	0.70	5.4	0.0924
308.15	6.85	1.50	1.67	0.766	0.70	5.4	0.101
318.15	7.19	1.54	1.60	0.801	0.70	5.4	0.0403
328.15	7.00	1.57	1.51	0.792	0.70	5.4	0.0278
338.15	7.13	1.59	1.47	0.814	0.70	5.4	0.0368

[a] Units: τ_j in ps, $\nu_{0,j}$ in THz, γ_j in THz; [b] Parameter was fixed;

Table 4.6: DR fit parameters of [P_{14}][DCA] as a function of temperature: static permittivity, ε_s, relaxation and resonance amplitudes S_j, relaxation times, τ_1, Cole-Cole parameter α_1, resonance frequencies, $\nu_{0,j}$, damping constants, γ_j, high frequency limit of ε', ε_∞, and reduced error function, χ^2_r.[a]

T / K	ε_s	S_1	α_1	τ_1	S_{CL}	S_{DHO1}	γ_{DHO1}	$\nu_{0,DHO1}$
278.15	13.3	6.04	0.227	128	3.28	1.13	3.80	1.80
288.15	13.2	5.78	0.224	91.9	3.52	1.06	3.00[b]	1.55[b]
298.15	12.6	5.22	0.222	75.7	3.49	1.10	3.15	1.57
308.15	12.9	5.47	0.280	66.8	3.49	1.04	2.62	1.48
318.15	11.8	4.87	0.242	36.2	3.02	1.09	3.17	1.52
328.15	11.9	4.24	0.201	43.7	3.83	1.08	2.79	1.54
338.15	11.3	4.12	0.203	31.1	3.32	0.944	2.78	1.46

T / K	S_G	γ_G	$\nu_{0,G}$	$(S_{DHO2})^b$	$(\gamma_{DHO2})^b$	$(\nu_{0,DHO2})^b$	ε_∞	χ^2_r
278.15	0.364	1.03	2.77	0.0287	0.70	5.4	2.42	0.00147
288.15	0.487	1.06	2.63	0.0284	0.70	5.4	2.29	0.00260
298.15	0.517	1.04	2.67	0.0192	0.70	5.4	2.26	0.00187
308.15	0.491	1.03	2.69	0.0165	0.70	5.4	2.35	0.00240
318.15	0.665	1.17	2.48	0.0128	0.70	5.4	2.18	0.00420
328.15	0.571	1.16	2.54	0.0115	0.70	5.4	2.14	0.00279
338.15	0.626	1.27	2.39	0.00955	0.70	5.4	2.30	0.00412

[a] Units: τ_j in ps, $\nu_{0,j}$ in THz, γ_j in THz; [b] Parameter was fixed;

4.4 Discussion

4.4.1 Static permittivities

From dielectric spectra ε_s is obtained via extrapolation of the relative permittivity, $\varepsilon'(\nu)$, in the limit of $\nu \to 0$. In Figure 4.10 ε_s of $[S_{221}][TFSA]$, $[S_{222}][TFSA]$, $[C_4pyr][TFSA]$ and $[P_{14}][DCA]$ is plotted as a function of temperature. The absolute values of ε_s of $[S_{221}][TFSA]$, $[S_{222}][TFSA]$, $[C_4pyr][TFSA]$ and $[P_{14}][DCA]$ and the temperature coefficient of $[S_{221}][TFSA]$, $[S_{222}][TFSA]$, and $[P_{14}][DCA]$ ($d\varepsilon_s/dT$=–0.05 K^{-1}, –0.05 K^{-1} and –0.033 K^{-1}, respectively) are of similar magnitude as those of common 1-alkyl-3-methylimidazolium ILs (e.g. $\varepsilon_s([C_4mim][BF_4])$=14.6 at 25 °C with $d\varepsilon_s/dT$=–0.041 K^{-1})[58] but significantly smaller than those of protic ILs like EAN and PAN (Section 3.1).[55]

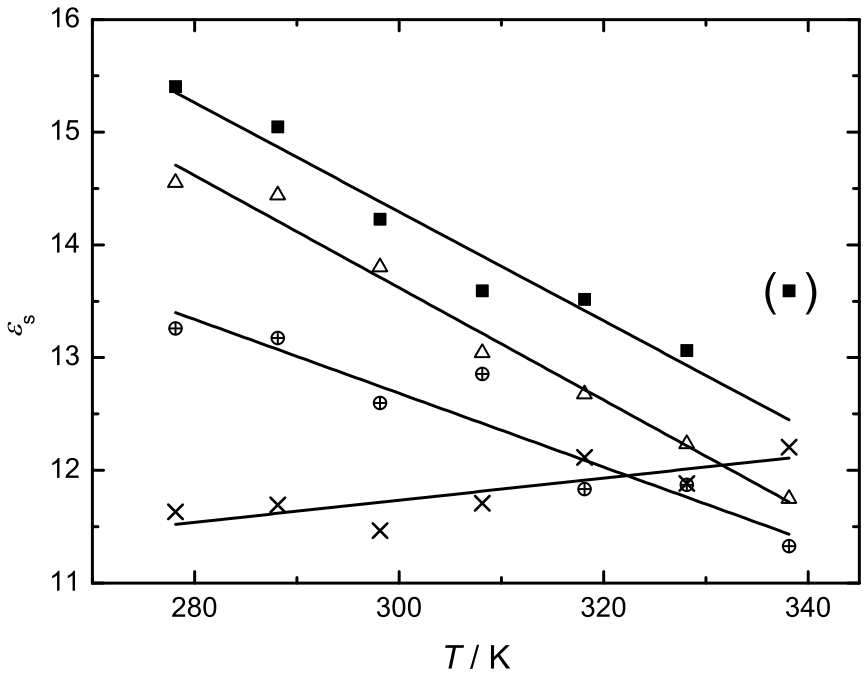

Figure 4.10: Static permittivity, ε_s, of $[S_{221}][TFSA]$ (■), $[S_{222}][TFSA]$ (△), $[C_4pyr][TFSA]$ (×) and $[P_{14}][DCA]$ (⊕) as a function of temperature; solid lines (—) are linear regressions.

In contrast to that, ε_s of $[C_4pyr][TFSA]$ increases with increasing T. In principle, such a behavior could be ascribed to a structural change associated with a break-up of antiparallel aligned dipoles as observed for some neat carboxylic acids,[293] however, it could be also a result of the increased uncertainty of ε_s, because ε' of $[C_4pyr][TFSA]$ does not reach its low-frequency plateau (Figure 4.4). Extension of the frequency range to lower ν was not successful, as the Ohmic loss swamps ε'' (Eq. 1.22). This also almost certainly accounts for the significant difference of literature values for $[C_4pyr][TFSA]$ of ε_s = 15.3[54] and 11.3,[55] whereas the latter agrees well the present value of 11.5 at 25 °C.

Literature values of ε_s for [TAS][TFSA] ILs are very scarce. To the authors knowledge, only Weingärtner *et al.*[54] have determined $\varepsilon_s(= 13.2)$ of $[S_{222}]$[TFSA] at 25 °C, which reasonably agrees with our value of 13.8.
For $[P_{14}]$[DCA] the present value of $\varepsilon_s = 12.6$ at 25 °C is consistent with the slightly larger value of $[P_{12}]$[DCA] of 14.0[46,58] as ε_s is known to increase with decreasing alkyl chain, as observed for 1-alkyl-3-methylimidazolium ILs,[55,58] thus suggesting that $\varepsilon_s = 18.0 \pm 0.8$ reported by Huang *et al.*[55] is overestimated.

4.4.2 Low-Frequency processes

4.4.2.1 General aspects

The dominant intensity of DR and OKE spectra of ILs is generally associated with cooperative relaxations of molecular-level species and/or (if present) fluctuation and reorientation of larger clusters. In contrast to EAN and PAN (Section 3.1), where cooperative cation reorientation dominates the DR signal but anion relaxation is primarily detected by OKE spectroscopy, all cations (S^+_{221}, S^+_{222}, C_4pyr^+ and P^+_{14}) and anions ($TFSA^-$ and DCA^-) of the present ILs contribute to the DR and OKE intensity, as all of them exhibit permanent dipole moments and polarizability anisotropy (Table 4.7). In addition, the present anions and cations have considerably higher internal degrees of freedom, due to their longer alkyl chains, compared to the rather simple-structured EAN and PAN. Thus, apart from ion relaxation, torsional motions of the alkyl chains are also expected to contribute to the diffusive response.

Table 4.7: Apparent dipole moments, μ_{app}, and polarizability anisotropies, γ, of the ionic species S^+_{221}, S^+_{222}, C_4pyr^+, P^+_{14}, $TFSA^-(C_1)$, $TFSA^-(C_2)$ and DCA^-.

	S^+_{221}	S^+_{222}	C_4pyr^+	P^+_{14}	$TFSA^-(C_1)$	$TFSA^-(C_2)$	DCA^-
μ_{app} / D*	1.2	1.1	4.0	5.5	5.3	0.5	$\sim 1^\dagger$
γ / Å^3	2.43♯	2.26♯	8.19♮	3.48♮	3.78♯	3.91♯	8.3*

* Obtained from MOPAC calculations;[174] † Refs. 214 and 294; ♯ Obtained from DFT calculations using ORCA program system;[179] ♮ Ref. 69;

Concerning $TFSA^-$, two stable conformers of C_1 (cisoid) and C_2 (transoid) symmetry (denoted as C_1 and C_2) are known to be present in liquid state, with the latter being thermodynamically more stable by 2-3 kJ mol^{-1}.[295] For the present analysis it is important to note that C_1 has a considerably higher dipole moment than C_2, whereas the polarizability anisotropy, γ, of C_1 and C_2 is virtually identical for the two isomers.[a] Thus, whilst C_1 and C_2 should equally contribute to the OKE signal, DRS predominantly detects motions of C_1.

[a]The values of γ obtained in this work (Table 4.7) agree with those reported by Fujisawa *et al.*[69] of $\gamma_{C1} = 3.79$ Å^3 and $\gamma_{C2} = 3.95$ Å^3.

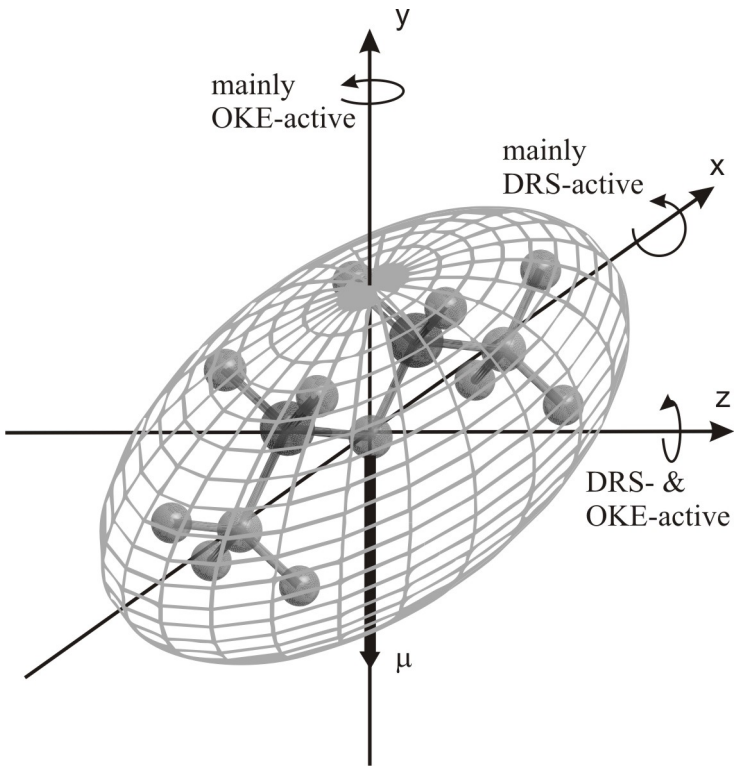

Figure 4.11: Sketch of the C_1 conformer of the $TFSA^-$ anion. Spheroidal grid represents the polarizability ellipsoid calculated from the polarizability tensor and black arrow is the dipole vector, $\vec{\mu}$. The denotation of the axis of the coordinate system follows that of the MOPAC calculation.

In addition, the pronounced prolate shape of $TFSA^-$ ($a \approx 2b = 2c$) associated with an anisotropic moment of inertia, I,($I_x \approx 2.5I_y \approx 2.9I_z$) with its most polarizable axis (half axis a) in x direction and its dipole vector, $\vec{\mu}$, oriented along the y-axis, results in different sensitivities of DRS and OKE spectroscopy to rotations of $TFSA^-$ around different principle axes (Figure 4.11). Whilst a dielectric experiment primarily probes rotations of $\vec{\mu}$ around axes perpendicular to y (i.e. x- and z-axes), OKE spectroscopy is predominantly sensitive to rotations around axes perpendicular to the most polarizable axis (x); i.e. rotations of both C_1 and C_2 around the y- and z-axes.
In general, the present cations (S^+_{221}, S^+_{222}, C_4pyr^+ and P^+_{14}) most likely also adopt several stable conformations in liquid state.[296,297] However, as the dipole moments of the present cations only moderately change with conformation ($\Delta\mu \approx 1.5\,D$) as derived from MOPAC calculations,[174] dipole moments in Table 4.7 are given as average values.

4.4.2.2 Relaxation times

The relaxation times of all relaxation processes, τ_0, τ_1 and τ_2, in the DR and OKE spectra of the present AILs are decreasing with increasing T (Tables 4.1, 4.2, 4.3, 4.4, 4.5, 4.6). The viscosity dependence of τ_j is described by the SED theory, although this approach is

Table 4.8: Effective volumes of rotation, $V_{\mathrm{eff},j}$, obtained from $\tau_0(\eta)$, $\tau_1(\eta)$ and $\tau_2(\eta)$, of the DR and OKE fit of $[S_{221}][TFSA]$, $[S_{222}][TFSA]$, $[C_4pyr][TFSA]$ and $[P_{14}][DCA]$.[a]

	τ_0	τ_1		τ_2	
IL	$V_{\mathrm{eff},0}^{\mathrm{OKE}}$	$V_{\mathrm{eff},1}^{\mathrm{OKE}}$	$V_{\mathrm{eff},1}^{\mathrm{DR}}$	$V_{\mathrm{eff},2}^{\mathrm{OKE}}$	$V_{\mathrm{eff},2}^{\mathrm{DR}}$
$[S_{221}][TFSA]$	27.2 ± 3.8	5.1 ± 1.3	1.6 ± 0.1	1.0 ± 0.3	0.24 ± 0.06
$[S_{222}][TFSA]$	17.8 ± 2.4	2.9 ± 0.7	1.7 ± 0.2	0.5 ± 0.2	0.17 ± 0.03
$[C_4pyr][TFSA]$	19.3 ± 1.6	4.6 ± 0.8	2.3 ± 0.2	1.0 ± 0.3	0.19 ± 0.07
$[P_{14}][DCA]$	18.3 ± 0.5	6.4 ± 1.5[b]	1.4 ± 0.1	—	—

[a] Units: $V_{\mathrm{eff},j}$ in Å^3; [b] τ_2^{OKE} at 5 °C was omitted from linear regression;

Table 4.9: Activation energies, E_{A}, obtained from $\tau_0(T)$, $\tau_1(T)$ and $\tau_2(T)$ of DR and OKE fit and from $\eta(T)$, and resistivity, $\kappa^{-1}(T)$, of $[S_{221}][TFSA]$, $[S_{222}][TFSA]$, $[C_4pyr][TFSA]$ and $[P_{14}][DCA]$.[a]

	τ_0	τ_1		τ_2			
IL	$E_{\mathrm{A},0}^{\mathrm{OKE}}$	$E_{\mathrm{A},1}^{\mathrm{OKE}}$	$E_{\mathrm{A},1}^{\mathrm{DR}}$	$E_{\mathrm{A},2}^{\mathrm{OKE}}$	$E_{\mathrm{A},2}^{\mathrm{DR}}$	E_{A}^{η}	E_{A}^{κ}
$[S_{221}][TFSA]$	23.5 ± 2.5	16.9 ± 3.1	14.5 ± 0.9	11.9 ± 2.3	9.7 ± 1.5	27.0 ± 0.7	24.4 ± 0.7
$[S_{222}][TFSA]$	20.1 ± 2.3	16.0 ± 2.7	13.4 ± 1.7	11.0 ± 3.2	6.5 ± 1.2	26.5 ± 0.8	24.5 ± 0.7
$[C_4pyr][TFSA]$	20.9 ± 1.8	19.3 ± 3.6	19.0 ± 1.5	17.3 ± 4.5	12.0 ± 2.0	32.0 ± 1.1	29.7 ± 1.0
$[P_{14}][DCA]$	21.1 ± 0.8	19.7 ± 2.4[b]	18.2 ± 2.2	—	—	26.0 ± 0.6	23.6 ± 0.6

[a] Units: $E_{\mathrm{A},j}$ in kJ mol^{-1}; [b] τ_2^{OKE} at 5 °C was omitted from linear regression;

strictly speaking only valid for macroscopic systems within the model of rotational diffusion (Section 1.3.4). Nevertheless, it has proven to be useful for molecular-level interpretations and allows the determination of the effective volume of rotation, V_{eff}, from the slope of a SED plot (Eq. 1.63).[b] The so obtained values of V_{eff} are listed in Table 4.8.
The temperature dependence of τ_0, τ_1 and τ_2 is reasonably described by the Arrhenius equation[c] allowing the determination of activation energies, E_{A}, associated with the resolved relaxation processes in OKE and DR spectra of the present ILs (Table 4.9).

TFSA-based ILs. As discussed in Section 4.3.2 OKE and DR spectra ($\nu \lesssim 100\,\text{GHz}$) of [$S_{221}$][TFSA], [$S_{222}$][TFSA] and [$C_4$pyr][TFSA] were best described by three (Di_0, Di_1 and Di_2; OKE) and two (CCi and Di_2; DRS) relaxation processes, respectively (Figures 4.7 and 4.8). Consistent with the temperature dependence of the dielectric amplitudes (Section 4.4.2.3) the Di_2 mode is reasonably assigned to the reorientation of $TFSA^-$, whereas the Di_1 mode in OKE and the CCi mode in DRS are mainly related to cation reorientations as observed for several 1-alkyl-3-methylimidazolium ILs.[47,48,58]
This assignment is supported by the similarity of the effective volumes of rotation for the TFSA-based ILs as $V_{\text{eff},1}^{\text{DR}} \approx V_{\text{eff},1}^{\text{OKE}}$ and $V_{\text{eff},2}^{\text{DR}} \approx V_{\text{eff},2}^{\text{OKE}}$ (Table 4.8). According to the definition of V_{eff},[122] this indicates that a similar amount of volume is swept out in the course of the underlying molecular motion in the OKE and DR processes, indicating that both techniques detect similar dynamics. The observed difference between $V_{\text{eff},2}^{\text{OKE}}$ and $V_{\text{eff},2}^{\text{DR}}$ (Table 4.8) could be reasonably explained within the "idealized" picture illustrated in Figure 4.11, that OKE and DR spectroscopy are sensitive to more (rotations around y and z probed by OKE) or less (rotations around x probed by DRS) bulky $TFSA^-$ rotations, which therefore require more or less volume, respectively. The fact that $V_{\text{eff},1}^{\text{OKE}} > V_{\text{eff},2}^{\text{OKE}}$ and $V_{\text{eff},1}^{\text{DR}} > V_{\text{eff},2}^{\text{DR}}$ suggests that not only cations but possibly also anions contribute to the Di_1 mode (OKE) and the CCi mode (DRS) consistent with the findings for [C_2mim][$EtSO_4$] that some anions are slowed down to the time scale of cation dynamics.[47]
Generally, it is observed that the present values of $V_{\text{eff},1}$ and $V_{\text{eff},2}$ are considerably smaller than that derived for slip boundary conditions ($V_{\text{slip}} = 21.3\,\text{Å}^3$; calculated for $TFSA^-$). In principle, *sub*-slip behavior[121] is indicative for a non-diffusive relaxation mechanism and has been observed for several 1-alkyl-3-methylimidazolium ILs.[58] To scrutinize the nature of the underlying relaxation mechanism, use can be made from a comparison of the corresponding relaxation times τ_j^{DR} and τ_j^{OKE} (with $j = 1, 2$). As presented in Section 1.3.4 for isotropic rotational diffusion, the ratio of a first- (DR) and a second-rank (OKE) relaxation time is 3. In the present case, however, the ratio is found to be $\tau_1^{\text{DR}}/\tau_1^{\text{OKE}} \approx \tau_2^{\text{DR}}/\tau_2^{\text{OKE}} \approx 1.3 \pm 0.3$ on average, for all present TFSA-based ILs. This clearly shows that the relaxation mechanism of cations (τ_1) and anions (τ_2) is not through rotational diffusion but occurs via large-angle

[b] Note that the dielectric relaxation times were not converted into microscopic rotational correlation times, as no practical equivalent approach is available for the OKE relaxation times. According to Eq. 1.63 slopes of dielectric SED plots were divided by a factor of 3.

[c] Note that although transport properties of glass-forming liquids typically follow the VFT equation,[201] the simplified Arrhenius approach is applied, due to the limited temperature range studied here and the rather scattered data points. For comparison $\eta(T)$ and $\kappa(T)$ were also approximated by the Arrhenius equation in the limited temperature range $5 \leq \vartheta/°\text{C} \leq 65$, although both quantities follow the VFT function over the entirely measured range (Appendix A.1).

jumps consistent with the results observed for 1-alkyl-3-methylimidazolium ILs.[36,44] Moreover, this is corroborated by the fact that $E_{A,1}$ and $E_{A,2}$ of both DRS and OKE spectroscopy are considerably smaller than E_A^η and E_A^κ implying a decoupling of rotational motions from translations, which is incompatible with a rotational diffusive relaxation mechanism (Table 4.9).
Regarding $E_{A,1}$ and $E_{A,2}$ of both DR and OKE spectra of the present TFSA-based ILs, the sequence $E_{A,j}$([C_4pyr][TFSA])> $E_{A,j}$([S_{221}][TFSA]> $E_{A,j}$([S_{222}][TFSA]) (with $j = 1, 2$) (Table 4.9) is observed and indicates that the energy barriers for ion relaxation are significantly higher in [C_4pyr][TFSA] than in [S_{221}][TFSA] and [S_{222}][TFSA]. This implies that the interionic interactions between $TFSA^-$ and C_4pyr^+ are stronger than those between $TFSA^-$ and TAS^+, consistent with η([C_4pyr][TFSA])> η([S_{221}][TFSA]> η([S_{222}][TFSA]) (Tables A.3 and A.5). With respect to molecular properties (Table 4.7), this can be rationalized in terms of enhanced dipole-dipole interactions as $\mu_{app,C4pyr+} > \mu_{app,TAS+}$, but possibly also of the larger mean polarizability of C_4pyr^+ than that of TAS^+ (Appendix A.1.2) leading to stronger induced moments.

The most remarkable feature of the present OKE spectra is the presence of a large-amplitude low-frequency mode (Di_0), which obviously has no direct counterpart in the DR spectra (Figures 4.7 and 4.8). This is in analogy to 1-alkyl-3-methylimidazolium ILs, where a so-called sub-α mode dominated the OKE spectra, but was found to be almost undetectable in the DR spectra.[36] Consistent with the large value of $V_{eff,0}^{OKE}$ (Table 4.8), the present Di_0 mode of the TFSA-based ILs can be also reasonably labelled as sub-α mode and it seems likely that its weak dielectric intensity, which could not be resolved as a separate process in the present DR spectra, is incorporated in the CCi mode, thus explaining the symmetrical broadening of the dielectric low-frequency peak. This difference in amplitudes in OKE and DR spectra suggests that the underlying molecular-level process is associated with a considerable change in polarizability anisotropy, whereas the macroscopic dipole moment is rather unaffected in the course of this motion. According to the large relaxation time, τ_0, the process must be related to fluctuations of larger aggregates. In case of 1-alkyl-3-methylimidazolium ILs it has been suggested to associate it with a breathing mode of π-stacked clusters,[36] based on results of DRS of RTIL mixtures[294] and MD simulations.[44] Whilst such a motion would be in principle realistic for [C_4pyr][TFSA], the molecular-level origin in [TAS][TFSA] salts must be different, due to the lack of aromatic groups. However, MD simulations of [C_4pyr][BF_4][74] have shown that the pyridinium cations are preferentially oriented in a "T-shaped" manner (i.e. two pyridinium rings are orthogonal to each other), suggesting that also in [C_4pyr][TFSA] π-stacking is of minor importance.[74,298] The fact that a sub-α mode is also observed in the OKE spectra of [P_{14}][DCA] (see below), suggests that the underlying process is independent of the presence of aromatic moieties. Interestingly, no indications for a similar mode have been observed for protic ILs (EAN and PAN, Section 3.1) suggesting that such a contribution is an universal feature of AILs only.
For a microscopic-level interpretation of such a low-frequency mode, fluctuations of large aggregates have to be considered, consistent with the results of MD simulations that, in imidazolium-based ILs, translational fluctuations contribute down to quite low frequencies

(MHz region).[42–45] Due to the high degree of charge ordering in ILs[40,299,300] phonon-like low-energy density fluctuations could possibly explain the observed intensity, which have been already used to interpret light scattering spectra of molten salts[301–304] and glasses.[305,306] Recently, ultra-sound absorption measurements have detected a dispersion at MHz frequencies for imidazolium-based ILs[307] compatible with a rapid fluctuation of larger clusters. Moreover, low-frequency dielectric spectroscopy revealed that for [C_6mim][PF_6] the relaxation time of the electric modulus, τ_{el}, coincides with that of the dominant low-frequency peak in depolarized light scattering (DLS) spectra.[308] Within the theory of Scher and Lax,[309] τ_{el} can be associated with the mean residence time of an ion in its cage between successive hops,[308] which is thought to represent the determining step for the conductivity in ILs.[310] As OKE probes dynamics equivalent to DLS[311] this suggests that the sub-α mode observed in the present OKE spectra could be understood as a translational fluctuation of cage-like structures representing a prerequisite of ion hopping.[270,312,313] The relaxation time of the present Di_0 mode, τ_0, may then be interpreted as the average lifetime of the cage, which determines the hopping rate (jump frequency) of the ions.[308,314]
Furthermore, it is observed that the sub-α process correlates considerably more with the viscosity than the cooperative jump relaxation of anions and cations, which can be inferred from $V_{eff,0}^{OKE} \approx V_{slip} = 21.3\,Å^3$ (Table 4.8) and $E_{A,1}^{OKE} \approx E_A^{\eta} \approx E_A^{\kappa}$ (Table 4.9) suggesting that these aggregates or cluster-structures may be responsible for the high viscosities of RTILs.[36] The amplitude of the sub-α mode scales with the polarizability anisotropy of the cation as it is considerably larger for [C_4pyr][TFSA] and imidazolium ILs[36] than for the [TAS][TFSA] salts, thus reflecting $\gamma_{C4pyr+} > \gamma_{TAS+}$ (Table 4.7).

[P_{14}][DCA]. According to the permanent dipole moments of P_{14}^+ and DCA^- (Table 4.7), cation dynamics should dominate over anion dynamics in the DR signal, whereas the situation is expected to be vice versa for the OKE signal with respect to the polarizability anisotropies ($\gamma_{DCA-} > \gamma_{P14+}$; Table 4.7). This suggests that both techniques detect similar dynamics with different weights, which reasonably explains the difference between $V_{eff,1}^{OKE}$ and $V_{eff,1}^{DR}$ (Table 4.8). The absence of a distinct anion reorientation process in the DR spectra of [P_{14}][DCA], which is commonly observed for ILs consisting of dipolar anions[47] (see above) is a result of the small permanent dipole moment of DCA^- (Table 4.7) and is consistent with the best fit for the DR spectra of [P_{12}][DCA], where also no relaxation mode specific for DCA^- was observed.[46,58] This indicates that the dielectric CCi mode of [P_{14}][DCA] is a composite that is dominated by cation dynamics, which manifests itself in the increase of $V_{eff,1}^{DR}$ from $0.46\,Å^3$ for [P_{12}][DCA][58] to $1.4\,Å^3$ for [P_{14}][DCA] as a result of the elongated cation alkyl chain (Table 4.8).
As for the TFSA-based ILs the ratio of relaxation times τ_1^{DR}/τ_1^{OKE}, of [P_{14}][DCA] can be used to obtain information on the underlying relaxation mechanism. Although DRS and OKE spectroscopy do not probe identical molecular-level dynamics of [P_{14}][DCA], the present value of $\tau_1^{DR}/\tau_1^{OKE} \approx 0.8$ is incompatible with rotational diffusion. Rather than that, it suggests ion relaxation to occur via large-angle jumps as observed for all other ILs studied to date.[36,44,208]
The dominant low-frequency process in the OKE spectra (CDi mode) of [P_{14}][DCA] can be reasonably associated with a sub-α mode (Figures 4.7, 4.8 and 4.9). As for the TFSA-based

ILs the value of $V_{\mathrm{eff},0}^{\mathrm{OKE}}$ is considerably larger than that of $V_{\mathrm{eff},1}^{\mathrm{OKE}}$ and $V_{\mathrm{eff},1}^{\mathrm{DR}}$ but similar to that of $V_{\mathrm{slip}} = 14.7\,\text{Å}^3$ (for DCA^-) suggesting that the CDi mode correlates with the viscosity. Likewise, $E_{\mathrm{A},1}^{\mathrm{OKE}} \approx E_{\mathrm{A}}^{\eta} \approx E_{\mathrm{A}}^{\kappa}$ as observed for the TFSA-based ILs (Table 4.9) supporting the assumption that independent of the molecular structure of anions and cations a sub-α mode is a universal feature AILs, which dominates the OKE response but is (almost) undetectable in the DR spectra.

4.4.2.3 Amplitudes.

Evaluation of the amplitudes of the dielectric low-frequency processes, S_1 and S_2 is accomplished by the Cavell equation (Eq. 1.52), which relates S_j of process j with the effective dipole moment, $\mu_{\mathrm{eff},j}$.[115]

[TAS][TFSA] ILs. It is observed that for $[S_{221}][TFSA]$ and $[S_{222}][TFSA]$ $\mu_{\mathrm{eff},1}$ decreases, whereas $\mu_{\mathrm{eff},2}$ increases with increasing T.

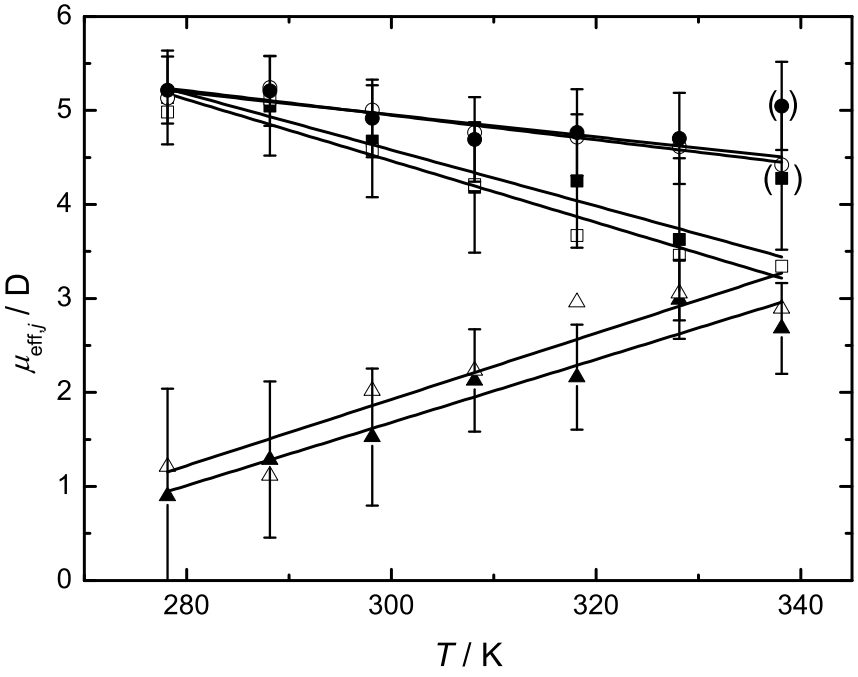

Figure 4.12: Effective dipole moments, $\mu_{\mathrm{eff},1}$ (squares), $\mu_{\mathrm{eff},2}$ (triangles) and $\mu_{\mathrm{eff},1+2}$ (circles, calculated from $S_1 + S_2$) of $[S_{221}][TFSA]$ (full symbols) and $[S_{222}][TFSA]$ (open symbols) as a function of temperature; solid lines (—) are linear regressions. Data points in brackets were omitted from the linear fit. Error bars are only displayed for $\mu_{\mathrm{eff},j}$ of $[S_{221}][TFSA]$ for visual clarity.

As discussed above, the Di_2 mode of the present TFSA-based ILs can be reasonably assigned to reorientations of $TFSA^-$. Because of the isomeric equilibrium[295] between the

weakly dipolar C_2 ($\mu_{\mathrm{app,C2}} = 0.5\,\mathrm{D}$) and the *strongly* dipolar C_1 ($\mu_{\mathrm{app,C1}} = 5.3\,\mathrm{D}$)[d] it is expected that the mol fraction of C_1, x_{C1}, increases at the expense of the thermodynamically more stable C_2 with increasing T thus, being partially responsible for the increase of $\mu_{\mathrm{eff},2}$. Accordingly, this should permit $\mu_{\mathrm{eff},2}$ to be expressed by the following equation

$$\mu^2_{\mathrm{eff},2} = x_{\mathrm{C1}} g_{\mathrm{TFSA-}} \mu^2_{\mathrm{app,C1}} + (1 - x_{\mathrm{C1}}) g_{\mathrm{TFSA-}} \mu^2_{\mathrm{app,C2}} \tag{4.1}$$

with two unknown variables x_{C1} and $g_{\mathrm{TFSA-}} = g_{\mathrm{C1}} = g_{\mathrm{C2}}$. A solution of Eq. 4.1 is provided

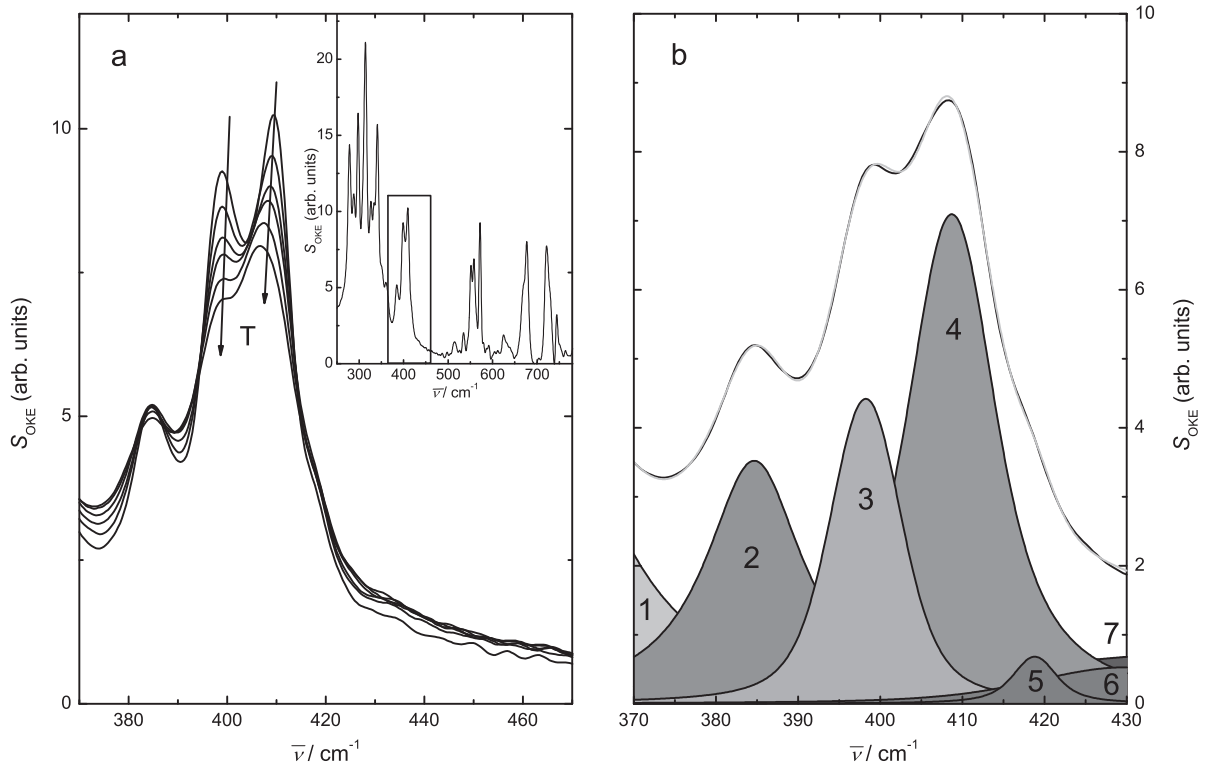

Figure 4.13: (**a**) Re-measured OKE spectra of $[S_{221}][TFSA]$ in the temperature range $240 \leq T/\mathrm{K} \leq 340$ in 20 K steps. (**b**) Deconvolution of the spectrum at 300 K using a sum of 7 Voigt functions (shaded areas). Gray line represents the total fit.

by band-fitting analysis of the OKE spectra in the frequency range $380 \lesssim \bar{\nu}/\mathrm{cm}^{-1} \lesssim 430$ ($11.4 \lesssim \nu/\mathrm{THz} \lesssim 12.9$) where the SO_2-wagging motion (ω-SO_2) specific for C_1 and C_2 takes place, allowing the determination of x_{C1}.[315,317,318] Therefore, OKE spectra of $[S_{221}][TFSA]$ were re-measured[e] over the temperature range $240 \leq T/\mathrm{K} \leq 340$ (20 K steps) with a higher resolution in the frequency region of interest (Figure 4.13a). Figure 4.13b shows the deconvolution of the spectrum at 300 K using a sum of seven Voigt functions,[f] where

[d]The present values of $\mu_{\mathrm{app,C2}}$ and $\mu_{\mathrm{app,C1}}$ obtained from MOPAC agree with those in the literature, which were calculated on a higher level of theory.[214,315,316]

[e]OKE spectra of Figure 4.13 were measured and processed (baseline correction etc.) by Dr. D. A. Turton (Glasgow University, Glasgow, UK).

[f]The multipeak fitting package 2 implemented in the IGOR software (Wavemetrics V.6.31) was used.

mode 3 and 5 are assigned to ω-SO_2 of C_2 and mode 4 to ω-SO_2 of C_1.[315,318] Comparison to the Raman spectra of [C_2mim][TFSA] published by Fujii *et al.*[315,319] suggests that mode 2 is specific for S^+_{221} as it is absent in their spectra. Similar fits were obtained at all other temperatures. Through $I = cJ$ the integrated intensity, I, is related to the concentration, c, and the scattering coefficient, J.[315,319] Thus, x_{C1} can be obtained from the ratio I_{C1}/I_{C2} (with $I_{C1} = I_4$ and $I_{C2} = I_3 + I_5$) via

$$x_{C1} = \frac{1}{1 + \frac{c_{C2}}{c_{C1}}} \tag{4.2}$$

provided that J_{C1}/J_{C2} is known. The latter can be obtained from the slope of a plot of I_{C1} against I_{C2} according to the relation $I_{C1} = J_{C1}c_{TFSA-} - J_{C1}/J_{C2}I_{C2}$,[296,318] where c_{TFSA-} is the total concentration of $TFSA^-$. In the present case $J_{C1}/J_{C2} = 0.74$. The so derived values of x_{C1} (Eq. 4.2) are shown in Figure 4.14 and it is found that on average C_1 is present to $\sim 73\,\%$ in [S_{221}][TFSA]. This value is compatible with that reported by Herstedt *et al.*[297] of $x_{C1} \sim 70\,\%$ for [Et_4N][TFSA] determined by Raman spectroscopy. The present x_{C1} were interpolated and inserted into Eq. 4.1 allowing the calculation of g_{TFSA-} (Figure 4.14). It is observed that $g_{TFSA-} \ll 1$ for all T indicating strong antiparallel dipole-dipole correlations of $TFSA^-$ dipoles. This is consistent with what has been observed for all anion relaxation processes in ILs studied to date (Section 3.2),[47,256] where μ_{eff} obtained from their corresponding dielectric amplitudes are considerably underestimated with respect to theoretical dipole moments. Moreover, the fact that $dg_{TFSA}/dT > dx_{C1}/dT$ implies that the large value of $d\mu^2_{eff,2}/dT$ (Figure 4.14, $\oplus$) and thus dS_2/dT (Table 4.2) of the present [TAS][TFSA] ILs is mainly caused by decreasing antiparallel dipole-dipole correlations but also by the increase of x_{C1}.

From the thermodynamic point of view, the enthalpic and entropic nature of the conformational equilibrium of $TFSA^-$ in the present [TAS][TFSA] ILs can be estimated on the basis of I_{C1}/I_{C2}.[297,315,318,319] With the definition of the equilibrium constant, $K_{iso} = c_{C1}/c_{C2}$, the species distribution varies with temperature according to $-R \ln K_{iso} = \Delta_{iso}H^\circ/T - \Delta_{iso}S^\circ$. Thus, using $I = cJ$, the following relation is obtained

$$-R \ln\left(\frac{I_{C1}}{I_{C2}}\right) = \Delta_{iso}H^\circ/T - \Delta_{iso}S^\circ - R \ln\left(\frac{J_{C1}}{J_{C2}}\right) \tag{4.3}$$

enabling the determination of $\Delta_{iso}H^\circ = (4.9 \pm 0.6)\,kJ\,mol^{-1}$ and $\Delta_{iso}S^\circ = (26 \pm 2)\,J\,mol^{-1}$ from the slope and the intercept, respectively, of a plot of $-R\ln(I_{C1}/I_{C2})$ vs. T^{-1} (Figure 4.15). The value of $\Delta_{iso}H^\circ$ is compatible with that reported for [C_2mim][TFSA] of $(3.5 \pm 0.1)\,kJ\,mol^{-1}$ [315] and [Et_4N][TFSA] of $(7 \pm 1)\,kJ\,mol^{-1}$,[297] whereas the present $\Delta_{iso}S^\circ$ is consistent with that reported for the $TFSA^-$-derivative bis(fluoromethanesulfonyl)amide (FSA^-) in [C_2mim][FSA] of $(19 \pm 5)\,J\,mol^{-1}$.[319] Accordingly, at 25 °C, $\Delta_{iso}G^\circ = (-2.9 \pm 0.8)\,kJ\,mol^{-1}$ for [S_{221}][TFSA], which is rather close to zero indicating that both conformers exist in the present TAS ILs in liquid state.[315]

The effective dipole moment, $\mu_{eff,1}$, decreases for [S_{221}][TFSA] and [S_{222}][TFSA] with increasing T (Figure 4.12), which implies that dipole-dipole correlations decrease with increasing T. On the basis of uncorrelated dipole moments of S^+_{221}, S^+_{222}, C_1 and C_2 obtained

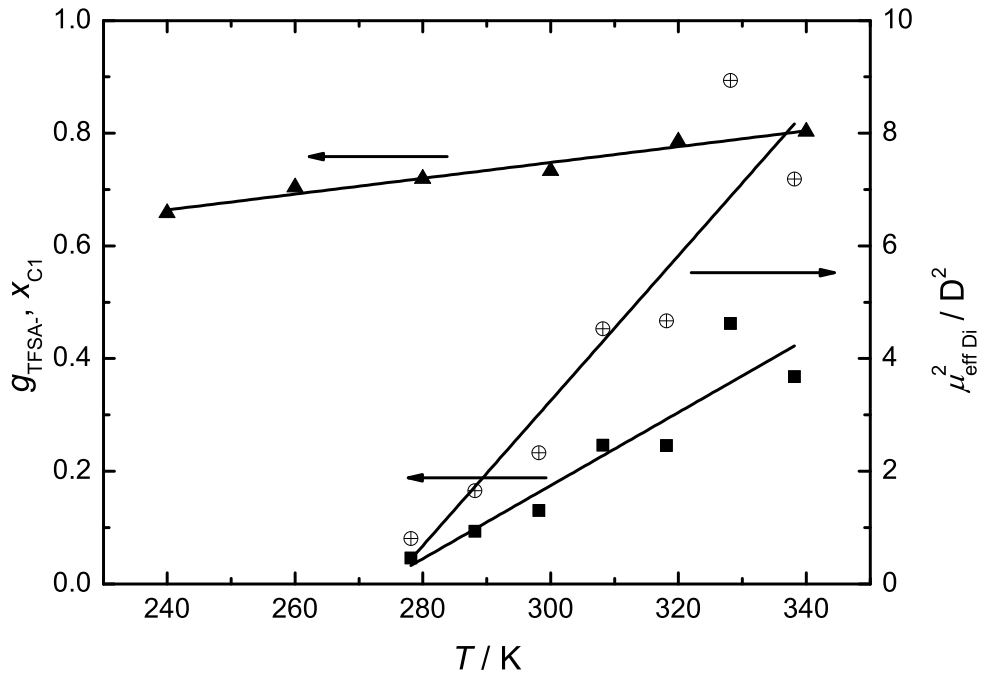

Figure 4.14: Fraction of C_1, x_{C1} (▲), correlation factor of $TFSA^-$, g_{TFSA-} (■), and $\mu^2_{eff,2}$ (⊕) of $[S_{221}][TFSA]$ as a function of T. Solid lines are linear regressions.

from MOPAC the value of $\mu_{eff,1}$ can neither be explained solely by cation nor anion reorientation, consistent with the conclusions drawn from the effective volumes (Section 4.4.2.2) that S_1 is a composite. Assuming that reorientations of anions *and* cations are responsible for S_1 of the present [TAS][TFSA] ILs a correlation factor of the cations g_+ can be *formally* calculated by approximating $\mu_{eff,1}$ as

$$\mu^2_{eff,1} = g_+\mu^2_{app,+} + \underbrace{x_{C1}g_{TFSA-}\mu^2_{app,C1} + (1-x_{C1})g_{TFSA-}\mu^2_{app,C2}}_{\mu^2_{eff,2} \text{ see Eq. 4.1}} \tag{4.4}$$

where $\mu_{app,+}$ is $\mu_{app,S221+} = 1.2\,D$ or $\mu_{app,S222+} = 1.1\,D$ (Table 4.7). The correlation factor, g_+, is displayed in Figure 4.16. It is observed that $g_+ \gg 1$ indicating strong parallel dipole-dipole correlations, which are decreasing consistent with decreasing intermolecular interactions with increasing T. However, the absolute values of g_+ are unrealistically high. This indicates that the rotational contribution assumed to contribute to the CCi mode is considerably underestimated by the present approach (Eq. 4.4) and suggests that additional contributions may contribute to S_1. Keeping in mind the assumption that the sub-α mode, which is not resolved in the present DR spectra, is incorporated in the CCi mode (Section 4.4.2.2), could plausibly explain the extraordinary large value of g_+.

In addition, it should be noted that in the present analysis using Eqs. 4.1 and 4.4 cations and anions were assumed to contribute to S_1 and S_2 with their analytical concentration, c. However, as suggested for $[C_2mim][EtSO_4]$ the dynamics of *some* anions (normally relaxing with τ_2) are possibly slowed down (synchronized) to the timescale of cation relaxation (τ_1),

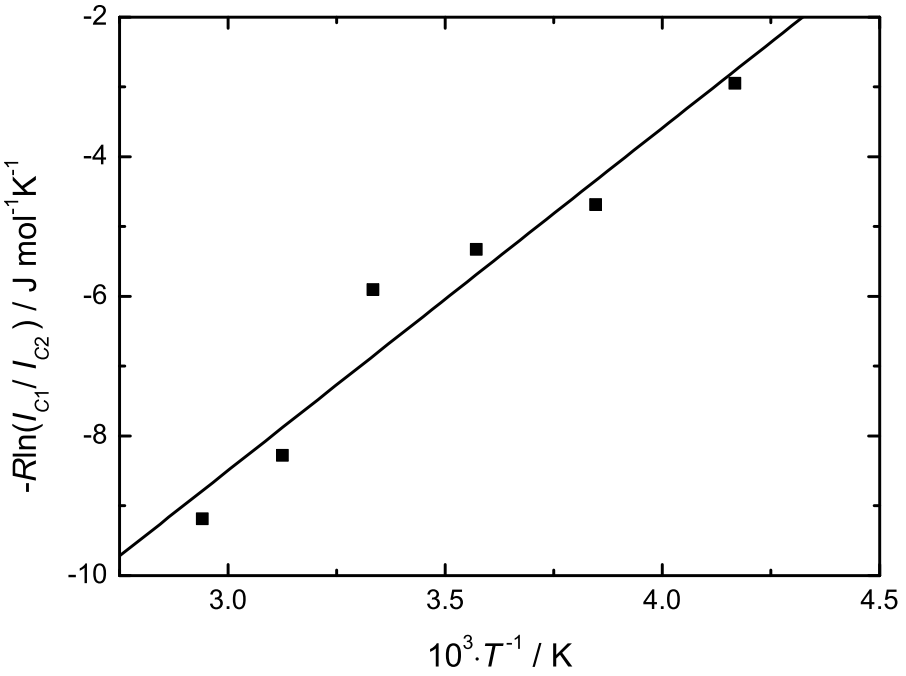

Figure 4.15: Van't Hoff plot of the conformational equilibrium of $TFSA^-$ in $[S_{221}][TFSA]$ according to Eq. 4.3.

due to the strong intermolecular interactions[47,59] indicating a high degree of cooperativity in the liquids. As a result, the concentration of anions contributing to S_2 is smaller than c, whereas the dipole density contributing to S_1 is higher, thus leading to $g_+ > 1$ and $g_{\mathrm{TFSA}-} < 1$. Nevertheless, considerable dipole-dipole correlations are present in the investigated [TAS][TFSA] salts, which can be inferred from the significant decrease of $\mu_{\mathrm{eff},1+2}$, obtained from $S_1 + S_2$, with increasing T (Figure 4.12).

$[P_{14}]$[DCA] & $[C_4pyr]$[TFSA]. In Figure 4.17 $\mu_{\mathrm{eff},1}$ of $[P_{14}]$[DCA] and $[C_4pyr]$[TFSA] and $\mu_{\mathrm{eff},2}$ of $[C_4pyr]$[TFSA] calculated from the corresponding dielectric amplitudes S_1 and S_2 via Eq. 1.52 are plotted as a function of T. For $[C_4pyr]$[TFSA] it is observed that by trend both $\mu_{\mathrm{eff},1}$ and $\mu_{\mathrm{eff},2}$ slightly increase with increasing T. As discussed for the [TAS][TFSA] salts, the latter can be reasonably attributed to a decrease of antiparallel dipole-dipole correlations but also due to the increasing amount of the stronger dipolar C_1 species at the expense of C_2. Although the considerable scatter of the data points prevents a detailed analysis, an average value of $g_{\mathrm{TFSA}-}$ for $[C_4pyr]$[TFSA] can be estimated via Eq. 4.1 using the temperature average of $\mu_{\mathrm{eff},2} = 2.0 \pm 0.4\,\mathrm{D}$ and approximating $x_{\mathrm{C1}} \approx 0.73$ by the average value determined for $[S_{221}]$[TFSA] (Figure 4.14). This yields $g_{\mathrm{TFSA}-} = 0.19$ for $[C_4pyr]$[TFSA], which is of similar magnitude as that of the studied [TAS][TFSA] ILs indicating strong antiparallel dipole-dipole correlations.

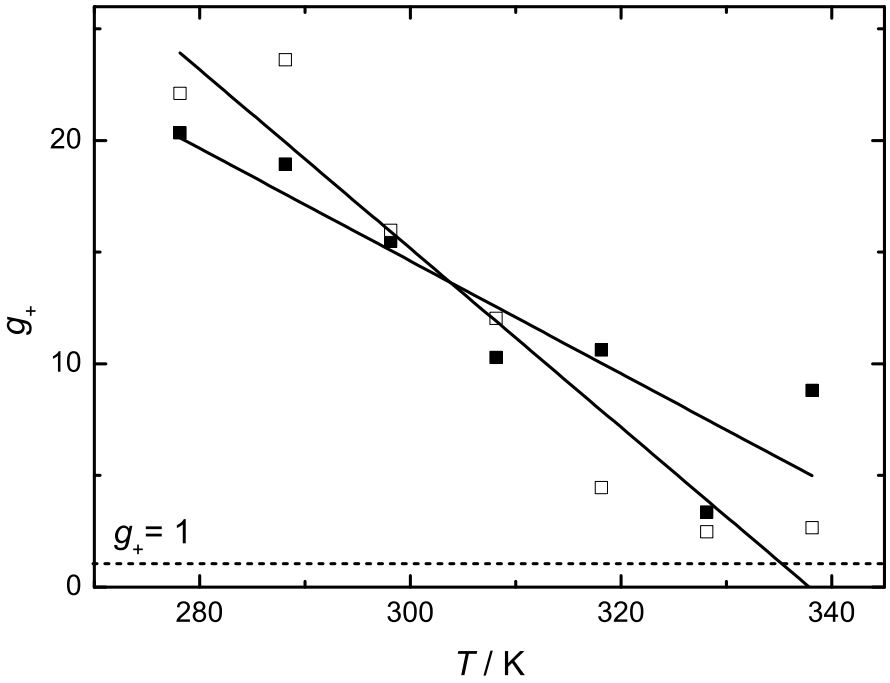

Figure 4.16: Orientational correlation factor of TAS^+ cations, g_+, of $[S_{221}][TFSA]$ (■) and $[S_{222}][TFSA]$ (□) as a function of T. Solid lines are linear regressions.

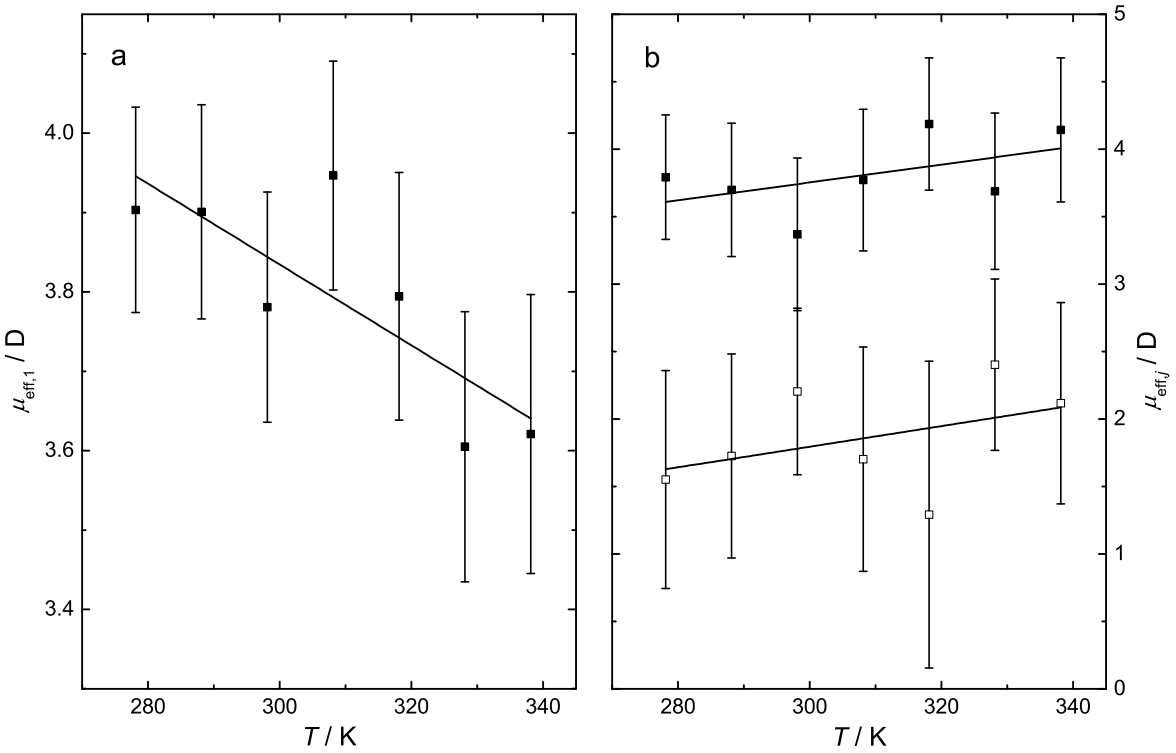

Figure 4.17: Effective dipole moment, $\mu_{eff,1}$ of (**a**) $[P_{14}][DCA]$ (■) and (**b**) $\mu_{eff,1}$ (■) and $\mu_{eff,2}$ (□) of $[C_4pyr][TFSA]$ as a function of temperature; solid line (—) represent linear regressions.

Furthermore, insertion of $g_{\mathrm{TFSA}-} = 0.19$ and $\mu_{\mathrm{app},+} = \mu_{\mathrm{app,C4pyr}+} = 4.0\,\mathrm{D}$ (Table 4.7) into Eq. 4.4 gives $g_+ = 0.66$. This is in contrast to $[S_{221}][TFSA]$ and $[S_{222}][TFSA]$, where $g_+ \gg 1$, which suggests that also cation-cation and/or cation-anion dipoles are arranged in an antiparallel manner. Keeping in mind the uncertainties associated with the determination of ε_s and thus S_1 (Section 4.4.1), this would also explain the observed increase of ε_s with increasing T suggesting a break-up of antiparallel aligned dipoles.
For $[P_{14}][DCA]$ $\mu_{\mathrm{eff},1}$ decreases with increasing T, however much less than $\mu_{\mathrm{eff},1}$ of the present [TAS][TFSA] ILs. Nevertheless, the decrease suggests decreasing dipole-dipole correlations, as observed for [TAS][TFSA] ILs and the present average value for $[P_{14}][DCA]$ of $\mu_{\mathrm{eff},1} = 3.8 \pm 0.1\,\mathrm{D}$ agrees well with that obtained for $[P_{12}][DCA]$ of $3.9 \pm 0.1\,\mathrm{D}$.[58]

4.4.3 High-Frequency processes

The intensity at $\nu \gtrsim 100\,\mathrm{GHz}$ of OKE and DR spectra of ILs is generally associated with resonance type processes, which are associated with intermolecular vibrations, such as "cage-rattling" motions and librations of ions.[36,51,67,320,321] However, a decomposition of experimental DR and OKE spectra using common line-shapes such as damped harmonic oscillators or Gaussians does not account for all complex dynamical processes, taking place on this time scale.[322] In particular, cross-terms that arise from coupling between translational and reorientational motions are not describable within such a line-shape analysis.[69,290] Moreover, the small temperature effects in the present spectra are superimposed by the considerable noise of the dielectric data leading to rather scattered fitting parameters (Tables 4.1, 4.2, 4.3, 4.4, 4.5 and 4.6), thus, preventing a detailed analysis.
Figure 4.18 shows the high frequency part ($\nu \gtrsim 10\,\mathrm{GHz}$) of OKE and DR spectra of $[S_{222}][TFSA]$, $[C_4pyr][TFSA]$ and $[P_{14}][DCA]$ at 25 °C. In the present spectra the intensity arising from relaxation processes and the CL contribution were subtracted from OKE and DR spectra.
For ILs consisting of aromatic cations such as imidazolium salts[36,69] and the present $[C_4pyr][TFSA]$ a pronounced peak at $\sim 100\,\mathrm{cm}^{-1}$, in the present analysis labelled as G_2 mode (Figure 4.18b,e), is observed. As suggested by MD simulations for simple aromatic liquids such as benzene or pyridine it is mainly associated with the tumbling motion of their aromatic rings.[322,323] For imidazolium ILs Giraud *et al.*[33] assigned this intensity to the out-of-plane libration of the aromatic ring. This is consistent with the present decomposition of OKE and DR spectra, as the relative amplitude in the OKE spectra (Figure 4.18b) is significantly larger than that in the DR spectra (Figure 4.18e), which can be attributed to the large polarizability anisotropy of C_4pyr^+ (Table 4.7). Moreover, this is corroborated by the absence of such a mode in the OKE and DR spectra of the non-aromatic [TAS][TFSA] ILs (Figure 4.7a,b and 4.18a,d) and $[P_{14}][DCA]$ (Figure 4.18c,f).
A general feature of OKE spectra of TFSA-based ILs is the presence of a significant peak at $\sim 20\,\mathrm{cm}^{-1}$.[33,67,291,324] In the present spectra the DHO_1 mode in the OKE spectra of $[S_{221}][TFSA]$, $[S_{222}][TFSA]$ and $[C_4pyr][TFSA]$ (Figure 4.18a,b) accounts for this intensity and it has been suggested to assign this peak to the interionic vibrational dynamics and librational motions of $TFSA^-$.[68,69] Despite the considerable scatter in the DR spectra of

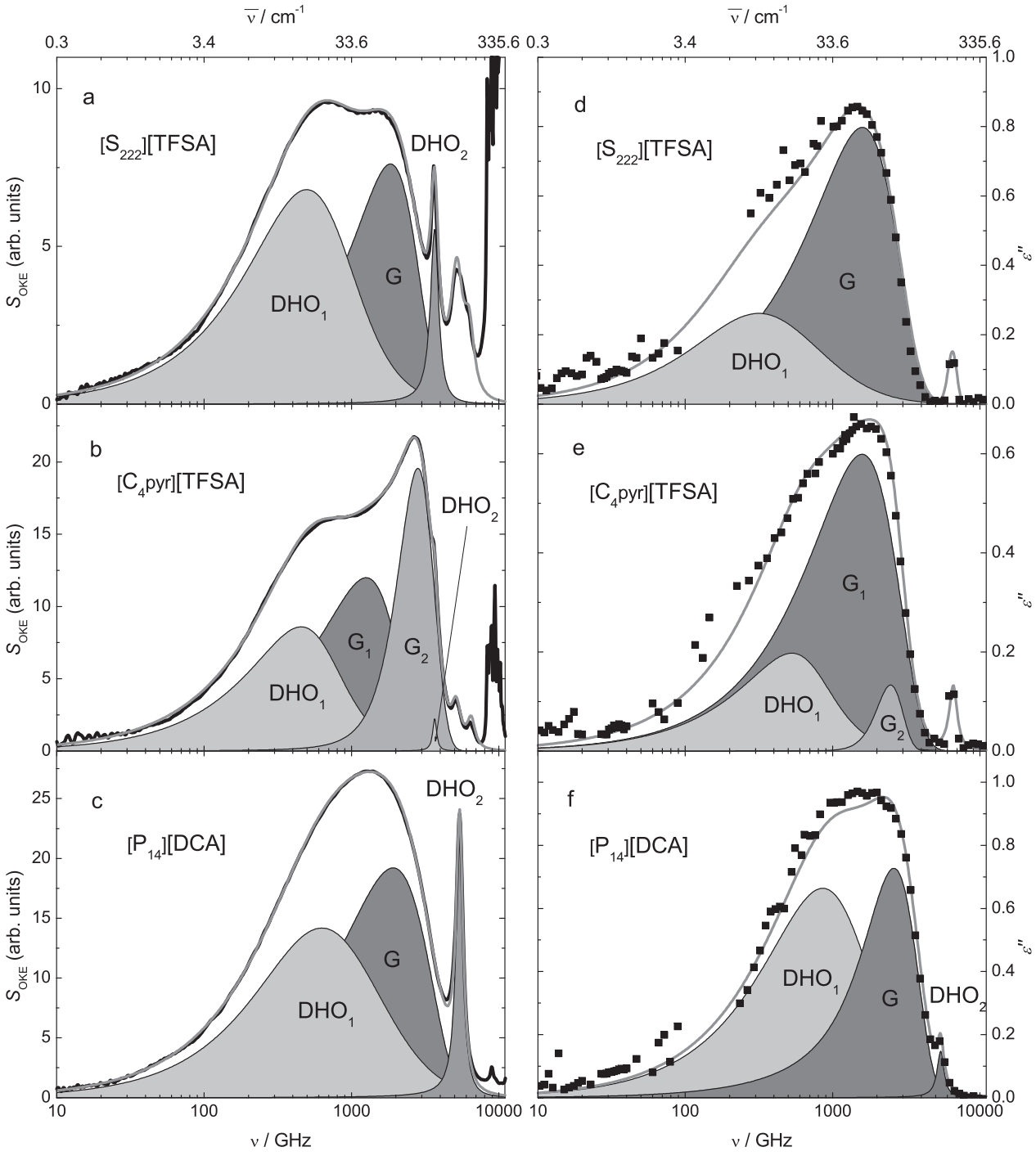

Figure 4.18: Decomposition of the high frequency part ($\nu \gtrsim 10\,\mathrm{GHz}$) of OKE and DR spectra of (**a**) & (**d**) [S_{222}][TFSA], (**b**) & (**e**) [C_4pyr][TFSA] and (**c**) & (**f**) [P_{14}][DCA], respectively. Low-frequency relaxation modes and CL contributions were subtracted. Black solid lines (OKE) and full symbols (DRS) are experimental data. Gray solid lines represent total fits and shaded areas indicate individual resonance functions.

[S_{222}][TFSA] and [C_4pyr][TFSA], a distinct peak at $\sim 20\,\mathrm{cm}^{-1}$ seems to be absent. Keeping in mind the prolate shape of $TFSA^-$ (Figure 4.11) librational motions around a specific axis could explain the significant peak in the OKE spectra. However, as the DHO_1 mode is also required to describe the OKE and DR spectra of [P_{14}][DCA] this suggests that unspecific contributions arising from multi-particle interactions of anions and cations contribute on this time scale, which, in case of TFSA-based ILs, are superimposed by $TFSA^-$-specific dynamics.
Generally, the same applies to the contribution at $\sim 60\,\mathrm{cm}^{-1}$, which, for the present ILs, was modelled by a Gaussian, G, in [S_{222}][TFSA] and [P_{14}][DCA] and G_1 in [C_4pyr][TFSA]. Independent of the structure of cations or anions such an intensity is observed in the present ILs, reflecting the collective nature of IL-dynamics in this frequency range and indicates that librations of anions and cations are strongly overlapping.

4.5 Conclusions

The dynamics of four aprotic non-imidazolium ILs, based on trialkylsulfonium, pyridinium and pyrrolidinium cations, have been studied by a combined experimental approach using DR and OKE spectroscopy in the exceptional wide frequency range $0.2 \lesssim \nu/\mathrm{GHz} \lesssim 10\,000$ at temperatures between 5 and 65 °C.
Deconvolution of the low-frequency part ($\nu \lesssim 100\,\mathrm{GHz}$) of OKE and DR spectra of TFSA-based ILs revealed that in addition to the commonly observed cation relaxation process,[36,58] a relaxation mode specific for anions could be resolved. Quantitative analysis of the corresponding dielectric amplitude indicated strong antiparallel dipole-dipole correlations of $TFSA^-$ dipoles, which in [S_{221}][TFSA] was found to be present in its *cisoid* form to approximately 73 %. Likewise, strong correlations were found to exist between cation and anion dipoles. As a consequence of such strong interionic forces (dipole-dipole and coulombic interactions), it was shown that ion relaxation in the present ILs occurs through large-angle jumps rather than rotational diffusion, similar to what has been observed for imidazolium-based ILs (Section 3.2)[36,58] and alkylammonium nitrates (Section 3.1).[208] Moreover, the observed dynamics are highly cooperative, which, at least for [TAS][TFSA] ILs, manifests itself in a partial slow down of some anions to the time scale of cation dynamics.
The most remarkable feature of the OKE spectra of the studied AILs was the presence of an intense low-frequency mode, which could not be resolved in the DR spectra of the present ILs, similar to what has been observed for 1-alkyl-3-methylimidazolium ILs.[36] From comparison of the present DR and OKE spectra it was concluded that this sub-α mode is not associated with the cooperative relaxation of ions, but as suggested for imidazolium-based ILs,[36] is likely related to the fluctuations of mesoscale structures. Phonon-like modes associated with translational low-energy vibrations of larger aggregates could account for the observed intensity and a relation to the charge hopping transport mechanism appears plausible. Moreover, the corresponding relaxation time, τ_0, seems to be correlated to η, suggesting that such clusters may be responsible for the high viscosities of RTILs. The fact that such a mode is present in the OKE spectra of AILs, but absent in those of EAN and PAN, suggests that a sub-α mode is a general feature of AILs.

These findings should motivate further research to investigate the nature of the sub-α mode and the orientational dynamics of non-imidazolium ILs in general. For example, it would be interesting to study the behavior of the sub-α mode as a function of composition in binary mixtures with molecular solvents by means of OKE spectroscopy. Particularly, MD simulations, which are able to quantitatively reproduce OKE and DR spectra of ILs would be desirable to render more precisely the results of the present study and to disentangle the strongly overlapping contributions in the THz frequency range.

Chapter 5

Binary mixture of EAN + Acetonitrile

The material presented in this chapter forms the basis of the paper:

Thomas Sonnleitner, Viktoria Nikitina, Andreas Nazet, and Richard Buchner *"Do H-Bonds Explain Strong Ion Aggregation in Ethylammonium Nitrate + Acetonitrile Mixtures?"*, *Phys. Chem. Chem. Phys.* **2013**, *15*, 18445-18452.

5.1 Introduction

Probably the most intensively studied PIL is ethylammonium nitrate (EAN).[7] Due to its ability to form a three dimensional hydrogen bond network reminiscent to that of water,[28,64] it has attracted particular interest as possible replacement for aqueous solutions in organic synthesis[7] and as self-assembling medium.[28,185,325,326]
In practical applications ILs are generally mixed with other components, either acting as co-solvents or as reactants. To understand interactions in such systems knowledge on their structure and dynamics is essential. Up to now, most publications dealing with the dynamics of ILs and their mixtures with non-ionic compounds focus on salts with 1-alkyl-3-methylimidazolium cations[30,48,49,51,58] but only little is known about PIL-containing systems.[80,81] In this contribution we present a first systematic study of the cooperative dynamics of EAN+dipolar aprotic solvent mixtures. Acetonitrile (AN) was chosen as the non-ionic component as this industrially important solvent[327,328] is miscible with EAN over the entire composition range. Additionally, its structure and dynamics are well characterized.[60,329–331]
As the main technique dielectric relaxation spectroscopy (DRS) was used as it has proven to be a powerful tool to study the dynamics of electrolyte solutions[57,77,332] and ILs.[36,58,107] DRS measures fluctuations of the macroscopic dipole moment of the sample and is therefore sensitive to the reorientation of dipolar species in general and to ion-pairs in particular.[57] Furthermore, this technique yields information on solute-solvent interactions and is the only method allowing determination of the static permittivity of conducting samples. Note that the frequency-dependent dielectric properties of a solvent also determine how fast and efficient it can respond to changes in the charge distribution of a solute, affecting thus fast photochemical and electron transfer reactions therein.[38,333]

5.2 Experimental

5.2.1 Materials and auxiliary measurements

Purification of EAN and AN and sample preparation of the binary EAN + AN mixtures was conducted as described in Section 2.1.

Densities, ρ, required for calculating the molar concentrations of EAN, c_{EAN}, and AN, c_{AN}, were measured at $(25.00 \pm 0.01)\,^{\circ}\mathrm{C}$ by a vibrating-tube densimeter (Anton Paar, Graz, Austria, DMA 5000 M) with a nominal uncertainty of $\pm 5 \cdot 10^{-6}\,\mathrm{g\,cm^{-3}}$ (Section 2.5.1). Viscosities, η, measured at $(25.00 \pm 0.05)\,^{\circ}\mathrm{C}$ were obtained with the help of an automated rolling ball microviscometer (Anton Paar, Graz, Austria, AMVn) having a repeatability of $\sim$0.5 % (Section 2.5.2). Electrical conductivities, κ, were determined at $(25.000 \pm 0.003)\,^{\circ}\mathrm{C}$ with an overall uncertainty of 0.5 % using the setup described previously (Section 2.5.3).[154,172] The obtained data for ρ, κ, molar conductivity, $\Lambda = \kappa/c_{\mathrm{EAN}}$, and η are summarized in Table 5.1.

Table 5.1: Density, ρ, electrical conductivity, κ, molar conductivity, Λ, and viscosity, η, of EAN+AN mixtures as a function of EAN mole fraction, x_{EAN}, at 25 °C.

x_{EAN}	ρ / g cm^{-3}	κ / S m^{-1}	Λ / mS m^2 mol^{-1}	x_{EAN}	η / mPa s
0	0.78664	–	–	0	0.3413[a]
0.0091	0.78536	0.291	1.694	0.1000	0.730
0.0155	0.79093	0.383	1.318	0.2000	1.43
0.0312	0.80407	0.565	0.9717	0.3500	3.20
0.0570	0.82491	0.832	0.7938	0.4998	6.36
0.0996	0.85879	1.264	0.7051	0.5999	9.67
0.1166	0.87039	1.468	0.7068	0.7000	15.1
0.1501	0.89057	1.791	0.6849	0.8002	20.9
0.2000	0.92578	2.319	0.6820	0.9500	33.6
0.2398	0.94666	2.718	0.6840	1	38.6
0.3008	0.98195	3.135	0.6498	–	–
0.3500	1.00768	3.368	0.6161	–	–
0.4002	1.02858	3.619	0.5968	–	–
0.5017	1.07085	3.599	0.5003	–	–
0.6123	1.11355	3.436	0.4137	–	–
0.6989	1.13739	3.118	0.3448	–	–
0.7967	1.16500	2.800	0.2850	–	–
0.8948	1.18790	2.525	0.2401	–	–
0.9500	1.19966	2.381	0.2188	–	–
1	1.21047	2.238	0.1998	–	–

[a] Taken from Ref. 334

5.2.2 Dielectric Spectroscopy

Dielectric spectra were recorded in the frequency range of $0.2 \leq \nu/\,\mathrm{GHz} \leq 89$ at $(25.00 \pm 0.05)\,^{\circ}\mathrm{C}$. For $0.2 \leq \nu/\,\mathrm{GHz} \leq 50$ a dielectric probe kit consisting of two reflection probe heads (Agilent 85070E-020 for 0.2-20 GHz, Agilent 85070E-050 for 1.0-50 GHz) was connected to a vector network analyzer (VNA, Agilent E8364B) via an electronic calibration module (ECal, Agilent N4693A).[59,213] Prior to measurement the probes were calibrated with air, mercury and DMA as primary calibration standards. To account for calibration errors a complex Padé-correction was applied using AN, BN and 1-BuOH as secondary standards.[46] For selected samples the Padé-correction was assessed with the help of a variable-pathlength waveguide transmission cell covering $27 \leq \nu/\,\mathrm{GHz} \leq 40$ that was mounted to the VNA as such measurements do not require calibration.[59,139] In Figure 5.1 it is shown that for mixtures with $0 \leq x_{\mathrm{EAN}} \leq 0.2398$ combination of AN+BN+1-BuOH provided the best data set, whereas for $0.2398 < x_{\mathrm{EAN}} \leq 1$, DMA+BN+1-BuOH were more appropriate.

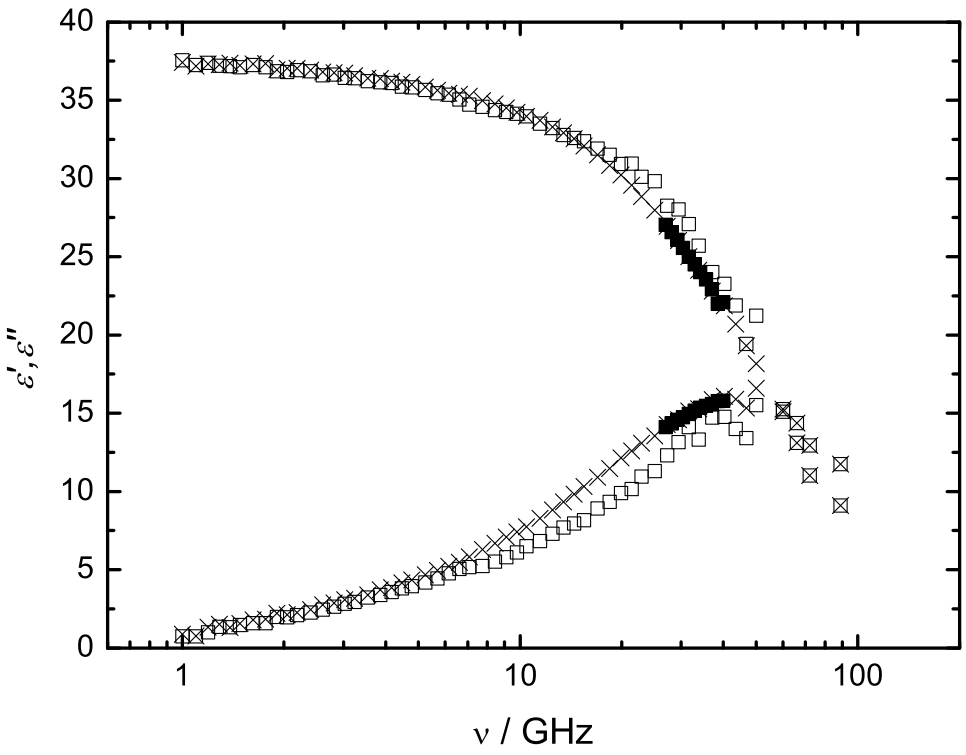

Figure 5.1: Dielectric permittivity, $\varepsilon'(\nu)$, and loss, $\varepsilon''(\nu)$, spectra of EAN+AN mixture with $x_{\mathrm{EAN}} = 0.0091$ obtained from VNA measurements with the 50 GHz probe head compared to A-band data (■). 50 GHz probe head data were Padé-corrected using DMA+BN+1-BuOH (□) and AN+BN+1-BuOH (×), respectively.

The 60-89 GHz region was covered with a waveguide interferometer.[139] The combined $0.2 \leq \nu/\,\mathrm{GHz} \leq 89$ spectra of $\hat{\eta}(\nu)$ were then corrected for dc conductivity to extract $\hat{\varepsilon}(\nu)$ for further processing. In this procedure κ was treated as an adjustable parameter with the

experimental data as the starting values to account for fringing-field contributions arising from geometrical imperfections of the VNA probes.[57] The dielectric data obtained from fitting these spectra are summarized in Table 5.2.

Table 5.2: Dielectric relaxation parameters of EAN+AN mixtures at 25 °C: static permittivity, ε_s, high frequency limit of permittivity, ε_∞, relaxation amplitudes, S_j, relaxation times, τ_j, symmetrical, α_1, and asymmetrical, β_1, width parameter and reduced error function, χ^2_r, as a function of EAN mole fraction, x_{EAN}, and molar concentration of EAN, c_{EAN}.[a]

x_{EAN}	c_{EAN}	ε_s	S_1	α_1	β_1	τ_1	S_2	τ_2	ε_∞	$\chi^2_r \cdot 10^4$
0	0	35.84	–	–	–	–	32.51	3.32	3.33	–
0.0091	0.172	38.28	4.85	0.31	1.00	20.4	29.92	3.42	3.51	174
0.0155	0.291	39.88	9.08	0.36	1.00	16.7	28.19	3.36	2.61	141
0.0312	0.582	43.79	17.16	0.38	1.00	20.4	24.58	3.45	2.05	511
0.0570	1.048	49.12	26.63	0.44	1.00	27.7	20.62	3.82	1.87	489
0.0996	1.793	52.87	32.91	0.42	1.00	37.3	17.66	4.60	2.30	528
0.1166	2.077	54.71	37.52	0.45	1.00	36.7	15.64	4.96	1.56	429
0.1501	2.615	53.31	37.57	0.42	1.00	34.5	13.55	5.05	2.19	605
0.2000	3.400	48.95	35.01	0.38	1.00	29.7	10.94	5.17	3.00	463
0.2398	3.973	47.54	37.13	0.36	1.00	25.4	7.87	6.36	2.54	361
0.3008	4.825	43.80	31.41	0.33	1.00	31.0	7.91	7.23	4.48	100
0.3500	5.467	38.02	30.48	0.25	1.00	22.7	3.28	4.93	4.26	258
0.4001	6.063	35.62	27.56	0.23	1.00	24.4	3.32	6.02	4.74	177
0.5017	7.193	31.17	23.52	0.18	1.00	28.8	2.71	4.09	4.93	226
0.6123	8.304	28.54	20.87	0.18	1.00	39.1	2.16	3.62	5.51	45.1
0.6989	9.042	27.39	21.13	0.13	0.79	60.3	2.57	0.816	3.68	82.5
0.7968	9.825	27.65	21.69	0.12	0.70	92.5	2.25	0.746	3.70	150
0.8947	10.519	28.21	22.64	0.07	0.57	153	2.64	0.204	2.92	64.4
0.9500	10.880	27.98	22.50	0.04	0.55	162	3.33	0.192	2.16	124
1	11.198	28.38	22.89	0.00	0.51	203	3.38	0.171	2.11	148

[a] Units: c_{EAN} in mol L^{-1}, τ_j in ps;

5.3 Results and Discussion

5.3.1 Choice of fit model

In the frequency range of 0.2-89 GHz the dielectric spectrum of neat AN at 25 °C is very well fitted by a single Debye (D) equation centered at ∼48 GHz (parameters $S = 32.51$, $\tau = 3.32$ ps, $\varepsilon_\infty = 3.33$). This mode is associated with the rotational diffusion of AN dipoles[60,332] and accounts for ∼95 % of the total dispersion from $\varepsilon_s = 35.84$ at $\nu \to 0$ to $\varepsilon_\infty^{FIR} = 1.81$ in the far infrared so that the small resonance-type processes outside the present

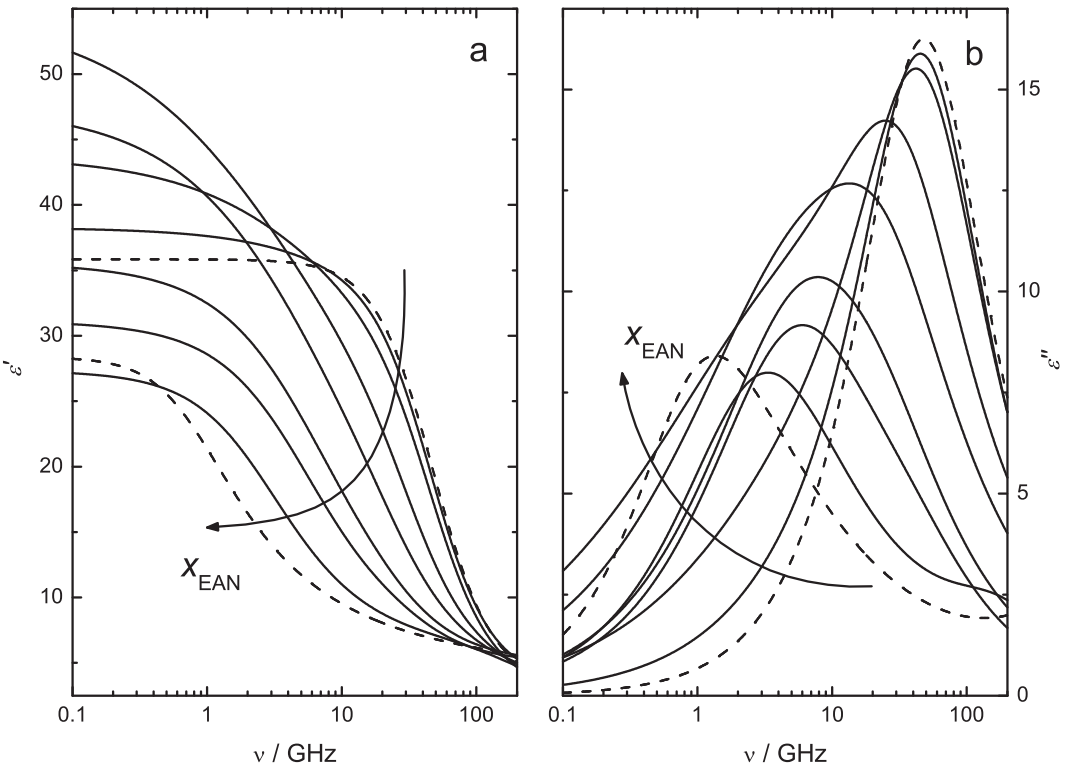

Figure 5.2: (**a**) Dielectric permittivity, $\varepsilon'(\nu)$, and (**b**) loss, $\varepsilon''(\nu)$, spectra of neat AN and EAN (dashed lines) and EAN+AN mixtures with x_{EAN} of 0.0312, 0.1167, 0.2398, 0.4002, 0.5017 and 0.6989 (solid lines) at 25 °C.

frequency range at $\sim$ 0.5 and 2 THz[49,60,329] can be neglected in the present analysis. On the other hand, two modes (the CDi+D model) are required to fit $\hat{\varepsilon}(\nu)$ of pure EAN in the same frequency range, see Table 5.2 for the parameters. This spectrum is dominated by the jump relaxation of $[EtNH_3]^+$ ions[107,208] peaking at $\sim$1 GHz which is best described by an inertia-corrected[106] CD equation (Eq. 1.37) with 5 THz rise rate (Section 3.1). Additionally, a small high-frequency D equation peaking outside the present frequency range is required to summarize the small contributions from intermolecular vibrations and librations at THz frequencies that extend below 89 GHz (Section 3.1).[107]

Data analysis revealed that for all mixture spectra a sum of two modes ($n = 2$ in Eq. 1.30) yielded the best fit (Figures 5.2 & 5.3). Up to IL mole fractions of $x_{\mathrm{EAN}} = 0.61$ a CC+D model was sufficient but above that concentration the shape of the lower-frequency mode becomes increasingly asymmetric ($\beta_1 < 1$; Figure 5.4b), so that a HNi+D model had to be used. For the HNi mode (Eq. 1.37) the inertial rise rate was fixed to the value of pure EAN, 5 THz. The so obtained parameters (Table 5.2) vary smoothly with x_{EAN} over the entire mixture range (Figures 5.4-5.8). The other tested models generally produced inferior fits and/or widely scattering parameters and were thus rejected. Note that this empirical decomposition of the dielectric spectra has to be taken with a grain of salt as computer simulations of Schröder *et al.* have clearly shown that at least for imidazolium-based ionic liquids and their mixtures with water rotational and translational modes of

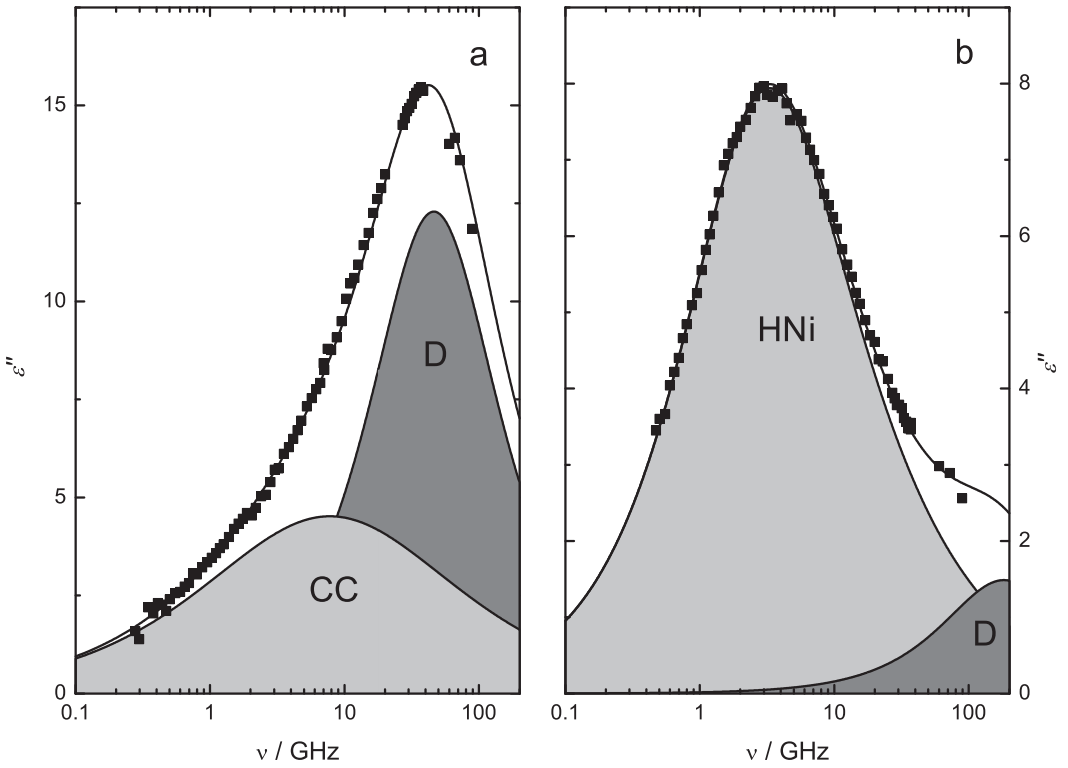

Figure 5.3: Dielectric loss spectra, $\varepsilon''(\nu)$, of EAN+AN mixtures at 25 °C and EAN mol fractions, x_{EAN}, of (**a**) 0.0312 and (**b**) 0.6989. Symbols represent experimental data, lines show (**a**) the CC+D and (**b**) the HNi+D fit; shaded areas indicate the individual processes.

all components stretch over large frequency ranges and strongly overlap.[42,45,205] However, as long as quantitative agreement between experimental and simulated dielectric spectra cannot be routinely achieved empirical decompositions, like the present CC+D or HNi+D models, have to be used.

Compared to mixtures of 1-alkyl-3-methylimidazolium ILs with AN[49] and dichloromethane (DCM),[47,48] where the spectra can be fitted with a CC+D model, some similarities but also marked differences are apparent. From the evolution of the resolved amplitudes and relaxation times it is obvious that for all mixtures studied so far, including the present EAN+AN system, the lower-frequency mode (1) is associated with the IL. At low IL content the higher-frequency mode (2) is dominated by the dipolar solvent (AN or DCM) but at $x_{\mathrm{IL}} \gtrsim 0.5$ essentially only the IL contribution remains. All mixtures exhibit a maximum in the static permittivity at low IL content, which is an indication for ion-pair formation.[47–49] However, whilst only a small increase was observed for the static permittivity of imidazolium IL + AN mixtures, followed by a monotonic decrease to the value of the pure IL, the present mixtures show a huge rise from $\varepsilon_{\mathrm{s}} = 35.84$ for pure AN to 54.71 at $x_{\mathrm{EAN}} = 0.12$ (Figure 5.4a). This suggests considerable formation of a species with large dipole moment, namely contact ion pairs (CIPs, see below) for $0 < x_{\mathrm{EAN}} \lesssim 0.5$. Interestingly, the static permittivity shows also a weak minimum at $x_{\mathrm{EAN}} \approx 0.7$, the

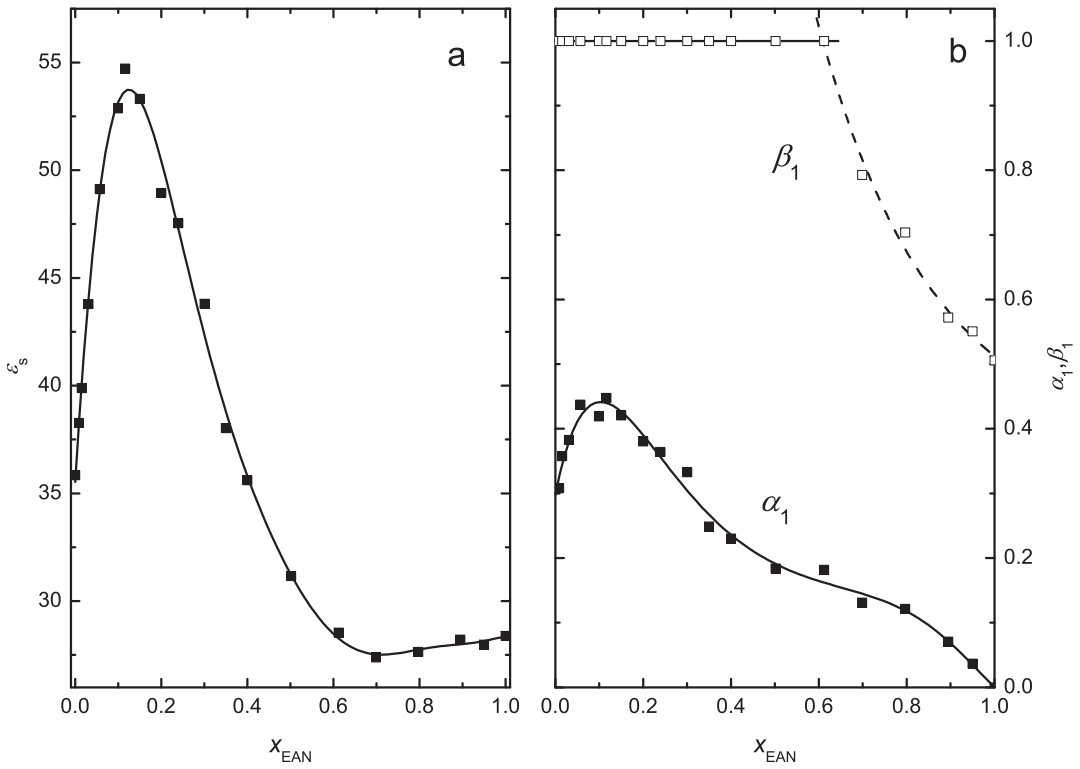

Figure 5.4: (**a**) Static permittivity, ε_s, and (**b**) width parameters α_1 (■) and β_1 (□). Solid and dashed lines are just a guide to the eye.

composition where the transition from the CC+D to the HNi+D model occurs (Figure 5.4).

5.3.2 Higher frequency mode

5.3.2.1 Relaxation times.

The concentration dependence of relaxation time, τ_2 (Figure 5.5), and amplitude, S_2 (Figure 5.6a), reveals that at low IL content the higher-frequency mode 2 is associated with the reorientation of AN dipoles. Information on the underlying relaxation mechanism comes from the corresponding rotational correlation time, τ_2', obtained from the cooperative relaxation time τ_2 with the help of the Powles-Glarum equation[125] (Eq. 1.71 with $j = 2$, where $\varepsilon_2 = \varepsilon_s - S_1$ and $\varepsilon_3 = \varepsilon_\infty$). For $x_{EAN} \leq 0.3$ τ_2' is proportional to viscosity, η (Figure 5.5), suggesting that in this region, corresponding to IL concentrations $c_{EAN} \lesssim 4.8\,M$, solvent relaxation is through rotational diffusion of individual dipoles. This is typical for electrolyte solutions in dipolar aprotic solvents.[49,332,335] For $x_{EAN} \geq 0.3$ the linear relation between τ_2' and η breaks down, suggesting a rapid decrease of "freely" rotating AN dipoles and increasing dominance of fast EAN modes.

From the slope of the linear range of Figure 5.5 the very small effective volume, $V_{eff} = V_m f_\perp C$, of 2.02 Å^3 can be extracted.[122] For values of $V_m = 43.9$ Å^3 and $f_\perp = 1.208$ taken as the molecular volume and shape factor of the AN molecule[336,337] this results in a friction

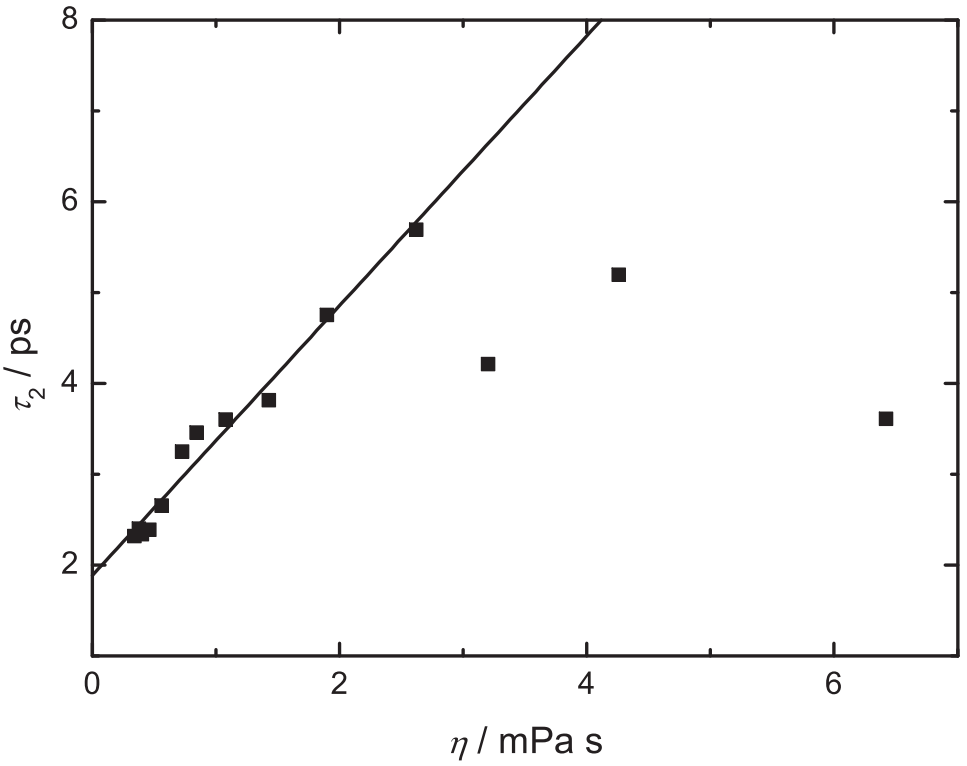

Figure 5.5: Dielectric relaxation time, τ_2 (■), as a function of solution viscosity, η.

coefficient of $C = 0.038$. Similar small values were found for AN solutions of 1-alkyl-3-methylimidazolium tetrafluoroborates ($C = 0.033$),[49] NaI (0.063) and Bu_4NBr (0.068).[332] On the other hand, from the temperature dependence of the relaxation time of pure AN a value of $C = 0.119$ was obtained,[60] which is virtually identical to the theoretically predicted friction factor for rotation under slip hydrodynamic boundary conditions, $C_{\text{slip}} = 1 - f_{\perp}^{2/3} = 0.118$.[122] As argued previously,[49,57] this indicates that for dipolar aprotic solvents, like AN, the rise of solution viscosity with salt/IL content is due to mixing particles of different size but not to long-range electrostatic interactions. Although ion solvation occurs in the present mixtures and manifests in "freezing" AN molecules adjacent to the cations, see below, it appears that the influence of the ions on solvent rotational dynamics is limited to their first solvation shell. It is interesting to note that this simple behavior prevails up to $x_{\text{EAN}} = 0.3$, *i.e.* almost a 1:1 ratio of ions to solvent molecules.

5.3.2.2 Amplitudes.

For dipole mixtures where the modes resolved in the dielectric spectrum can be assigned to individual species the Cavell equation (Eq. 1.52; with $A = 1/3$) relates the amplitude, S_j, of mode j to the concentration, c_j, and the effective moment, $\mu_{\text{eff},j}$, of the dipole.[115,117] From the amplitude of pure AN, $S_2 = 32.51$ (Table 5.2), and its density and molar mass the effective dipole moment of $\mu_{\text{eff,AN}} = 4.34\,\text{D}$ was obtained. Assuming that this value applies for the entire mixture range, the expected AN amplitude, $S_{\text{AN}}^{\text{calc}}$, shown as the solid

line in Figure 5.6a was obtained from the analytical AN concentration, c_{AN} of the mixtures. Except for $x_{\mathrm{EAN}} > 0.9$, $S_{\mathrm{AN}}^{\mathrm{calc}}$ always exceeds the experimentally determined amplitude S_2, indicating that at least at low IL content only part of the AN is detected by DRS.
The DRS detectable (apparent) AN concentration, $c_{\mathrm{AN}}^{\mathrm{app}}$, can be calculated with Eq. 1.52 from the EAN corrected amplitude of mode 2, $S_{\mathrm{AN}} = S_2 - S_{\mathrm{EAN}}$ (dotted line in Figure 5.6a), assuming $S_{\mathrm{EAN}} = x_{\mathrm{EAN}} \times S_2(x_{\mathrm{EAN}} = 1)$. This in turn allows determination of the effective solvation number

$$Z_{\mathrm{ib}} = \frac{c_{\mathrm{AN}} - c_{\mathrm{AN}}^{\mathrm{app}}}{c_{\mathrm{EAN}}} \tag{5.1}$$

shown in Figure 5.6b. At low IL content the obtained data exhibit a pronounced linear decrease from $Z_{\mathrm{ib}}^0 = 6.9 \pm 0.2$ at infinite dilution to ∼2 at $x_{\mathrm{EAN}} \approx 0.2$. Beyond this breakpoint Z_{ib} continues to decrease with significantly smaller slope. A similar behaviour was observed for the effective solvation numbers of 1-alkyl-3-methylimidazolium tetrafluoroborates in AN, which also drop from ∼6-7 at $x_{\mathrm{IL}} \to 0$ to ∼2 at $x_{\mathrm{IL}} \approx 0.2$.[49] For electrolyte solutions decreasing Z_{ib} with increasing salt concentration is common and explained in terms of solvation-shell overlap.[57,338] This certainly also applies to the dilute IL solutions. The breakpoint at $x_{\mathrm{EAN}} \approx 0.2$ may be related to the pronounced formation of contact ion pairs (CIPs) for this system (see below) which should be associated with at least partial desolvation of the CIPs due to charge neutralization. This interpretation would explain, why the maximum of S_1 (Table 5.2) and thus of the CIP concentration is at $x_{\mathrm{EAN}} \approx 0.2$.
The infinite dilution value, Z_{ib}^0, is a measure for the strength of ion-solvent interactions and can be compared to coordination numbers from scattering experiments or computer simulations, as well as to other effective solvation numbers.[57] Apparently, no literature data for solvation numbers of EAN in AN are available but Perron *et al.*[81] conclude from the viscosity B parameter that "electrostriction or coulombic solvation is the leading effect in AN" (in contrast to the structure breaking effect claimed for aqueous solutions). Also, the present $Z_{\mathrm{ib}}^0 = 6.9 \pm 0.2$ is broadly compatible with values observed for alkaline ($Z_{\mathrm{ib}}^0(\mathrm{LiClO_4^-}) = 6.3$; $Z_{\mathrm{ib}}^0(\mathrm{NaClO_4^-}) = 4.9$) and alkaline earth perchlorates ($Z_{\mathrm{ib}}^0(\mathrm{Mg(ClO_4)_2^-}) = 9.9$; $Z_{\mathrm{ib}}^0(\mathrm{Ca(ClO_4)_2^-}) = 6.9$).[338] The latter data can be interpreted as cation solvation numbers as $\mathrm{ClO_4^-}$ was found to be unsolvated in AN.[339] No direct information on nitrate solvation is available but because of the small acceptor number of AN also only weak interactions with this anion are expected.[332,340] On the other hand, in addition to electrostatic ion-dipole interactions, also hydrogen bonding between $[\mathrm{EtNH_3}]^+$ and the nitrile group of AN is possible, similar to what was observed for AN + water mixtures.[341,342] Thus, it appears reasonable to attribute also the present Z_{ib} values mainly to cation-solvent interactions.
From its definition Z_{ib} is the number of "missing" AN molecules per EAN ion pair, *i.e.* of solvent molecules that differ so much in their dynamics from "free" AN that they do not contribute to mode 2 anymore. The question then appears whether these solvent molecules interact so strongly with the ions that they are completely immobilized or just slowed down and therefore pop up as a new lower-frequency mode in the dielectric spectrum.[57] For the investigated AN + 1-alkyl-3-methylimidazolium tetrafluoroborate mixtures the latter was found, with the "slow AN" contribution accidentally overlapping with the IL mode.[49] However, for the present EAN + AN mixtures an analysis along the lines of Ref.

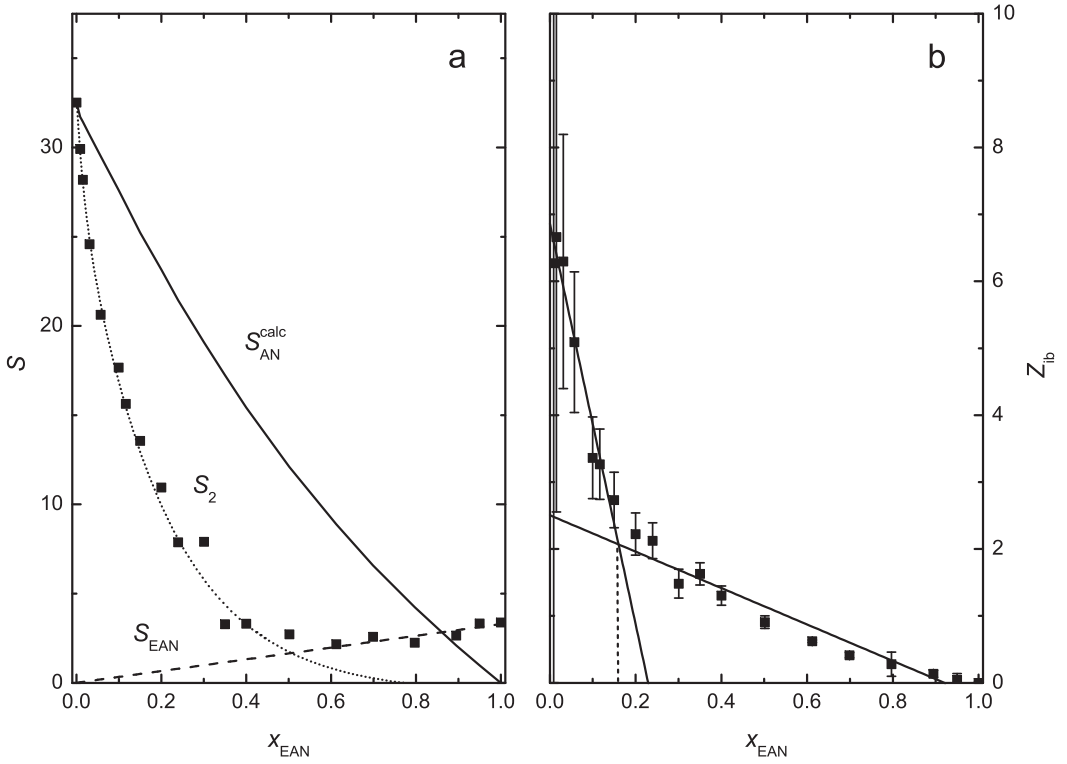

Figure 5.6: (**a**) Observed amplitudes, S_2 (■), of mode 2 and (**b**) effective solvation numbers, Z_{ib}, as a function of EAN mole fraction, x_{EAN}. In (**a**) the full line shows the expected AN amplitude, $S_{\mathrm{AN}}^{\mathrm{calc}}$; the dashed line represents the contribution of EAN, S_{EAN}, to S_2, assumed to increase linearly with x_{EAN}, and the dotted line indicates the contribution of "free" AN, S_{AN}. Solid lines in (**b**) indicate linear fits.

49 yielded incompatible results. In particular, the derived ion-pair association constant was at variance with the literature (see below). Thus, we may conclude that $[EtNH_3]^+$-AN interactions are strong enough to immobilize the solvating molecules on the timescale probed by our dielectric spectra.

5.3.3 Lower frequency mode

5.3.3.1 Relaxation times.

Although the $[EtNH_3]^+$ cation possesses a significant permanent dipole moment, its value of $\mu_+ = 3.9\,\mathrm{D}$[214] is not sufficient to explain the pronounced maxima of ε_s (Figure 5.4a) and S_1 (Figure 5.8a). Therefore, similar to other IL+aprotic solvent mixtures,[47–49] the simultaneous presence of free cations and ion pairs can be reasonably assumed, although the individual contributions of both dipolar species to the dielectric spectra of the mixtures cannot be resolved. However, their existence is clearly manifested in the concentration dependence of relaxation time, τ_1 (Figure 5.7a), and α_1 parameter (Figure 5.4b) of mode 1. The initial increase of both quantities, with maxima at $x_{\mathrm{EAN}} \approx 0.1$ and subsequent decrease indicates that shape and peak position of mode 1 are determined by the relative

weights of the ion-pair and cation relaxations of (unknown) relaxation times $\tau_{IP} > \tau_+$. The observed variation of τ_1 and α_1 can be rationalized as follows: As shown below ion pairs largely predominate at low x_{EAN}, thus a rather small α_1 with τ_1 dominated by the lower-frequency ion-pair relaxation, but with increasing x_{EAN} the fraction of free cations increases, so that α_1 increases. As both relaxation times, τ_{IP} and τ_+, will increase with increasing viscosity τ_1 also increases despite growing cation contribution. At $x_{EAN} \approx 0.1$ ion-pair and cation contributions are comparable, thus maximum width of mode 1. For larger EAN mole fractions ion pairs re-dissociate and free cations become more and more important. Therefore, α_1 and τ_1 decrease again. This scenario of pronounced ion-pair formation up to $x_{EAN} \approx 0.1$ followed by subsequent re-dissociation is supported by the initial strong decrease and subsequent plateau of the molar conductivity, Λ (for better comparison with corresponding relaxation times and viscosities normalized reciprocal molar conductivities, Λ_{EAN}/Λ, are shown in Figure 5.7a). Note, that the rather small relaxation times ($\tau_1 < 40$ ps, Table 5.2) for $x_{EAN} \leq 0.4$, as well as the fact that ion-pair and cation modes could not be separated, indicate that the sizes of the cation and the formed ion pair are rather similar. This points at contact ion pairs (CIPs) as the dominating aggregate.

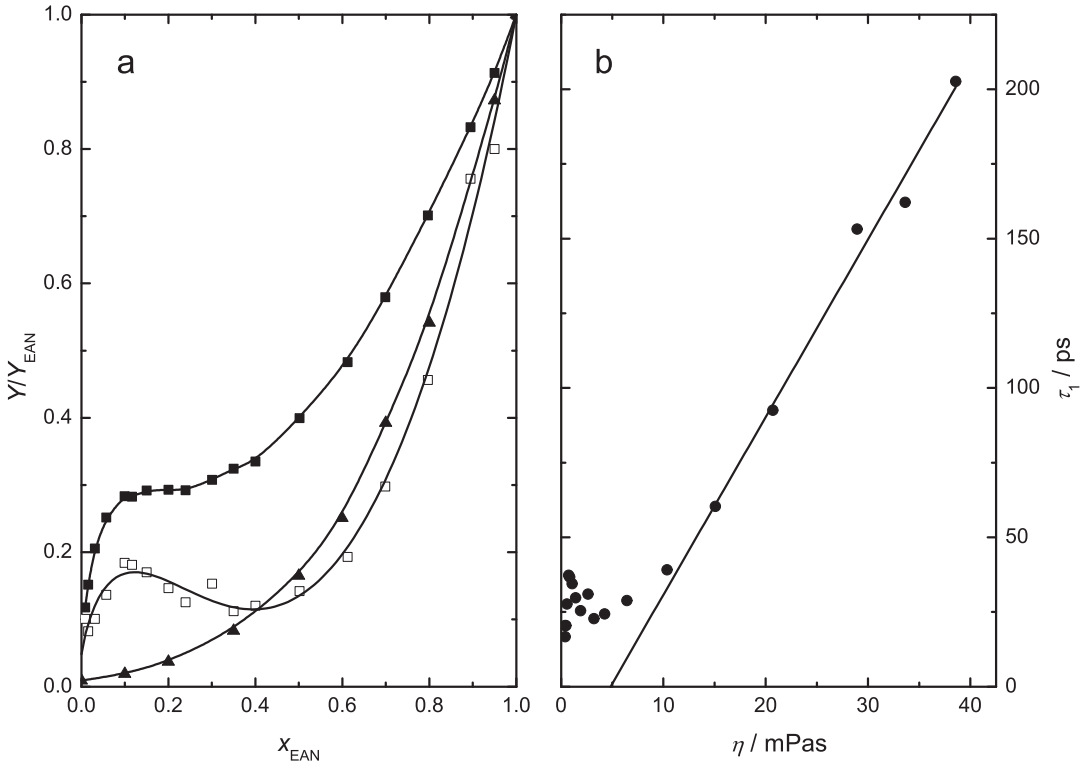

Figure 5.7: (**a**) Normalized transport quantities, Y/Y_{EAN}, of EAN+AN mixtures at 25 °C with $Y = \tau_1$ (relaxation time of mode 1; □), $Y = \eta$ (solution viscosity; ▲) and $Y = \Lambda^{-1}$ (reciprocal molar conductivity; ■) where Y_{EAN} is the corresponding quantity of neat EAN. Lines are visual guides only. (**b**) Relaxation time τ_1 (•) as a function of viscosity, η, with linear fit (solid line) for $0.7 \leq x_{EAN} \leq 1$.

At $x_{\mathrm{EAN}} \approx 0.5$ the strong increase of viscosity causes τ_1 to rise again and for $0.7 \leq x_{\mathrm{EAN}} \leq 1$ the relaxation time is even proportional to viscosity (Figure 5.7b). From the slope of τ_1 *vs.* η a friction coefficient of $C = 0.127$ can be calculated, which is close to that of neat EAN ($C = 0.091$), obtained from temperature-dependent measurements (Section 3.1). This implies that the dynamical properties of pure EAN are preserved down to a dilution of $x_{\mathrm{EAN}} \approx 0.5$ (Figure 5.7a) and suggests that AN acts as a "lubricant" accelerating the overall dynamics, similar to what was found for 1-alkyl-3-methylimidazolium IL+AN mixtures.[49] The similar friction coefficients also suggest that at least down to $x_{\mathrm{EAN}} \approx 0.7$ the $[\mathrm{EtNH_3}]^+$ cation relaxes via large-angle jumps as the pure IL (Section 3.1).[107,208]

5.3.3.2 Amplitude.

With Eq. 1.52 the conclusions made in Section 5.3.2.1 can be confirmed and extended quantitatively. Figure 5.8a shows that, except for the most EAN-rich mixtures, cation relaxation alone cannot explain the amplitude of mode 1. With decreasing IL content the effective dipole moment, $\mu_{\mathrm{eff,EAN}}$, calculated with Eq. 1.52 from S_1 and the analytical EAN concentration, c_{EAN}, strongly increases from $\mu_{\mathrm{eff,EAN}} = 4.8\,\mathrm{D}$, for pure EAN to 19.3 D at $x_{\mathrm{EAN}} \to 0$ (Figure 5.8b). This pronounced change of $\mu_{\mathrm{eff,EAN}}$, together with the changes of τ_1 and α_1 at low x_{EAN} (Figure 5.7), strongly hints at an equilibrium between free cations and EAN ion pairs.

Indeed, the $x_{\mathrm{EAN}} = 1$ value (4.8 D) can be attributed to the effective dipole moment of the $[\mathrm{EtNH_3}]^+$ cation,[107,208] $\mu_{\mathrm{eff},+}$, as it is in excellent agreement with semiempirical calculations[174] for this entity, yielding 4.9 D. Also, the infinite-dilution limit of $\mu_{\mathrm{eff,EAN}}$ (19.3 D) is compatible with the dipole moment of a contact ion-pair (CIP) as semiempirical calculations[174] yielded 15.8 D and 18 D, depending on the relative orientations of $\mathrm{NO_3^-}$ and $[\mathrm{EtNH_3}]^+$. For the solvent-shared ion pair (SIP) the considerably larger value of 40.1 D was obtained. The present $x_{\mathrm{EAN}} \to 0$ limit of $\mu_{\mathrm{eff,EAN}}$ also agrees well with the estimate of 16.3 D by Weingärtner *et al.*[52]

For mixtures of imidazolium ILs with AN $\mu_{\mathrm{eff,IL}}$ values remained essentially equal to $\mu_{\mathrm{eff},+}$ down to $x_{\mathrm{IL}} \approx 0.2$ before steeply increasing to $\mu_{\mathrm{eff,CIP}}$ on further dilution. Together with other characteristic changes of the relaxation parameters this was attributed to a rather rapid transition of the dynamics from IL-like to electrolyte-solution-like behavior.[49] For EAN+AN the transition is much smoother. This observation, as well as the sharply increasing asymmetry of mode 1 (*i.e.* decreasing β_1, Figure 5.4b) for $x_{\mathrm{EAN}} \gtrsim 0.6$ may hint at microheterogeneities with AN-rich domains containing CIPs and EAN-rich domains showing the same dynamics as the pure IL. As strong hydrogen bonds between anions and cations are a dominant feature for pure EAN (Section 3.1)[64,208] such a hypothesis is supported by a comparison to mixtures of AN+water, where the formation of water clusters induced by hydrogen-bonding is well known.[341,343]

To account for the simultaneous contributions of CIPs and free dipolar cations to S_1 Eq. 1.52 modifies to

$$S_1 = \frac{\varepsilon_{\mathrm{s}}}{2\varepsilon_{\mathrm{s}} + 1} \frac{N_{\mathrm{A}}}{k_{\mathrm{B}} T \varepsilon_0} [(c_{\mathrm{EAN}} - c_{\mathrm{CIP}}) \mu_{\mathrm{eff},+}^2 + c_{\mathrm{CIP}} \mu_{\mathrm{eff,CIP}}^2] \tag{5.2}$$

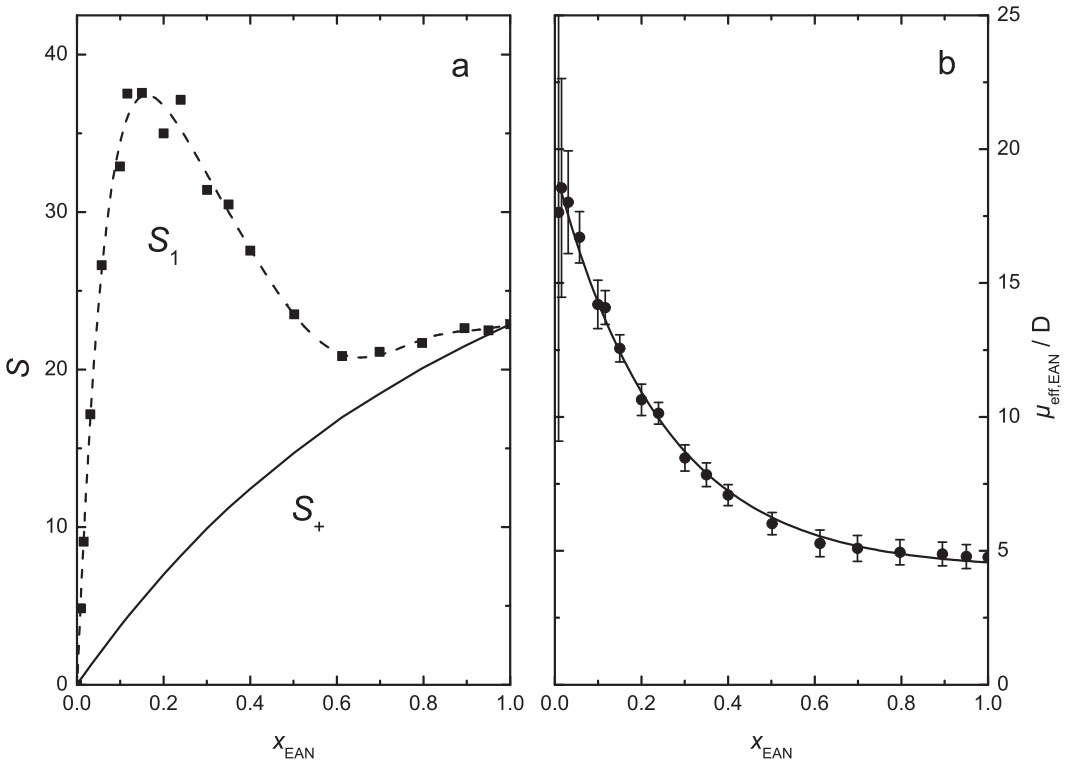

Figure 5.8: (**a**) Amplitude of the lower-frequency mode, S_1 (■), of EAN+AN mixtures at 25 °C and predicted amplitude, S_+ (solid line), if only $[EtNH_3]^+$ cations would contribute. (**b**) Effective dipole moment, $\mu_{\mathrm{eff,EAN}}$ (•), calculated from S_1 and c_{EAN} with Eq. 1.52. The solid line represents an exponential fit; error bars correspond to the standard error ($\sigma(S_1) = 1.1$) for the polynomial fit of S_1 (broken line in (**a**)).

where $c_{\mathrm{EAN}} = c_+ + c_{\mathrm{CIP}}$ is the total concentration of EAN, and c_+ and c_{CIP} are the concentrations of free cations and CIPs, respectively. Here it is assumed that dipole-dipole correlations between cations and ion pairs are negligible. At least for dilute solutions this should be reasonable so that the determined value of the standard-state association constant is not significantly affected.
Inserting the limiting values of $\mu_{\mathrm{eff,EAN}}$, 4.8 D and 19.3 D, for $\mu_{\mathrm{eff},+}$ and $\mu_{\mathrm{eff,CIP}}$ into Eq. 5.2 then yields c_{CIP} and c_+, and thus the corresponding association constants

$$K_{\mathrm{A}} = \frac{c_{\mathrm{CIP}}}{(c_{\mathrm{EAN}} - c_{\mathrm{CIP}})^2} \tag{5.3}$$

shown in Figure 5.9b. This, in turn, allows determination of the standard state association constant, K_{A}^0, by extrapolation with a Guggenheim-type equation[77]

$$\log K_{\mathrm{A}} = \log K_{\mathrm{A}}^0 - \frac{2A_{\mathrm{DH}}\sqrt{I}}{1 + R_{ij}B_{\mathrm{DH}}\sqrt{I}} + A_{\mathrm{K}}I + B_{\mathrm{K}}I^{3/2} \tag{5.4}$$

where $I(\equiv c_{\mathrm{EAN}})$ is the stoichiometric (nominal) ionic strength. The required Debye-Hückel constants for the activity coefficients in AN, $A_{\mathrm{DH}} = 1.643\,\mathrm{L}^{1/2}\,\mathrm{mol}^{-1/2}$ and $B_{\mathrm{DH}} = 4.857 \times$

$10^{-9}\,\mathrm{L}^{1/2}\,\mathrm{mol}^{1/2}\,\mathrm{m}^{-1}$, were calculated according to Ref. 344. For the upper limit of ion association, $R_{ij} = 0.325\,\mathrm{nm}$, the MOPAC[174] value for the contact distance was used; $A_\mathrm{K}(= -2.149\,\mathrm{L\,mol^{-1}})$ and $B_\mathrm{K}(= 0.5772\,\mathrm{L}^{3/2}\,\mathrm{mol}^{-3/2})$ are empirical fit parameters.

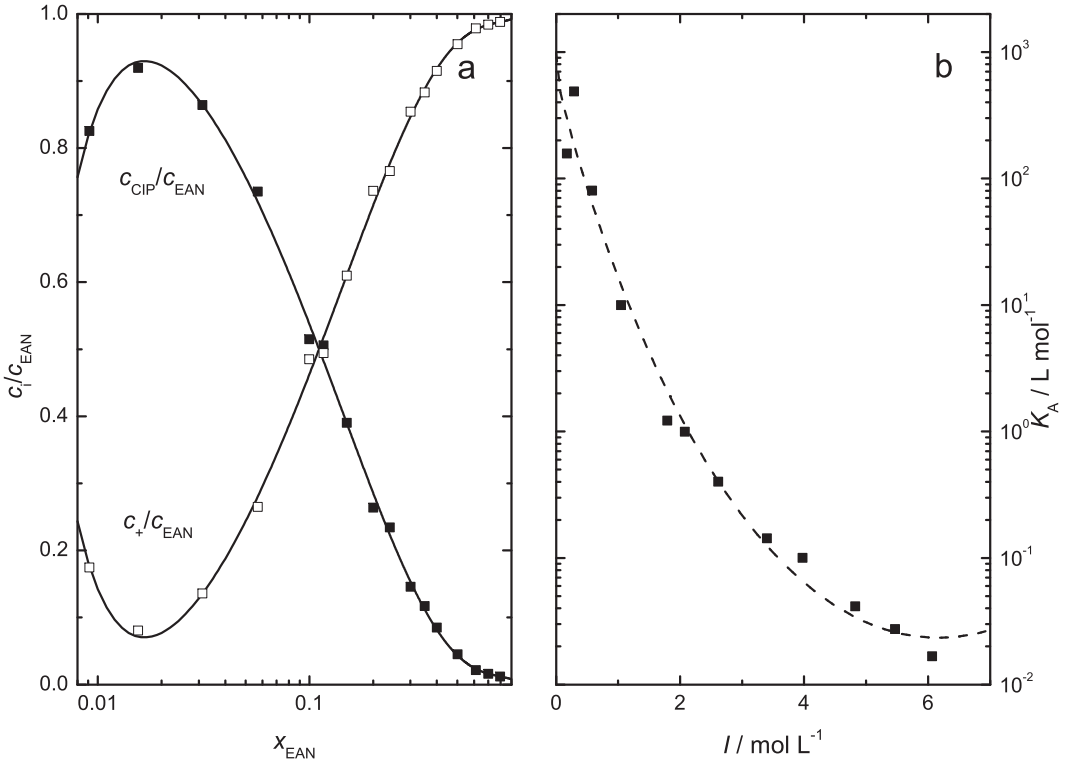

Figure 5.9: (**a**) Relative concentrations of contact ion pairs, $c_\mathrm{CIP}/c_\mathrm{EAN}$ (■) and $[\mathrm{EtNH_3}]^+$, c_+/c_EAN (□). (**b**) Association constants, K_A (■) as a function of nominal ionic strength, I, at 25 °C. Solid lines (**a**) are visual guides; the dashed line (**b**) represents the fit with eq. 5.4.

Since dielectric spectra were only recorded for $c_\mathrm{EAN} \geq 0.172\,\mathrm{mol\,L^{-1}}$ the so extrapolated value for the standard-state equilibrium constant, $K_\mathrm{A}^0 = (970 \pm 350)\,\mathrm{L\,mol^{-1}}$, is only an estimate. Nevertheless, it is in very good agreement with the value determined by Perron *et al.*[81] with dilute-solution conductivity measurements ($K_\mathrm{A}^0 = 1094\,\mathrm{L\,mol^{-1}}$). Together with the inference from τ_1 (see above) this confirms CIPs as the predominating ion-pair species as the assumption of solvent-shared ion pairs would lead to unreasonably small K_A^0 but require significantly larger τ_1. Unrealistic association constants were also obtained for the assumption that the bound solvent, corresponding to $Z_\mathrm{ib} > 0$ derived from S_2, contributes to S_1.

Except may be for $[\mathrm{C_2mim}][\mathrm{BF_4}]$ ($K_\mathrm{A}^0([\mathrm{C_2mim}][\mathrm{BF_4}])= 245\,\mathrm{L\,mol^{-1}}$), which is probably an outlier when compared to the conductivity value,[49] the standard-state association constants found for 1-alkyl-3-methylimidazolium tetrafluoroborates in AN ($K_\mathrm{A}^0([\mathrm{C_4mim}][\mathrm{BF_4}])= 33.9$ $\mathrm{L\,mol^{-1}}$; $K_\mathrm{A}^0([\mathrm{C_6mim}][\mathrm{BF_4}])= 9.77\,\mathrm{L\,mol^{-1}}$) are very similar to data for other 1:1 electrolytes in this solvent.[49] The large value of $K_\mathrm{A}^0 = (970 \pm 350)\,\mathrm{L\,mol^{-1}}$ for EAN, which even exceeds the association constants of 2:1 electrolytes by a factor of at least 2 ($K_\mathrm{A}^0(\mathrm{Ca(ClO_4)_2})=$

$550\,\mathrm{L\,mol^{-1}}$)[338] but generally $\gtrsim 5$,[338,345] is thus exceptional and indicates that Coulomb interactions are not the main driving force for EAN association in AN. This conclusion is supported by the prevalence of CIPs despite strong cation solvation. Keeping in mind the importance of hydrogen bonding for the properties of pure EAN[28,52,64] we may therefore safely conclude that strong hydrogen bonding between $[EtHN_3]^+$ and NO_3^- dominates ion-ion interactions in mixtures with AN and possibly also other dipolar aprotic solvents.

5.4 Concluding Remarks

To some extent the dielectric relaxation behaviour of the present EAN+AN mixtures is reminiscent to that of AN+imidazolium tetrafluoroborate systems.[49] In particular, mixture dynamics has molten-salt character down to $x_{\mathrm{EAN}} \approx 0.5$ with added AN acting as a "lubricant" for the collective translational and rotational motions. In this region only bound but no free AN molecules can be detected by DRS, in line with recent MD simulations and optical Kerr-effect studies on $[C_5mim][NTf_2]$+AN, showing AN dipoles oriented towards the imidazolium moiety of the cations.[346] With aprotic imidazolium ILs EAN also shares the smooth transition to electrolyte-solution behaviour at $x_{\mathrm{EAN}} \approx 0.4 - 0.5$. What differs is the stronger cation-solvent interaction of $[EtNH_3]^+$, compared to imidazolium cations, as for the latter solvating AN molecules are only slowed down[49] but not frozen on the timescale of the present experiments. The major distinction between protic and aprotic ILs in mixtures with aprotic solvents (as far as the present results can be generalized) is the strong tendency of EAN to form CIPs, which seem to prevail to some extent even at $x_{\mathrm{EAN}} > 0.5$ (Figure 5.8).

It would be interesting to see how this combination of stronger cation solvation **and** H-bond driven CIP formation affects other mixture properties, in particular solvation dynamics. In this area dielectric continuum models are know to work surprisingly well for polar liquids[347] and even for protic solvents like water.[348] Although the treatment of dc conductivity is still a matter of discussion, continuum models appear also to be suitable for aprotic ionic liquids.[38,349,350] For imidazolium ILs+water the situation is not so clear yet[351] as the experimental solvation response functions neither agree with a continuum treatment of the dielectric data nor with a more elaborate molecular model.[352]

From their structure acetonitrile, ethylammonium and nitrate are rather simple molecules/ions and thus within the reach of modern theoretical and simulation methods (although proper treatment of hydrogen bonding may be a problem). This makes EAN+AN a benchmark system for mixtures of protic ionic liquids with aprotic solvents. It is therefore hoped that the present dielectric relaxation study stimulates further experimental and theoretical research into the dynamics of such mixtures with potential practical interest.

Summary and Conclusions

In this study a detailed investigation of the dielectric properties and cooperative dynamics of room-temperature ionic liquis (RTILs) is reported. In addition, physicochemical properties such as density, viscosity and electrical conductivity were collected for most of the studied samples. A major part of the present thesis focused on the analysis of temperature-dependent broadband DR and OKE spectra of neat model PILs and non-imidazolium AILs recorded over the exceptional wide frequency range $0.2 \lesssim \nu/\mathrm{GHz} \lesssim 10\,000$. In addition, a set of neat 1-methylimidazolium PILs was investigated in the limited frequency range $0.2 \leq \nu/\mathrm{GHz} \leq 89$. Furthermore, the binary mixture of the archetypal PIL ethylammonium nitrate (EAN) with acetonitrile (AN), representing a model system, was characterized with respect to solvent and solute dynamics over the entire composition range.

Dielectric relaxation spectroscopy (DRS) has been used as the main technique in this study. Extension of the frequency range up to 10 THz was accomplished by data sets obtained from THz-TDS and FIR spectroscopy in collaboration with groups from Freiburg (Prof. Dr. M. Walther, Albert-Ludwigs-Universität, Freiburg, Germany) and Glasgow (Prof. Dr. K. Wynne, Glasgow University, Glasgow, UK). Concatenation of the individual spectra yielded complete dielectric spectra capturing the entire intensity arising from orientational polarization. Within the present work, mathematical procedures, which have been first applied to RTILs for data processing and concatenation of the individual spectra by Hunger,[59] were implemented in convenient MATLAB routines.
Optical heterodyne-detected Kerr-effect (OKE) spectroscopy was used as a complementary technique to DRS, likewise, covering the wide time span from femtoseconds to nanoseconds. Whilst DRS is sensitive to fluctuations of the macroscopic dipole moment, OKE probes changes of the anisotropic part of the many-body polarizability tensor. Comparison of the spectra obtained from the two techniques enabled critical tests of the applied mathematical models to decompose the experimental data. Particular use was made of the different rank of relaxation times of DR and OKE spectroscopy allowing inferences on the underlying relaxation mechanism.
Within this thesis, a new fitting routine (DRSFit) was established in our group in close collaboration with Dr. D. A. Turton (Glasgow University, Glasgow, UK). The key advantage over the hitherto used program is the ability of fitting OKE spectra in addition to DR spectra. Furthermore, new empirical model functions such as the antisymmetrized Gaussian and the inertia-corrected and modified HN function were implemented, which are required to describe OKE and DR spectra over such a broad frequency range. Normalized amplitudes are automatically calculated by DRSFit and although it was not required for

the present work, a convenient tool to correct DR spectra for parasitic effects contributing at low frequencies such as electrode polarization was implemented.

Static Permittivity of neat RTILs

The static permittivity, ε_s, represents an important physical quantity that characterizes the solvation properties of a solvent. Whilst for non-conducting solvents capacitor experiments are commonly the method of choice to determine ε_s, such measurements are inapplicable to electrically conducting samples like ILs. In this regard, DRS represents the only technique available to directly determine ε_s by extrapolation of the frequency-dependent relative permittivity, $\varepsilon'(\nu)$, to zero frequency. Weingärtner *et al.*[55,353] have reported the most extensive set of static permittivities of RTILs at room temperature. Generally, their results are broadly consistent with those published by our group[46,58] but also show that the extrapolation procedure significantly depends on the applied relaxation model and is particularly exacerbated for rather viscous ILs, where ε' does not reach its plateau value at low frequencies within the accessible frequency range. Nevertheless, Weingärtner pointed out that the overall accuracy of ε_s is probably within $\sim 4\,\%$.[353]
In the present work, static permittivities of all investigated ILs were reported. Consistent with values from literature,[52,55] ε_s of the studied PILs EAN (27.3) and PAN (23.4) are considerably higher than those of most 1-alkyl-3-methylimidazolium ILs, which are typically in the range of $10 \lesssim \varepsilon_s \lesssim 18$ (Section 3.1).[55,58] In case of water and other hydrogen-bonded organic solvents, high static permittivities have been attributed to strong parallel dipole-dipole correlations,[86] which in some 2-hydroxy-ethylammonium PILs ($45 \lesssim \varepsilon_s \lesssim 86$),[353,354] are almost certainly present to a considerable extent. Dipole-dipole correlations also play a role in EAN and PAN as shown in the present work, although their values of ε_s can be primarily explained by the permanent dipole moments of $EtNH_3^+$ and $PrNH_3^+$. For 1-methylimidazolium PILs it was observed, that depending on the degree of proton transfer ε_s considerably varies from values typical for AILs (complete proton transfer, $[C_1ImH][DFA]$, $[C_1ImH][TFA]$ and $[C_1ImH][TFSA]$) to values similar to other PILs (incomplete proton transfer, $[C_1Im][HOAc]$). It was shown that this difference in ε_s can be explained by the considerable difference of permanent dipole moments between neutral and ionic species ($\mu_{C1Im} > \mu_{C1ImH+}$) but also by strong correlations of cation/anion dipoles (Section 3.2). Strong dipole-dipole correlations were also observed in the studied non-imidazolium AILs ($[S_{221}][TFSA]$, $[S_{222}][TFSA]$, $[C_4pyr][TFSA]$ and $[P_{14}][DCA]$), whose values of ε_s are in the same order of magnitude as those of common 1-alkyl-3-methylimidazolium ILs.[55,58]

Dynamics of RTILs

Intermolecular dynamics of representative neat PILs and non-imidazolium AILs were investigated by means of DRS and, for most of the samples, by OKE spectroscopy in the very broad frequency range $0.2 \lesssim \nu/\mathrm{GHz} \lesssim 10\,000$.
Particular focus was on the low-frequency part ($\nu \lesssim 100\,\mathrm{GHz}$), where relaxation processes dominate both DR and OKE spectra of RTILs. Decomposition and comparison of DR and OKE spectra of EAN, PAN, 1-methylimidazolium PILs, and non-imidazolium AILs

revealed that the relaxation of anions and cations takes place on the picosecond timescale, consistent with the dynamics of 1-alkyl-3-methylimidazolium ILs.[36,58,107] For ILs comprised of dipolar anions such as $TFSA^-$, $HOAc/OAc^-$, DFA^-, and TFA^- a distinct process assigned to anion relaxation could be resolved. A relaxation process mainly associated with cation reorientation was present in the spectra of all studied ILs and was found to contribute at lower frequencies than anion reorientation, consistent with the findings of 1-alkyl-3-methylimidazolium ILs.[36,58] However, as indicated by the strong dipole-dipole correlations in [TAS][TFSA] ILs, this mode appears to be a composite, where apart from cations also some anions may contribute, similar to what has been observed for $[C_2mim][EtSO_4]$.[47] All investigated neat ILs have in common that the relaxation of anions and cations occurs through large-angle jumps rather than rotational diffusion. This can be attributed to the strong inter-ionic interactions arising from dipole-dipole correlations and coulombic forces and thus is in line with all RTILs studied to date.[36,44] As a consequence, ion relaxation is partially decoupled from macroscopic transport properties such as viscosity and electrical conductivity. For EAN it has been shown,[208] that the jump-angle of 106 ° approximately resembles the pseudo-tetrahedral geometry of the ethylammonium cation and suggests that H-bonding plays an important role for the molecular-level dynamics of EAN and (as far as this can be generalized) of other alkylammonium nitrates such as PAN.
Investigation of the only partially dissociated PIL ($[C_1Im][HOAc]$) and its comparison to fully dissociated PILs ($[C_1ImH][DFA]$, $[C_1ImH][TFA]$ and $[C_1ImH][TFSA]$) revealed that the mechanism of ion relaxation strongly depends on the degree of proton transfer and thus, on the extent of intermolecular coulombic interactions present in the system. Whilst the mechanism of rotational diffusion dominates in mixtures of low degree of proton transfer, indications for jump relaxation were observed for PILs with high protonation ratio.

The most remarkable feature of the OKE spectra of the present AILs was the detection of a sub-α mode. The term "sub-α" refers to the fact that this mode is centered at lower frequencies than the process associated with dipole reorientation, which is commonly referred to as the α-relaxation - a terminology that has been established for the dynamics of glasses indicating the structural relaxation of a system.[231] Comparison of OKE and DR spectra indicates that the sub-α mode is not associated with ion relaxation, but must correspond to fluctuations of larger aggregates as concluded for 1-alkyl-3-methylimidazolium ILs.[36] This is consistent with MD simulations, which suggest that in ILs translational motions contribute down to MHz frequencies.[45] The fact that the sub-α mode dominates the OKE spectra but cannot be resolved in the present DR spectra is also similar to the observations for imidazolium-based ILs.[36] Interestingly, a sub-α mode was not observed in the DR and OKE spectra of the PILs, EAN and PAN, which suggests that the sub-α mode is probably an universal feature of AILs only. Such a mode can be reasonably associated with a translational fluctuation of mesoscale aggregates. Because its relaxation time, τ_0, is comparable to the hopping rate (jump frequency) of ions and seems to scale with viscosity, this suggests that the underlying process may represent the rate-determining step for macroscopic transport properties such as viscosity and electrical conductivity. For 1-alkyl-3-methylimidazolium ILs this may be reasonably explained by some kind of "breathing" motion of π-stacked cation aggregates.[36] For the present AILs, where π-stacking seems to

play a minor role, a translational motion of cage-like structures seems plausible. For future studies, mixtures of representative AILs with molecular solvents investigated by DRS and OKE spectroscopy could provide further insight into the nature of this process.

The high frequency part ($\nu \gtrsim 100\,\mathrm{GHz}$) of DR and OKE spectra of RTILs arises from "cage-rattling motions" such as intermolecular vibrations and librations. Due to the strong coupling and overlap of translational and rotational motions line-shape analysis as used in the present work cannot account for all the complex dynamics taking place in the studied frequency range. This became apparent for the studied AILs, where a detailed analysis of the high-frequency intensity was not possible. Although some contributions specific for TFSA-based ILs and ILs containing aromatic groups could be identified, the intensity seems to be dominated by multi-particle contributions.
For EAN and PAN, however, it was possible to disentangle the individual contributions arising from intermolecular H-bond vibrations and librations. This was primarily enabled by the complementary sensitivity of DRS and OKE spectroscopy to cation and anion motions, respectively. Supplemented by OKE and DR spectra of d_3-EAN, it was shown that the resolved resonance processes arise from H-bond bending and stretching as suggested by Fumino *et al.*[64] but also to a considerable amount from anion and cation librations, which have been completely ignored in previous publications.[64,66] The molecular-level origin of the intensity at intermediate frequencies ($0.1 \lesssim \nu/\mathrm{THz} \lesssim 1$), which is commonly associated with β-relaxations,[268] still remains unclear. The rather simple chemical structure of EAN and PAN make them benchmark systems and particularly attractive for high-quality MD simulations, which are indispensable for a complete understanding of IL dynamics. This should motivate further research to investigate the complex dynamics of EAN and PAN.

The binary mixture of EAN+AN

The binary mixture EAN+AN was studied by DRS at 25 °C in the frequency range $0.2 \leq \nu/\mathrm{GHz} \leq 89$. It was shown that the dynamics of the mixture exhibit IL-like character down to $x_{\mathrm{EAN}} = 0.5$ with added AN acting as a "lubricant", similar to what has been observed for 1-alkyl-3-imidazolium IL+AN mixtures.[49] At such high IL concentrations ($0.5 \lesssim x_{\mathrm{EAN}} \leq 1$) all AN molecules were found to be bound (preferably to cations) and not present as free relaxing dipoles. The strength of cation-solvent interactions in EAN+AN differs from that in imidazolium+AN mixtures. Whilst for the latter AN dipoles were only slowed down,[49] they were found to be frozen in case of EAN+AN mixtures on the time scale of the present experiment. With increasing amount of AN ($x_{\mathrm{EAN}} \approx 0.4 - 0.5$) a smooth transition to dynamics similar to those of conventional electrolyte solutions was observed. This manifested itself in the strong tendency of EAN to form CIPs, which dominated the low-frequency part of the spectra in diluted solutions. The present results suggest that the considerable association of EAN in AN is mainly driven by strong H-bond interactions between $EtNH_3^+$ and NO_3^-. Indications for strong ion-association have been recently observed for EAN+DMA mixtures within a Master thesis.[354] Thus, mixtures of the model PIL EAN (but also other PILs) with other molecular solvents, can provide further valuable information for understanding structure and dynamics of PIL+solvent

mixtures. Furthermore, temperature-dependent measurements and comparison to other spectroscopic techniques such as OKE spectroscopy would be desirable to scrutinize and refine the hitherto obtained molecular-level picture.

Appendix

A.1 Physical Properties of neat Aprotic ILs

A.1.1 Densities, Viscosities and Conductivities

Table A.3: Temperature dependence of density, ρ, viscosity, η, and conductivity, κ, of $[S_{221}][TFSA]$ and $[S_{222}][TFSA]$.

	$[S_{221}][TFSA]$			$[S_{222}][TFSA]$		
T / K	ρ^* / g cm^{-3}	η / mPa s	κ / S m^{-1}	ρ^* / g cm^{-3}	η / mPa s	κ / S m^{-1}
258.15	–	–	0.0975	–	–	0.0989
268.15	–	–	0.182	–	–	0.186
278.15	1.52053	98.6	0.305	1.47969	80.5	0.314
288.15	1.51056	61.0	0.473	1.46986	49.9	0.487
298.15	1.50071	40.7	0.688	1.46014	33.4	0.728
308.15	1.49096	28.5	0.950	1.45051	23.5	0.977
318.15	1.48130	21.0	1.26	1.44097	17.3	1.29
328.15	1.47173	15.7	1.61	1.43152	13.3	1.66
338.15	1.46225	12.3	2.00	1.42215	10.4	2.10
348.15	–	9.94	2.43	–	8.45	2.60
358.15	–	8.18	2.89	–	6.96	–
368.15	–	6.83	3.37	–	5.85	–
378.15	–	5.79	3.89	–	4.99	–
388.15	–	4.98	4.43	–	4.31	–
398.15	–	4.33	4.99	–	3.77	–
418.15	–	–	6.16	–	–	–
438.15	–	–	7.38	–	–	–
458.15	–	–	8.63	–	–	–

* The present densities of $[S_{221}][TFSA]$ and $[S_{222}][TFSA]$ follow the linear relations $\rho(T/\mathrm{K}) = 1.79038 - 9.71079 \cdot 10^{-4} \cdot T/\mathrm{K}$ and $\rho(T/\mathrm{K}) = 1.74620 - 9.58954 \cdot 10^{-4} \cdot T/\mathrm{K}$, respectively.

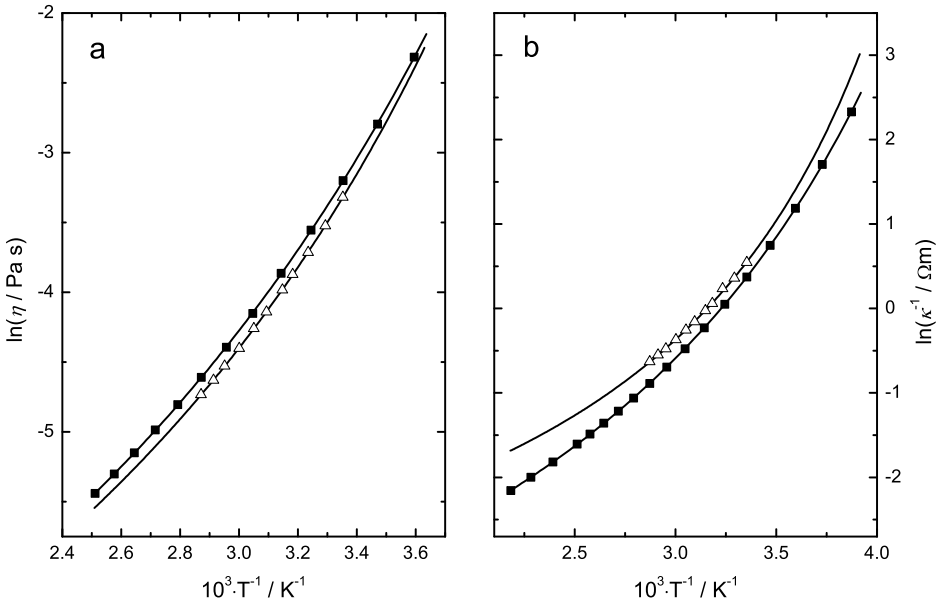

Figure A.10: Physical properties of $[S_{221}][TFSA]$ (■) as a function of temperature: (**a**) Viscosity, η, and (**b**) electrical resistivity, κ^{-1}. (△) are literature data[277] and solid lines are VFT-fits (Eq. 1.79).

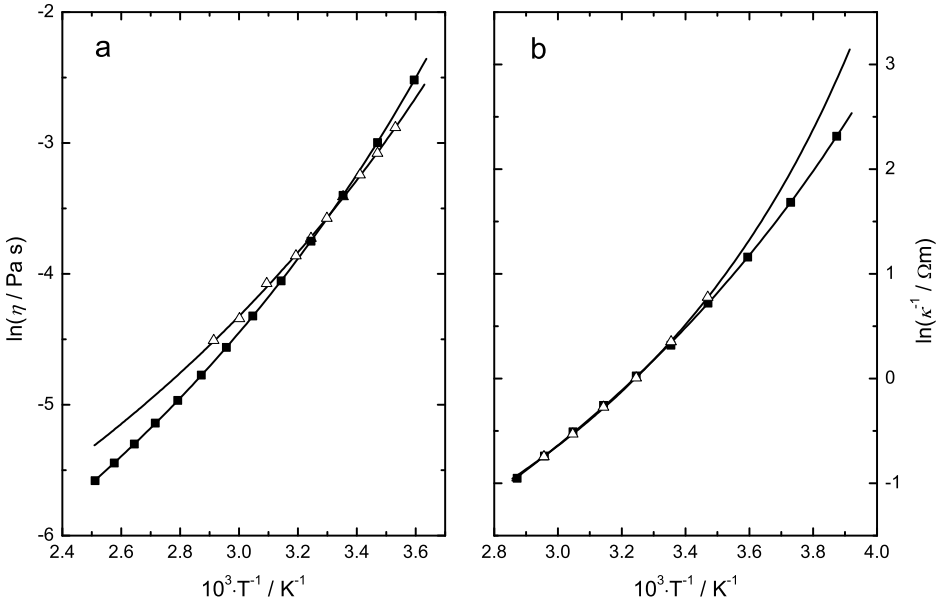

Figure A.11: Physical properties of $[S_{222}][TFSA]$ (■) as a function of temperature: (**a**) Viscosity, η, and (**b**) electrical resistivity, κ^{-1}. (△) are literature data[280,283] and solid lines are VFT-fits (Eq. 1.79).

Table A.4: VFT parameters for viscosity, $\eta(T)$, and resistivity, $\kappa^{-1}(T)$, of $[S_{221}][TFSA]$ and $[S_{222}][TFSA]$.

	$[S_{221}][TFSA]$		$[S_{221}][TFSA]$	
VFT parameters	$\eta(T)$	$\kappa^{-1}(T)$	$\eta(T)$	$\kappa^{-1}(T)$
$\ln Y_0$	-8.63	-4.29	-8.60	-4.47
B_{VFT} / K	774.8	630.6	722.2	662.2
T_0 / K	155.4	162.9	159.3	160.5

Table A.5: Temperature dependence of density, ρ, viscosity, η, and conductivity, κ, of [C_4pyr][TFSA].

T / K	ρ^* / g cm^{-3}	η / mPa s	κ / S m^{-1}
278.15	1.46788	182	0.119
288.15	1.45826	101	0.206
298.15	1.44874	61.4	0.326
308.15	1.43932	40.1	0.483
318.15	1.43002	27.9	0.678
328.15	1.4208	20.4	0.909
338.15	1.41166	15.4	1.17
348.15	1.4026	12.0	1.47
358.15	1.39362	9.66	1.80
368.15	–	7.90	2.16
378.15	–	–	2.54
388.15	–	–	2.94
398.15	–	–	3.36
418.15	–	–	4.27
438.15	–	–	5.24

* The present densities of [C_4pyr][TFSA] follow the linear relation, $\rho(T/\mathrm{K}) = 1.7255 - 9.27788 \cdot 10^{-4} \cdot T/\mathrm{K}$.

Table A.6: VFT parameters for viscosity, $\eta(T)$, and resistivity, $\kappa^{-1}(T)$, of [C_4pyr][TFSA].

VFT parameters	$\eta(T)$	$\eta(T)$ of Ref. 279	$\eta(T)$ of Ref. 284
$\ln Y_0$	-8.49	-8.66	-8.57
B_{VFT} / K	710.0	726.8	730.3
T_0 / K	173.5	174.0	171.8
	$\kappa^{-1}(T)$	$\kappa^{-1}(T)$ of Ref. 279	$\kappa^{-1}(T)$ of Ref. 285
$\ln Y_0$	-4.08	-4.00	-4.42
B_{VFT} / K	638.5	625.5	740.9
T_0 / K	175.4	175.9	165.8

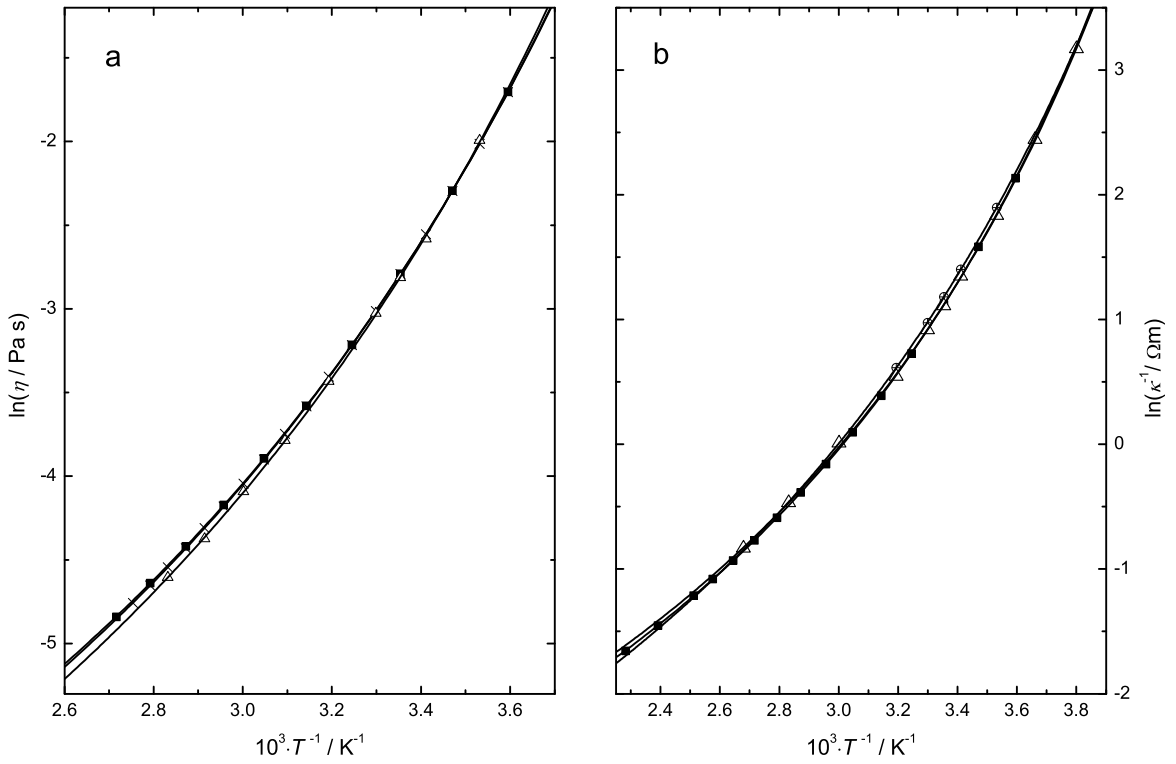

Figure A.12: Physical properties of [C_4pyr][TFSA] (■) as a function of temperature: (**a**) Viscosity, η, and (**b**) electrical resistivity, κ^{-1} with literature data (△) of Tokuda *et al.*[279], (×) of Oliviera *et al.*[284] and (⊕) of Zhang *et al.*[285] Solid lines are VFT-fits (Eq. 1.79).

Table A.7: Temperature dependence of density, ρ, viscosity, η, and conductivity, κ, of $[P_{14}][DCA]$.

T / K	ρ^* / g cm^{-3}	η / mPa s	κ / S m^{-1}
238.15	–	–	0.0337
248.15	–	–	0.0810
258.15	–	–	0.166
268.15	–	–	0.299
278.15	1.02900	95.5	0.491
288.15	1.02324	61.2	0.746
298.15	1.01756	41.8	1.07
308.15	1.01195	30.0	1.46
318.15	1.00640	21.4	1.92
328.15	1.00091	16.5	2.44
338.15	0.99547	13.1	3.02
348.15	–	10.6	–
358.15	–	8.80	–
368.15	–	7.47	–
378.15	–	6.44	–
388.15	–	5.60	–
398.15	–	4.96	–

* The present densities of $[P_{14}][DCA]$ follow the linear relation, $\rho(T/\mathrm{K}) = 1.18419 - 5.58546 \cdot 10^{-4} \cdot T/\mathrm{K}$.

Table A.8: VFT parameters for viscosity, $\eta(T)$, and resistivity, $\kappa^{-1}(T)$, of $[P_{14}][DCA]$.

VFT parameters	$\kappa^{-1}(T)$	$\eta(T)$	$\eta(T)$ of Ref. 287
$\ln Y_0$	-4.84	-8.25	-7.79
B_{VFT} / K	683.1	697.7	563.6
T_0 / K	155.2	160.2	170.7

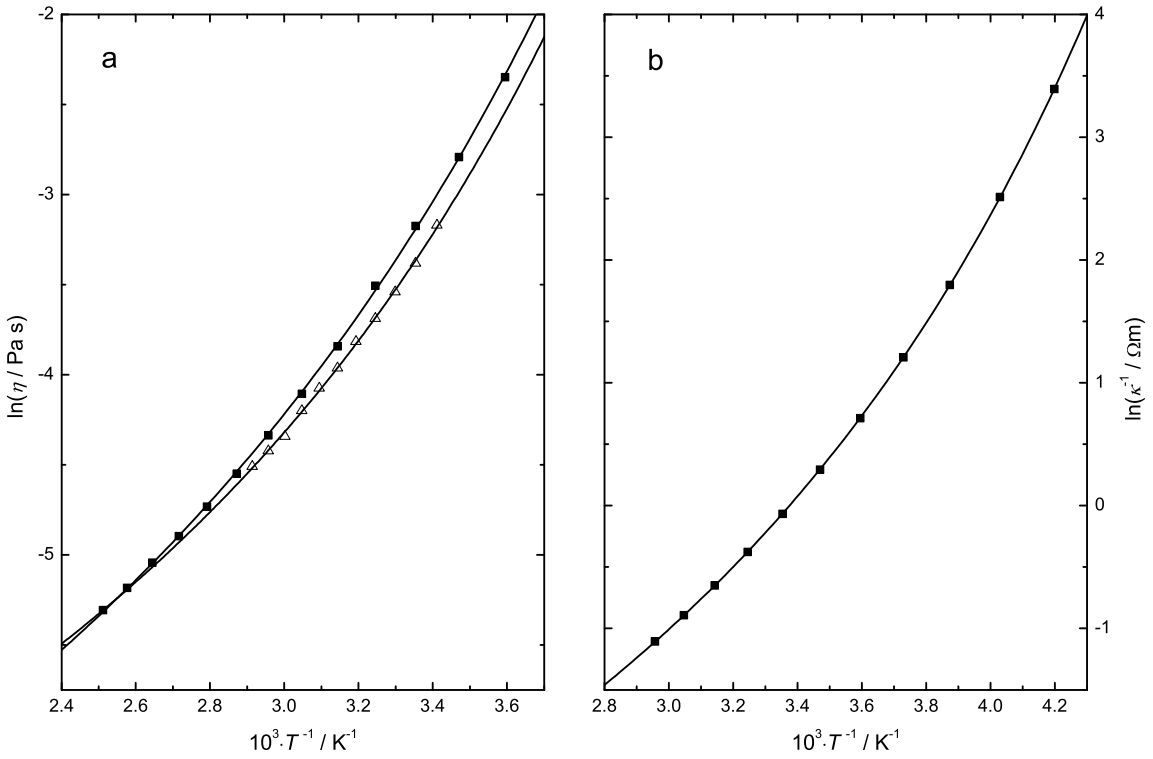

Figure A.13: Physical properties of $[P_{14}][DCA]$ (■) as a function of temperature: (**a**) Viscosity, η, and (**b**) electrical resistivity, κ^{-1}. (△) are literature data[287] and solid lines are VFT-fits (Eq. 1.79).

A.1.2 Refractive indices and polarizabilities

The refractive index, n_D, of EAN, [S_{221}][TFSA], [S_{222}][TFSA], [P_{14}][DCA] and [C_4pyr][TFSA] was measured as a function of temperature in the range $10 \leq \vartheta/\,^\circ\mathrm{C} \leq 70$ (Table A.9; Section 2.5.4). The present value of EAN ($n_D = 1.45363$) at 25 °C is in acceptable agreement with those reported in literature of 1.4534[7] and 1.4524.[196,204] The refractive index is connected to the molar polarizability, α_{mol}, and density, ρ, of the IL via the Lorentz-Lorenz equation,[86]

$$\frac{n_D^2 - 1}{n_D^2 + 2} = \frac{4\pi\rho}{3N_A M} \times \alpha_{mol} \tag{A.5}$$

with molar mass, M, and Avogadro constant, N_A. The values of α_{mol} so obtained were averaged over all measured temperatures and are summarized in Table A.10. In literature, reliable values of the polarizabilities of various typical anions, α_-, are available.[355,356] Assuming additivity of anion and cation polarizabilities, α_+ can be determined ($\alpha_+ = \alpha_{mol} - \alpha_-$). The values of α_+ so derived are in good agreement with those determined by present DFT calculations using the ORCA program package[179] and literature data.[69,214]

Table A.9: Temperature dependence of the refractive index, n_D, of EAN, [S_{221}][TFSA], [S_{222}][TFSA], [P_{14}][DCA] and [C_4pyr][TFSA].

T / K	EAN	[S_{221}][TFSA]	[S_{222}][TFSA]	[P_{14}][DCA]	[C_4pyr][TFSA]
283.15	–	1.42759	1.43078	–	1.44742
288.15	1.45598	1.42618	1.42933	1.48618	1.44593
293.15	1.45482	1.42474	1.42785	1.48532	1.44443
298.15	1.45363	1.42328	1.42639	1.48474	1.44293
303.15	1.45246	1.42186	1.42489	1.48419	1.44140
308.15	1.45130	1.42038	1.42338	1.48363	1.43991
313.15	1.45015	1.41895	1.42194	1.48316	1.43838
318.15	1.44901	1.41747	1.42041	1.48255	1.43690
323.15	1.44786	1.41608	1.41898	1.48181	1.43538
328.15	1.44676	1.41464	1.41751	1.48096	1.43389
333.15	1.44563	1.41323	1.41614	1.47999	1.43243
338.15	1.44451	1.41178	1.41476	1.47896	1.43090
343.15	1.44342	1.41030	1.41344	1.47788	1.42942

Table A.10: Polarizabilities (in Å^3) of the present ILs, α_{mol}, anions, α_-, and cations α_+. Present values of α_+ of $EtNH_3^+$, S_{221}^+, S_{222}^+, P_{14}^+ and C_4pyr^+ were determined via $\alpha_+ = \alpha_{\mathrm{mol}} - \alpha_-$.

IL	α_{mol}	α_- from lit.	α_+	α_+ from lit.
EAN	9.59 ± 0.01	4.13[a]	5.46	4.67[c]
[S_{221}][TFSA]	25.96 ± 0.02	13.59[b]	12.37	11.34[d]
[S_{222}][TFSA]	27.83 ± 0.03	13.59[b]	14.24	13.08[d]
[P_{14}][DCA]	23.4 ± 0.1	6.11[b]	17.29	16.0[e]
[C_4pyr][TFSA]	30.22 ± 0.03	13.59[b]	16.63	16.0[e]

[a] Ref. 355; [b] Ref. 356; [c] Ref. 214; [d] values were obtained by DFT calculation using the ORCA program package;[179] [e] Ref. 69;

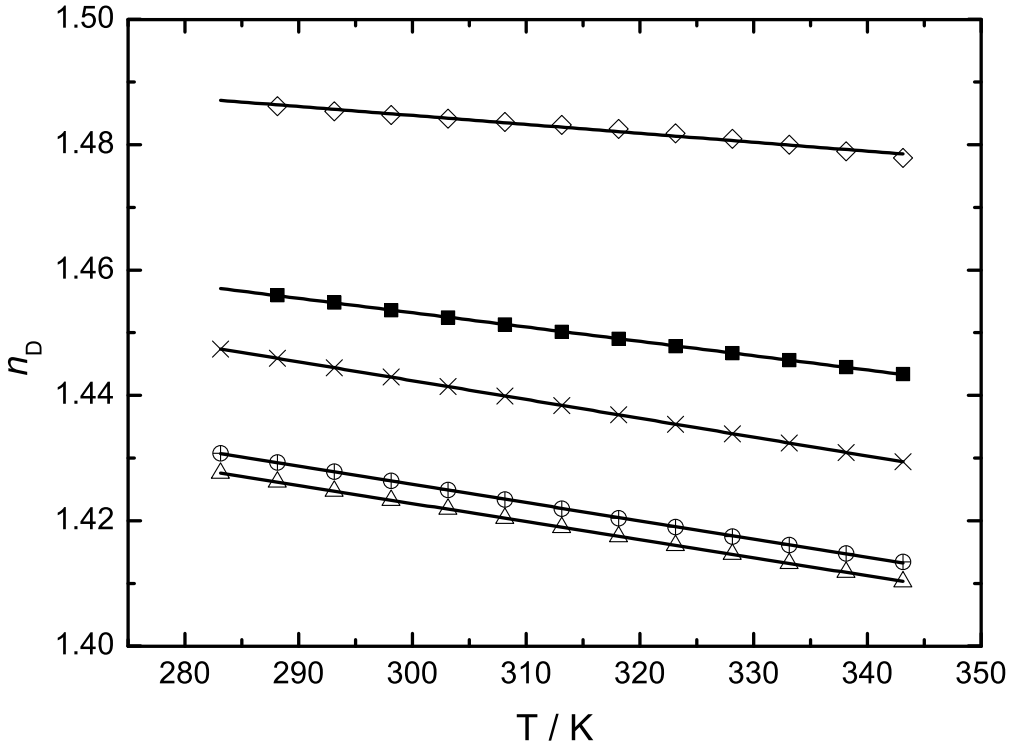

Figure A.14: Refractive index of EAN (■), [S_{221}][TFSA] (△), [S_{222}][TFSA] (⊕), [P_{14}][DCA] (◊) and [C_4pyr][TFSA] (×) as a function of temperature.

A.2 DRSFit Manual

DRSFit is a Macro developed in Regensburg/Glasgow for the commercial fitting program IGOR (V. 6.22A, Wavemetrics) to fit dielectric and Optical Kerr-Effect (OKE) spectra.

General Aspects

Dielectric Relaxation Spectroscopy (DRS) probes the macroscopic polarization $\vec{P}(t)$ as the response of a sample to a time-dependent electric field $\vec{E}(t)$. The experimentally accessible quantity is the frequency dependent generalized complex permittivity, $\hat{\eta}(\nu)$,

$$\hat{\eta}(\nu) = \eta'(\nu) - \mathrm{i}\eta''(\nu) \tag{A.6}$$

with η' as the in-phase and η'' as the out-of-phase response containing contributions from rotational, vibrational and translational motions.[86] For conducting samples of dc conductivity, κ, the generalized permittivity spectrum, $\hat{\eta}(\nu)$, contains an additional Ohmic loss term, which originates from diffusive (steady-state) charge transport in the sample. In order to obtain the dielectric permittivity spectrum, $\hat{\varepsilon}(\nu)$, the raw data has to be corrected for this effect:

$$\hat{\varepsilon}(\nu) = \hat{\eta}(\nu) + \frac{\mathrm{i}\kappa}{2\pi\nu\varepsilon_0} \tag{A.7}$$

where ε_0 is the permittivity of free space.[84] Then, the dielectric spectrum can be expressed as the frequency dependent complex permittivity, $\hat{\varepsilon}(\nu)$:

$$\hat{\varepsilon}(\nu) = \varepsilon'(\nu) - \mathrm{i}\varepsilon''(\nu) \tag{A.8}$$

The relative permittivity, $\varepsilon'(\nu)$, shows a dispersion from the static permittivity, $\varepsilon_\mathrm{s} = \lim_{\nu\to 0}\varepsilon'(\nu)$ to the permittivity at infinite frequencies, $\varepsilon_\infty = \lim_{\nu\to\infty}\varepsilon'(\nu)$ and represents the ability of the sample to respond in phase to an external field. The dielectric loss, $\varepsilon''(\nu)$, describes the dissipation of energy within the sample arising from the coupling of $\vec{E}(t)$ to dipole fluctuations.[57]
In order to obtain information about molecular level dynamics, a proper mathematical description of the experimental data is required. Therefore, the spectrum is generally fitted by a sum of n individual functions of certain band-shape, $\tilde{F}_j(\nu)$ (see section **SetParams** panel for details), and amplitude, S_j:

$$\hat{\varepsilon}(\nu) = \varepsilon_\infty + \sum_{j=1}^{n} S_j \cdot \tilde{F}_j(\nu) \tag{A.9}$$

Due to the broad nature of the spectra, finding the correct model is not trivial. Therefore, a few general criteria have to be obeyed:

- The value of the reduced error function, χ_r^2, should be minimized.
- The number of model functions should be small and the obtained parameters have to be physically reasonable.

- Except for physical reasons, the relaxation model should not change within a temperature or concentration series.

Nevertheless, a priori any description of $\hat{\varepsilon}(\nu)$ based on eq. A.9 is purely based on formal criteria. Wether the resolved $\tilde{F}_j(\nu)$ can be traced back to molecular-level processes or not is a problem to be solved in the subsequent interpretation of the obtained relaxation parameters (amplitudes, S_j, relaxation times, τ_j etc.).
The non-linear fitting routine implemented in IGOR minimizes the error function χ^2,

$$\chi^2 = \left[w_{\varepsilon'}(\nu_k) \sum_{k=1}^{N} \delta\varepsilon'(\nu_k)^2 + w_{\varepsilon''}(\nu_k) \sum_{k=1}^{N} \delta\varepsilon''(\nu_k)^2 \right] \tag{A.10}$$

with weights $w_{\varepsilon'} = w_{\varepsilon''} = 1$ using the Levenberg-Marquardt algorithm. In order to compare results of different models, the reduced fit variance, χ_r^2, is calculated according to

$$\chi_\mathrm{r}^2 = \frac{\chi^2}{2N - m - 1}. \tag{A.11}$$

where N is the number of data triples (ν,ε',ε'') and m the number of adjustable fit parameters.

Starting the Fit Program

Before starting IGOR, the IGOR procedure file *DRSFitProcedure.ipf* has to be copied into the IGOR Procedures folder. For Windows XP this folder is located in C:\Program Files\WaveMetrics\Igor Pro Folder. For Windows 7 it is in C:\Users\\LocalAdmin\Documents \WaveMetrics\Igor Pro 6 User Files.

- **IGOR** software is started by executing the *Igor.exe* file
- To start the fitting program, click the *Macros* drop-down menu and select *DRSFit*
- *Select file* dialog is displayed to select an *eps*-file containing the experimental data. The *eps*-file has to be structured as follows:
  - 3 comment lines
  - comment line containing conductivity correction in $\mathrm{S\,m^{-1}}$
  - comment line containing number of data triples (ν, ε', ε'');
  - 1. column: point number
  - 2. column: frequency, ν, in GHz;
  - 3. column: permittivity, ε';
  - 4. column: uncertainty, $\delta\varepsilon'$, of ε'; For VNA data, $\delta\varepsilon'$ is set to 0.1;
  - 5. column: dielectric loss, ε'';
  - 6. column: uncertainty, $\delta\varepsilon''$, of ε''; For VNA data, $\delta\varepsilon''$ is set to 0.1;

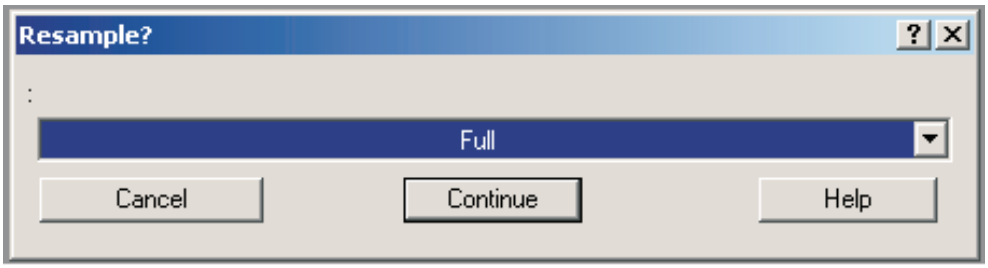

Figure A.15: Resample dialog

  - 7. column: Flags to activate (1) and deactivate (0) data triple (ν,ε',ε'');

- Press *Öffnen* to import *eps*-file.

- Resample dialog appears, providing 3 options (*Gaps*, *Full*, *No*) for resampling the spectrum:
  - *Gaps*: resamples experimental data to a regular logarithmic frequency scale, excluding gaps;
  - *Full*: resamples experimental data to a regular logarithmic frequency scale, including gaps;
  - *No*: aborts resampling procedure;(**recommended**)
- *Continue* button executes selected operation; *Cancel* button acts as *No*;(**recommended**)
- Subsequently, *SetParams* panel, *FitGraph* window, *ShowParams* table and *Expdata* table are created.

SetParams Panel

The *SetParams* panel (Fig. A.16) is divided into several group boxes: *H-N* (Havriliak-Negami), *Gaussian*, *Brownian*, *Normalization*, *EP* (electrode polarization), *plot range* and a box to load and save experimental data and parameter sets.

H-N (Havriliak-Negami) group box

The *H-N* group box allows the selection of band-shape functions typical for relaxation processes that dominate $\hat{\varepsilon}(\nu)$ at $\nu \leq 100\,\mathrm{GHz}$. Up to 7 (0 to 6) Havriliak-Negami functions (eq. A.12) are available whose band-shape function is expressed by

$$\tilde{F}_{j,\mathrm{HN}}(\nu) = \frac{1}{[1 + (\mathrm{i}2\pi\nu\tau_j)^{1-\alpha_j}]^{\beta_j}} \tag{A.12}$$

with broadening parameters, α (symmetrical; $0 \leq \alpha < 1$) and β (asymmetrical; $0 < \beta \leq 1$) and relaxation time, τ of the jth process. Depending on α and β, the H-N function is

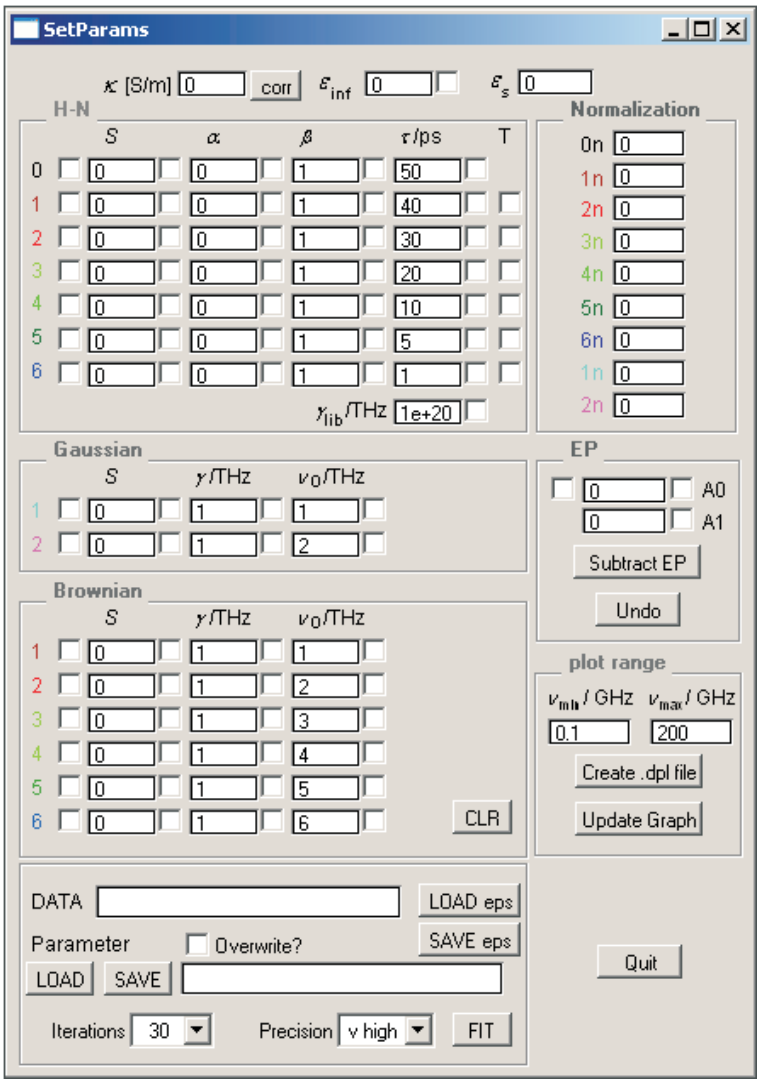

Figure A.16: SetParams panel to set starting parameters

turning into its limiting forms Cole-Davidson (CD; $\alpha = 0$), Cole-Cole (CC; $\beta = 1$) and Debye (D; $\alpha = 0$, $\beta = 1$). Each function is activated by checking the most left checkbox. Starting values for the parameters of each process, including its amplitude, S_j, can be set in the corresponding fields and confirmed by pressing *Enter*. Now, the function is displayed in the graph *FitGraph*. Note that a parameter will only be adjustable if its checkbox is ticked.

- To account for inertial effects in the THz regime, an initial rise rate, γ_{lib}, was introduced. The value of γ_{lib} is approximately the average of the librational resonance frequencies and causes a faster decay of the function at higher frequencies.[106] By default the value of the initial rise rate, γ_{lib} is set to 10^{20} THz in order to disable this modification. A typical value for γ_{lib} is ~ 2 THz.

- To truncate the H-N function at lower frequencies, the so called α termination (T) can be applied by checking the most right checkbox. Then, the function is terminated on its low-frequency tail with respect to the relaxation time, τ_0, of the 0th H-N equation in the H-N group box.[106]

Applying these two corrections to eq. A.12 yields the modified H-N equation (mHN; eq. A.13):

$$\tilde{F}_{j,\mathrm{HNm}}(\nu) = (S^0_{j,\mathrm{HNm}})^{-1} \cdot \left[\frac{1}{(1 + (\mathrm{i}2\pi\nu\tau_j + \tau_j/\tau_0)^{1-\alpha_j})^{\beta_j}} - \frac{1}{(1 + (\mathrm{i}2\pi\nu\tau_j + \gamma_{\mathrm{lib}}\tau_j + \tau_j/\tau_0)^{1-\alpha_j})^{\beta_j}} \right] \tag{A.13}$$

In this equation, $S^0_{j,\mathrm{HNm}}$ is a normalization factor (see **Normalization group box**).

Gaussian group box

In order to describe the far-infrared region of dielectric and OKE spectra antisymmetrized Gaussians (G) (eq. A.14) are commonly used for modelling inter- and intramolecular vibrations and librations. Moreover, the Gaussian band-shape function has proven to describe the steep decay of the imaginary part at high frequencies properly. In this program the following function is used,

$$\begin{aligned} \tilde{F}_{j,\mathsf{G}}(\nu) = (S^0_{j,\mathsf{G}})^{-1} \Bigg[& \frac{2}{\sqrt{\pi}} \mathsf{D}\left(\frac{\nu + \nu_{0,j}}{\sqrt{2}\gamma_{j,\mathsf{G}}} \right) - \frac{2}{\sqrt{\pi}} \mathsf{D}\left(\frac{\nu - \nu_{0,j}}{\sqrt{2}\gamma_{j,\mathsf{G}}} \right) \\ & + \mathsf{i} \left(\exp\left[-\frac{(\nu - \nu_{0,j})^2}{2\gamma^2_{j,\mathsf{G}}} \right] - \exp\left[-\frac{(\nu + \nu_{0,j})^2}{2\gamma^2_{j,\mathsf{G}}} \right] \right) \Bigg] \end{aligned} \tag{A.14}$$

with resonance frequency $\nu_{j,0}$ and half band width $\gamma_{j,\mathrm{G}}$. D is Dawson's integral[111] and $S^0_{j,\mathrm{G}}$ is the normalization factor (see **Normalization group box**). Currently, up to 2 Gaussians are possible.
Just as for H-N functions, each Gaussian is activated by checking its most left checkbox.

Brownian group box

The damped harmonic oscillator (DHO) is primarily used to model the intermolecular motions usually showing up in the THz and FIR region of dielectric and OKE spectra. Currently, up to 6 DHO's are possible. The mathematical form of a DHO used in this program is

$$\tilde{F}_{j,\mathrm{DHO}}(\nu) = \left[\frac{\omega^2_{j,0}}{(\omega^2_{j,0} - \omega^2) + \mathrm{i}\omega/\tau_{j,\mathrm{DHO}}} \right] = \left[\frac{\nu^2_{j,0}}{(\nu^2_{j,0} - \nu^2) + \mathrm{i}\nu\gamma_{j,\mathrm{DHO}}} \right] \tag{A.15}$$

with resonance frequency $\nu_{j,0}$ and damping constant $\gamma_{j,\mathrm{DHO}} = 1/(2\pi\tau_{j,\mathrm{DHO}})$.[92] Activation of a DHO works as for H-N functions and Gaussians.

Normalization group box

Since the modified H-N function (eq.A.13) and the Gaussian (eq. A.14) are not normalized (i.e. $\int_0^\infty \tilde{F}_{j,\mathrm{x}}\mathrm{d}\nu \neq 1$; x =HNm,G), not the true amplitude, S_j, is given as the output. Therefore, the output amplitudes, S'_j have to be corrected by a normalization factor, S^0_j, which is obtained by calculating the $\nu \to 0$ limit of eq. A.13 and A.14.

- Normalization factor for the modified H-N function:

$$S^0_{j,\mathrm{HNm}} = \frac{1}{(1+(\tau_j/\tau_{j-1})^{1-\alpha_j})^{\beta_j}} - \frac{1}{(1+(\gamma_{\mathrm{lib}}\tau_j+\tau_j/\tau_{j-1})^{1-\alpha_j})^{\beta_j}} \tag{A.16}$$

- Normalization factor for the antisymmetrized Gaussian:

$$S^0_{j,\mathsf{G}} = \frac{4}{\sqrt{\pi}}\mathsf{D}\left(\frac{\nu_{0,j}}{\sqrt{2}\gamma_{j,\mathsf{G}}}\right) \tag{A.17}$$

Consequently, the normalized amplitudes, S_j, are calculated according to

$$S_j = S'_j \cdot S^0_j \tag{A.18}$$

and displayed in the *Normalization* group box.
The static permittivity, ε_s, is calculated as the sum of all normalized amplitudes ($S_{\mathrm{HN/HNm}}$, S_{DHO}, S_{G}) plus the high-frequency limit of the dispersion, ε_∞,

$$\varepsilon_\mathrm{s} = \varepsilon_\infty + \sum_j S_j, \tag{A.19}$$

and displayed in the top line of the *SetParams* panel. Note that ε_s is just an output value and can not be set or fitted. In contrast to that, ε_∞ is a fit parameter and is adjusted by checking its right checkbox.

Electrode polarization (EP) group box

Electrode polarization is a parasitic effect of conducting samples which contributes to the dielectric response. Depending on the conductivity of the sample it appears in the kHz to MHz region of the spectrum. It is caused by accumulation of charged particles at the electrode surface, resulting in an electrical double layer.[357] This polarization leads to an additional dispersion step of ε' which masks the dielectric response (Fig A.17). There are several, more or less sophisticated, methods to account for these polarization effects. However, for our purpose it is sufficient to follow the assumptions of Kremer and Schönhals who model this contribution, S^{EP}, by an empirical fractal power-law:[84]

$$S^{\mathrm{EP}} = A_0 \cdot \nu^{A_1} \tag{A.20}$$

with A_0 and A_1 ($A_1 < 0$) as two fitting parameters.
To apply *EP* correction, check the left checkbox for activation and set the parameters A_0 and A_1.

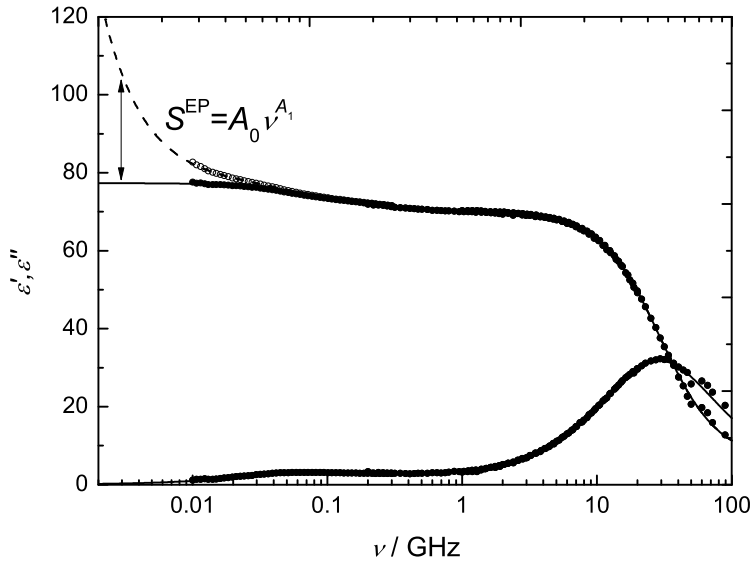

Figure A.17: Subtraction of electrode polarization. Raw data (○) and corrected data (●) with corresponding fits (– – – and —, respectively).

- After fitting, the contribution can be subtracted from the total fit by deselecting the left checkbox (deactivation).
- To subtract the *EP* contribution from the experimental data, click the *Subtract EP* button.
- To add the contribution again, press the *Undo* button.

Note that after subtracting the amplitude of electrode polarization, just the spectrum displayed by IGOR is corrected but not the data in the *eps*-file. Use *Save eps* button to save modified data as an *eps*-file.

plot range group box

In the *plot range* group box, the values of $\nu_{\min}$ and $\nu_{\max}$ define the frequency range in which the fit functions are plotted. By default they are set to 0.1 GHz and 200 GHz, respectively. To change the plot range, set the required limits and press *Enter*.

- *Create .dpl file* button, see section **Load-Save group box**
- *Update Graph* button, see chapter **Expdata Table**

Conductivity Correction

In a DRS experiment, the accessible quantity is the generalized complex permittivity, $\hat{\eta}(\nu)$ which contains dielectric, $\hat{\varepsilon}(\nu)$, and conductivity contributions, $\hat{\kappa}(\nu)$. However, both quantities are not separately measurable. Therefore, it is advantageous to subtract the effect

of dc conductivity, κ, from $\hat{\eta}$ in order to obtain the pure dielectric response, $\hat{\varepsilon}$. Note that a possible dispersion of conductivity[96], if present, will contribute to $\hat{\varepsilon}(\nu)$. Similar to electrode polarization an asymptotical frequency dependence is assumed for the contribution of κ to η'', thus

$$\varepsilon''(\nu) = \eta''(\nu) - \frac{\kappa}{2\pi\varepsilon_0\nu} \tag{A.21}$$

where ε_0 represents the permittivity in vacuum.

- To correct the dielectric spectrum for the conductivity contribution, enter the value for κ in $\mathrm{S\,m^{-1}}$ in the corresponding field in the upper left corner of the panel.
- Press *corr* button to apply correction. The value of the current correction is printed in the command line. Additionally, this value is added to previous conductivity corrections stored in the header of the *eps*-file. The sum is displayed as *total conductivity correction* in the command line as well.

Note that after conductivity correction just the spectrum displayed in IGOR is corrected but not the data in the *eps*-file. Use *Save eps* button to save modified data as an *eps*-file.

Load-Save group box

In this group box, the fitting parameters as well as the experimental data can be loaded and saved.

- To load experimental data (*eps*-file) press *Load eps* button. The data have to be formatted described in section **Starting the Fit Program**.
- To save experimental data (*eps*-file) press *Save eps* button.
- To save a set of parameters, press *Save* button. The parameters are saved as a *fpw*-file.
- To load a set of parameters (*fpw*-file), press *Load* button.
- To save contributions of the individual fit functions and the total fit displayed in the Graph, use the button *Create dpl-file* in the *plot range* group box. Structure of *dpl*-file:
  - 1. column: frequency, ν, of experimental data in GHz;
  - 2. column: permittivity, ε', of experimental data;
  - 3. column: dielectric loss, ε'', of experimental data;
  - 4. column: frequency, ν, of fit functions in GHz;
  - 5. column: total permittivity of fit, $\varepsilon'_{\mathrm{fit}}$;
  - 6. column: total dielectric loss of fit, $\varepsilon''_{\mathrm{fit}}$;
  - 7. to 21. column: dielectric loss of single fit functions, $\varepsilon''_{\mathrm{i}}$;

Starting the Fit

- To fit a dielectric spectrum, reasonable starting parameters are required.
- Only parameters of an activated function (marked blue in Fig. A.18) are fitted.
- Each parameter to be optimized has to be specified by checking the checkbox on its right side (marked red in Fig. A.18).

Figure A.18: Single equation in the **SetParams** panel.

- All parameters with an unchecked checkbox are kept fixed during the fit.
- By default, the precision of the fit is set to *v high* (very high; **recommended**).
- The number of iterations can be set to 30, 300 or 3000.
- To start a fit, press the *Fit* button. A fit dialog is displayed while the fit routine is decreasing the χ_r^2 value until a certain stop criterion (depending on the selected precision) is reached.
- Subsequently, the value of the reduced error function, χ_r^2, is printed in the command line, indicating the quality of the fit.
- It is recommended to repeat pressing the *Fit* button until no significant improvement of the χ_r^2 value is achieved any more.
- Finally, the optimized parameters have to be saved as a *fpw*-file using the *Save* button. These *fpw*-files can be imported into **Origin** and **EXCEL** for further analysis.

FitGraph Window

In the *FitGraph* panel (Fig. A.19) three quantities are plotted as a function of frequency:

- lower left y axis: dielectric loss, ε'';
- right y axis: dielectric permittivity, ε';
- upper left y axis: deviation of fit from experimental complex permittivity, $\Delta\hat{\varepsilon}$;

In the upper bar of the window two sliders are available which allow to specify the set of data points to be fitted. By default, the red and the green slider are located on the first and the last data point of the *eps*-file, respectively.

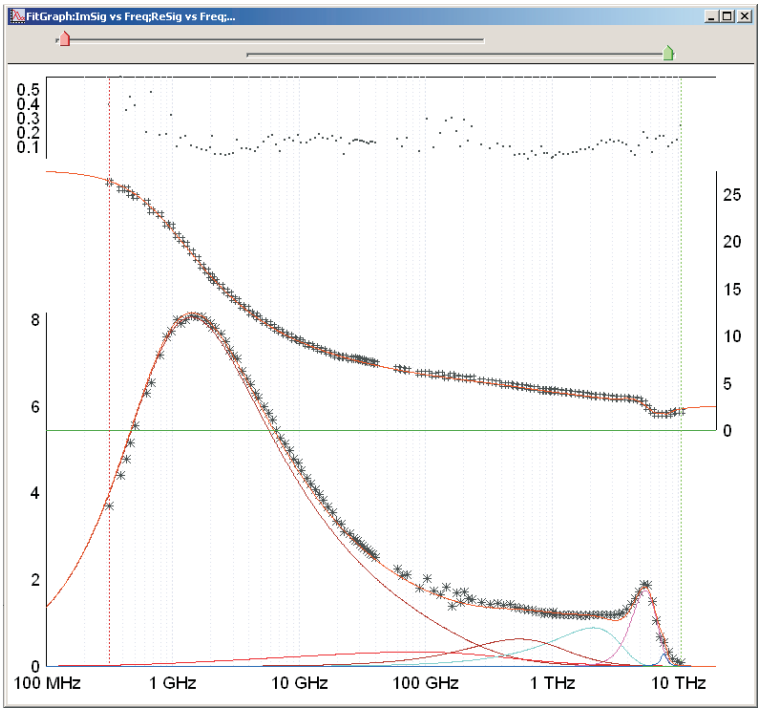

Figure A.19: Dielectric spectrum of ethylammonium nitrate at 25 °C plotted in the *FitGraph* Window. $*$ represent the dielectric loss, ε'', ♯ the permittivity, ε', and ■ the fit deviations, $\Delta\hat{\varepsilon}$. Additionally, the total fit (orange line) and the single equations are displayed. Colors of the latter correspond to those of the equation numbers in the **SetParams** panel.

Expdata Table

In the *Expdata* table, the experimental data of the *eps*-file are listed (Fig.A.20).

- 1. column: point number;
- 2. column: frequency in THz;
- 3. column: permittivity, ε';
- 4. column: dielectric loss, ε'';
- 5. column: flags;

Using the flag column, a certain data triple can be activated or deactivated by setting the corresponding value to 1 or 0, respectively. In this way, outliers can be excluded from the fit. However, deactivated data triples are still modified by conductivity or electrode polarization correction. By pressing the *Update Graph* button in the *plot range* group box, the *FitGraph* window is recreated and modifications which were made in the flag column are applied to the graph.
Note that after modifying the flag column, just the flags in the *Expdata* table are changed but not in the *eps*-file. Use *Save eps* button to save modified data as an *eps*-file.

Point	Freq0	ReSig0	ImSig0	Flags
0	0.000317	26.2693	3.7102	1
1	0.0003911	25.5364	4.395	1
2	0.0004282	25.5881	4.7899	0
3	0.0004653	25.0597	5.1639	0
4	0.0005024	24.7797	5.5414	1
5	0.0006199	24.1762	6.3094	0

Figure A.20: Expdata table containing the experimental data of the *eps*-file.

ShowParams Table

In the *ShowParams* table, all the parameters entered in the *SetParams* panel are listed. Additionally, the χ_r^2 value of the fit and the conductivity correction, κ, in $\mathrm{S\,m^{-1}}$ are displayed. When using the *Save* button, this table is saved as an *fpw*-file. Alternatively, parameters can also be set in the *ShowParams* table.

Acknowledgements

I thank Dr. David Turton (University of Glasgow) for providing a provisional version of the DRSfit routine and I appreciate the competent assistance in programming by B.Sc. Andreas Nazet and thank him for constructive suggestions to improve the program.

Bibliography

[1] Freemantle, M. *An Introduction to Ionic Liquids*; Royal Society of Chemisty, Cambridge, UK, 2010.

[2] Wasserscheid, P.; Welton, T. *Ionic Liquids in Synthesis*; Wiley-VCH, Weinheim, 2003.

[3] Rogers, R. D.; Seddon, K. R. *Science* **2003**, *302*, 792–793.

[4] Angell, C. A.; Ansari, Y.; Zhao, Z. *Faraday Discuss.* **2012**, *154*, 9–27.

[5] Wasserscheid, P. *Chemie in Unserer Zeit* **2003**, *37*, 52–63.

[6] Gabriel, S.; Weiner, J. *Ber. der Deutschen Chem. Ges.* **1888**, *21*, 2669–2679.

[7] Greaves, T. L.; Drummond, C. J. *Chem. Rev.* **2008**, *108*, 206–237.

[8] Walden, P. *Bull. Acad. Impér. Soc. St. Petersburg* **1914**, *8*, 405.

[9] Wilkes, J. S.; Levisky, J. A.; Wilson, R. A.; Hussey, C. L. *Inorg. Chem.* **1982**, *21*, 1263–1264.

[10] Wilkes, J. S.; Zaworotko, M. J. *J. Chem. Soc., Chem. Commun.* **1992**, 965–967.

[11] Swatlowski, R. P.; Holbrey, J. D.; Rogers, R. D. *Green Chem.* **2003**, *5*, 361–363.

[12] Bonhôte, P.; Dias, A. P.; Papageorgiou, N.; Kalyanasundaram, K.; Grätzel, M. *Inorg. Chem.* **1996**, *35*, 1168–1178.

[13] Plechkova, N. K.; Seddon, K. R. *Chem. Soc. Rev.* **2008**, *37*, 123–150.

[14] http://www.dfg-spp1191.de.

[15] Wishart, J. F. *Energy Environ. Sci.* **2009**, *2*, 956–961.

[16] Martins, M. A. P.; Frizzo, C. P.; Moreira, D. N.; Zanatta, N.; Bonacorso, H. G. *Chem. Rev.* **2008**, *108*, 2015–2050.

[17] Hallett, J. P.; Welton, T. *Chem. Rev.* **2011**, *111*, 3508–3576.

[18] Earle, M. J.; Esperanca, J. M. S. S.; Gilea, M. A.; Lopes, J. N. C.; Rebelo, L. P. N.; Magee, J. W.; Seddon, K. R.; Widegren, J. A. *Nature* **2006**, *439*, 831–834.

[19] Ohno, H. e. *Electrochemical Aspects of Ionic Liquids*; Wiley-Interscience, Hoboken, 2005.

[20] Hapiot, P.; Lagrost, C. *Chem. Rev.* **2008**, *108*, 2238–2264.

[21] Maton, C.; De Vos, N.; Stevens, C. *Chem. Soc. Rev.* **2013**, *42*, 5963–5977.

[22] Pinkert, K. N., A. adn Marsh; Pang, S.; Staiger, M. P. *Chem. Rev.* **2009**, *109*, 6712–6728.

[23] Wang, H.; Gurau, G.; Rogers, R. D. *Chem. Soc. Rev.* **2012**, *41*, 1519–1537.

[24] Le Bideau, J.; Viau, L.; Vioux, A. *Chem. Soc. Rev.* **2011**, *40*, 907–925.

[25] MacFarlane, D. R.; Forsyth, M.; Howlett, P. C.; Pringle, J. M.; Sun, J.; Annat, G.; Neil, W.; Izgorodina, E. I. *Acc. Chem. Res.* **2007**, *40*, 1165–1173.

[26] Zhao, D.; Liao, Y.; Zhang, Z. *Clean* **2007**, *35*, 42–48.

[27] Matzke, M. Ph.D. thesis, Universität Bremen, 2008.

[28] Evans, D. F.; Chen, S.-H. *J. Am. Chem. Soc.* **1981**, *103*, 481–482.

[29] Triolo, A.; Russina, M.; Hardacre, C.; Nieuwenhuyzen, M.; Gonzalez, M. A.; Grimm, H. *J. Phys. Chem. B* **2005**, *109*, 22061–22066.

[30] Weingärtner, H. *Angew. Chem. Int. Ed.* **2008**, *47*, 654–670.

[31] Heimer, N. E.; Wilkes, J. S.; Wahlbeck, P. G.; Carper, W. R. *J. Phys. Chem. A* **2006**, *110*, 868–874.

[32] Fumino, K.; Wittler, K.; Ludwig, R. *J. Phys. Chem. B* **2012**, *116*, 9507–9511.

[33] Giraud, G.; Gordon, C. M.; Dunkin, I. R.; Wynne, K. *J. Chem. Phys.* **2003**, *119*, 464.

[34] Cang, H.; Novikov, N.; Fayer, M. D. *J. Chem. Phys.* **2003**, *118*, 2800–2807.

[35] Hyun, B.-R.; Dzyuba, S.; Bartsch, R.; Quitevis, E. L. *J. Phys. Chem. A* **2002**, *106*, 7579–7585.

[36] Turton, D. A.; Hunger, J.; Stoppa, A.; Hefter, G.; Thoman, A.; Walther, M.; Buchner, R.; Wynne, K. *J. Am. Chem. Soc.* **2009**, *131*, 11140–11146.

[37] Samanta, A. *J. Phys. Chem. Lett.* **2010**, *1*, 1557–1562.

[38] Maroncelli, M.; Zhang, X.-X.; Liang, M.; Roy, D.; Ernsting, N. P. *Faraday Discuss.* **2012**, *154*, 409–424.

[39] Hardacre, C.; Holbrey, J. D.; Mullan, C. L.; Youngs, T. G. A.; Bowron, D. T. *J. Chem. Phys.* **2010**, *133*, 074510.

[40] Schröder, C.; Rudas, T.; Steinhauser, O. *J. Chem. Phys* **2006**, *125*, 244506.

[41] Schröder, C.; Rudas, T.; Neumayr, G.; Gansterer, W.; Steinhauser, O. *J. Chem. Phys.* **2007**, *127*, 044505.

[42] Schröder, C.; Hunger, J.; Stoppa, A.; Buchner, R.; Steinhauser, O. *J. Chem. Phys.* **2008**, *129*, 184501.

[43] de Andrade, J.; Böes, E. S.; Stassen, H. *J. Phys. Chem. B* **2008**, *112*, 8966–8974.

[44] Shim, Y.; Kim, H. *J. Phys. Chem. B* **2008**, *112*, 11028–11038.

[45] Schröder, C.; Sonnleitner, T.; Buchner, R.; Steinhauser, O. *Phys. Chem. Chem. Phys.* **2011**, *13*, 12240–12248.

[46] Schrödle, S.; Annat, G.; MacFarlane, D. R.; Forsyth, M.; Buchner, R.; Hefter, G. *Chem. Commun.* **2006**, 1748–1750.

[47] Hunger, J.; Stoppa, A.; Buchner, R.; Hefter, G. *J. Phys. Chem. B* **2009**, *113*, 9527–9537.

[48] Hunger, J.; Stoppa, A.; Buchner, R.; Hefter, G. *J. Phys. Chem. B* **2008**, *112*, 12913–12919.

[49] Stoppa, A.; Hunger, J.; Hefter, G.; Buchner, R. *J. Phys. Chem. B* **2012**, *116*, 7509–7521.

[50] Asaki, M. L. T.; Redondo, A.; Zawodzinski, T. A.; Taylor, A. J. *J. Chem. Phys.* **2002**, *116*, 10377.

[51] Castner, E. W.; Wishart, J. F. *J. Chem. Phys.* **2010**, *132*, 120901.

[52] Weingärtner, H.; Knocks, A.; Schrader, W.; Kaatze, U. *J. Phys. Chem. A* **2001**, *105*, 8646–8650.

[53] Weingärtner, H. *Z. Phys. Chem.* **2006**, *220*, 1395.

[54] Weingärtner, H.; Sasisanker, P.; Daguenet, C.; Dyson, P. J.; Krossing, I.; Slattery, J. M.; Schubert, T. *J.Phys. Chem. B* **2007**, *111*, 4775–4780.

[55] Huang, M.-M.; Jiang, Y.; Sasisanker, P.; Driver, G. W.; Weingärtner, H. *J. Chem. Eng. Data* **2011**, *56*, 1494–1499.

[56] Stoppa, A.; Hunger, J.; Buchner, R.; Hefter, G.; Thoman, A.; Helm, H. *J. Phys. Chem. B* **2008**, *112*, 4854–4858.

[57] Buchner, R.; Hefter, G. *Phys. Chem. Chem. Phys.* **2009**, *11*, 8984–8999.

[58] Hunger, J.; Stoppa, A.; Schrödle, S.; Hefter, G.; Buchner, R. *Chem. Phys. Chem.* **2009**, *10*, 723–733.

[59] Hunger, J. Ph.D. thesis, Universität Regensburg, 2009.

[60] Stoppa, A. Ph.D. thesis, Universität Regensburg, 2010.

[61] Hayamizu, K.; Tsuzuki, S.; Seki, S.; Fujii, K.; Suenaga, M.; Umebayashi, Y. *J. Chem. Phys.* **2010**, *133*, 194505.

[62] Castiglione, F.; Moreno, M.; Raos, G.; Famulari, A.; Mele, A.; Appetecchi, G. B.; Passerini, S. *J. Phys. Chem. B* **2009**, *113*, 10750–10759.

[63] Kaintz, A.; Baker, G.; Benesi, A.; Maroncelli, M. *J. Phys. Chem. B* **2013**, *117*, 11697–11708.

[64] Fumino, K.; Wulf, A.; Ludwig, R. *Angew. Chem. Int. Ed.* **2009**, *48*, 5184–5186.

[65] Fumino, K.; Wulf, A.; Ludwig, R. *Phys. Chem. Chem. Phys.* **2009**, *11*, 8790–8794.

[66] Fumino, K.; Reichert, E.; Wittler, K.; Hempelmann, R.; Ludwig, R. *Angew. Chem. Int. Ed.* **2012**, *51*, 6236–6240.

[67] Shirota, H.; Funston, A. M.; Wishart, J. F.; Castner, E. W. *J. Chem. Phys.* **2005**, *122*, 184512.

[68] Fukazawa, H.; Ishida, T.; Shirota, H. *J. Phys. Chem. B* **2011**, *115*, 4621–4631.

[69] Fujisawa, T.; Nishikawa, K.; Shirota, H. *J Chem. Phys.* **2009**, *131*, 244519.

[70] Zhang, X.; Liang, M.; Ernsting, N. P.; Maroncelli, M. *J. Phys. Chem. B* **2013**, *117*, 4291–4504.

[71] Embs, J. P.; Burankova, T.; Reichert, E.; Hempelmann, R. *J. Phys. Chem. B* **2012**, *116*, 13265–13271.

[72] Cadena, C.; Zhao, Q.; Snurr, R. Q.; Maginn, E. J. *J. Phys. Chem. B* **2006**, *110*, 2821–2832.

[73] Borodin, O.; Smith, G. D. *Macromolecules* **2006**, *39*, 1620–1629.

[74] Sun, H.; Qiao, B.; Zhang, D.; Liu, C. *J. Phys. Chem. A* **2010**, *114*, 3990–3996.

[75] Krüger, M.; Bründermann, E.; Funkner, S.; Weingärtner, H.; Havenith, M. *J. Chem. Phys.* **2010**, *132*, 101101.

[76] Wakai, C.; Oleinikova, A.; Ott, M.; Weingärtner, H. *J. Phys. Chem.* **2005**, *109*, 17028–17030.

[77] Buchner, R. *Pure Appl. Chem.* **2008**, *80*, 1239–1252.

[78] Kanzaki, R.; Doi, H.; Song, X.; Hara, S.; Ishiguro, S.; Umebayashi, Y. *J. Phys. Chem. B* **2012**, *116*, 14146–14152.

[79] Doi, H.; Song, X.; Minofar, B.; Kanzaki, R.; Takamuku, T.; Umebayashi, Y. *Chem. Eur. J.* **2013**, *19*, 11522–11526.

[80] Allen, M.; Evans, F.; Lumry, R. *J. Sol. Chem.* **1985**, *14*, 549–560.

[81] Perron, G.; Hardy, A.; Justice, J.-C.; Desnoyers, J. E. *J. Sol. Chem.* **1993**, *22*, 1159–1178.

[82] Buchner, R.; Chen, T.; Hefter, G. *J. Phys. Chem. B* **2004**, *108*, 2365–2375.

[83] Maxwell, J. C. *A treatise on electricity and magnetism*; Claredon Press: Oxford, 1881.

[84] Kremer, F.; Schönhals, A. *Broadband Dielectric Spectroscopy*; Springer, Berlin, 2003.

[85] Barthel, J.; Buchner, R. *Chem. Soc. Rev.* **1992**, *21*, 263–270.

[86] Böttcher, C. J. F.; Bordewijk, P. *Theory of electric polarization*; Vol.1 & 2, Elsevier, Amsterdam, 1978.

[87] Barthel, J.; Buchner, R.; In, *Encyclopedia of Physical Science and Technology*; Academic Press: Orlando, 2002.

[88] Buchner, R.; Barthel, J. *Annu. Rep. Prog. Chem. Sect. C* **2001**, *97*, 349–382.

[89] Hölzl, C. Ph.D. thesis, Universität Regensburg, 1998.

[90] Buchner, R. Ph.D. thesis, Universität Regensburg, 1986.

[91] Wagner, K. W. *Arch. Electrotechn.* **1914**, *2*, 371.

[92] Chalmers, J. M.; Griffiths, P. R. *Handbook of Vibrational Spectroscopy*; Wiley-VCH: Weinheim, 2001.

[93] Pehl, E. *Mikrowellentechnik*; Band 1, Hüthig, Heidelberg, 1984.

[94] Moldover, M. R.; Marsh, K. N.; Barthel, J.; Buchner, R. *Experimental Thermodynamics, Vol. IV: Measurement of the Thermodynamic Properties of Single Phases*; Elsevier: Amsterdam, 2003.

[95] Debye, P.; Falkenhagen, H. *Phys. Z.* **1928**, *29*, 121.

[96] Wittmann, H. J. Ph.D. thesis, Universität Regensburg, 1985.

[97] Birch, J. R.; Parker, T. J. *Infrared and Millimeter Waves*; Academic Press: New York Vol.2, 1979.

[98] Reider, G. A. *Photonik, Eine Einführung in die Grundlagen*; Springer, Wien, New York, 2005.

[99] Debye, P. *Polar molecules*; Dover: New York, 1930.

[100] Pellat, H. *Ann. Chim. Phys.* **1899**, *18*, 150.

[101] Havriliak, S.; Negami, S. *J. Polym. Sci., Part C* **1966**, *14*, 99–117.

[102] Davidson, D. W.; Cole, R. H. *J. Phys. Chem.* **1950**, *18*, 1417.

[103] Davidson, D. W.; Cole, R. H. *J. Phys. Chem.* **1951**, *19*, 1484.

[104] Cole, R. H.; Cole, K. S. *J. Phys. Chem.* **1941**, *9*, 341–351.

[105] Cole, K. S., R. H. Cole *J. Phys. Chem.* **1942**, *10*, 98–105.

[106] Turton, D.; Wynne, K. *J. Chem. Phys.* **2008**, *128*, 154516.

[107] Turton, D. A.; Sonnleitner, T.; Ornter, A.; Walther, M.; Hefter, G.; Seddon, K. R.; Stana, S.; Plechkova, N.; Buchner, R.; Wynne, K. *Faraday Discuss.* **2012**, *154*, 145–153.

[108] Chang, Y. J.; Castner, E. W. *J. Phys. Chem.* **1996**, *100*, 3330–3343.

[109] Ribeiro, M. C. C. *J. Chem. Phys.* **2011**, *134*, 244507.

[110] Turton, D. A., *personal communication*, 2011.

[111] http://mathworld.wolfram.com/DawsonsIntegral.html.

[112] Onsager, L. *J. Am. Chem. Soc.* **1936**, *58*, 1486–1493.

[113] Kirkwood, J. G. *J. Chem. Phys.* **1939**, *7*, 911.

[114] Fröhlich, H. *Theory of Dielectrics*; 2nd ed.; Oxford University Press: Oxford, 1965.

[115] Cavell, E. A. S.; Knight, P. C.; Sheikh, M. A. *J. Chem. Soc. Faraday Trans.* **1971**, *67*, 2225–2233.

[116] Hetzenauer, H. Ph.D. thesis, Universität Regensburg, 1990.

[117] Barthel, J.; Hetzenauer, H.; Buchner, R. *Ber. Bunsen-Ges. Phys. Chem.* **1992**, *96*, 1424–1432.

[118] Scholte, T. *Physica XV* **1949**, *5–6*, 437–449.

[119] Osborn, J. A. *Phys. Rev.* **1945**, *67*, 351–357.

[120] Stoner, E. C. *Phil. Mag.* **1945**, *36*, 803–821.

[121] Dote, J. L.; Kivelson, D.; Schwartz, R. N. *J. Phys. Chem.* **1981**, *85*, 2169–2180.

[122] Dote, J. L.; Kivelson, D. *J. Phys. Chem.* **1983**, *87*, 3889–3893.

[123] Kalman, B.; Clarke, N.; Johansson, B. *J. Chem. Phys.* **1989**, *93*, 4608–4615.

[124] Powles, J. G. *J. Chem. Phys.* **1953**, *21*, 633.

[125] Glarum, S. H. *J. Chem. Phys.* **1960**, *33*, 1371–1375.

[126] Kivelson, D.; Madden, P. *J. Chem. Phys.* **1984**, *88*, 6557–6559.

[127] Atkins, P.; de Paula, J. *Physical Chemistry*; Oxford University Press, 2006.

[128] Czeslik, C.; Seemann, H.; Winter, R. *Basiswissen Physikalische Chemie*; Vieweg+Teubner, 2010.

[129] Eyring, H. *J. Chem. Phys.* **1935**, *3*, 107–115.

[130] Laidler, K. J.; King, C. *J. Phys. Chem.* **1983**, *87*, 2657–2664.

[131] Fulcher, G. S. *J. Am. Chem. Cer. Soc.* **1925**, *8*, 339–355.

[132] Vogel, H. *Phys. Z.* **1921**, *22*, 645.

[133] Doolittle, A. K. *J. Appl. Phys.* **1951**, *87*, 1471–1475.

[134] Dagdug, L. *J. Phys. Condens. Matter* **2000**, *12*, 9573–9589.

[135] Angell, C. A. *Science* **1995**, *267*, 1924–1935.

[136] Kauzmann, W. *Chem. Rev.* **1948**, *43*, 219–256.

[137] Evans, D. F.; Yamauchi, A.; Roman, R.; Casassa, E. Z. *J. Colloid Interface Sci.* **1982**, *88*, 89–96.

[138] Seddon, K. R.; Stark, A.; Torres, M.-J. *Pure Appl. Chem.* **2000**, *72*, 2275–2287.

[139] Barthel, J.; Bachhuber, K.; Buchner, R.; Hetzenauer, H.; Kleebauer, M. *Ber. Bunsen-Ges. Phys. Chem.* **1991**, *95*, 853–859.

[140] Schrödle, S. Ph.D. thesis, Universität Regensburg, 2005.

[141] Agilent Application Note 5965-7707E, *Understanding the Fundamental Principles of Vector Network Analysis*, September 2012.

[142] Blackham, D. V.; Pollard, R. D. *IEEE Trans. Instr. Meas.* **1997**, *46*, 1093–1099.

[143] Wu, M.; Yao, X.; Zhang, L. *Meas. Sci. Technol.* **2000**, *11*, 1617–1622.

[144] Maury Microwave Corporation, Application Note 5C-026, *Verifying the Performance of Vector Network Analyzers*, February 2006.

[145] Agilent Reference Guide N4693-90001, *Electronic Calibration Modules*, August 2012.

[146] Levine, H.; Papas, C. H. *J. Appl. Phys.* **1951**, *22*, 29–43.

[147] Misra, D.; Chabbra, M.; Epstein, B. R.; Mirotznik, M.; Foster, K. R. *IEEE Trans. Microwave Theory Tech.* **1990**, *38*, 8–14.

[148] Barthel, J.; Buchner, R.; Wurm, B. *J. Mol. Liq.* **2002**, *98–99*, 51–69.

[149] Schrödle, S.; Hefter, G.; Kunz, W.; Buchner, R. *Langmuir* **2006**, *22*, 924–932.

[150] Göttmann, O.; Kaatze, U.; Petong, P. *Meas. Sci. Technol.* **1996**, *7*, 525–534.

[151] Barthel, J.; Buchner, R.; Eberspächer, P. N.; Münsterer, M.; Stauber, J.; Wurm, B. *J. Mol. Liq.* **1998**, *78*, 83–109.

[152] Buchner, R.; Hefter, G.; May, P. M. *J. Phys. Chem. A* **1999**, *103*, 1–9.

[153] Jepsen, P.; Fischer, B. M.; Thoman, A.; Helm, H.; Suh, J. Y.; Lopez, R.; Haglund, R. F. *Phys. Rev. B* **2006**, *74*, 205103.

[154] Stoppa, A.; Zech, O.; Kunz, W.; Buchner, R. *J. Chem. Eng. Data* **2010**, *55*, 1768–1773.

[155] Franz, M.; Fischer, B. M.; Walther, M. *J. Mol. Struct.* **2011**, *1006*, 34–40.

[156] Thoman, A. Ph.D. thesis, Albert-Ludwigs-Universität Freiburg, 2009.

[157] Walther, M.; Fischer, B. M.; Ortner, A.; Thoman, A.; Helm, H. *Analytical and Bioanalytical Chemistry* **2010**, *397*, 1009–1017.

[158] Fischer, B. M. Ph.D. thesis, Albert-Ludwigs-Universität Freiburg, 2005.

[159] Birch, J. R.; Domrey, J. D.; Lesurf, J. *NPL Report DES 69*; NPL: Teddington, UK, 1981.

[160] Bertie, J. E.; Zhang, S. L.; Keefe, C. D. *Vib. Spectr.* **1995**, *8*, 215–229.

[161] Kanwal, R. P. *Linear Integral Equations: Theory and Technique*; Birkhäuser: Boston, 1996.

[162] Castner, E. W.; Maroncelli, M. *J. Mol. Liq.* **1998**, *77*, 1–36.

[163] Turton, D.; Corsaro, C.; Candelaresi, M.; Brownlie, A.; Seddon, K. R.; Mallamace, F.; Wynne, K. *Faraday Discuss.* **2011**, *150*, 493–504.

[164] Shen, Y. R. *The Principles of Nonlinear Optics*; Wiley: New York, 1984.

[165] Smith, N. A.; Meech, S. R. *Int. Rev. Phys. Chem.* **2002**, *21*, 75–100.

[166] Fecko, C. J.; Eaves, J. D.; Tomakoff, A. *J. Chem. Phys.* **2002**, *117*, 1139–1154.

[167] McMorrow, D.; Lotshaw, W. T. *Chem. Phys. Lett.* **1990**, *174*, 85–94.

[168] Lotshaw, W. T.; McMorrow, D.; Thantu, N.; Melinger, J. S.; Kitchenham, R. *J. Raman Spectrosc.* **1995**, *26*, 571–583.

[169] Geiger, L. C.; Ladanyi, B. M. *Chem. Phys. Lett.* **1989**, *159*, 413–420.

[170] Gregory, A. P.; Clarke, R. N. *Meas. Sci. Technol.* **2007**, *18*, 1372–1386.

[171] Bevington, P. R. *Data Reduction and Error Analysis for the Physical Sciences*; McGraw Hill: New York, 1969.

[172] Shaukat, S.; Buchner, R. *J. Chem. Eng. Data* **2011**, *56*, 4944–4949.

[173] Barthel, J.; Feuerlein, F.; Neueder, R.; Wachter, R. *J. Sol. Chem.* **1980**, *9*, 209–219.

[174] Stewart, J. J. P. M. *Stewart Computational Chemistry*; Colorado Springs, CO, USA, 2009.

[175] Stewart, J. J. P. *J. Mol. Mod.* **2007**, *13*, 1173–1213.

[176] Klamt, A.; Schüürmann, G. *J. Chem. Soc. Perkin Trans.* **1993**, *2*, 799.

[177] Bondi, A. *J. Phys. Chem.* **1964**, *68*, 441–451.

[178] Senda, N.; Furukawa, Y. *Winmostar, version (V4.019)*, http://winmostar.com.

[179] Neese, F. *WIREs Comput. Mol. Sci.* **2012**, *2*, 73–78.

[180] Shetty, P. H.; Poole, S. K.; Poole, C. F. *Anal. Chim. Acta* **1990**, *236*, 51–61.

[181] MacFarlane, D. R.; Pringle, J. M.; Johansson, K. M.; Forsyth, S.; Forsyth, M. *Chem. Commun.* **2006**, 1905–1917.

[182] Susan, M. A. B. H.; Noda, A.; Mitsushima, S.; Watanabe, M. *Chem. Commun.* **2003**, 938–939.

[183] Rana, U. A.; Forsyth, M.; MacFarlane, D. R.; Pringle, J. M. *Electrochimica Acta* **2012**, *84*, 213–222.

[184] Fernicola, A.; Scrosati, B.; Ohno, H. *Ionics* **2006**, *12*, 95–102.

[185] Zech, O.; Thomaier, S.; Kolodziejski, A.; Touraud, D.; Grillo, I.; Kunz, W. *J. Colloid Interface Sci.* **2010**, *347*, 227–232.

[186] Shi, L.; Zheng, L. *J. Phys. Chem. B* **2012**, *116*, 2162–2172.

[187] Atkin, R.; Warr, G. *J. Phys. Chem. B* **2008**, *112*, 4146–4166.

[188] Hayes, R.; Imberti, S.; Warr, G.; Atkin, R. *Phys. Chem. Chem. Phys.* **2011**, *13*, 3237–3247.

[189] Wakeham, D.; Nelson, A.; Warr, G.; Atkin, R. *Phys. Chem. Chem. Phys.* **2011**, *13*, 20828–20835.

[190] Gontrani, L.; Bodo, E.; Triolo, A.; Leonelli, F.; D'Angelo, P.; Migliorati, V.; Caminiti, R. *J. Phys. Chem. B* **2012**, *116*, 13024–13032.

[191] Umebayashi, Y.; Chung, W.; Mitsugi, T.; Fukuda, S.; Takeuchi, M.; Fujii, K.; Takamuku, T.; Kanzaki, R.; Ishiguro, S. *J. Comput. Chem. Jpn.* **2008**, *7*, 125–134.

[192] Song, X.; Hamano, H.; Minofar, B.; Kanzaki, R.; Fujii, K.; Kameda, Y.; Kohara, S.; Watanabe, M.; Ishiguro, S.; Umebayashi, Y. *J. Phys. Chem. B* **2012**, *116*, 2801–2813.

[193] Hunger, J. M.Sc. thesis, Universität Regensburg, 2006.

[194] Hunger, J.; Stoppa, A.; Thoman, A.; Walther, M.; Buchner, R. *Chem. Phys. Lett.* **2009**, *471*, 85–91.

[195] Barthel, J.; Wachter, R.; Gores, H.-J. *Modern Aspects of Electrochemistry*; Plenum, New York, 1979.

[196] Greaves, T. L.; Weerawardena, A.; Fong, C.; Krodkiewska, I.; Drummond, C. J. *J. Phys. Chem. B* **2006**, *110*, 22479–22487.

[197] Poole, C. F.; Kersten, B. R.; Ho, S. S.; Coddens, M. E.; Furton, K. G. *J. Chromatogr.* **1986**, *352*, 407–425.

[198] Shetty, P. H.; Youngberg, P. J.; Kersten, B. R.; Poole, C. F. *J. Chromatogr.* **1987**, *411*, 61–79.

[199] Belieres, J.-P.; Angell, C. A. *J. Phys. Chem. B* **2007**, *111*, 4926–4937.

[200] Oleinikova, A.; Bonetti, M. *J. Sol. Chem.* **2002**, *31*, 397–413.

[201] Ferry, J. D. *Viscoelastic Properties of Polymers*; Wiley: New York, 1980.

[202] Angell, C. A. *J. Non-Cryst. Solids* **1991**, *131-133*, 13.

[203] Smith, J. A.; Webber, G. B.; Warr, G. G.; Atkin, R. *J. Phys. Chem. B* **2013**, *117*, 13930–13935.

[204] Bouzón Capelo, S.; Méndez-Morales, T.; Carrete, J.; López Lago, E.; Vila, J.; Cabeza, O.; Rodriguez, J. R.; Turmine, M.; Varela, L. M. *J. Phys. Chem. B* **2012**, *116*, 11302–11312.

[205] Schröder, C.; Steinhauser, O. In *Computational Spectroscopy: Methods, Experiments and Applications*; Grünenberg, J., Ed.; Wiley-VCH: Weinheim, Germany, 2010.

[206] Wiedersich, J.; Blochowicz, T.; Benkhof, S.; Kudlik, A.; Surovtsev, N. V.; Tschirwitz, C.; Novikov, V. N.; Rössler, E. *J. Phys. Condens. Matter* **1999**, *11*, A147–A156.

[207] Salvador, P.; Curtis, J. E.; Tobias, D. J.; Jungwirth, P. *Phys. Chem. Chem. Phys.* **2003**, *5*, 3752–3757.

[208] Hunger, J.; Sonnleitner, T.; Liu, L.; Buchner, R.; Bonn, M.; Bakker, H. J. *J. Phys. Chem. Lett.* **2012**, *3*, 3034–3038.

[209] Diaz-Calleja, R. *Macromolecules* **2000**, *33*, 8924.

[210] Laage, D.; Hynes, J. T. *Science* **2006**, *311*, 832–835.

[211] Laage, D.; Stirnemann, G.; Sterpone, F.; Rey, R.; Hynes, J. T. *Annu. Rev. Phys. Chem.* **2011**, *62*, 395–416.

[212] Ohmine, I.; Tanaka, H. *Chem. Rev.* **1993**, *93*, 2545–2566.

[213] Sonnleitner, T.; Turton, D.; Waselikowski, S.; Hunger, J.; Stoppa, A.; Walther, M.; Wynne, K.; Buchner, R. *J. Mol. Liq.* **2013**, http://dx.doi.org/10.1016/j.molliq.2013.09.019.

[214] Izgorodina, E. I.; Forsyth, M.; MacFarlane, D. R. *Phys. Chem. Chem. Phys.* **2009**, *11*, 2452–2458.

[215] Heisler, I. A.; Meech, S. R. *J. Phys. Chem. B* **2008**, *112*, 12976–12984.

[216] Turton, D. A.; Martin, D. F.; Wynne, K. *Phys. Chem. Chem. Phys.* **2010**, *12*, 4191–4200.

[217] Fukasawa, T.; Sato, T.; Watanabe, J.; Hama, Y.; Kunz, W.; Buchner, R. *Phys. Rev. Lett.* **2005**, *95*, 197802.

[218] Hasted, J. B.; Husain, S. K.; Frescura, F. A. M.; Birch, J. R. *Chem. Phys. Lett.* **1985**, *118*, 622–625.

[219] Bartoli, F. J.; Litovitz, T. A. *J. Chem. Phys.* **1972**, *56*, 413–425.

[220] Zelsmann, H. R. *J. Mol. Struct.* **1995**, *350*, 95–114.

[221] Stassen, H.; Dorfmüller, T.; Ladanyi, B. M. *J. Chem. Phys.* **1994**, *100*, 6318–6330.

[222] Palombo, F.; Paolantoni, M.; Sassi, P.; Morresi, A.; Giorgini, M. G. *Phys. Chem. Chem. Phys.* **2011**, *13*, 16197–16207.

[223] Ladanyi, B. M.; Klein, S. *J. Chem. Phys.* **1996**, *105*, 1552–1561.

[224] Amo, Y.; Tominaga, Y. *Physica A* **2000**, *276*, 401–412.

[225] Gaiduk, V. I.; Nielsen, O. F.; Crothers, D. S. F. *J. Mol. Liq.* **2008**, *137*, 92–103.

[226] Brubach, J.-B.; Mermet, A.; Filabozzi, A.; Gerschel, A.; Roy, P. *J. Chem. Phys.* **2005**, *122*, 184509.

[227] Johari, G. P.; Goldstein, M. *J. Chem. Phys.* **1970**, *53*, 2372–2388.

[228] Johari, G. P.; Goldstein, M. *J. Chem. Phys.* **1971**, *55*, 4245–4252.

[229] Johari, G. P.; Whalley, E. *Faraday Symp. Chem. Soc.* **1972**, *6*, 23–42.

[230] Goldstein, M. *J. Chem. Phys.* **1969**, *51*, 3728–3739.

[231] Götze, W.; Sjogren, L. *Rep. Prog. Phys.* **1992**, *55*, 241–376.

[232] Zahn, S.; Thar, J.; Kirchner, B. *J. Chem. Phys.* **2010**, *132*, 124506.

[233] Yoshizawa, M.; Xu, W.; Angell, C. A. *J. Am. Chem. Soc.* **2003**, *125*, 15411–15419.

[234] Johansson, K. M.; Izgorodina, E. I.; Forsyth, M.; MacFarlane, D. R.; Seddon, K. R. *Phys. Chem. Chem. Phys.* **2008**, *10*, 2972–2978.

[235] Vitorino, J.; Bernardes, C. E. S.; Minas da Piedade, M. E. *Phys. Chem. Chem. Phys.* **2012**, *14*, 4440–4446.

[236] Del Pópolo, M. G.; Kohanoff, J.; Lynden-Bell, R. M. *J. Phys. Chem. B* **2006**, *110*, 8798–8803.

[237] Noda, A.; Susan, M. A. B. H.; Kudo, K.; Mitsushima, S.; Hayamizu, K.; Watanabe, M. *J. Phys. Chem. B* **2003**, *107*, 4024–4033.

[238] Ogihara, W.; Kosukegawa, H.; Ohno, H. *Chem. Commun.* **2006**, 3637–3639.

[239] Doi, H. *personal communication*, 2013.

[240] Barthel, J.; Buchner, R.; Hölzl, C.; Münsterer, M. *Z. Phys. Chem.* **2000**, *214*, 1213–1231.

[241] Konrat, H., R.and Sterk *J. Phys. Chem.* **1990**, *94*, 1291–1293.

[242] Pickl, H. Ph.D. thesis, Universität Regensburg, 1998.

[243] Nakabayashi, T.; Kosugi, K.; Nishi, N. *J. Phys. Chem. A* **1999**, *103*, 8595–8603.

[244] Takamuku, T.; Kyoshoin, Y.; Nogichi, H.; Kusano, S.; Yamaguchi, T. *J. Phys. Chem. B* **2007**, *111*, 9270–9280.

[245] Tjahjono, M.; Allian, A. D.; Garland, M. *J. Phys. Chem. B* **2008**, *112*, 6448–6459.

[246] For molecular volumes, V_{m}, van der Waals volumes calculated by Winmostar (V4.019) software[178] were used.

[247] Doi, H.; Umebayashi, Y. Unpublished results, 2013.

[248] Shirota, H.; Castner, E. W. *J. Phys. Chem. A* **2005**, *109*, 9388–9392.

[249] Roy, D.; Patel, N.; Conte, S.; Maroncelli, M. *J. Phys. Chem. B* **2010**, *114*, 8410–8424.

[250] Angell, C. A. a. *Acc. Chem. Res.* **2007**, *40*, 1228–1236.

[251] Zech, O.; Stoppa, A.; Buchner, R.; Kunz, W. *J. Chem. Eng. Data* **2010**, *55*, 1774–1778.

[252] Nishi, N.; Nakabayashi, T.; Kosugi, K. *J. Phys. Chem. A* **1999**, *103*, 10851–10858.

[253] Walrafen, G. E.; Fisher, M. R.; Hokmabadi, M. S.; Yang, W.-H. *J. Chem. Phys.* **1985**, *85*, 6970–6982.

[254] Ueki, T.; Watanabe, M. *Macromolecules* **2008**, *41*, 3739–3749.

[255] Hoarfrost, M. L.; Tyagi, M.; Segaman, R. A.; Reimer, J. A. *J. Phys. Chem. B* **2012**, *116*, 8201–8209.

[256] Sonnleitner, T.; Buchner, R. Unpublished results, 2013.

[257] Rey, I.; Johansson, P.; Lindgren, J.; Lassègues, J. C.; Grondin, J.; Servant, L. *J. Phys. Chem. A* **1998**, *102*, 3249–3258.

[258] Lopes, J. N. C.; Shimizu, K.; Padua, A.; Umebayashi, Y.; Fukuda, S.; Fujii, K.; Ishiguro, S. *J Phys. Chem. B* **2008**, *112*, 1465–1472.

[259] Bešter-Rogač, M.; Stoppa, A.; Buchner, R. *in preparation* **2013**.

[260] Meyer, M. *J. Mol. Struct. THEOCHEM* **1994**, *304*, 45–51.

[261] Hückel, W. *Z. physik. chem. Abt., A* **1940**, *106*, 129.

[262] Orzechowski, K.; Pajdowska, M.; Czamecki, M.; Kaatze, U. *J. Mol. Liq.* **2007**, *133*, 11–16.

[263] Hepler, L. G.; Fenby, D. V. *J. Chem. Thermodyn.* **1973**, *5*, 471–475.

[264] Literature values from Ref. 358; references are therein cited.

[265] Chocholousová, J.; Vacek, J.; Hobza, P. *J. Phys. Chem. A* **2003**, *107*, 3086–3092.

[266] Bruneau, A.; Génin, F.; Quilès, F. *Phys. Chem. Chem. Phys.* **2000**, *2*, 5020–5029.

[267] Nakabayashi, T.; Sato, H.; Hirata, F.; Nishi, N. *J. Phys. Chem. A* **2001**, *105*, 245–250.

[268] Turton, D.; Hunger, J.; Stoppa, A.; Hefter, G.; Thoman, A.; Walther, M.; Buchner, R.; Wynne, K. *Proc. SPIE* **2010**, *7601*, 76010H.

[269] Russina, O.; Triolo, A.; Gontrani, L.; Caminiti, R.; Xiao, D.; Hines Jr, L. G.; Bartsch, R.; Quitevis, E. L.; Plechkova, N.; Seddon, K. R. *J Phys.: Condens. Matter* **2009**, 424121.

[270] Sangoro, J.; Iacob, C.; Naumov, S.; Valiullin, R.; Rexhausen, H.; Hunger, J.; Buchner, R.; Strehmel, V.; Kärger, J.; Kremer, F. *Soft Matter* **2011**, *7*, 1678–1681.

[271] Lopes, J. N. C.; Padua, A. *J. Phys. Chem. B* **2006**, *110*, 3330–3335.

[272] Gerhard, D.; Alpslan, S. C.; Gores, H.-J.; Uerdingen, M.; Wasserscheid, P. *Chem. Commun.* **2005**, 5080–5082.

[273] Best, A. S.; Bhatt, A. I.; Hollenkamp, A. F. *J. Electrochem. Soc.* **2010**, *157*, A903–A911.

[274] Zhang, Q.; Liu, S.; Li, Z.; Li, J.; Chen, Z.; Wang, R.; Lu, L.; Deng, Y. *Chem. Eur. J.* **2009**, *15*, 765–778.

[275] Wei, D.; Wing Ng, T. *Electrochem. Commun.* **2009**, *11*, 1996–1999.

[276] Xi, C.; Cao, Y.; Cheng, Y.; Wang, M.; Jing, X.; Zakeeruddin, S. M.; Grätzel, M.; Wang, P. *J. Phys. Chem. C* **2008**, *112*, 11063–11067.

[277] Fang, S.; Yang, L.; Wei, D.; Peng, C.; Tachibana, K.; Kamijima, K. *Electrochemistry Communications* **2007**, *9*, 2696–2702.

[278] Han, H.-B.; Nie, J.; Liu, K.; Li, W.-K.; Feng, W.-F.; Armand, M.; Matsumoto, H.; Zhou, Z.-B. *Electrochimica Acta* **2010**, *55*, 1221–1226.

[279] Tokuda, H.; Tsuzuki, S.; Susan, M. A. B. H.; Hayamizu, K.; Watanabe, M. *J. Phys. Chem. B* **2006**, *110*, 19593–19600.

[280] Matsumoto, H.; Matsuda, T.; Miyazaki, Y. *Chem. Lett.* **2000**, *12*, 1430–1431.

[281] Janus, E.; Bittner, B. *Catal. Lett.* **2010**, *134*, 147–154.

[282] Yang, L.; Zhang, Z. X.; Gao, X. H.; Zhang, H. Q.; Mashita, K. *J. Power Sources* **2006**, *162*, 614.

[283] Okoturo, O. O.; VanderNoot, T. J. *J. Electroanalytical Chem.* **2004**, *568*, 167–181.

[284] Oliviera, F. S.; Freire, M. G.; Carvalho, P. J.; Coutinho, J. A. P.; Lopes, J. N. C.; Rebelo, L. P. N.; Marrucho, I. M. *J. Chem. Eng. Data* **2010**, *55*, 4515–4520.

[285] Zhang, Q.-G.; Sun, S.-S.; Pitula, S.; Liu, Q.-S.; Welz-Biermann, U.; Zhang, J.-J. *J. Chem. Eng. Data* **2011**, *56*, 4659–4664.

[286] McHale, G.; Hardacre, C.; Ge, R.; Doy, N.; Allen, R. W. K.; MacInnes, J. M.; Bown, M. R.; Newton, M. *Anal. Chem.* **2008**, *80*, 5806–5811.

[287] González, E. J.; González, B.; Macedo, E. A. *J. Chem. Eng. Data* **2013**, *58*, 1440–1448.

[288] Blahut, A.; Dohnal, V. *J. Chem. Eng. Data* **2011**, *56*, 4909–4918.

[289] MacFarlane, D. R.; Golding, J.; Forsyth, S.; Forsyth, M.; Deacon, G. B. *Chem. Commun.* **2001**, 1430–1431.

[290] Ishida, T.; Shirota, H. *J. Phys. Chem. B* **2013**, *117*, 1136–1150.

[291] Shirota, H.; Castner, E. W. *J. Phys. Chem. B* **2005**, *109*, 21576–21585.

[292] Hu, Z.; Huang, X.; Annapureddy, H. V. R.; Margulis, C. J. *J. Phys. Chem. B* **2008**, *112*, 7837–7849.

[293] Marcus, Y. *The Properties of Solvents*; New York, 1999.

[294] Stoppa, A.; Buchner, R.; Hefter, G. *J. Mol. Liq.* **2010**, *153*, 46–51.

[295] Johansson, P.; Gejji, S. P.; Tegenfeldt, J.; Lindgren, J. *Electrochimica Acta* **1998**, *43*, 1375–1329.

[296] Umebayashi, Y.; Fujimori, T.; Sukizaki, T.; Asada, M.; Fujii, K.; Kanzaki, R.; Ishiguro, S. *J. Phys. Chem. A* **2005**, *109*, 8976–8982.

[297] Herstedt, M.; Henderson, W. A.; Smirnov, M.; Ducasse, L.; Servant, L.; Talaga, D.; Lassègues, J. C. *J. Mol. Liq.* **2006**, *783*, 145–156.

[298] Qiao, B.; Kerkeler, C.; Berger, R.; Delle Site, L.; Holm, C. *J. Phys. Chem. B* **2008**, *112*, 1743–1751.

[299] Urahata, S. M.; Ribeiro, M. C. C. *J. Chem. Phys.* **2004**, *120*, 1855.

[300] Hardacre, C.; Holbrey, J. D.; McMath, S. E. J.; Bowron, D. T.; Soper, A. K. *J. Chem. Phys.* **2003**, *118*, 273.

[301] Madden, P. A.; O'Sullivan, K. F. *J. Chem. Phys.* **1991**, *95*, 1980.

[302] Ribeiro, M. C. C.; Wilson, M.; Madden, P. A. *J. Chem. Phys.* **1998**, *109*, 9859.

[303] Ribeiro, M. C. C.; Oliviera, L. F. C.; Goncalves, N. S. *Phys. Rev. B* **2001**, *63*, 104303.

[304] Kobrak, M. N. *J. Chem. Phys.* **2006**, *125*, 064502.

[305] Novikov, N. V. *Phys. Rev. B* **1997**, *55*, R14 685.

[306] Fuchs, M.; Latz, A. *J. Chem. Phys.* **1991**, *95*, 7074.

[307] Zorebski, E.; Geppert-Rybczynska, M.; Zorebski, M. *J. Phys. Chem. B* **2013**, *117*, 3867–3876.

[308] Rivera, A.; Brodin, A.; Pugachev, A.; Rössler, E. A. *J. Chem. Phys.* **2007**, *126*, 114503.

[309] Scher, H.; Lax, M. *Phys. Rev. B* **1973**, *7*, 4491.

[310] Sangoro, J.; Kremer, F. *Acc. Chem. Res.* **2012**, *45*, 525–532.

[311] Brodin, A.; Rössler, E. *J. Chem. Phys.* **2006**, *125*, 114502.

[312] Sangoro, J.; Iacob, C.; Serghei, A.; Naumov, S.; Galvosas, P.; Kärger, J.; Wespe, C.; Bordusa, F.; Stoppa, A.; Hunger, J.; Buchner, R.; Kremer, F. *J. Chem. Phys.* **2008**, *128*, 214509.

[313] Krause, C.; Sangoro, J.; Iacob, C.; Kremer, F. *J. Phys. Chem. B* **2010**, *114*, 382–386.

[314] Ngai, K. L.; Leon, C. *Phys. Rev. B* **1999**, *60*, 9396.

[315] Fujii, K.; Fujimori, T.; Takamuku, T.; Kanzaki, R.; Umebayashi, Y.; Ishiguro, S. *J. Phys. Chem. B* **2006**, *110*, 8179–8183.

[316] Herstedt, M.; Smirnov, M.; Johansson, P.; Chami, M.; Grondin, J.; Servant, L.; Lassègues, J. C. *J. Raman Spectrosc.* **2005**, *36*, 762–770.

[317] Castriota, M.; Caruso, T.; Agostino, R.; Cazzanelli, E.; Henderson, W. A.; Passerini, S. *J. Phys. Chem. A* **2005**, *109*, 92–96.

[318] Umebayashi, Y.; Mori, S.; Fujii, K.; Tsuzuki, S.; Seki, S.; Hayamizu, K.; Ishiguro, S. *J. Phys. Chem. B* **2010**, *114*, 6513–6521.

[319] Fujii, K.; Seki, S.; Fukuda, S.; Kanzaki, R.; Takamuku, T.; Umebayashi, Y.; Ishiguro, S. *J. Phys. Chem. B* **2007**, *111*, 12829–12833.

[320] Turton, D.; Hunger, J.; Stoppa, A.; Thoman, A.; Candelaresi, M.; Hefter, G.; Walther, M.; Buchner, R.; Wynne, K. *J. Mol. Liq.* **2011**, *159*, 2–8.

[321] Rajian, J. R.; Shengfu, L.; Bartsch, R.; Quitevis, E. L. *Chem. Phys. Lett.* **2004**, *393*, 372–377.

[322] Ryu, S.; Stratt, R. *J. Phys. Chem. B* **2004**, *108*, 6782–6795.

[323] Tao, G.; Stratt, R. *J. Phys. Chem. B* **2006**, *110*, 976–987.

[324] Shirota, H.; Wishart, J. F.; Castner, E. W. *J. Phys. Chem. B* **2007**, *111*, 4819–4829.

[325] Evans, D. F. *Langmuir* **1988**, *4*, 3–12.

[326] Greaves, T. L.; Weerawardena, A.; Krodkiewska, I.; Drummond, C. J. *J. Phys. Chem. B* **2008**, *112*, 896–905.

[327] Parker, A. J. *Pure Appl. Chem.* **1981**, *53*, 1437–1445.

[328] Chu, A.; Braatz, P. *J. Power Sources* **2002**, *112*, 236.

[329] Ohba, T.; Ikawa, S. *Mol. Phys.* **1991**, *73*, 985–997.

[330] Barthel, J.; Kleebauer, M. *J. Sol. Chem.* **1991**, *20*, 977–993.

[331] Foggi, P.; Bartolini, P.; Bellini, M.; Giorgini, M. G.; Morresi, A.; Sassi, P.; Cataliotto, R. S. *Eur. Phys. J. D* **2002**, *21*, 143–151.

[332] Barthel, J.; Kleebauer, M.; Buchner, R. *J. Sol. Chem.* **1995**, *24*, 1–17.

[333] Raineri, F. O.; Friedman, H. L. *Adv. Chem. Phys.* **1999**, *107*, 81–189.

[334] Barthel, J.; Neueder, R.; Schröder, P. *Electrolyte Data Collection, Part 1c: Conductivites, Transfer Numbers, Limiting Ionic Conductivities of Solutions of Aprotic, Protophobic Solvents. I: Nitriles*; Dechema: Franfurt, 1996; Vol. XII.

[335] Wurm, B.; Münsterer, M.; Richardi, J.; Buchner, R.; Barthel, J. *J. Mol. Liq.* **2005**, *119*, 97–106.

[336] Jellema, R.; Bulthuis, J.; van der Zwan, G. *J. Mol. Liq.* **1997**, *73*, 179–193.

[337] Barthel, J.; Gores, H.-J.; Schmeer, G.; Wachter, R. In *Topics in Current Chemistry*; Boschke, F. L., Ed.; Springer: Berlin/Heidelberg, 1983; Chapter Vol. 111,, pp 33–144.

[338] Eberspächer, P. N.; Wismeth, E.; Buchner, R.; Barthel, J. *J. Mol. Liq.* **2006**, *129*, 3–12.

[339] Barthel, J.; Deser, R. *J. Sol. Chem.* **1994**, *23*, 1133–1146.

[340] Clare, B.; Hefter, G.; Singh, P. *J. Aust. J. Chem.* **1990**, *43*, 257–261.

[341] Takamuku, T.; Tabata, M.; Yamaguchi, A.; Nishimoto, J.; Kunamoto, M.; Wakita, H.; Yamaguchi, T. *J. Phys. Chem. B* **1998**, *102*, 8880–8888.

[342] Venables, D. S.; Schmuttenmaer, C. A. *J. Chem. Phys.* **1998**, *108*, 4935–4944.

[343] Tee, E. M.; Awichi, A.; Zhao, W. *J. Phys. Chem. A* **2002**, *106*, 6714–6719.

[344] Bockris, J. O.; Reddy, A. K. N. *Modern Electrochemistry: Ionics*; Plenum Press: New York, 1998.

[345] Apelblat, A. *J. Solution Chem.* **2011**, *40*, 1234–1257.

[346] Bardak, F.; Xiao, D.; Hines, L. G.; Son, P.; Bartsch, R. A.; Quitevis, E. L.; Yang, P.; Voth, G. A. *ChemPhysChem* **2012**, *13*, 1687–1700.

[347] Horng, M. L.; Gardecki, J. A.; Papazyan, A.; Maroncelli, M. *J. Phys. Chem.* **1995**, *99*, 17311–17337.

[348] Sajadi, M.; Obernhuber, T.; Kovalenko, S. A.; Mosquera, M.; Dick, B.; Ernsting, N. P. *J. Phys. Chem. A* **2009**, *113*, 44–55.

[349] Zhang, X.-X.; Schröder, C.; Ernsting, N. P. *J. Chem. Phys.* **2013**, *138*, 111102.

[350] Zhang, X.-X.; Liang, M.; Ernsting, N. P.; Maroncelli, M. *Phys. Chem. Lett.* **2013**, *4*, 1205–1210.

[351] Zhang, X.-X.; Liang, M.; Hunger, J.; Buchner, R.; Maroncelli, M. *J. Phys. Chem. B* **2013**, *117*, doi: 10.1021/jp4043528.

[352] Daschakraborty, S.; Biswas, R. *J. Phys. Chem. B* **2011**, *115*, 4011–4024.

[353] Weingärtner, H. *J. Mol. Liq.* **2013**, http://dx.doi.org/10.1016/j.molliq.2013.07.020.

[354] Nazet, A. M.Sc. thesis, Universität Regensburg, 2013.

[355] Marcus, Y. *Ion Properties*; New York, Dekker, 1997.

[356] Bica, K.; Deetlefs, M.; Schröder, C.; Seddon, K. R. *Phys. Chem. Chem. Phys.* **2013**, *15*, 2703–2711.

[357] Bordi, F.; Cametti, C.; Gili, T. *Bioelectrochemistry* **2001**, *54*, 53–61.

[358] McClellan, A. L. *Tables of experimental dipole moments*; Rahara Enterprises, 1989; Vol. 3.

Regensburg, den 10. Dezember 2013

Thomas Sonnleitner